Interlaminar Bonding
in
Ultrasonic Consolidation

By

Hannah Catherine Edmonds

Doctoral thesis submitted in partial fulfilment of the requirements
for the award of
Doctor of Philosophy of Loughborough University

July 2012

Abstract

Ultrasonic Consolidation (UC) is a solid state additive manufacturing process which fabricates three-dimensional objects by ultrasonically joining metal foils together, layer-by-layer, to form a solid part. A wide range of materials can be used to fabricate parts by UC and products with complex internal geometry can be generated by shaping the cross-section throughout the build using Computer Numerically Controlled (CNC) milling. As a result of its ability to embed various secondary materials and fibres in metal matrices, UC has emerged as a potential method of fabricating multi-functional materials and structures.

On some occasions the mechanical properties of parts manufactured by conventional UC can be relatively poor compared to the base material as a result of interlaminar porosity and low bond strength. In order to establish the feasibility of UC as a viable method of manufacturing robust smart materials, interlaminar porosity and part strength must be understood, controlled and improved.

The aim of this research was to investigate the effect of different UC operating parameters, specifically; sonotrode weld surface texture, UC substrate surface texture and foil surface texture, on interlaminar bonding so that appropriate process parameters can be selected to produce parts with different properties for a range of different applications.

Within the investigation white light interferometry was used to characterise the weld surface texture of three sonotrodes and statistical analysis was used to quantify the significance of their effect on UC substrate average surface roughness (S_a) and bond strength over a range of processing conditions. Topology transfer between the different sonotrode weld surfaces and UC substrate surface textures was the examined and the subsequent effect on interlaminar porosity, bond strength and microstructure was measured using optical microscopy, peel testing and Focussed Ion Beam (FIB) microscopy. Stock foil was textured prior to processing by sonotrode rolling (without the ultrasonics engaged) and a comparison of the topology transfer, interlaminar porosity, bond strength and microstructure of samples fabricated using pre-textured foils was conducted compared to samples made with standard stock foil.

Sonotrode weld surface S_a was identified as the most significant factor in determining the resulting substrate surface S_a and interlaminar peel strength in UC, followed by sonotrode oscillation amplitude and weld speed, while weld force did not appear to have a measurable effect over the range of processing conditions examined. The transfer of weld surface texture characteristics from sonotrodes to the samples they produced was observed.

Sonotrode weld surface texture feature amplitude (S_a), spacing (Sal), shape (Sku) and the volume of plastic deformation it generates through contact with the foil surface during processing emerged as factors that appear to effect interlaminar porosity, bond strength and grain morphology in UC. A relationship between the degree of sonotrode-induced deformation and the apparent level of interlaminar recovery and grain growth was proposed and discussed in relation to existing UC bonding theory, including the influence of the surface, volume and Bauschinger effects.

A significant element that was discovered was that UC samples manufactured with pre-textured foils exhibited increased interlaminar porosity but exhibited higher resistance to delamination compared to samples made with stock foil. The change in interlaminar bond characteristics was attributed to the plastic deformation experienced by the foil during the modification process.

The particular vulnerability of sonotrodes with lower S_a to wear and build-up of material in sonotrode surface cavities was also noted.

This investigation has contributed to expanding the existing understanding of how different UC operating parameters effect interlaminar bonding, specifically the significance of plastic deformation. It is anticipated that the results can be used to inform the specification of sonotrode weld surface texture to achieve improved mechanical properties in UC production parts. It is also the authors hope that the research will encourage further investigation into the influence of foil surface modification and how it effects interlaminar bonding in UC.

Publications

Journal Publications:

- Johnson, K., **Edmonds, H.C.**, Higginson, R. L. & Harris, R. A. (2011) New discoveries in ultrasonic consolidation nano-structures using emerging analysis techniques. *Proceedings of the Institution of Mechanical Engineers, Part L: Journal of Materials Design and Applications*, SAGE Publications, 225 (4), pp. 277-287, ISSN: 1464-4207. (**Winner of the 2011 SAGE Best Paper Award**).

- **Edmonds, H.C.** & Harris, R.A. (2011) The effect of electro-discharge machined sonotrode topology on interlaminar bonding in ultrasonic consolidation. *Proceedings of SPIE*, SPIE, 7978 (1), pp. 797814-1 - 797814-13, ISSN: 0277-786X.

- **Edmonds, H.C.** & Harris, R.A. (2012) The effect of sonotrode topology on interlaminar bonding in ultrasonic consolidation. *Journal of Materials Processing Technology*, Elsevier, (in preparation).

- **Edmonds, H.C.** & Harris, R.A. (2012) Substrate surface texture modification and its effects on interlaminar bonding in ultrasonic consolidation. *Materials Science and Engineering: A*, Elsevier, (in preparation).

Conference Presentations:

- **Edmonds, H.C.**, Fitzgerald, C. & Masurtschak, S. (2009) Ultrasonic consolidation research at loughborough university. *Ultrasonic Additive Manufacturing Technology Symposium*, Edison Welding Institute, Columbus, Ohio, USA, October 20th-21st.

- **Edmonds, H.C.** & Harris, R.A. (2011) The effect of electro-discharge machined sonotrode topology on interlaminar bonding in ultrasonic consolidation. *SPIE Smart Structures/NDE*, San Diego, California, 6th-10th March.

Acknowledgements

I would like to thank my PhD supervisor Dr Russell Harris for his advice, support and for providing me with the opportunity to pursue my research. The support and expertise of my second supervisor, Dr Rebecca Higginson, has also been invaluable.

I am grateful for the assistance I have received from Dr Ross Friel throughout my PhD. I would like to thank him for training me to use the UC equipment and allowing me to benefit from his previous research experience in the area.

I would like to acknowledge Mr Andy Sandaver, Mr Jagpal Singh and Dr Geoff West for the technical support they have offered me. I would like to thank them for their generosity in providing their time and expertise.

I would like to thank the EPSRC and IMCRC for funding this research.

I am grateful for the friendship of my fellow PhD students and colleagues within the Wolfson School of Mechanical and Manufacturing Engineering. I would like to particularly acknowledge Simona Masurtschak who has shared the UC research journey with me. I have been lucky to have the support and companionship of someone in a similar position and her unique insight never failed to make me smile.

I would like to thank my family and friends for their unwavering support, willingness to listen and for providing a welcome distraction from my work when it was needed.

Very special thanks go to my partner, Alex Eden, for his patience and support throughout my studies. Thank you for always expecting the best of me and knowing how to help me achieve it.

Finally, I would like to dedicate this work to my Father, Roger Edmonds, who passed away during the period of my research. I have attempted to follow his example of courage and strength in the face of adversity and I hope he would have been proud.

Contents Page

List of Figures

List of Tables

Abbreviations

3D	Three Dimensional
ANOVA	Analysis of Variance
Al	Aluminium
Al_2O_3	Aluminium Oxide
CAD	Computer Aided Design
CDRX	Continuous dynamic recrystalisation
CNC	Computer Numerically Controlled
CW	Continuous Wave
DAZ	Deformation Affected Zone
DBFIB	Dual Beam Focussed Ion Beam
DC	Direct Current
DW	Direct Write
EB	Electron Beam
EBSD	Electron Backscatter Diffraction
EDM	Electrode Discharge Machining
EDM	Electro-Discharge Machined
EDS	Energy-dispersive X-ray spectroscopy
EPSRC	Engineering and Physical Sciences Research Council
FEGSEM	Field Emission Gun Scanning Electron Microscope
FIB	Focussed Ion Beam
FZ	Fusion Zone
HAZ	Heat Affected Zone
IMCRC	Innovative Manufacturing and Construction Research Council
IR	Infra Red
LE	Laser Etching
LMCC	Loughborough Materials Characterisation Centre
LMP	Laser Material Processing
LWD	Linear Weld Density
Ni	Nickel
PMZ	Partially Melted Zone
Q	Quality Factor
RF	Radio-Frequency
RPCAM	Rapid Prototyping Computer Aided Manufacture
S_a	Average Surface Roughness
Sal	Auto-Correlation Length
Sdr	Developed Interfacial Ratio
Sds	Density of Summits
SEM	Scanning Electron Microscopy
SiC	Silicon Carbide
Sku	Kurtosis
SMA	Shape Memory Alloy
SMA	Shape Memory Alloys
SMUC	Smart Material Structures by Ultrasonic Consolidation
SMUC	Smart Material Structures by Ultrasonic Consolidation
S_q	Root Mean Square Roughness
Ssc	Mean Summit Curvature
Ssk	Skewness
Std	Texture Direction
STEM	Scanning Transmission Electron Microscopy

Str	Texture Aspect Ratio
TEM	Transmission Electron Microscopy
UBE	Ultrasonic Bauschinger Effect
UC	Ultrasonic Consolidation
UHR	Ultra High Resolution
Vmc	Core Material Volume
Vmp	Peak Material Voulme
Vvc	Core Void Volume
Vvv	Pit Void Volume

1 Introduction

The following thesis details the work undertaken by the author during their research on interlaminar bonding in ultrasonic consolidation. The current chapter introduces the primary motivation for undertaking an investigation of the research area and presents an overview of the thesis structure.

1.1 Research Motivation

The investigation was undertaken as part of the Smart Material Structures by Ultrasonic Consolidation (SMUC) project in collaboration with Solidica, Inc. and was funded by the Engineering and Physical Sciences Research Council (EPSRC) through the Innovative Manufacturing and Construction Research Centre (IMCRC).

In conventional UC parts interlaminar bond strength can be relatively low, with decreased shear and transverse tensile strength compared to the original base material strength (Schick et al. 2010). Therefore, alongside exploring fibre consolidation capabilities of UC the scope of the SMUC project also included an investigation into factors which effect interlaminar bonding, with a view to optimising the mechanical properties of parts manufactured by UC. Previous research by Johnson (2008) had indicated that sonotrode and pre-process substrate surface topology likely influenced interlaminar bonding in UC and the intention was to further investigate this phenomenon with the view to extensively examine their effect on interlaminar bonding following UC.

Therefore the focus of this investigation was related to specific SMUC project objectives, namely using morphological and mechanical analysis techniques to understand bond formation and identify the predominant factors which influence interlaminar bonding in order to drive refinement of the UC process.

1.2 Thesis Structure

An overview of the thesis structure is shown in Figure 1-1. A critical appraisal of current knowledge in the field of interlaminar bonding in UC and interrelated areas was undertaken (Chapter 2: Literature Review). Research areas which warranted further attention were identified and used to refine the scope of the investigation (Chapter 3: Research Approach). Research Objectives were devised based on the outputs of the literature review and a series of Factors were defined to examine different aspects of the Research Objectives.

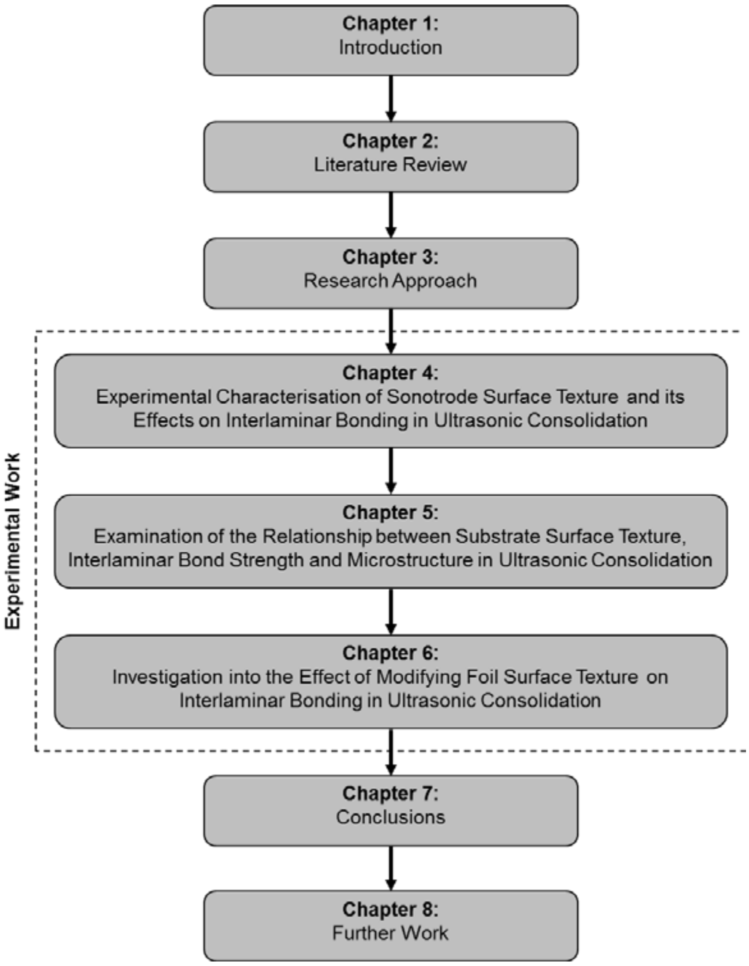

Figure 1-1: Thesis organisation.

A program of experimental work was devised in order to examine the different Research Factors and test the Research Objectives (Chapter 4 - 6). As a result of the experimental investigation of the Research Objectives an updated description of the UC process was developed. A series of conclusions were drawn based on the research findings (Chapter 7).

Finally, recommendations for future work which could further support the stated conclusions or that exceeded the scope of the investigation were suggested (Chapter 8: Further Work).

2 Literature Review

2.1 Deformation Mechanics of Metals

2.1.1 Elastic Deformation

At low loads the relationship between the deformation and applied load in metals is proportional. The magnitude of the reversible dimensional change is normally small and is referred to as elastic deformation (Figure 2-1). Within the elastic deformation range the removal of any applied load results in a return to the original dimensions. Higher loads, that exceed the elastic limit, cause the metal to yield. The load at which elastic behaviour ceases and plastic deformation occurs is the yield point (Lal & Venkata Reddy 2009).

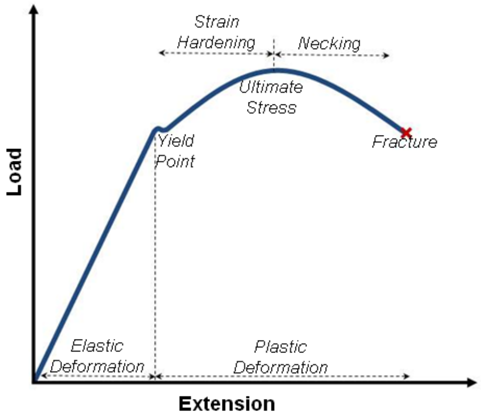

Figure 2-1: Load-extension curve (Adapted from Lal & Venkata Reddy 2009).

On an atomic scale, elastic deformation is a small change in the inter-atomic spacing of the crystal lattice in response to the applied force (Figure 2-2ii). The movement is reversible and the atoms return to their original location when the force is removed (Guy & Hren 1974).

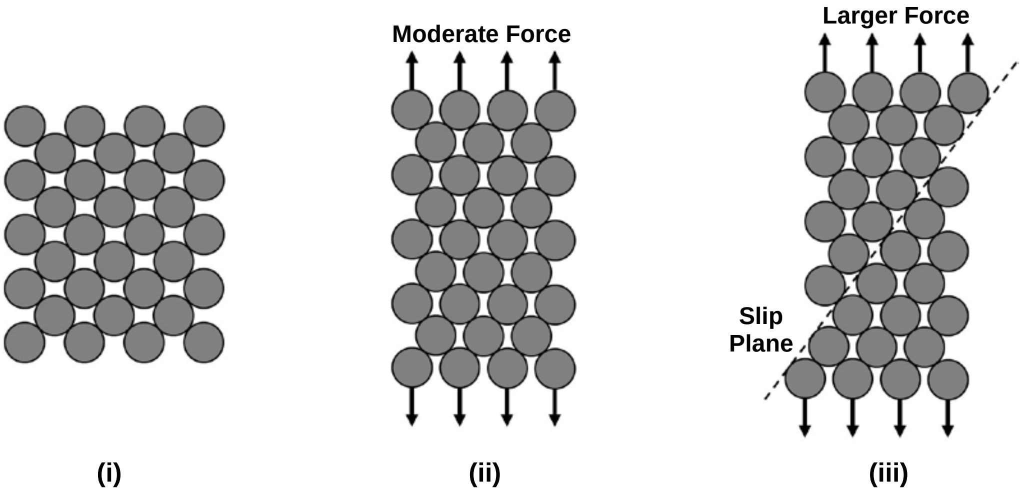

Figure 2-2: Schematic illustration of metallic crystal structure prior to deformation (i), during elastic deformation (ii) and during plastic deformation (iii) (Guy & Hren 1974).

2.1.2 Plastic Deformation

Above the yield point (Figure 2-1) any deformation of the metal is no longer proportional to the applied load and the dimensional changes are permanent (Guy & Hren 1974). At an atomic level the principle mechanism for plastic deformation is slip. The process involves a permanent change in the relative position of adjacent atomic planes by whole atomic spacing's (Figure 2-2iii) (Callister & Rethwisch 2008). The direction of movement occurs along slip planes, most commonly in the direction of closest atomic spacing of the crystal lattice, and is dependent on the cubic cell structure of the material (Figure 2-3).

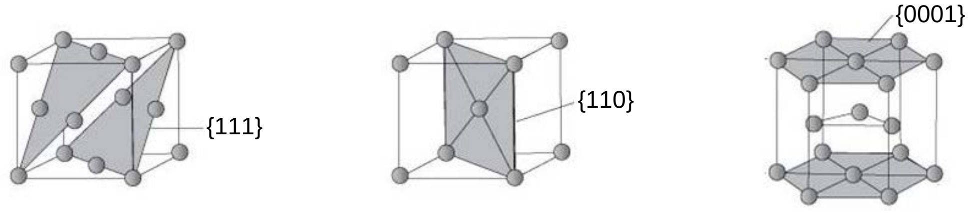

(i) (ii) (iii)

Figure 2-3: Closest packed planes of face centred cubic (i), body centred cubic (ii) and hexagonal close packed (iii) cell structures (ASM International).

Slip occurs when the force applied exceeds the metals yield strength. Large scale plastic deformation is achieved by the sum of numerous small scale slips. The slipped arrangement persists after the force has been removed (Lal & Venkata Reddy 2009).

Within polycrystalline metals the direction of slip varies due to the random orientation of individual grain crystallographic structures. Slip occurs along the orientation of highest shear stress. Individual grains are constrained by their neighbours and cannot deform unless the surrounding grains are also capable of slip.

Deformation can also occur by a process called twinning, where homogenous shear within the crystal recreates the original structure in a different orientation. Unlike slip, where the crystal orientation remains after deformation, in twinning the twin product crystal is a mirror image of the original. With movement of less than an atomic distance, the gross deformation as a result of twinning is minimal compared to slip. Twinning takes place at low temperatures or under shock loading conditions where slip is limited. The key role of twinning is to generate new slip systems, in an orientation favourable to the axis of stress, so that further slip can take place. This is particularly important in body centred cubic and hexagonal close packed structures with a smaller number of slip systems.

Plastic deformation at temperatures significantly below a metals absolute melting temperature, known as cold working, not only results in a change in grain shape due to slip but also causes an increase in dislocation density (Callister & Rethwisch 2008).

2.1.2.1 Dislocations

Dislocations are one dimensional crystalline defects in an otherwise continuous isotropic medium. The mechanism by which deformation occurs is attributed to the movement of dislocations, where the movement of multiple dislocations in various directions results in a net change in shape (Guy & Hren 1974). Dislocations commonly occur in two varieties; edge and screw. Edge dislocations occur along the end of an additional half plane of atoms (Figure 2-4ii), while screw dislocations are generated from shear distortion of the crystal lattice (Callister & Rethwisch 2008).

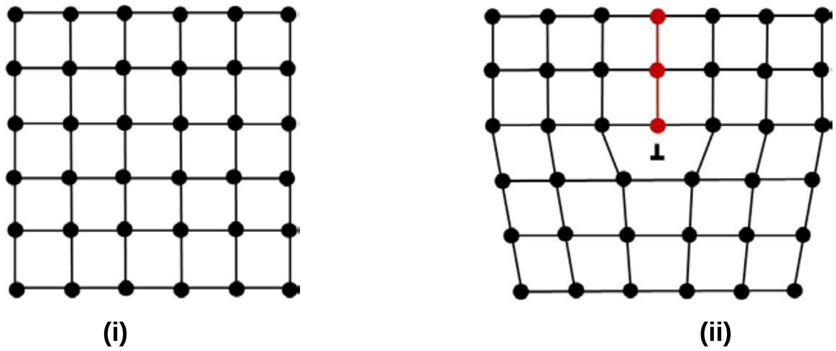

Figure 2-4: Diagram showing a dislocation-free lattice structure (i) and a lattice containing an edge dislocation, ⊥, (ii) (Guy & Hren 1974).

The application of sufficient shear force can cause dislocations to move through the crystal to the surface, generating a unit step of slip (Figure 2-5).

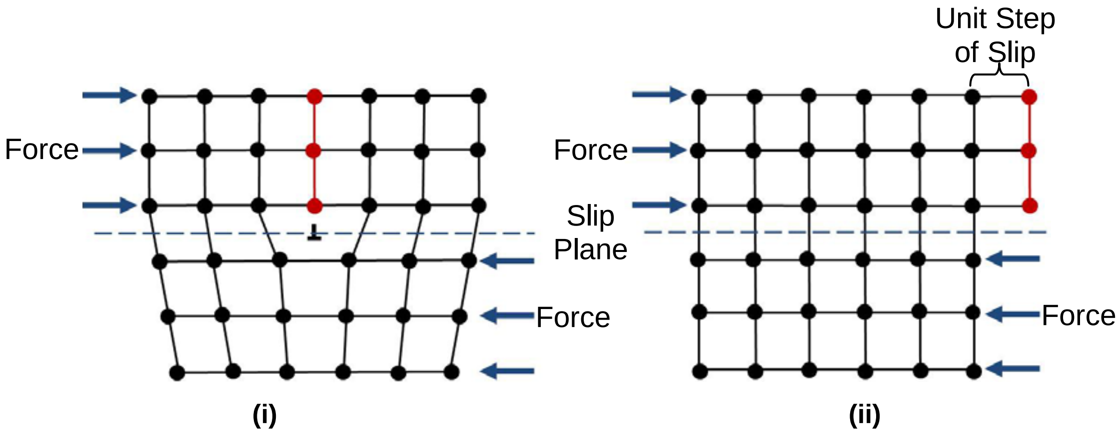

Figure 2-5: Diagram illustrating edge dislocation movement under the application of a shear force (i), resulting in a unit step of slip at the crystal surface (ii) (Guy & Hren 1974).

Edge dislocations move parallel to applied shear forces and perpendicular to the dislocation line along the slip plane through the crystal lattice (Figure 2-6i). Screw dislocations move perpendicular to applied shear forces and parallel to their dislocation line (Figure 2-6ii) (Guy & Hren 1974).

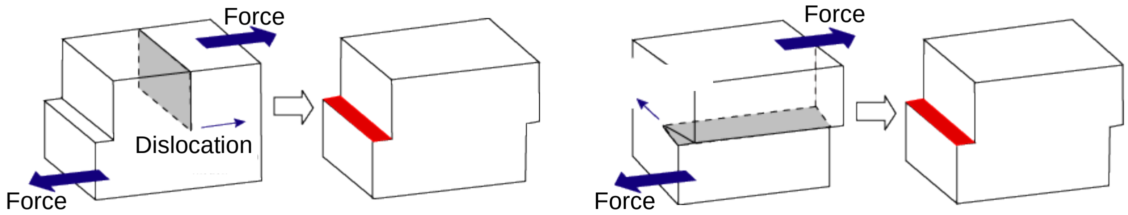

(i) **(ii)**

Figure 2-6: Motion of edge (i) and screw (ii) dislocations through a crystal to form a unit step of slip (NDT Resource Centre).

All metals and alloys contain some dislocations which can arise from thermal stresses during rapid cooling as well as those which are continuously generated during the course of mechanical working. Dislocations cause the surrounding lattice structure to distort as atoms are displaced from their normal position. Strain fields are generated around the line of dislocation, described in magnitude and direction by their Burgers vector. These lattice strains act on surrounding atoms, generating compression above the dislocation and tension below. The movement of dislocations causes the strain fields of dislocations to interact and become tangled. The compressive stress field of one dislocation can be annihilated by the tensile stress field of another, dynamic recovery, while dislocations of the same sign repel each other. At grain boundaries with a high level of misorientation, high angle grain boundaries, dislocations build up and the stress concentrations of these dislocations generate new dislocations in adjacent grains (Callister & Rethwisch 2008)(Guy & Hren 1974)(Hosford 2005).

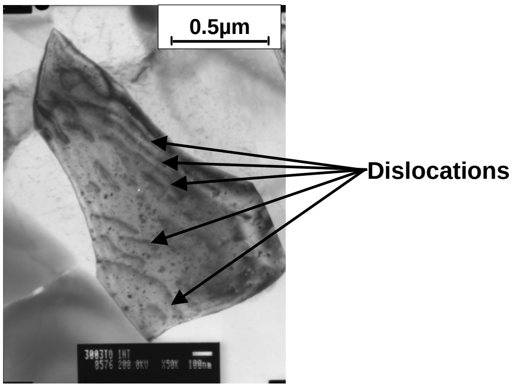

Figure 2-7: Transmission Electron Microscopy (TEM) micrograph highlighting the dislocations present within an Aluminium (Al) 3003-T0 UC sample (Johnson 2008).

The effects of deformation on lattice dislocations can be measured indirectly through changes in material mechanical properties and the local distribution of dislocations can be directly observed through the use of Transmission Electron Microscopy (TEM)(Figure 2-7)(Cotterill & Mould 1976).

2.1.2.2 Strain hardening

Plastic deformation of metals and alloys is dependent on the ability of dislocations to move and it is understood that the interactions between deformations account for much of the strength of crystalline materials. Metals become more resistant to deformation as a result of strain field interactions between dislocations as their density increases (Arsenlis & Parks 2002). Obstruction in the movement of dislocations causes an increase in the yield, tensile strength and hardness of the metal and a reduction in ductility (Figure 2-1). This process is referred to as work hardening, strain hardening or cold working, as it occurs at a temperature low when compared to a given metal's melting point (Callister & Rethwisch 2008).

The deformation behaviour of a metal is dependent upon the temperature and strain rate. Dislocation density increases as the strain rate increases and temperature decreases. At low strain rates dislocations appear uniform in distribution, while at higher strain rates the density is increased and dislocations build up at grain boundaries to form a cell structure. An increase in temperature reduces the yield stress and reduces the effects of strain hardening, while higher strain rates increase the yield stress. During hot working, plastic deformation above the metals recrystallisation temperature, the metal does not strain harden and larger deformation is possible without the embrittlement and cracking which occurs as a result of excessive cold working (Cotterill & Mould 1976)(Guy & Hren 1974)(Lal & Venkata Reddy 2009).

2.1.2.3 Grain Size

As a result of plastic deformation grains subdivide into misorientated regions with high angle dislocation boundaries (Doherty et al.1997). Metals with a smaller average grain size are more resistant to the motion of dislocation and exhibit a higher yield strength due to their higher surface area to volume ratio than coarse-grained metals.

Equation 2-1: $$\sigma_y = \sigma_O + kd^{-1/2}$$ (Bonetti et al. 1997)

The relationship between yield strength and grain size can be calculated using the Hall-Petch equation (Equation 2-1), where the yield stress, σ_y, is dependent on the frictional stress of the lattice opposing the movement of dislocations, σ_O, strengthening coefficient, k, which is constant for a given metal and average grain size, d (Bonetti et al. 1997).

2.1.2.4 Recovery

Dislocations introduced during plastic deformation can be reduced through recovery at elevated temperatures. Recovery can occur dynamically during hot working or statically through annealing after cold work. An increase in temperature promotes atomic diffusion and rearrangement of the crystal structure is driven by a tendency to reduce the internal strain energy of individual grains by reducing the number of dislocations (Callister & Rethwisch 2008)(Cotterill & Mould 1976).

Original material properties are only partially restored through the annihilation and rearrangement of dislocations. Microstructural changes are relatively homogeneous and do not normally affect the boundaries between the deformed grains (Figure 2-2ii). Recovery is easier in metals with high stacking fault energy, such as aluminium (Slamova et al. 2004).

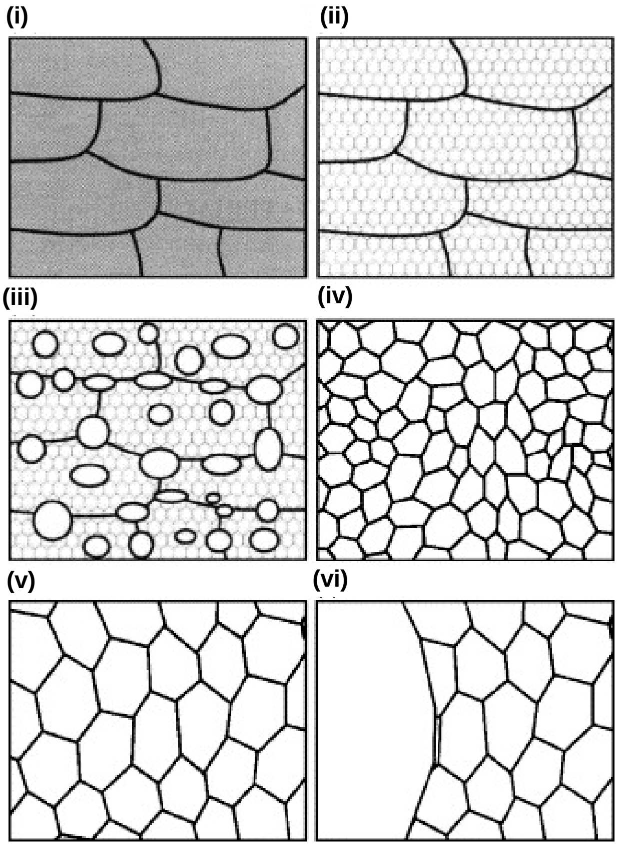

Figure 2-8: Schematic representation of the main softening processes: deformed state (i), recovered (ii), partially recrystallized (iii), fully recrystallized (iv), grain growth (v), and abnormal grain growth (vi) (Humphreys & Hatherly 1995).

2.1.2.5 Recrystallisation

Recrystallisation is the nucleation and growth of new, unstrained, equiaxed grains that occur at elevated temperatures (Figure 2-2iii). Short range diffusion enables the growth of these grains until they consume the parent material (Figure 2-2iv). Unlike recovery, recrystallisation involves a change in crystal orientation achieved by the passage of high angle grain boundaries through the material. The recrystallised metal has a low dislocation density, is less hard and more ductile. As with recovery, recrystallisation can occur dynamically during hot working or statically through annealing after deformation.

The temperature at which recrystallisation occurs is dependent upon the metal or alloy, but is normally between a third to half of the absolute melting point. The rate at which recrystallisation occurs is dependent upon the level of deformation and temperature; a high degree of cold working and higher temperatures result in a faster rate of recrystallisation (Callister & Rethwisch 2008)(Cotterill & Mould 1976).

Grain growth is commonly, but not necessarily proceeded by recovery or recrystallisation. The driving force for an increase in grain size is a reduction in internal energy and is achieved by the relative decrease in the boundary area of a grain. Continued grain growth is achieved by grain boundary migration, where large grains grow at the expense of smaller grains through the short range diffusion of atoms across the grain boundary (Figure 2-2v). The extent of grain growth is dependent upon the temperature and duration of heating (Callister & Rethwisch 2008).

2.2 Joining Mechanisms in Metal Welding

Messler (1999) defines welding as the joining of materials of the same fundamental type through the formation of primary, and sometimes secondary, chemical bonds under the combined action of heat and pressure. The mechanisms by which metal welding processes achieve metallic continuity can be classified as one or more of the following;

- Solid-phase plastic deformation.
- Diffusion.
- Melting and solidification.

Joining by solid-phase plastic deformation occurs when two solid-phase crystalline materials are brought sufficiently close enough to enable permanent bonds to be formed at equilibrium spacing. The rapprochement of material is achieved through plastic deformation and mutual attraction at an atomic level. Solid-phase plastic deformation can occur with or without the external application of thermal energy. Figure 2-9i shows how crystal lattices are deformed and remain in a strained state when joining occurs without any additional heating. In this case, referred to as cold welding, no recrystallisation occurs and the effects of work hardening remain at the interface. Increasing the temperature at which joining occurs to 40-50% of the materials melting point results in more plastic deformation, more disruption of any surface contaminants and subsequently better bonding. Figure 2-9ii shows how the hot deformation welding process removes cold work effects through dynamic recrystallisation, where new grains nucleate and grow across the weld interface. Dislocation density and lattice distortion decrease and atoms are rearranged into common orientation across the interface.

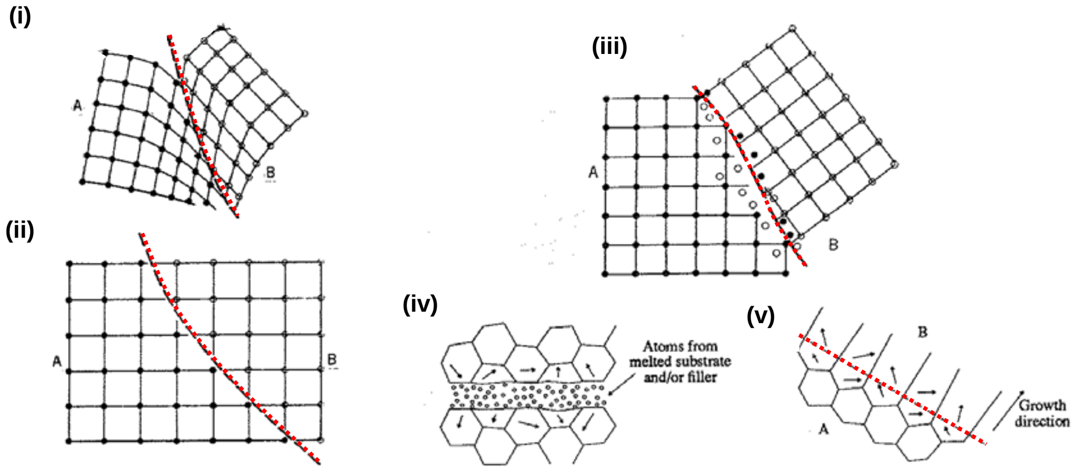

Figure 2-9: Mechanisms for obtaining metallic continuity; (i) Cold deformation and lattice strain, (ii) Hot deformation and dynamic recrystallisation, (iii) solid phase diffusion across original weld interface, (iv) melted parent material (v) epitaxial solidification of the parent materials establishing a bond (red line indicates location of the weld interface) (adapted from Messler 1999).

The properties of the base metal are then restored. Diffusion can be described as the “transport of mass from one place or piece to another across an interface through atom movement” Diffusion occurs in the majority of both solid or liquid-phase welding processes. Solid-phase diffusion occurs through simultaneous recrystallisation under the influence of heat and pressure as atoms move in both directions across interface (Figure 2-9iii). Joining by melting and subsequent solidification is seen in all welding processes where melting occurs. Gross mass movement is achieved through the melting and flow of material at the weld interface (Figure 2-9iv). Epitaxial growth occurs as crystals solidify onto the existing solid base metal along the interface. Favourably orientated grains, with respect to the existing structure, grow across the interface (Figure 2-9v). Microscopic scale diffusion into the base metal is seen upon solidification (Messler 1999).

2.2.1 Nonfusion Welding

Table 2-1 summarises some of the benefits and drawbacks of the nonfusion welding process.

Table 2-1: Relative advantages and shortcomings of nonfusion welding processes (Messler 1999).

Advantages	Disadvantages
1. General absence of melting and, thus, solidification (so structure is retained).	1. Stringent requirements for cleaning joint faying surfaces for some processes.
2. Minimal change to microstructure due to low heat input.	2. Elaborated tooling is required for some processes.
3. Wide variety of process embodiments.	3. Challenging inspection of joint quality.
4. Applicable to the joining of dissimilar metals (since there is little or no mixing).	4. Repairing process-induced defects is difficult.
5. High joint efficiency is possible for many situations where the same cannot be said for fusion welding processes.	5. Processes require specialized equipment which are rarely portable, and almost always must be automated.

2.2.1.1 Diffusion Welding

While the diffusion process appears to be an important aspect of most welding processes it is also a method of nonfusion joining in its own right. Diffusion welding refers to the joining of materials in their solid state using only the diffusion of atoms under pressure at elevated temperatures. Unlike friction welding no macroscopic deformation or relative motion is used in diffusion welding (Messler 1999).

Conditions for good diffusion bonding requires:

1. No contamination of mating surfaces and adequate surface finish, therefore clean, polished surfaces are required.
2. Plastic flow/creep capability of components to enable complete contact between interfaces to occur.
3. Time for diffusion to occur allowing microstructural instabilities to be eliminated and development of strong bonds (Brandon & Kaplan 1997).

Bonding occurs as a result of the development and expansion of contact points through material plastic flow. The contact area is inversely proportional to the local stress. As the contact area increases the rate of plastic flow decreases as the stress decreases (Brandon & Kaplan 1997).

2.2.1.2 Friction Welding

Friction welding is a nonfusion, solid state welding process where, instead of melting, solid-phase plastic deformation occurs as a result of the heating effects from friction. Friction welding joins objects utilising compressive force and relative motion. Parts are moved relative to each other in rotation or angular/linear reciprocation under moderate pressure. The consequential friction generates heat, scrubbing away surface oxides, causing material around the weld to soften. When sufficient thermal softening and plastic deformation has occurred the relative motion ceases and the applied pressure is increased. The forging step follows, where the applied pressure is maintained while the joined parts cool naturally and metallurgical continuity is established. Burr's or collars at the weld interface often occur (Messler 1999)(Vill 1962).

Figure 2-10 shows two different types of friction welding along with the direction of differential movement and applied force.

(i) (ii)

Figure 2-10: Schematic of rotary (i) and linear (ii) friction welding (Messler 1999).

Friction weld quality is dependent on the relative velocity of faying surfaces, the magnitude of applied pressure which affects the frictional heating and subsequent plastic deformation achieved. The presence of surface contaminants, surface finish, shape of part and processing temperature also affect bonding. The surfaces of metals are commonly covered with surface oxides or other surface contaminants; the relative motion of the faying surfaces disrupts these surface coatings to the exposure of the base material and enabling intimate contact and the formation of bonds (Brandon & Kaplan 1997)(Vill 1962).

The extent of geometrical interlocking and formation of contact points is dependent on materials surface roughness. Polished surfaces limit the depth of material affected at the surface, while the presence of any lubricants inhibit the formation of contact points. Contacts points between the surfaces of the reciprocating bodies are repeatedly made and broken. Sliding contact causes shear displacement of surface asperities parallel to plane of contact, resulting in shear stress failure. Plastic flow occurs to relieve the built up compressive stress. As the temperature increases due to frictional heating, the rate of plastic flow increases (Brandon & Kaplan 1997). A great number of metals and alloys can be friction welded together or to dissimilar materials and the process has low running cost compared to other welding processes. One drawback of friction welding is the limitations in size and shape of parts that can be joined (Vill 1962).

2.2.1.3 Ultrasonic Welding

In order to ultrasonically weld two parts overlapping work pieces must be clamped together between two jaws or a sonotrode tips and anvil. The ultrasonic vibrations are transmitted through one or both of the tips oscillating in a plane parallel to the weld interface. The motion in ultrasonic welding is achieved by converting an alternating current electrical power source using a piezoelectric transducer to generate by ultrasonic frequency mechanical vibration (Daniels 1965).

Figure 2-11 illustrates how the piezoelectric transducer induces ultrasonic vibrations between two parts, scrubbing the surfaces together under an applied weld force. The mechanism by which joining is achieved in ultrasonic welding is examined further, in the context of UC, within section (2.3.3).

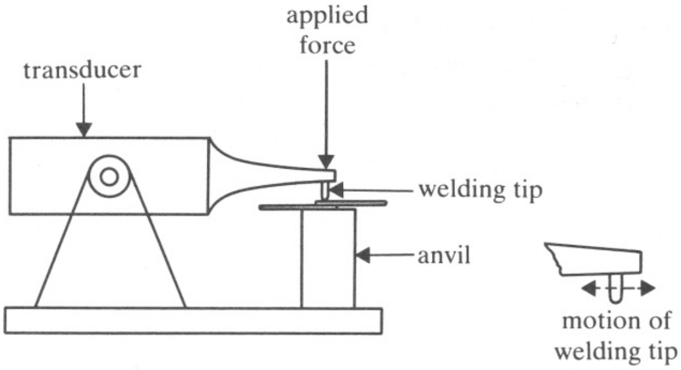

Figure 2-11: Schematic of ultrasonic welding system (Lancaster 1987).

Most conventional weld types can be achieved through ultrasonic welding, including; spot, seam, butt, area and ring-seam joints (Neppiras 1965). It is also possible to join dissimilar metals or metals to non-metals through ultrasonic welding (Daniels 1965).

2.3 Ultrasonic Consolidation

2.3.1 Process Overview

UC is a layered manufacturing process for fabricating three-dimensional (3D) objects by incrementally adding and consolidating material layers using ultrasonic vibrations and pressure (White 2002b). It was originally developed as a ‘direct’ metal component and tooling solution (Kong et al. 2003). The main principles of UC are similar to rapid prototyping and rapid tooling processes. UC uses ultrasonic welding as the basis of this solid freeform fabrication technique for the manufacture of near-fully dense metal parts at near-room temperature (Kong et al. 2005).

UC components are built up by ultrasonically welding thin material layers to previously deposited material, forming a solid part and then shaping that part by removing excess material using CNC milling.

2.3.1.1 Process Equipment

The UC process is currently commercially available as the SonicLayer™ 4000 from Fabrisonic LLC, but was previously known as the Formation^{TM} from Solidica Inc. (Figure 2-12).

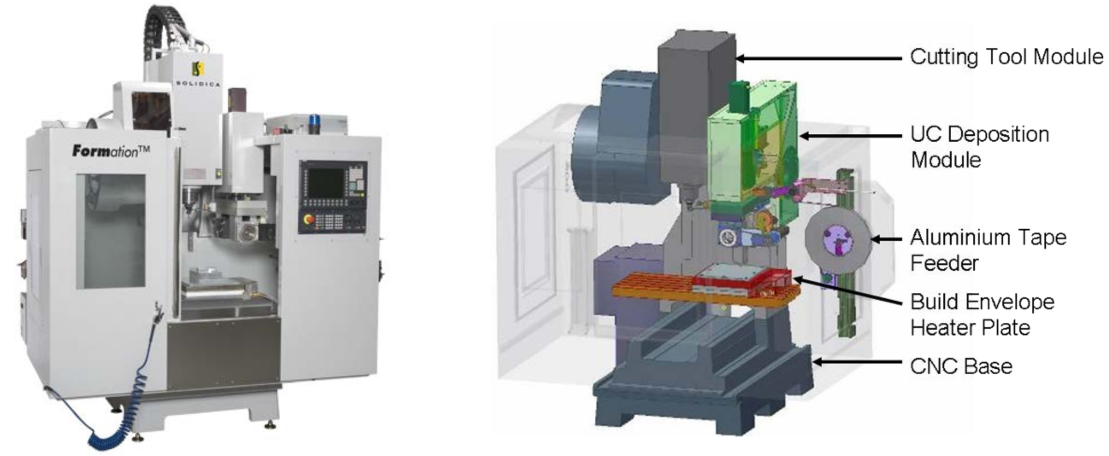

(i) **(ii)**

Figure 2-12: The Formation^{TM} (i) and a schematic of the machine (ii) (Johnson 2008).

In order to fabricate a UC part the desired geometry is initially represented in a Computer Aided Design (CAD) file. Then, using the Rapid Prototyping Computer Aided Manufacture (RPCAM) software, the CAD file is split into 0.1mm slices, representing each layer of the build (White 2003). The RPCAM software then calculates the appropriate tape lay patterns and G-code CNC tool paths to construct the part. The optimal weld speed, oscillation amplitude, weld force and build temperature for the material can then be specified by the user (George & Stucker 2006).

To form a base for the part a consumable base plate is bolted to the anvil of the Formation machine (Figure 2-13) which is heated to the required build temperature by an element in the anvil. UC parts can be built at room temperature (72^{o}F/22^{o}C) up to 400^{o}F (204^{o}C), although the build temperature is generally set to 300^{o}F (150^{o}C) (Siggard et al. 2006). The base plate undergoes a flat-pass milling operation to zero the plate with respect to the machine and remove oxides or contaminants on the plate surface (George & Stucker 2006).

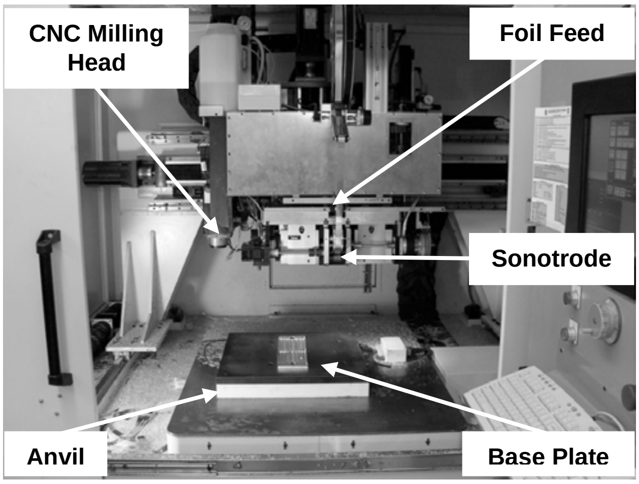

Figure 2-13: Key components of the Fabrisonic SonicLayer^{TM} 4000 UC machine (Janaki Ram et al. 2007).

The standard foil size used in commercial construction of UC parts is 0.15mm x 25mm (Janaki Ram et al. 2006b). The foil is fed and drawn under the rotating sonotrode which oscillates, at ultrasonic frequencies, perpendicular to the weld direction and applies a normal force, referred to as the weld force, onto the metal foil strip (Figure 2-14i). The movement of the sonotrode generates a scrubbing action between the metal foil and base plate which distributes the surface oxide layer of the metal and initiates the weld (Figure 2-14ii-iii). The weld progresses as the sonotrode traverses along the work-piece. Subsequent foils are ultrasonically consolidated to the base plate in adjacent rows until the first layer of the part is complete. The process repeats itself, building up the part layer-by-layer, consolidating foils on top of the previously deposited material.

After the consolidation of four foil layers the excess material is machined away to generate the contour of the part shape (Tuttle 2007) and any swarf is removed using compressed air (George & Stucker 2006). The part geometry is more accurately sculpted every 3-6 mm until the part is complete. Once completed, the part will require no further finishing processes. The UC build process itself is flexible and parts can be paused, modified and restarted during the build (White 2003).

The feature-to-feature accuracy of parts fabricated on the Formation 2030 is within +/-0.002in to +/-0.005in (+/-50.8µm to +/-127µm), depending on object geometry, with a build envelope of 24in X 36in (0.61m x 0.91m) (White 2002a). The Formation machine can lay and consolidate foils at approximately 2.5m/min (White 2003).

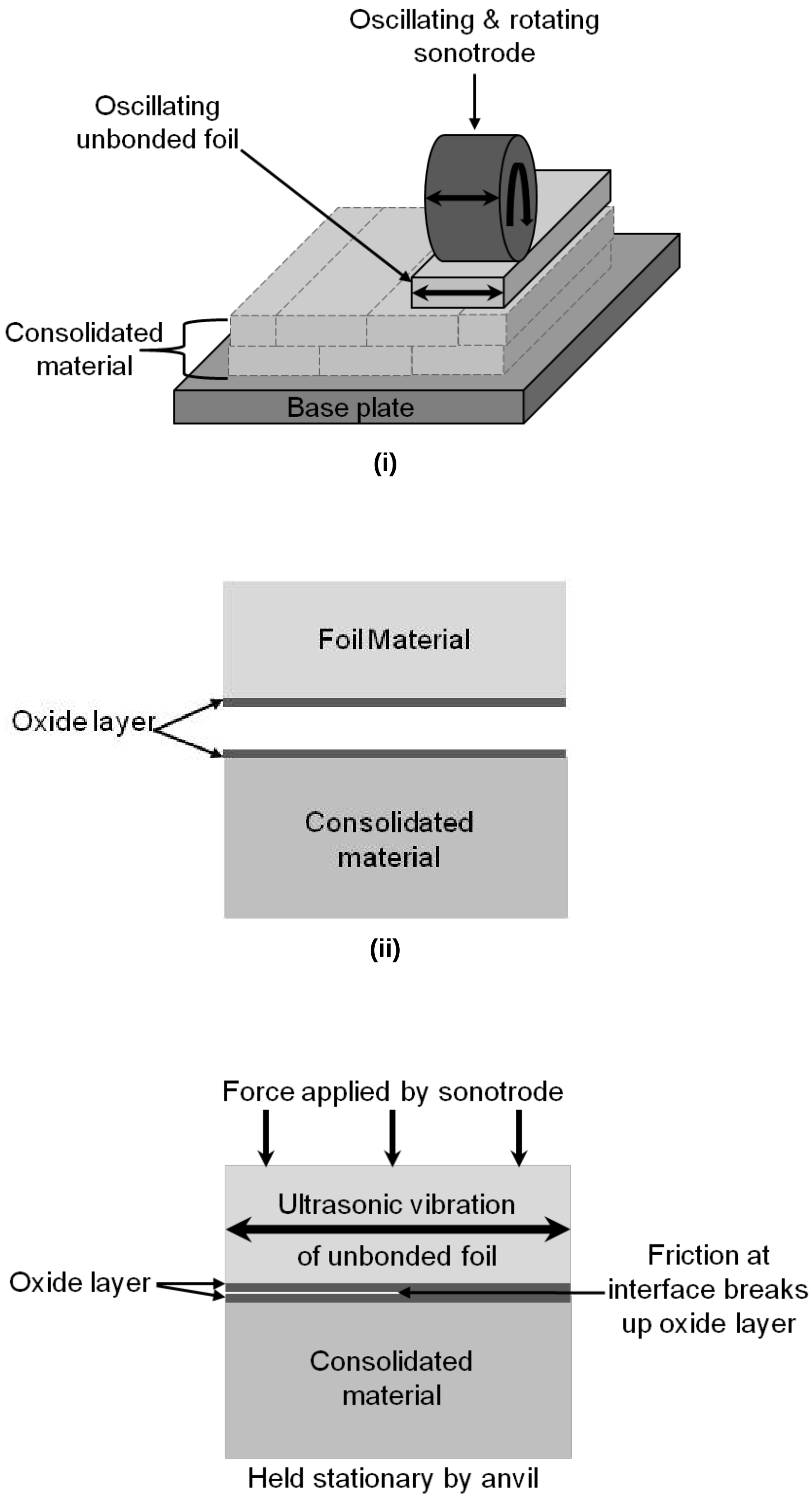

(i)

(ii)

(iii)

Figure 2-14: Schematic of the UC process illustrating the deposition of foil (i) and the bond interface (ii-iii).

2.3.1.1.1 Alpha 2 UC machine

The Alpha 2 UC machine is a research variant of the commercial UC equipment produced by Solidica Inc. The equipment is based on the same principles as the Formation machine from Solidica and enables research into various aspects of the UC process without the CNC milling capability.

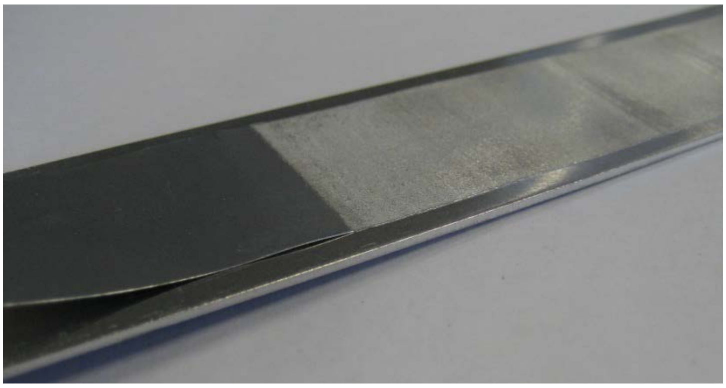

Figure 2-15: Individual foil width single layer UC sample fabricated by the Alpha 2 UC machine.

The Alpha 2 UC machine was built around a commercially available 3.3kW ultrasonic seam welder (Kong et al. 2003) and can be used to build up single foil width multilayer UC samples (Figure 2-15). This equipment has been used in a significant amount of research undertaken within the field of UC (Kong, Soar, & Dickens 2004) (Kong 2005) (Kong & Soar 2005a) (Kong & Soar 2005b) (Kong, Soar, & Dickens 2005) (Li & Soar 2009a) (Li & Soar 2009b) (Friel & Harris 2010) (Friel, Johnson, Dickens 2010) (Friel 2011).

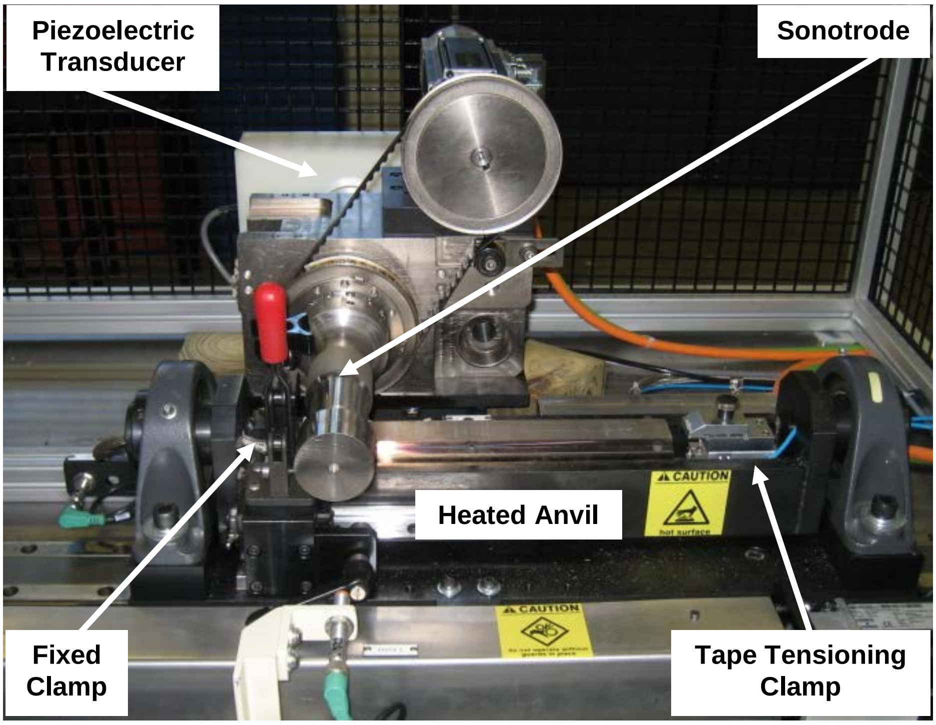

Figure 2-16: Alpha 2 UC machine.

The Alpha 2 UC machine (Figure 2-16) operates at a constant frequency of 20kHz and the sonotrode, which is in line with transducer and booster, rotates counter clockwise at a user defined speed. The piezoelectric transducer generates the sonotrode oscillations, perpendicular to the weld direction. A pneumatic cylinder supports the linear floating anvil and controls the applied weld force. The range of the operational parameters include sonotrode oscillation amplitude from 12 to 21µm, weld force between 100 to 2000N and weld speed from 0 to 100 mm/s. The anvil also contains an inbuilt heating element and temperature sensor to control and monitor the build temperature.

2.3.1.1.2 Higher Power UC Machine

The SonicLayer^{TM} 7200, from Fabrisonic LLC, (Figure 2-17i) is a production scale automated UC system that became commercially available in 2012. The higher power 9-kW machine includes an integrated 3-Axis CNC Machining and automated tape feed system similar to the original Formation^{TM} with an expanded load capacity of 5000lbs and larger build envelope of 72in x 72in x 36in (1.83 x 1.83 x 0.91m).

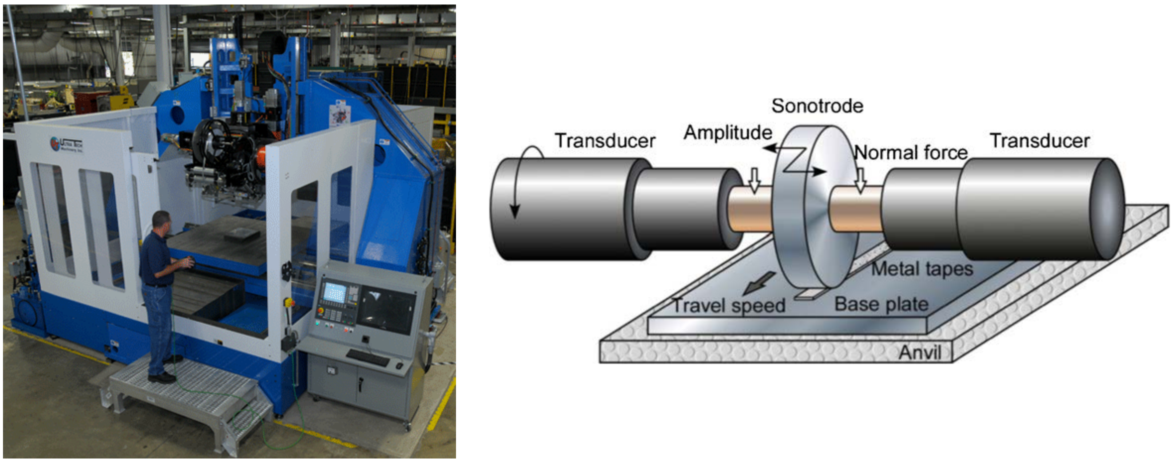

(i) (ii)

Figure 2-17: (i) The SonicLayer^{TM} 7200 High Power UC machine (Fabrisonic LLC 2012) and (ii) a schematic of the double transducer–sonotrode system which it utilises (Sriraman et al. 2011).

The higher power UC machine employs two transducers operating in tandem either side of the sonotrode which operate 180° out of phase to provide an increased range of vibration amplitudes to 52µm under higher weld forces (Figure 2-17ii) (Sriraman et al. 2012).

2.3.1.2 Materials

UC has the ability to process a wide variety of metals including aluminium, titanium, magnesium, copper and steel (Kong et al. 2003) (Tuttle 2007) in the form of thin foils. The common foil thickness used is 100-150µm, however thicker foils can be used for faster build times but this can sometimes lead to incomplete bonding between build layers (Kong et al. 2005).

UC could be potentially used to process the same range of metals as those which can be joined by ultrasonic welding (Figure 2-18). An advantage of UC is that it uses off the shelf materials and does not require any pre-processing which reduces running costs (George & Stucker 2006).

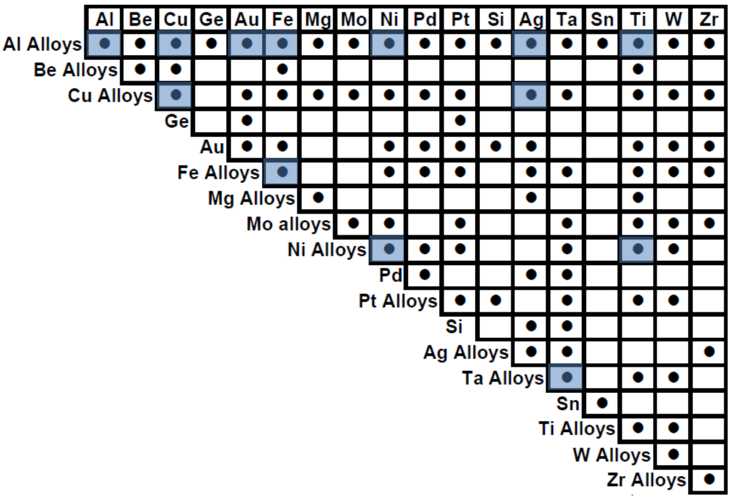

	Al	Be	Cu	Ge	Au	Fe	Mg	Mo	Ni	Pd	Pt	Si	Ag	Ta	Sn	Ti	W	Zr
Al Alloys	🟦●	●	🟦●	●	🟦●	🟦●	●	●	🟦●	●	●	●	🟦●	●	●	🟦●	●	●
Be Alloys		●	●			●										●		
Cu Alloys			🟦●		●	●	●	●	●	●	●		🟦●	●		●	●	●
Ge					●						●							
Au					●	●			●	●	●	●	●			●	●	●
Fe Alloys						🟦●			●	●	●		●	●		●	●	●
Mg Alloys							●						●			●		
Mo alloys								●	●		●			●		●	●	●
Ni Alloys									🟦●	●	●			●		🟦●	●	
Pd										●			●	●				
Pt Alloys											●	●		●		●	●	
Si													●	●				
Ag Alloys													●	●				●
Ta Alloys														🟦●		●	●	
Sn															●			
Ti Alloys																●	●	
W Alloys																	●	
Zr Alloys																		●

Figure 2-18: Table illustrating the ultrasonic welding compatibility of metals and those that have been processed by UC (highlighted in blue) (adapted from Johnson et al. 2007).

2.3.2 Applications

UC has found applications in a number of areas, including the electronics, automotive, aerospace and defence industries (Janaki Ram et al. 2006a). As well as building prototype and production components, UC has also been used to fabricate injection moulding, extrusion vacuum forming tooling applications (Figure 2-19) (White 2003).

Figure 2-19: An example of a tool cast from a UC manufactured mould (White 2003).

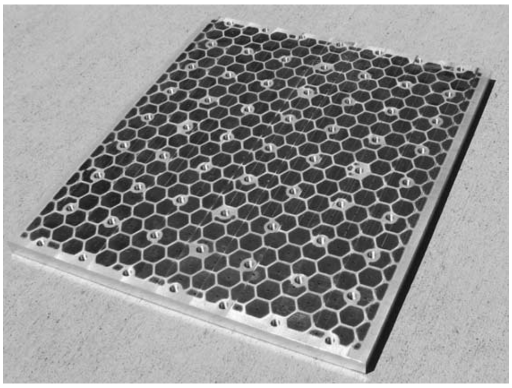

Figure 2-20: UC manufactured lightweight structural panel developed for use in small satellite systems (George & Stucker 2006).

Voids can also be purposefully included to make lightweight honeycomb structures (Figure 2-20) (George & Stucker 2006). UC's capability for constructing complex internal geometry in metal parts has also been used in the construction of thermal management devices (Figure 2-21).

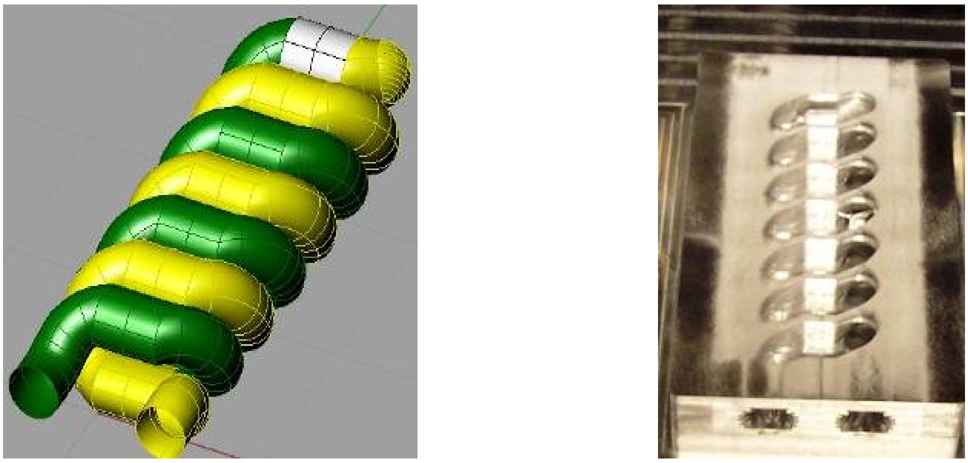

(i) **(ii)**

Figure 2-21: Double helix thermal management design (i) and partially built UC component (ii) (Graff 2009).

The UC process costs less than conventional methods of processing prototype parts, such as casting, forging and machining, with the added capability to fabricate complex internal geometries that are not possible through conventional milling alone (Dehoff & Babu 2010). With the advantages of both additive and subtractive processes, UC has the capability to produce parts with high dimensional accuracy and surface finish and complex internal structures (Janaki Ram et al. 2006a). The geometry of the finished part is not limited by feedstock geometry because of the in-built CNC milling capability and the surface finish is therefore equivalent to the quality of CNC machining (White 2003).

UC was originally developed as a fast production, low cost competitor for existing rapid tooling direct metal aluminium tooling processes (White 2002a). As a solid state process UC has numerous advantages over laser fusion freeform techniques. It is a low energy process as it requires relatively low temperatures and only a small volume of the material is affected. The low temperature nature of UC means that unlike liquid-phase processes heat dissipation time is faster and, as a result, deposition rates can be faster as cooling time is not an issue. As no phase change occurs during UC processing significantly less change in dimensions takes place and hence less thermal distortion and smaller thermal gradients and residual stresses are seen in parts. Unlike other fusion welding based processes, UC parts are not vulnerable to solidification defects (porosity, inclusions, incomplete fusion, columnar and segregated structures, etc.) Another benefit of solid state processing is that no atmospheric control or inert gas shielding is required to limit oxidation of molten metal. UC is also safer than liquid phase processes and enables the welding of dissimilar metals that would be hazardous when mixed together in powder form. No fillers or binders are required for UC and therefore the composition for the finished part is uniform (Doumanidis & Gao 2004)(Johnson 2008)(Kong et al. 2003)(Kong et al. 2004)(White 2003).

One drawback of the UC process is the part height to width ratio limit, an issue when building parts with tall, thin freestanding ribs. Because of the differential motion of the sonotrode, which is required to ultrasonically bond the foils together, the base material must be sufficiently stiff in order to resist the sonotrode vibration (Figure 2-22). This currently means that the UC process cannot fabricate tall thin ribs. Experimentation has shown that the maximum achievable height-to-width ratio for Al 3003 alloys is 1:1 (George & Stucker 2006).

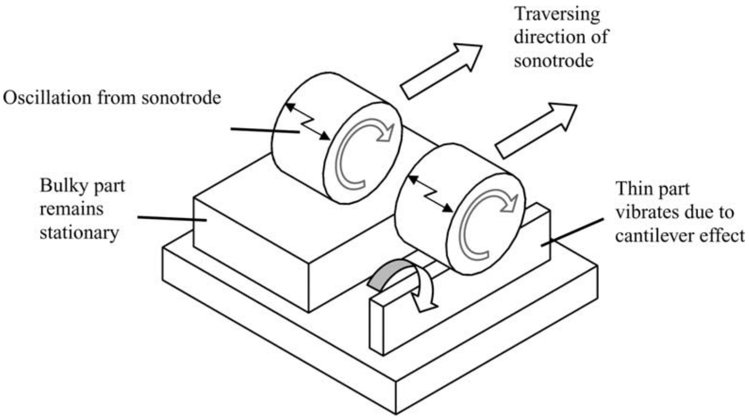

Figure 2-22: Illustration of the height-to-width ratio build limitations of UC parts (George & Stucker 2006).

2.3.2.1 Joining Dissimilar Metals

UC can be used to bond dissimilar metals to make low cost, lightweight laminate metal materials (Figure 2-23) or graded composition components (Kong et al. 2005). UC has the ability to chemically and mechanically enhance critical regions of components by varying the foil material used during fabrication and research has been undertaken into the potential production of nickel-titanium graded composition materials (Domack & Baughman 2005).

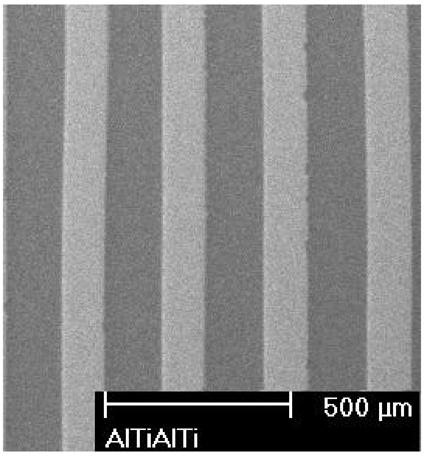

Figure 2-23 - Titanium/Aluminium laminate material fabricated using the UC process (Johnson 2008).

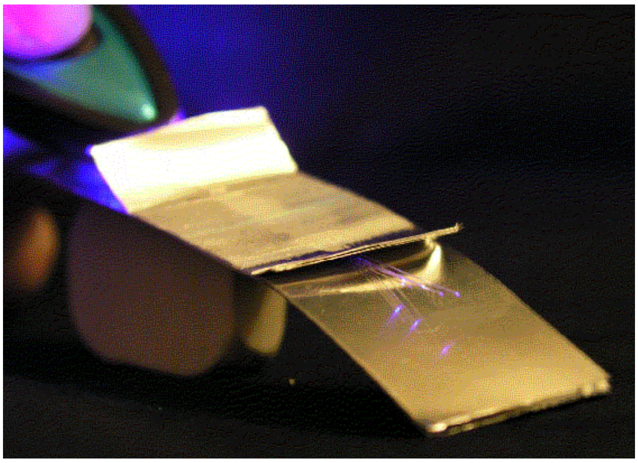

Figure 2-24 - Optical fibres embedded using UC.

2.3.2.2 Component Embedding

UC has emerged as a method of producing metal components with encapsulated mechanical and electrical components. The resulting electrical system is contained within a solid metal part, providing inherent barriers to the outside ensuring safety from hostile environments and external tampering (Siggard et al. 2006).

Direct Write is a process which prints passive or active electronic components, for example conductors, insulators batteries, capacitors, direct from a computer file. UC can be used in combination with the DW process to directly manufacture complex electronic systems e.g. electronic circuitry, antennas and other devices (Robinson et al. 2006).

Previous research has shown that UC can be used to embed sigma silicon carbide (SiC) fibres, shape memory alloy (SMA) wires and optical fibres into Al 3003 (Figure 2-24) (Friel & Harris 2010)(Kong et al. 2005b). This work was undertaken with the aim to construct adaptive composite structures, for use in aerospace and emerging sports and automotive applications, which can monitor external conditions and respond by adapting their structure accordingly.

Smart metal structures with embedded optical fibre sensors could allow continuous monitoring of that structures condition, reducing the need for front end electronics, enabling systems to be more light weight and less obtrusive with the in-built protection of the metal encapsulation. This monitoring would be a closed loop adaptive control system, as opposed to existing systems where maintenance is carried out on time-based schedule. Unlike alternative methods for embedding sensors, like casting or metal deposition, UC can also incorporate reinforcing or actuating fibres, like SiC and SMA, simultaneously (Kong & Soar 2005a). UC is emerging as a primary enabling technology for the creation of fully integrated ‘smart’ structures (Friel & Harris 2010).

2.3.3 Proposed Joining Mechanisms in Ultrasonic Consolidation

It has been proposed and debated that there are a number of competing mechanisms through which interlaminar bonding is thought to be achieved in UC; mechanical interlocking of asperities, melting and solidification, ceramic bonding, diffusion and atomic forces across nascent material. This lack of fundamental understanding of the key interfacial bonding mechanisms has proved a key limiting factor in optimising bond strength in UC and eliminating undesirable features, such as interlaminar voids (Johnson 2008). The different mechanisms, and supporting literature, are presented in the following sections.

2.3.3.1 Mechanical Interlocking

Within ultrasonic metal welding, interlocking of surface irregularities is presented as a potential mechanism of bonding. The alternating shear forces generated through the contact of mating surface asperities generate significant plastic deformation and material flow to accomplish joining through mechanical interlocking (Figure 2-25) (Prieb 1999).

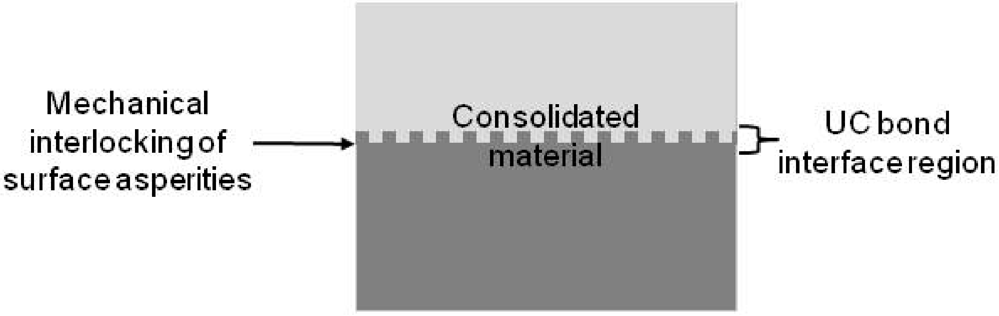

Figure 2-25: Schematic of the proposed joining mechanism in UC of mechanical interlocking of surface asperities

However, the study of ultrasonically consolidated similar and dissimilar metal samples by Yang et al. (2009) exhibited only flat interfaces, undermining the theory that bonding in UC might be achieved through mechanical interlocking alone (Figure 2-26).

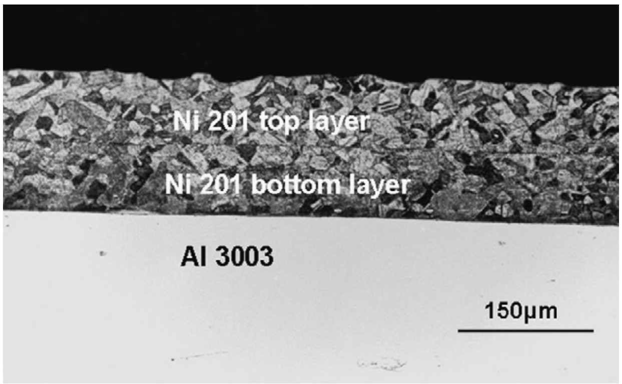

Figure 2-26: SEM micrograph of the UC bond interface between Al 3003 and Nickel (Ni) 201 (Yang et al. 2009).

While mechanical interlocking during UC may not occur in all instances it could still act as a contributing factor in the joining of dissimilar materials with a significant difference in hardness (Yang et al. 2009).

2.3.3.2 Melting and Solidification

UC is generally regarded as a solid state layer manufacturing process capable of generating wholly metallurgical bonded parts without any phase change (Siggard et al. 2006).

Frictional heating arises from the relative motion between the sonotrode and foil and the mating surfaces foil and substrate during UC. Heat is also thought to be generated through deformational heating at these interfaces (Schick, et al. 2011)(Siddiq & Ghassemieh 2009). Whether or not the magnitude of this heating effect is significant enough to cause localised melting at the weld interface is cause for some debate. The general consensus is that a local increase in temperature of up to 50% of the base metal melting point is seen at the weld interface during ultrasonic welding. The majority of experimental analysis using embedded thermocouples, infrared cameras during processing and post-process analysis of the weld interface microstructure has indicated that melting does not occur (Gao & Doumanidis 2002)(Koellhoffer et al. 2011)(Kong et al. 2004b)(Prieb 1999)(Schick et al. 2011)(Yang et al. 2009).

Some researchers (Gunduz et al. 2005)(Kreye 1977) (Weare et al. 1960) have reported evidence of localised melting at the ultrasonic welding interface and some evidence of localized melting and solidification with the microstructure surrounding an interface void in UC has also been reported (Figure 2-27). Melting was attributed to frictional sliding between the sonotrode and the upper surface of the foil material during consolidation. A region of columnar-shaped nano-grains, arranged in layered bands, with apparent grain growth in the direction of heat conduction through the bulk material (Prieb 1999).

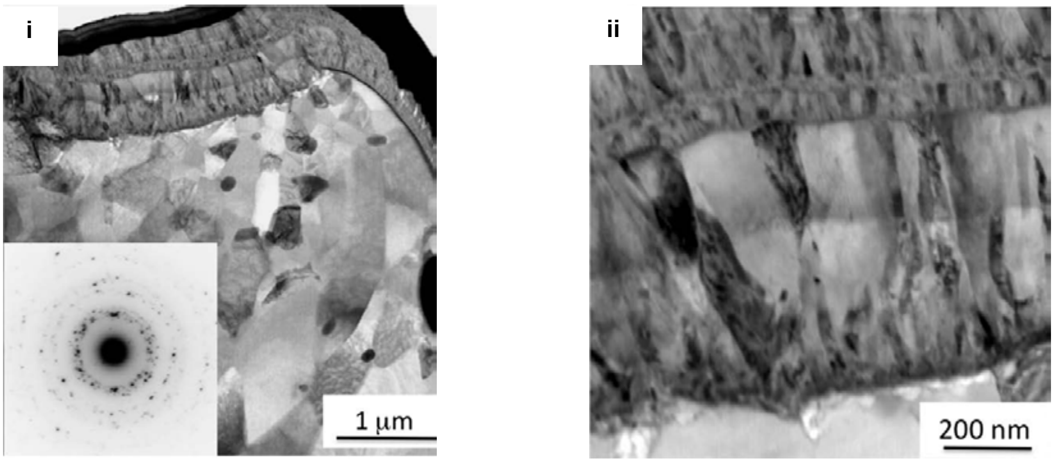

Figure 2-27: Bright-field Scanning Transmission Electron Microscopy (STEM) micrograph of UC bonded Al3003-H18 showing nano-grain regions at the void interface with the corresponding selected area diffraction pattern of the region showing variations in lattice parameters (i) and a higher magnification image of the nano-grain region exhibiting a columnar microstructure and band formation (ii) (Dehoff & Babu 2010).

Interface temperature measurements and modelling have been unable to account for temperatures in excess of the melting point of materials during UC, however one theory is that deformation-induced vacancies might cause significant melting point depression and therefore account for any evidence of melting at the interface (Gunduz et al. 2005).

It should be noted that melting at the UC weld interface is undesirable in some cases. Melting and solidification could cause structural changes or the development of brittle intermetalic compounds which would weaken the interlaminar bond strength (Prieb 1999).

It is the authors opinion, in agreement with Janaki Ram et al. (2007) that localised melting and subsequent solidification can be seen under extreme processing conditions or for specific dissimilar material combinations, however it is not evident in the examination of the majority of UC bond interfaces and therefore is not the main processes by which ultrasonic bonding occurs.

2.3.3.3 Ceramic Bonding

Previously, general consensus (White 2003) (Janaki Ram et al. 2006a) (Li & Soar 2009b) agreed that the surface oxides on the surface of ultrasonically consolidated foils was fractured and displaced into the local bulk material. Shearing of surface asperities and heat generated through friction as a result of the relative motion between the mating surfaces was thought to disrupt and displace these surface contaminants from the foils at the interface during bonding (Figure 2-28).

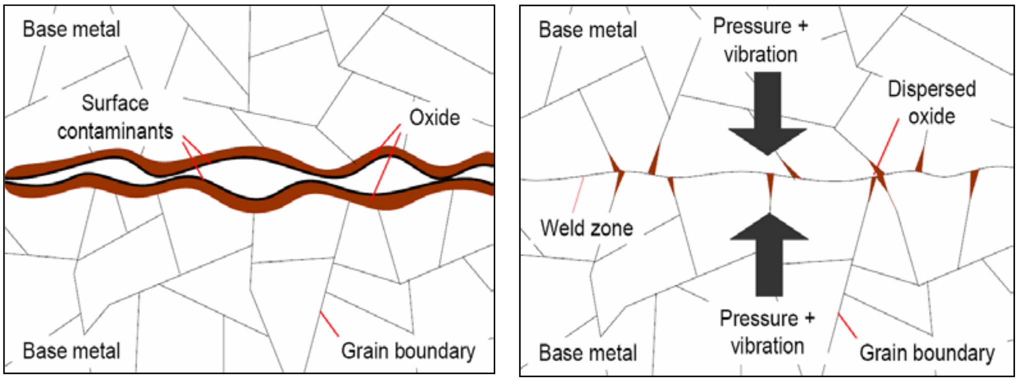

Figure 2-28 - Representation of theoretical dispersion of surface oxides during ultrasonic welding (Flood 1997).

Contrary to this opinion, Kong et al. (2003) used Scanning Electron Microscopy (SEM) to examine the UC weld interface of Al6061 and concluded that surface oxides appeared to remain intact along the length of the bond interface (Figure 2-29). Chemical analysis of ultrasonically welded aluminium by Domack & Baughman (2005) also identified high concentrations of carbon and oxygen within 1µm of the UC weld interface to support the theory.

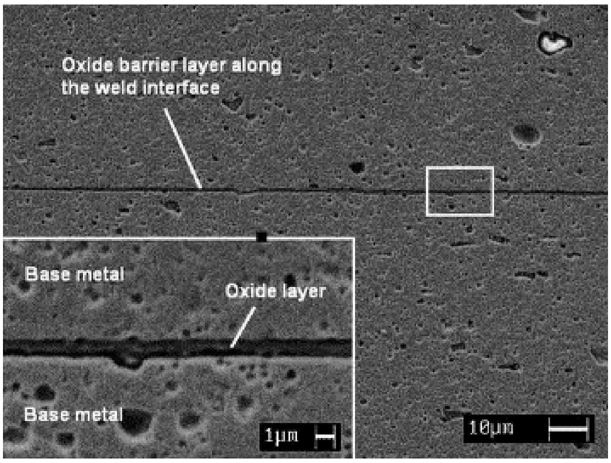

Figure 2-29: SEM cross section Al6061 UC specimen showing the approximately 500 nm thick oxide barrier layer along the weld interface. Insert shows close up of the oxide barrier layer (Kong et al. 2003).

Research by Johnson (2008) used both FIB etching and TEM to illustrate that a fine surface oxide layer, 5.0 x10^{-3}µm thick, not normally visible using SEM can remain after bonding in Al3003 (Figure 2-30).

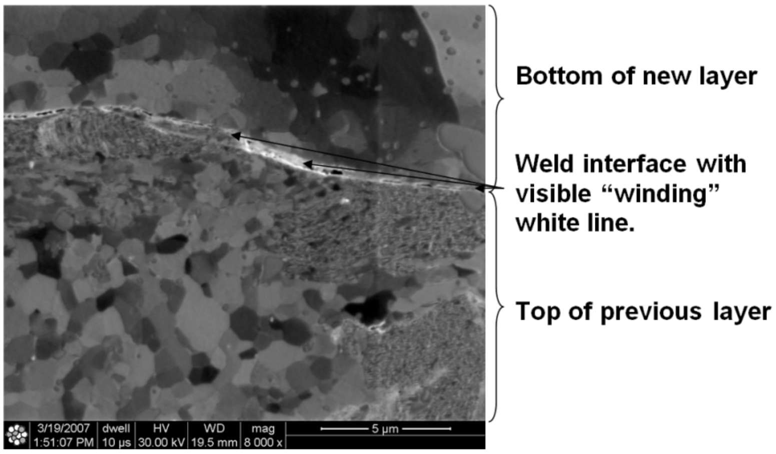

Figure 2-30: FIB micrograph of UC interface showing the distinct oxide boundary between previous (bottom) and new layer (top) of Al3003 (Johnson 2008).

Evidence of a persistent oxide layer between consolidated layers raises questions about the possibility of ceramic bonding between layers. In his research into ultrasonic welding of metals and ceramics Matsuoka (1998) postulated that oxides, compacted under high dynamic interfacial stresses, can form ceramic bonds (Figure 2-31). These ceramic bonds are brittle, yet highly resistant to delamination.

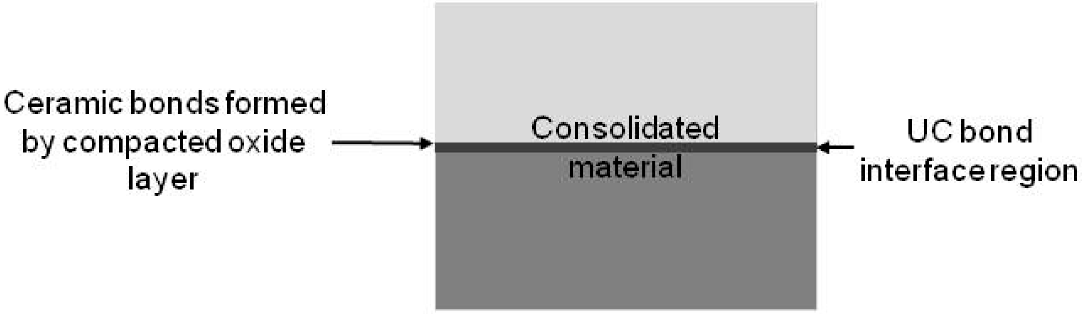

Figure 2-31: Schematic of the proposed joining mechanism in UC of ceramic bonding

Further research (Dehoff & Babu 2010) using FIB etching has since shown that the oxide layer is commonly found in the area surrounding interlaminar voids and defects, but is not wholly persistent across the weld interface (Figure 2-32) and therefore is not the sole mechanism by which joining occurs in UC.

In the absence of metallic bonding, ceramic bonding has been proposed as possible joining mechanism in UC, particularly in certain aluminium alloys under high pressure and slow weld speed processing conditions (Kong et al. 2003)(Li & Soar 2009b).

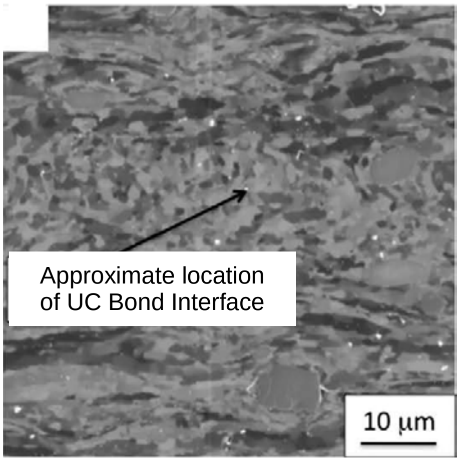

Figure 2-32: FIB micrograph of the of Al 3003 H18 UC bond interface showing complete disbursement of the interfacial oxide layer (adapted from Dehoff & Babu, 2010).

2.3.3.4 Diffusion

Diffusion across the bond interface of ultrasonically welded components has been observed in previous research (Figure 2-33). It was proposed that high strain rate plastic deformation enhances diffusion due to an instantaneous increase in vacancy concentration, although the exact mechanism is not entirely understood (Figure 2-34) (Gunduz et al. 2005). However, it should be noted that this level of diffusion was observed after high temperature, 513K, ultrasonic welding which tends to have an increased dwell time in relation to UC.

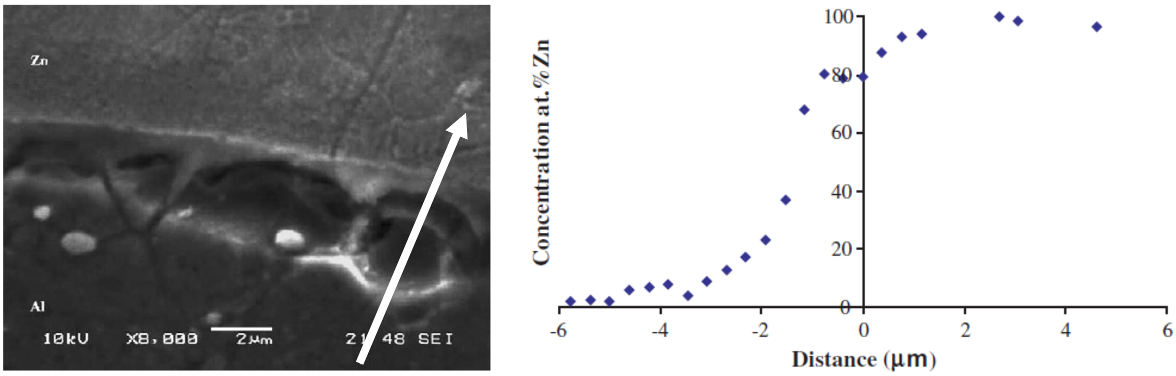

(i) **(ii)**

Figure 2-33: SEM micrograph showing the morphology of the weld after etching (i) and EDS profile across the weld interface showing the concentration of zinc (ii), indicated by the arrow in (i) (Gunduz, et al. 2005).

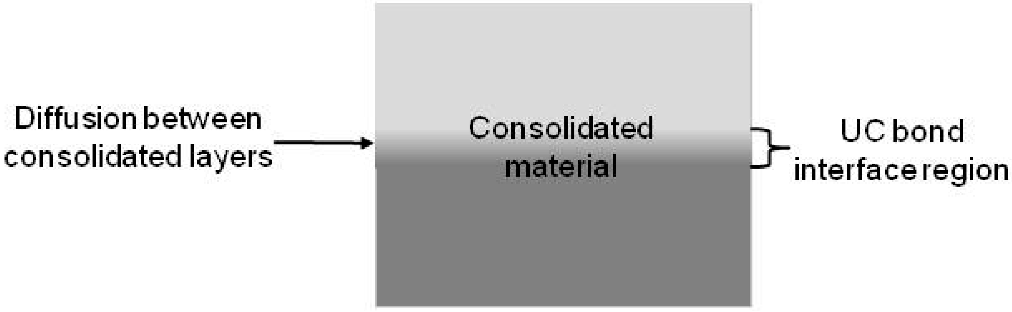

Figure 2-34: Schematic of the proposed joining mechanism in UC of diffusion.

While a small degree of diffusion may occur, no clear evidence of bulk diffusion has been identified during UC. The modest temperature increases and limited sonotrode residence time involved minimises the likelihood that significant diffusion occurs or that it is the primary mechanism of joining in UC (Yang et al. 2009).

Some chemical interactions, which might arise as a result of diffusion between different materials, can enhance the strength of the interface while others can produce undesirable brittle inter-metalics or low melting eutectics, therefore limited diffusion in UC is not necessarily a disadvantage (Yang et al. 2009).

2.3.3.5 Atomic Forces Across Nascent Material

The final proposed mechanism for interlaminar joining in UC is the attraction of atomic forces across nascent material surfaces. An essential requirement of this process is the existence of atomically clean surfaces that are in intimate contact, therefore the removal of the metals surface oxides and the deformation of any surface irregularities are crucial steps in the bonding process. These conditions are achieved by the repetition of the contact-bond process (Janaki Ram et al. 2007)(Kong et al. 2005).

The contact stage describes the bringing together of the surface asperities by the applied contact pressure and the initiation of contact points (Figure 2-35). The bond stage follows and refers to the formation of bonds across the contact points. During the bond stage oscillating shear forces from the sonotrode generate dynamic interfacial stresses at the contact points. These stresses crack the brittle oxide layer and induce plastic flow up to 20µm below the surface oxide layer. Nascent material extrudes through the gaps in the fractured oxide layer and the oxide layer is dispersed by plastic flow into the surrounding material. The nascent material establishes an anatomically clean interface and the mating surfaces are brought into intimate contact.

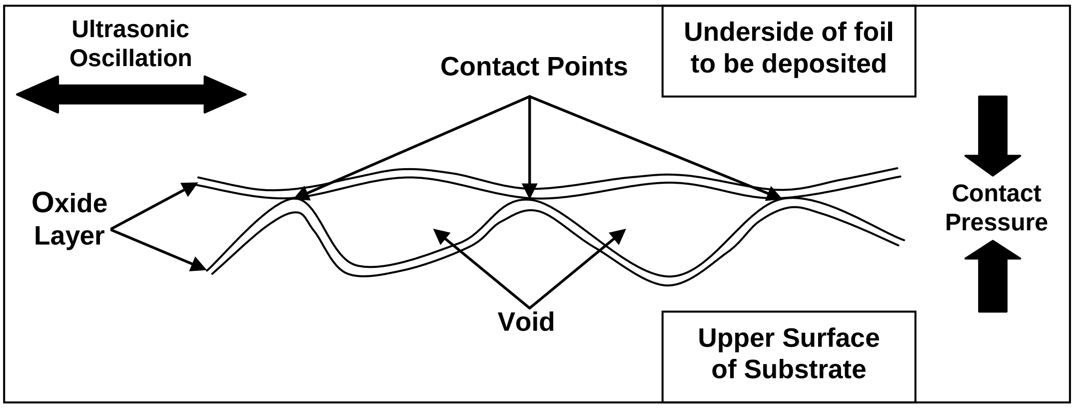

Figure 2-35: Schematic of contact point formation and bond initiation in ultrasonic consolidation.

Contact is initially confined to the highest surface asperities, which represent only a small fraction of the interface, but as the asperities shear and plastically deform under the normal force of the sonotrode the plastically deformed metal flows into surface voids and the mating of new contact points is initiated. Contact points between mating surfaces are continually made and broken; this continuous stick/slip process is referred to as the “stick-slip phenomena” (Kong, Soar, & Dickens 2005). As the contact area increases more surfaces are brought into intimate contact. The contact-bond, stick-slip process continues and the weld density of the interface increases (Janaki Ram et al. 2007)(Neppiras 1965).

Noble metals are also suitable for UC as they do not have an oxide layer. In more reactive metals, however, there are a number of factors which affect the ease with which the surface oxide layer is displaced during UC, including the relative properties of an oxide compared to the base metal, for example aluminium oxide (Al_2O_3) which is present on the surface of most aluminium alloys is harder and more brittle than the base metal itself and hence is easily fractured during processing. In cases where the surface oxide is persistent acids can be used to etch the oxide layer prior to welding (Janaki Ram et al. 2007)(Kong et al. 2003).

2.3.4 Mechanisms of Plastic Deformation in Ultrasonic Consolidation

Based on the current research the action of atomic forces across nascent material emerges as the most viable mechanism of joining in UC. In order for this to be achieved the following two factors are essential to develop the quality of solid state bonding in UC:

1. Dispersal of the oxide layer to generate atomically clean surfaces and expose nascent material.
2. Close contact of surfaces, to within a distance where atomic forces are effective.

For both of these factors plastic deformation of the mating surfaces during UC is a crucial process (Yang et al. 2009).

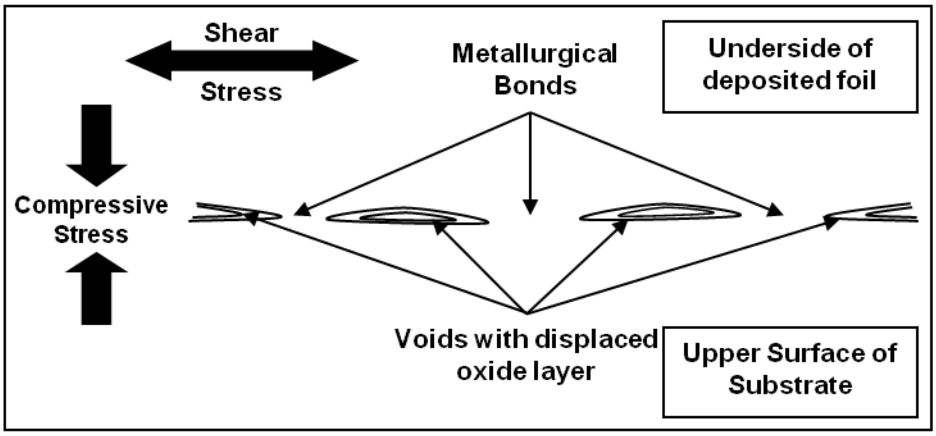

Figure 2-36: Schematic normal and shear forces which cause plastic deformation in ultrasonic consolidation.

The normal force of the sonotrode onto the foil and substrate surface plastically deforms individual surface asperities under compressive stress. The brittle surface oxide is broken up, exposing the base metal, enabling the initiation of contact points. The shear stress generated by the high frequency relative motion between the mating surfaces deforms and levels surface asperities further increasing the contact area at the weld interface (Gao & Doumanidis 2002).

In isolation the continuous stick-slip process would cause some degree of strain hardening and resistance to further plastic deformation along the weld interface during UC. However, it has been proposed that effects of strain hardening are minimised and the process of plastic deformation is facilitated by one or more of the following mechanisms;

- Surface Effect
- Volume Effect
- Bauschinger Effect

2.3.4.1 Surface Effect

The surface effect refers to the increase in plastic deformation at the UC interface as a result of localised temperature increases. According to Kong (Kong et al. 2005) the surface effect can be explained by friction theory. In UC friction is generated as a result of the high frequency relative motion between the mating surfaces of the foil and substrate under a normal force applied by the sonotrode. Plastic deformational heating, generated by the continuous stick-slip process, and frictional heating increase the temperature at the interface which, in turn, reduces the yield strength of the surrounding metal and minimises the effects of strain hardening. The reduction in flow stress of the material promotes increased plastic deformation, facilitating the breakup of the surface oxide layers and bringing the surfaces into more intimate contact to achieve an improvement in bond quality (Gao & Doumanidis 2002).

Modelling and experimentation from some researchers predicts that the increase in plastic deformation due to the thermal effects of friction is limited, as the friction coefficient decreases as the yield strength of the material increases. It was proposed that the effects of friction are only crucial in the displacement and dispersal of surface impurities and oxide along the interface (Siddiq & Gassemieh 2008)(Siddiq & Ghassemieh 2009)(Siddiq & Sayed 2012)(Zhang & Li 2008).

2.3.4.2 Volume Effect

The volume effect refers to the theoretical increase in plastic deformation at the UC interface as a result of acoustic softening (Kong et al. 2005). The principle is so called because it affects changes within the bulk volume of foils, as opposed to just the surface (Mariania & Ghassemieh 2010).

In the 1960’s Langenecker (1966) studied the effect of ultrasonic vibrations on metals and identified the incidence of “acoustic softening”. Acoustic softening refers to the reduction in the apparent static stress to cause plastic deformation in metals during the application of low amplitude ultrasonic vibrations.

The extent of acoustic softening, and hence reduction in static shear stress necessary for plastic deformation to occur, is proportional to the amount of ultrasonic energy applied (Figure 2-37) and as the intensity of the ultrasonic energy increases the magnitude of static shear stress required for plastic deformation to occur decreases. The acoustic softening effect is similar to what is seen when the sample is heated, however less ultrasonic energy input is necessary to achieve the equivalent reduction in shear stress than through the application of thermal energy (Langenecker 1966). Acoustic softening, sometimes referred to as the “Blaha effect” reduces the flow stress of the material by up to 75%, while bulk heating only shows a 45% reduction (Janaki Ram et al. 2007).

Langenecker stated that unlike thermal energy, which is distributed homogenously throughout the metal’s structure, ultrasonic energy is absorbed by dislocations and grain boundaries, which are the mechanisms by which plastic deformation takes place. It should be noted that a reduction in static shear stress as a result of acoustic softening is only seen while the metal is under the influence of low amplitude ultrasonic vibration, while the effects from heating are permanent (Langenecker 1966).

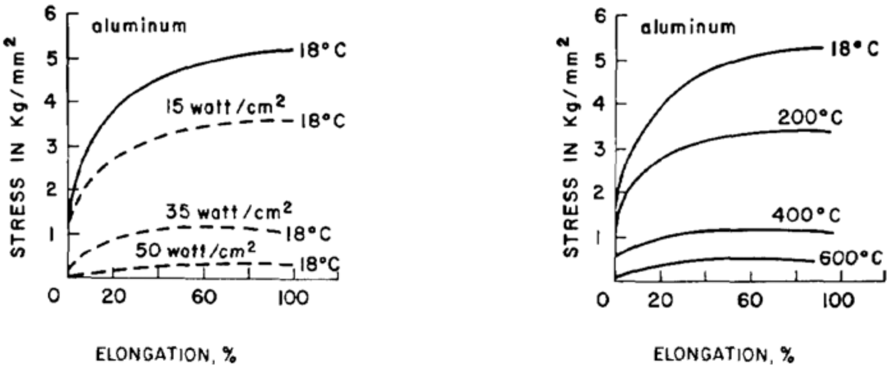

(i) **(ii)**

Figure 2-37: Graph (i) shows how the application of ultrasonic energy effects the relationship between stress and elongation in single aluminium crystals (dashed curve indicates the presence of acoustic softening at 20 kHz), while graph (ii) shows the effect of temperature (Langenecker 1966).

Dislocation theory states that for a single crystal the resolved shear stress, τ, is the stress required for substantial dislocation migration in the slip plane and continuous plastic flow. Under the influence of ultrasonic vibrations, plastic flow occurs without the application of additional shear stress. Therefore the acoustic (tensional) stress, X, generated by the ultrasonic vibration is equivalent to the amount of resolved shear stress, τ, required to induce plastic flow (Equation 2-2 and Equation 2-3) (Langenecker 1966).

Equation 2-2: $X \simeq \tau$

Equation 2-3: $X = \xi\rho\omega c = \rho U c = \sqrt{\frac{2}{v} I Y}$ (Langenecker 1966)

X = Acoustic (Tensional) Stress
ξ = Particle Displacement
ρ = Density
ω = Angular Frequency
c = Sound Velocity
U = Particle Velocity
I = Intensity
Y = Young's Modulus

The critical resolved stress, or yield point, occurs once the static yield stress has been offset by the applied ultrasonic energy. The yield point varies and is dependent on the metal's structure, crystallographic orientation and the presence of impurities. For example, the yield point of zinc is significantly lower than that of high strength metals such as steel. Above the yield point, when the critical shear stress is exceeded, dislocations can move from their pinned positions through the crystal. Langenecker backed up his theory using

SEM and TEM of aluminium which showed the build-up of dislocation networks at sub-boundaries after the application of ultrasonic vibrations (Langenecker 1966).

Langenecker also stated that internal friction increases as the dislocation density increased. A number of potential mechanisms were proposed to explain how the ultrasonic stress waves affected the observed change in dislocation density including; thermoelastic energy conversion, resonance of dislocations, relaxation mechanism, hysteresis, jog formation and energy transformation effect as a result of inelastic scattering. However, these theories were considered insufficient to generate the effects that can be seen. Langenecker therefore concluded that the proposed mechanism of acoustic softening was a result of the partial reflection and mode conversions of acoustic waves and localised heating. However, this mechanism has not been proved experimentally (Langenecker 1966).

The absorption of ultrasonic energy and subsequent localised heating can cause "weak spots" as static yield stress is lower compared to the apparent overall temperature of the specimen. Therefore the stress criterion should take into account this localised increase in temperature, where τ' is the apparent static shear stress with respect to the local temperature conditions (Equation 2-4) (Langenecker 1966).

Equation 2-4: $X \simeq \tau'$ (Langenecker 1966)

As seen in the surface effect, the volume effect of acoustic softening promotes increased plastic deformation, facilitating the breakup of the surface oxide layers and bringing the surfaces into more intimate contact to achieve an improvement in contact point density and bond quality. The theory that the volume effect plays a crucial role in ultrasonic welding and UC is well supported in the available literature (Kong et al. 2005)(Friel & Harris 2010)(Langenecker 1966)(Hansson & Tholen 1978)(Mariania & Ghassemieh, 2010)(Siddiq & Sayed 2012)(Yang et al. 2009).

2.3.4.3 Bauschinger effect

The Bauschinger effect is another competing theory for the primary mechanism through which interlaminar softening is achieved in UC. The Bauschinger effect is similar in character to the previously described volume effect as it also affects changes within the bulk volume of the substrate material, as opposed to the more localised surface effect (Johnson 2008).

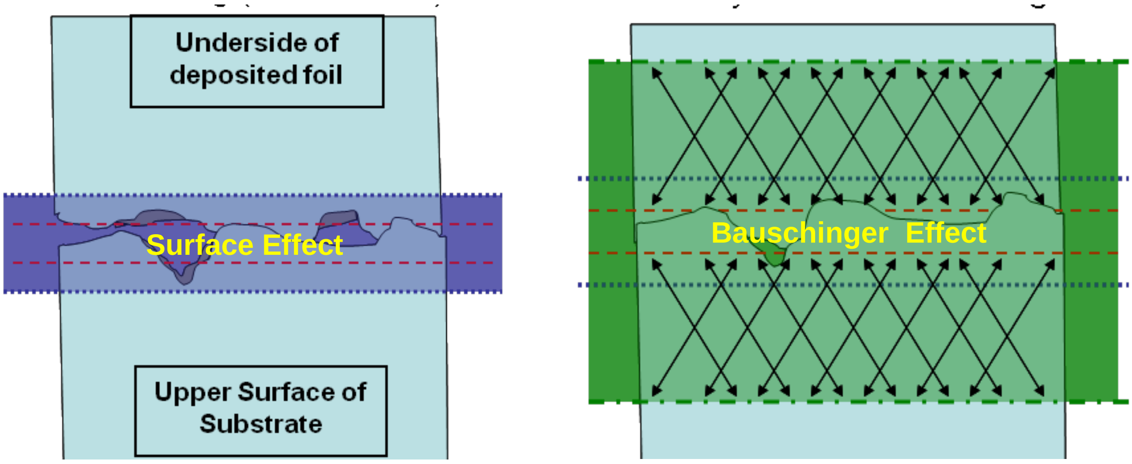

(i) (ii)

Figure 2-38: The surface effect of frictional heating is localised in the area surrounding the interface (i) while the Bauschinger effect penetrates the bulk of the substrate material (Johnson 2008).

The Bauschinger effect is a non-thermal, cyclic-mechanical softening effect. It affects an instantaneous decrease in material flow stress as a result of high frequency fully reversed loading conditions during UC. When a polycrystalline metal is plastically deformed beyond its yield stress in a given direction and, after unloading to zero stress, is then reloaded in the opposite direction. The yield stress of subsequent reloading is less than that of the original yield stress of material (Figure 2-39). The yield strength reduces over subsequent reloading (Johnson 2008).

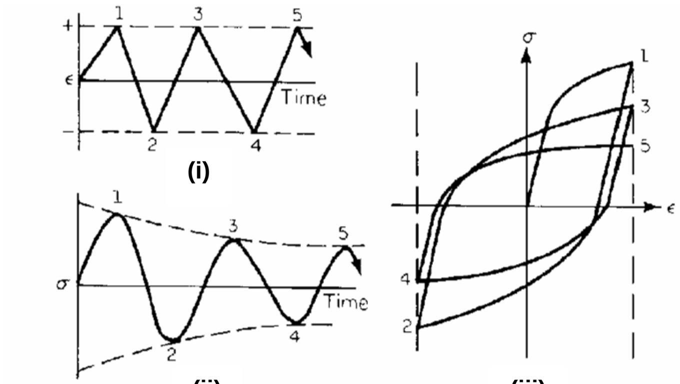

(i)

(ii) (iii)

Figure 2-39: Bauschinger effect: under a constant strain amplitude (i) the stress response (ii) decreases over a number of cycles, resulting in the characteristic cyclic stress-strain response (iii) (Bannantine et al. 1990).

The reduction in yield strength facilitates multi-axial plastic deformation of the substrate interface and surrounding material, facilitating the breakup of the surface oxide layers and bringing the surfaces into more intimate contact to achieve an improvement in contact point density and bond quality (Johnson 2008).

While there have been a number of models and theories developed to explain the Bauschinger effect, the majority have two aspects in common. Firstly, that long range internal stress is generated by the build-up of dislocations at barriers. This stress assists dislocation movement which causes the initial flow stress to drop when loading is reversed. Secondly, that pre-straining of particle hardened materials limits the directional movement of dislocations. Work hardening produces resistance to the forward motion of dislocations, while a lower level of stress is required in the reverse direction, as there are less barriers to motion (Hu et al. 1992).

Severe plastic deformation can be characterised by the gradual evolution of the ultrafine grained structures through dislocation activation, accumulation, rearrangement and sub-grain boundary leading to the formation of ultrafine grains (Orlov et al. 2009). However, under the repeated reverse straining conditions of the Bauschinger effect, dislocations moving in the opposite directions can be annihilated and sub-grain boundaries dissolved resulting in an increase in sub-grain size (Higginson & Sellars 2002).

From Kong et al.'s experimentation into embedding sigma SiC fibres (Kong et al. 2005b), SMA wires (Kong et al. 2004b) and optical fibres (Kong & Soar 2005a) into UC structures it is clear that significant plastic flow occurs deep into the base material and is necessary for full encapsulation to be achieved. Johnson (2008) estimates that the sub-interface plasticity occurs up to a depth of 20-60μm, and refers to the affected area as the Deformation Affected Zone (DAZ).

It should be noted that, strictly speaking, the Bauschinger effect cannot occur in UC as the process is not truly axial in nature as no two cycles are the same. However, the high frequency and/or slow weld speed can equate to almost identical cycles (Johnson 2008).

2.3.4.4 Evaluation of Bonding in UC

When samples fabricated by UC using Al3003 H18 were tested to evaluate their mechanical properties some deterioration of properties was noted. Decreases in the average shear strength, to 48% of the base material strength, and transverse tensile strength, to only 15% of the base material strength were measured. Longitudinal tensile test showed an increase in ultimate tensile strength of 17% and, while there were significant variations across the build cross-section, the average hardness was 15% higher than original foils (Schick et al.2010).

Interlaminar porosity is thought to cause a reduction in mechanical properties of UC structures compared to monolithic structures of the same material (Kong et al.

2005)(Janaki Ram et al. 2006b). Therefore the majority of UC research has been focussed on the optimisation of process parameters in order to eliminate the formation of voids along the bond interface (Dehoff & Babu 2010).

2.3.4.4.1 Microstructure

Kong et al**.** (Kong et al. 2005) developed an optical method of quantifying the level of bonding at the UC weld interface, called the Linear Weld Density (LWD) (Equation 2-5). Optical micrographs of UC bond cross-sections are collected and the quantity of contact points, voids and visible oxide layer are analysed. The LWD quantifies the percentage of interface which show evidence of metallic bonding, by comparing the real contact area, A_r, with the apparent weld region, A_p.

Equation 2-5:

$$\mathrm{LWD} = \frac{\mathrm{A_r}}{\mathrm{A_p}} \times 100\%$$

(Kong et al. 2005)

2.3.4.4.2 Mechanical Properties

The ability of the Alpha 2 UC machine to manufacture of standard mechanical test samples is limited and therefore other methods have been developed to quantify and compare the mechanical properties of UC samples.

Peel and lap shear testing have been used to quantify the relative bond strength of UC samples produced under different processing conditions. Peel testing evaluates the weld quality by determining the average resistance to delamination, based on the theory that as the number and size of contact points increase there is more resistance to peeling. This method of has been adopted by other researchers and has become the de-facto method by which weld effectiveness is measured (George & Stucker 2006)(Kong et al. 2005).

A high LWD can generally be equated to a greater maximum peel load for a given set of UC process parameters (Friel et al. 2010). However, excessive strain-hardening under extreme process parameters can produce weak, brittle welds that show a large number of contact points and hence high LWD (Kong et al. 2003).

Lap Shear testing of two overlapped foils has also been used to measure the strength of UC bonding under shear conditions (Kong et al. 2004a). Both of these methods, however, are limited by the tensile strength of the foil base material and therefore the weld strength above this threshold cannot be evaluated.

2.3.5 Factors that Effect Bonding

While the optimal processing conditions for each UC variant is machine specific there are general trends in the variation of process parameters which can be discussed (Dehoff & Babu 2010)

Figure 2-40 presents an example of the UC processing window for Al 3003-H18. Within this process window individual parameters can be chosen in order to optimise the bond strength of a finished part. Janaki Ram et al. (2006b) state, in order of their influence on LWD, that oscillation amplitude, weld speed, substrate temperature and applied contact pressure affect bonding in UC. The processing temperature (George & Stucker 2006) and sonotrode surface texture (Li & Soar 2009) are also factors that effect bonding in UC.

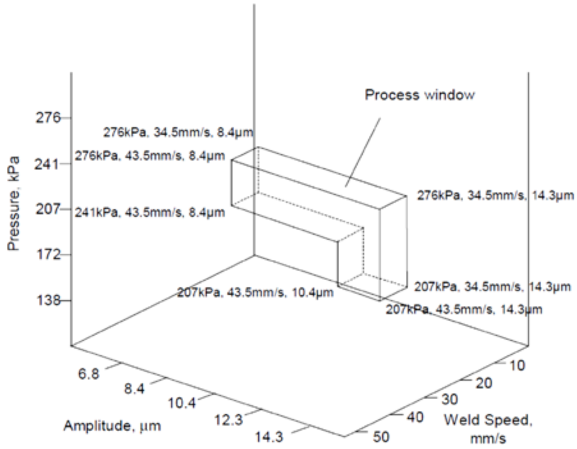

Figure 2-40: General process windows for Al 3003-H18 under UC conditions (Kong et al. 2004a).

2.3.5.1 Oscillation Amplitude

An increase in the oscillation amplitude of the sonotrode has been shown to increase the LWD of UC parts. Higher amplitudes increase the shear forces between surface asperities and a higher rate of ultrasonic energy input per unit time results in the increased disruption of surface oxides and more plastic deformation at the UC interface. Excessively high amplitudes are thought to cause excess stress and strain hardening which in turn, causes a small reduction in LWD (Kong et al. 2003) (Kong et al. 2005) (Janaki Ram et al. 2006b).

2.3.5.2 Weld Speed

A decrease in weld speed causes an increase in UC bond LWD. As more ultrasonic energy is input per unit area, more interfacial shear stress is generated and more plastic deformation and oxide removal occurs. In commercial applications this increase in LWD must be balanced against the associated increase in build time. Too slow a weld speed can also cause strain hardening of contact points and result in brittle bonds (Janaki Ram et al. 2006b)(Kong et al. 2003)(Kong et al. 2005).

2.3.5.3 Weld Force

Higher weld forces produce UC structures with higher LWD. The increase in applied normal force ensures intimate contact between mating surfaces and increases interfacial stresses. A larger number of contact points with increased area are formed. Excess force, however, can reduce the LWD as the relative motion of the interface surfaces are limited by the high contact pressure (Janaki Ram et al. 2006b)(Kong et al. 2003)(Kong et al. 2005).

2.3.5.4 Build Temperature

LWD increases as the temperature at which the substrate is processed increases. Experimentation by George & Stucker (2006) showed that Al UC parts processed at 150^{o}C on a heated base plate had a bond strength three times greater than parts processed at room temperature. The elevation in temperature reduces the material flow stress, the possibility of diffusion is enhanced and the effects of strain hardening are reduced (Janaki Ram et al. 2006b).

2.3.5.5 Sonotrode Surface Topology

One of the key requirements for effective bonding in UC is a sonotrode with a consistently rough surface. Over time the texture of a sonotrode can become worn down by abrasion and impact or material can become lodged in pits on the sonotrode surface. As the sonotrode texture wears the surface asperity peaks become blunt and their amplitude decreases. Uneven sonotrode texture causes uneven relative motion of mating surfaces due to poor mechanical coupling between the sonotrode and foil surfaces during UC. Excessive foil movement during UC can result in poor bonding as foils shift and crinkle (Figure 2-41).

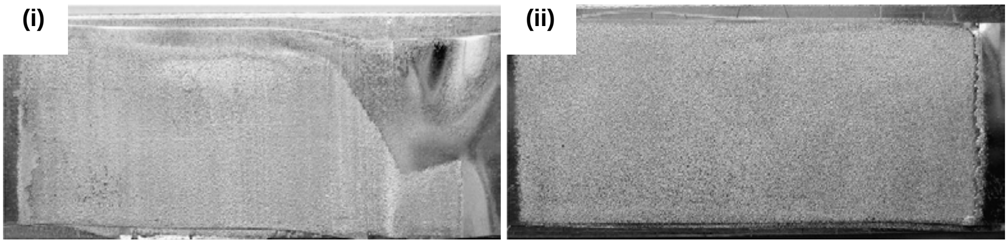

Figure 2-41: UC samples produced with (i) worn and (ii) retextured sonotrode under identical processing conditions (Li & Soar 2009a).

Li & Soar (2009a) postulated that the minimum effective average roughness of for a sonotrode in UC is 5µm, below this value interlaminar bonding becomes uneven and the sonotrode should be re-textured. The research also stated that a sonotrode with a higher surface roughness will tend to generate more voids at the interlaminar weld interface, although this can be reduced by processing at higher amplitudes with increased levels of plastic flow during bonding. An intermediate value for sonotrode average roughness of 6µm was estimated as the optimum for energy transfer with excessive generation of interlaminar voids.

2.3.5.5.1 Substrate Surface Topology

Kulakov & Rack (2010) examined the processes by which the upper surfaces of ultrasonically consolidated foils are damaged during UC. The interactions between sonotrode texture and foil surface during UC at each stage were considered. At the start of the UC process the sonotrode is brought into contact with the upper surface foil at a specified weld force. Prior to oscillation, Figure 2-42i shows the sonotrode imparts the texture of its surface asperities onto the top surface of the foil as it is plastically deformed by the harder sonotrode material. The cavities of the sonotrode surface become partially or fully filled as the foil material flows into the voids.

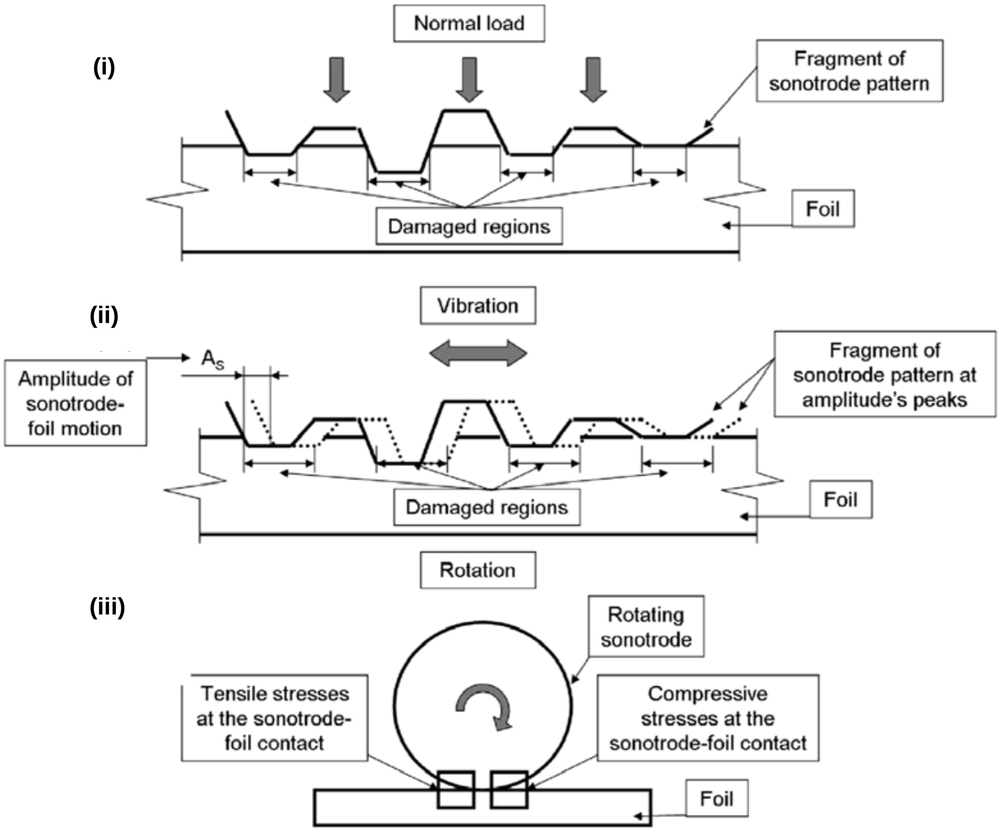

Figure 2-42: A model of the interactions between sonotrode texture and foil surface during ultrasonic consolidation (Kulakov & Rack 2010).

A shear stress condition occurs in the direction of the sonotrode motion as the sonotrode oscillates (Figure 2-42ii) and compressive and tensile stresses are generated as the sonotrode rotates forward and material fills and is extruded from the sonotrode surface cavities (Figure 2-42iii).

Plastically deformed regions on the foil top surface in UC are a result of the sonotrode relative motion between the sonotrode and foil as bonding progresses. The extent of the surface damage, or increased surface roughness, was described as "a complex function of the UC process control parameters involving normal load, vibration amplitude and rotational speed". An increase in upper foil surface plastic deformation was seen to correspond to an increase in linear weld density (Kulakov & Rack 2010).

Janaki Ram et al. (Janaki Ram at al. 2006b) identified sonotrode induced roughness as a major source of defects in UC. Contact with the sonotrode generates surface roughness effects of approximately 10-15µm thickness on the top surface of consolidated foils. Valley shaped indentations on the foil surface remain after consolidation and appear as parabola-shaped defects between layers. Research has been conducted into removing these roughness effects by machining 30µm off each newly consolidated foil which suggested that LWD is significantly improved as a result. It was asserted that smoother foil surfaces ensure intimate contact and hence more contact points for bond initiation are generated, that the oxide layer and any surface work hardening is removed and the incidence of defects/trapped air is reduced. A drawback of this technique is that it increases overall build time. It should also be noted that there was no evaluation of the mechanical properties of the samples in this study and therefore the effect of interface milling on the mechanical strength of samples was improved compared to standard UC samples (Dehoff & Babu 2010).

Johnson (2008) investigated the effects of sonotrode texture to determine how this affects bonding in UC. Processing foils using a sonotrode with lower surface roughness textured by Electrode Discharge Machining (EDM) generates a consistent imprint onto the foil surface, while a sonotrode with higher surface roughness textured by Laser Etching (LE) a rougher transfer imprint is generated and more voids occur in subsequent bonding (Figure 2-43).

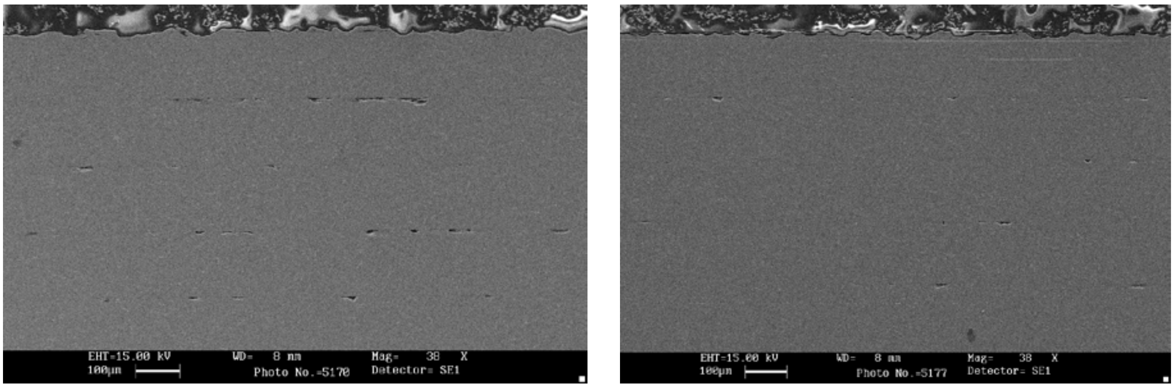

(i) (ii)

Figure 2-43: Cross section of five layer Al3003 UC samples produced using LE (i) and EDM (ii) textured sonotrodes under otherwise identical processing conditions (Johnson 2008).

The extent to which the topology of sonotrode weld surface textures is transferred to the consolidated foil surface is also thought to be effected by a number of UC process variables; higher oscillation amplitude, weld force and higher processing temperatures have been shown to result in more complete topology transfer. Excessive weld forces can limit the relative motion of foils during consolidation and result in a lower bond density. The modulus, yield strength and relative hardness of foil material in relation to the sonotrode also effects the degree of texture transfer. Topology transfer between a rough sonotrode, S_a = 12.94μm, and UC substrate surface during UC can result in large areas of unprocessed material and a significant reduction in the imparted surface texture (Friel et al. 2010).

Friel et al. (2010) describes the UC substrate surface topology as a critical factor in relation to bonding in UC, where excessively rough or smooth surfaces result in a reduction in linear weld density and peel strength. The residual substrate topology is intrinsically linked to the sonotrode topology and therefore the sonotrode texture is of fundamental importance to the quality of components produced via the UC process

It has been theorised that sonotrode topology could be optimised to increase the effectiveness of UC bonding with a view to produce fully dense components with more desirable mechanical properties. At this time the optimal material topology for bonding during UC has yet to be determined (Friel et al. 2010).

Surface asperities play a crucial role in bonding, it is also conceivable that asperity geometries be modified to enhance plastic shear strains and thus promote bonding. Such surface modification has been found to be beneficial in roll bonding (Liu et al. 2008).
In an attempt to investigate the effects of substrate surface texture in UC, without the effects of sonotrode contact, Johnson experimented with a range of foil textures (Figure

2-44) to evaluate how they affected bonding and interface microstructure in UC (Johnson 2008).

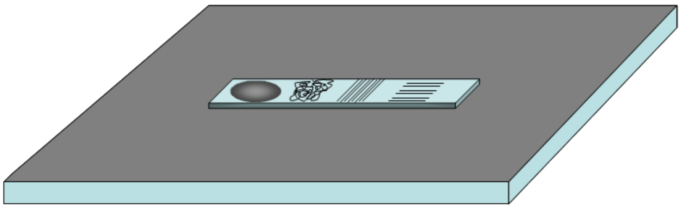

Figure 2-44: Textured foil with (r-l) smooth / rough surfaces, trenches perpendicular and parallel to the welding direction (Johnson 2008).

The engineered surface textures included;

- Smooth surface - 1µm hand polished finish.
- Rough surface - Rolled with sonotrode, without ultrasonic oscillation.
- 3-5 µm trenches perpendicular to the weld direction.
- 3-5 µm trenches parallel to the weld direction.

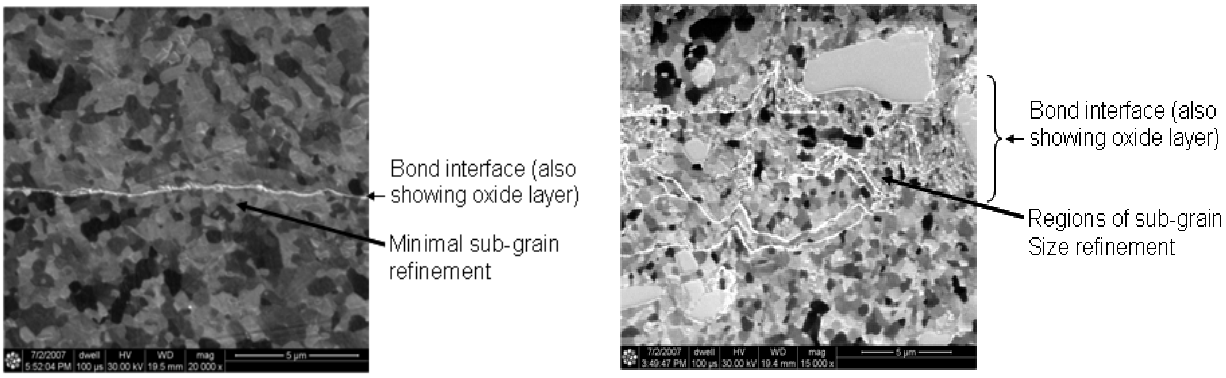

(i) (ii)

Figure 2-45: FIB micrograph of the UC interface showing the oxide boundary between (i) polished and (ii) sonotrode roughed foil surfaces in Al3003-T0 samples (Johnson 2008).

Bonding between smooth surfaces showed minimal grain refinement and a persistent oxide layer (Figure 2-45i). Bonding between foils with rough surfaces showed significant grain refinement at the bond interface (Figure 2-45ii). Analysis of bonding in foils with perpendicular and parallel trenches showed sub-grain refinement and where inconsistencies in the oxide layer has resulted in apparent grain growth across the weld interface. It was proposed by Johnson that a minimum level of foil roughness is required to induce sufficient plastic flow for bonding, although the optimum foil texture has not yet been determined (Johnson 2008).

2.3.5.5.2 Substrate Microstructure

In ultrasonic welding Prieb (1999) stated that the maximum amount of deformation occurs where the sonotrode contacts the upper surface of the foil material surface and that the deformation was not homogenous. It might be similarly assumed that the largest microstructural changes in UC occur where the sonotrode has been in contact with the foil surface.

Dehoff & Babu (2010) used FIB microscopy of the microstructure around a UC interface void to isolate and characterise the changes in grain morphology cause by direct contact with the sonotrode. The microstructure of Al3003 H18 foil prior to UC was typical of a cold rolling process with sub-grains, approximately 0.5 µm in size, heavily elongated along the rolling direction and linear, apart from where they deform around intermetallic phases. Dislocations were present in nearly all grains (Figure 2-46).

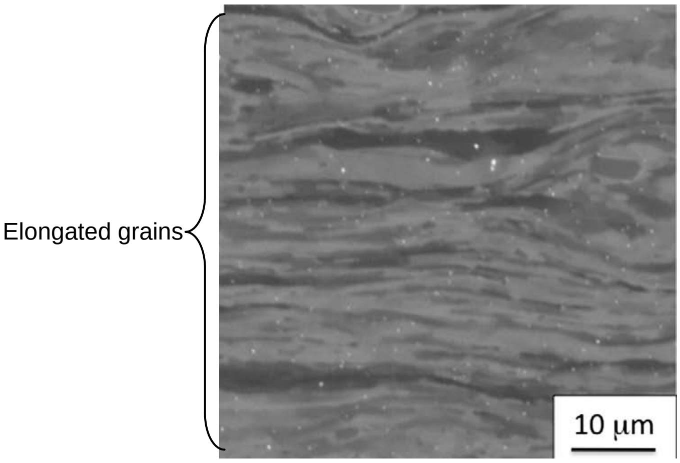

Figure 2-46: FIB image of Al3003 H18 prior to processing (Dehoff & Babu 2010).

The upper foil layer of the processed foil (Figure 2-47), above the void, is unchanged and maintains its original rolled microstructure, therefore it was maintained that changes in grain size and morphology within the lower foil are the direct result of plastic deformation cause by contact with the sonotrode only (Dehoff & Babu 2010).

The presence of the oxide layer and significant grain refinement along the surface of the lower foil layer and a greater depth of transformed grains were identified (Dehoff & Babu 2010). This indicates there is a change in the microstructure when sonotrode is in contact with the upper surface of the foil during consolidation and not just during the relative motion which would occur during consolidation of the next layer.

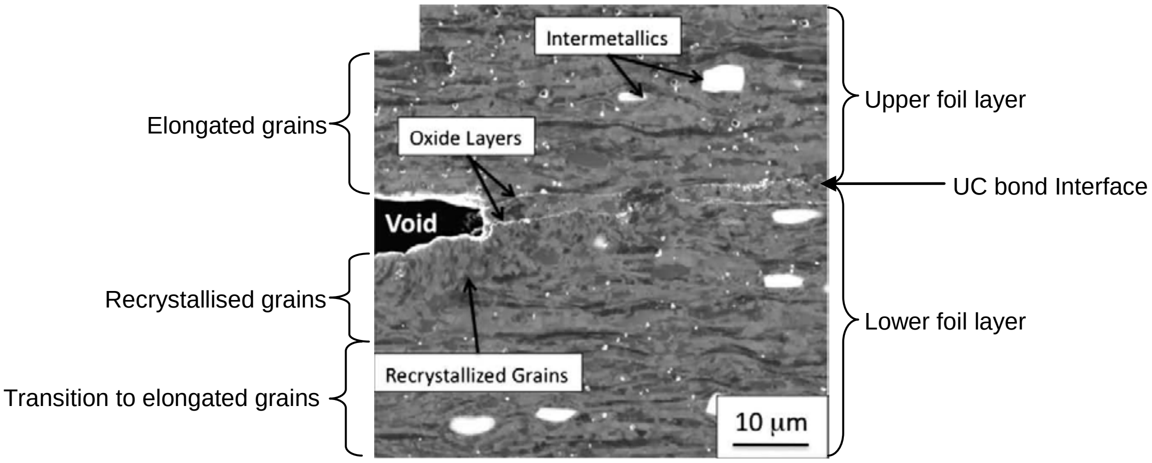

Figure 2-47: FIB micrograph of the interface region from the middle of the build containing a void and continuous oxide layer in Al3003-H18 (Dehoff & Babu 2010).

Regions of nano-scale grain refinement, as a result of contact with the sonotrode, were also seen when the UC substrate surface of Al3003 T0 foils was examined before consolidation of subsequent layers (Figure 2-48) (Johnson 2008). The presence of nano-grain refinement is thought to be a result of sub-grain division through dislocation pile up as a result of plastic deformation induced by sonotrode contact.

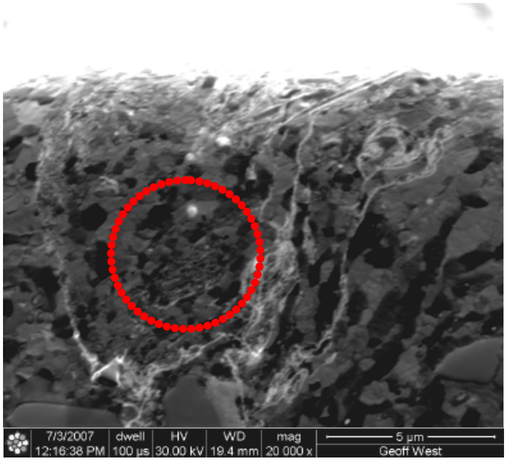

Figure 2-48: FIB micrograph of Al3003-T0 UC substrate surface illustrating the proximity of nano-grain colonies (highlight in red) to sub-surface flaws (Johnson 2008).

Research in embedding fibres in UC found that the fibre was forced into the upper foil during consolidation instead of the deformation being evenly distributed between layers. This uneven fibre distribution was attributed to increased relative hardness of the lower substrate surface, as a result of deformation by sonotrode contact, compared to the unprocessed surface of the upper foil. This theory is supported by the refined grain structure identified in the UC substrate microstructure and the Hall-Petch relationship between decreasing grain size and increasing hardness properties (Equation 2-1) (Friel & Harris 2010) (Johnson et al. 2011).

It has been shown that strain history effects not only the mechanical properties but also the recrystallisation behaviour of a material (Higginson & Sellars 2002). Therefore the deformation of the foil surface texture by the sonotrode under cyclic strain conditions in UC could have implications for the bonding quality of subsequent layers.

2.3.6 UC Bond Interface Microstructure Characterisation

At the present time the evidence and description of the microstructure of ultrasonically consolidated structures by Johnson et al. (2011) is the most complete.

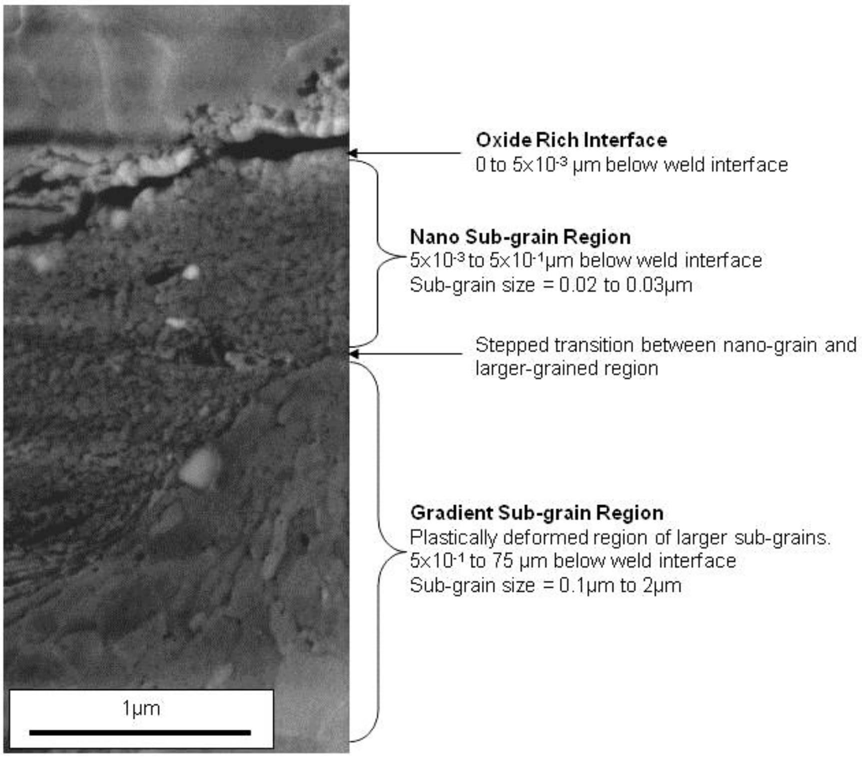

Figure 2-49: SEM micrograph of FIB-etched sample illustrating the three primary regions of the UC weld interface of Al3003-T0 (Johnson et al. 2011).

A region of persistent surface oxide between the UC bonded foils was found to remain (Figure 2-49). The oxide layer appears almost continuous in close proximity to interlaminar voids. However, as the distance from the void increases the layer becomes more disbursed resulting in direct contact between the two layers (Dehoff & Babu 2010).

Nano-grain colonies, as seen in the microstructure of the substrate material prior to consolidation, are attributed to the deformation effects of the sonotrode and can be found up to 10µm from the UC weld interface. A distinct stepped transition is apparent between nano-scale sub-grain region and the gradient sub-grain region, where refined sub-grains form a gradual transition as sub-grain size increases as the distance from the weld interface increases (Figure 2-49).

Marianai & Ghassemieh (2010) identified a smaller region of nano-scale grains in an Al 6061-T0 UC sample with gradient sub-grains regions above as well as below the bond interface.

35^{o} common strain microband sub-grain orientation have been identified in TEM electron micrographs of the UC interface (Figure 2-50). These are commonly seen in conventional rolling processes and a result of the normal force and rotation of the sonotrode during bonding. Persistent slip bands, dislocations with common orientations and extended length, were also found close to the UC weld interface (Figure 2-51) (Johnson et al. 2011).

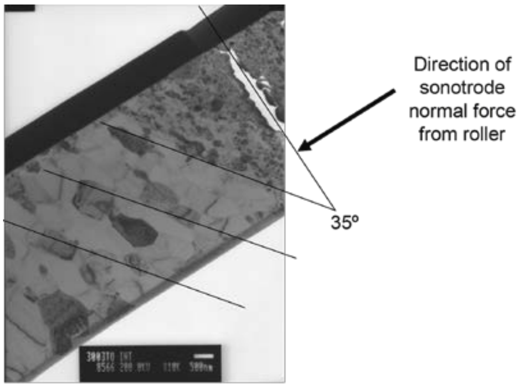

Figure 2-50: 35^{o} strain microband orientation in a TEM micrograph of the weld interface of Al3003-T0 UC samples (Johnson 2008).

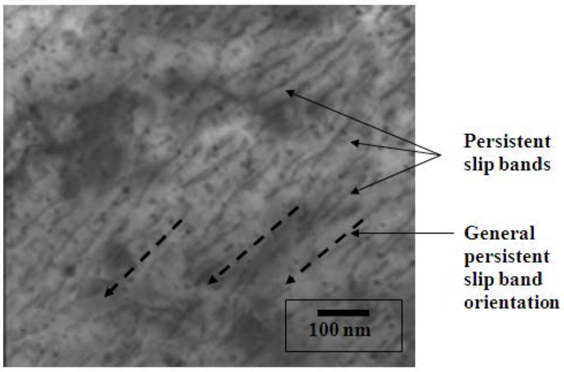

Figure 2-51: Persistent dislocation slip bands from TEM micrograph within 2.0µm of the weld interface of Al3003-T0 UC samples (Johnson 2008).

Electron Backscatter Diffraction (EBSD) analysis of the UC interface has shown a large variation in sub-grain rotation consistent with newly recrystallised grains, more than would be expected due to plastic deformation of the UC interface alone (Figure 2-52) (Dehoff & Babu 2010).

As previously mentioned, it has been proposed that the recrystallised microstructure develops by the progressive transformation of sub-grains into new grains within the original deformed grains, known as continuous dynamic recrystallisation (CDRX), as opposed to the classical nucleation mechanism (Gourdet & Montheillet 2003)(Siddiq & Sayed 2012). Dynamic recovery by sub-grain rotation has also been proposed as is the mechanism for grain growth within the gradient sub-grain region in UC and High Power UC (Mariania & Ghassemieh 2010)(Sojiphan et al. 2010)(Sriraman et al. 2010a)(Sriraman et al. 2010b)(Sriraman et al. 2011) .

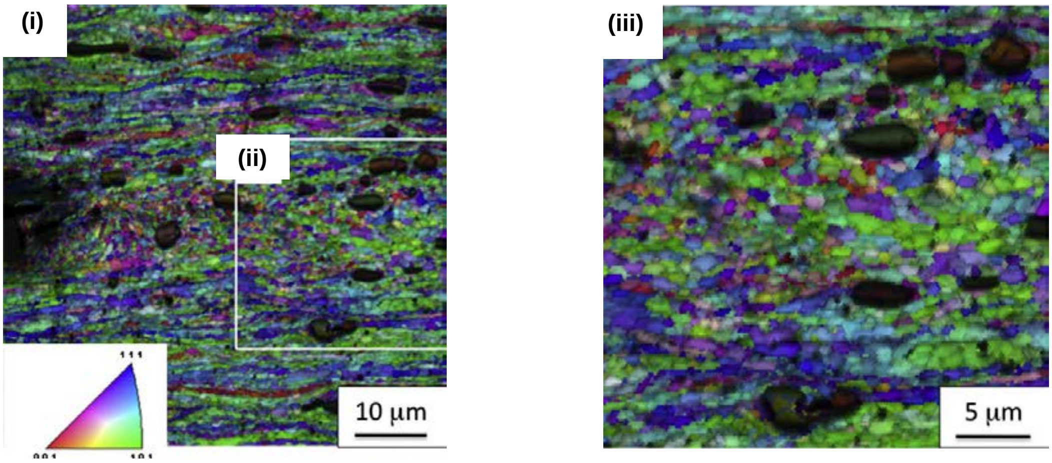

Figure 2-52: Orientation imaging microscopy of the Al3003-H18 UC interface region between two foils (i), with inlaid pole figure, and magnification of the area shown in (ii) showing large recrystallised grains at the interface region (iii) (dark areas are attributed to the presence of intermetallic phases) (Dehoff & Babu 2010).

2.4 Literature Review Summary

Despite a measured increase in longitudinal tensile strength and surface hardness, samples fabricated by UC have been shown to suffer a reduction in shear and transverse tensile strength compared to the original base material properties (Schick, et al., 2010). The incidence of interlaminar porosity is also an undesirable phenomenon noted within UC samples (Kong et al. 2005).

Sonotrode surface topology has been shown to effect bonding in UC. The generation of interlaminar voids has been attributed to the topology transfer from rough sonotrode surface textures (Janaki Ram et al. 2006b) while low magnitude surface texture can result in poor mechanical coupling between the sonotrode and foil, resulting in bond failure (Li & Soar 2009a)

The relationship between UC process parameters and substrate surface texture has been described as complex and is thought to be dependent upon sonotrode surface texture, weld force, oscillation amplitude and weld speed (Friel et al. 2010)(Kulakov & Rack 2010).

Some research has been conducted using different sonotrode surface roughness's and substrate surface roughness's and these have been shown to effect interlaminar bonding in UC (Friel et al. 2010). Within this research surface topology was only defined by the average magnitude of the surface features and not the nature of feature distribution.

It has been proposed that sonotrode topology and substrate surface topology could be optimised to increase the effectiveness of bonding in UC to produce fully dense components with more desirable mechanical properties (Friel et al. 2010).

Preliminary research into the modification of substrate surface topology has been undertaken and differences in oxide layer distribution and interlaminar microstructure were observed but the effect on sample mechanical properties was not reported (Johnson 2008).

It was noted that there are a number of competing mechanisms through which interlaminar bonding is thought to be achieved in UC, including; mechanical interlocking, melting and solidification, ceramic bonding and diffusion. However, interlaminar bonding through atomic forces across nascent material appears to be the most viable mechanism, where the displacement of surface oxides and close contact of surfaces are fundamental to the joining process (Janaki Ram et al. 2007)(Kong et al. 2003)(Prieb 1999)(Yang et al. 2009).

Plastic deformation emerged as one of the key processes in UC and there were a number of mechanisms which were thought to facilitate plastic deformation and minimise strain hardening at the UC weld interface. The influence of deformational and frictional heating as a result of the surface effect, acoustic softening through the volume effect and non-thermal, cyclic-mechanical softening through the Bauschinger effect have all been proposed. The mechanisms by which of interlaminar grain refinement occurs in UC have also been attributed to both the volume and Bauschinger effect (Kong et al. 2005) (Johnson 2008). Based on the available evidence the feasibility of these mechanisms cannot be confirmed nor denied.

3 Research Approach

3.1 Identification of Research Scope

The scope of this investigation was defined based on the findings from the Literature Review and the specific remit of the SMUC project as defined in Chapter 1. Expanding the current understanding of UC bonding phenomena with a view to improve interlaminar bond strength and reduce interlaminar porosity was the crux of the investigation.

3.1.1 Research Aim

To determine the effect of sonotrode weld surface texture, UC substrate surface texture and foil surface texture on interlaminar bonding in UC so that appropriate operating parameters could be identified to produce parts with different properties for a range of different applications.

3.1.2 Research Objectives

1. To establish if the extent to which the sonotrode weld surface texture is imparted onto the substrate surface during UC is dependent upon the operating parameters.
2. To investigate how interlaminar microstructure and bond strength in UC is dependent upon sonotrode weld surface texture.
3. To understand how modifying the surface texture of stock foil prior to manufacture could be used to modify interlaminar bonding in UC.

3.1.3 Research Factors

From the Research Aim and Objectives the following research factors were identified in order to break down the constituent elements and guide the experimental approach to enable informed analysis.

I. Characterise the weld surface texture of different sonotrodes.
II. Characterise the substrate surface texture and determine the degree of texture transfer from contact with each different sonotrode over a range of UC processing conditions.
III. Experimentally measure the interlaminar bond strength and characterise the failure mode of UC samples manufactured by each of the different sonotrodes over a range of UC processing conditions.
IV. Experimentally measure the linear weld density and characterise the interlaminar microstructure of UC samples manufactured by each of the different sonotrodes.

V. Implement and analyse a texturing method that can be applied to unprocessed foils used in the manufacture of UC samples.
VI. Evaluate the extent to which pre-textured foils affect interlaminar bond strength and microstructure in UC.

3.2 Experimental Approach

The experimental portion of the investigation was divided into three distinct stages, which are presented in Chapter's 4 - 6, in order to tackle the three different Research Objectives (Figure 3-1 and Figure 3-2).

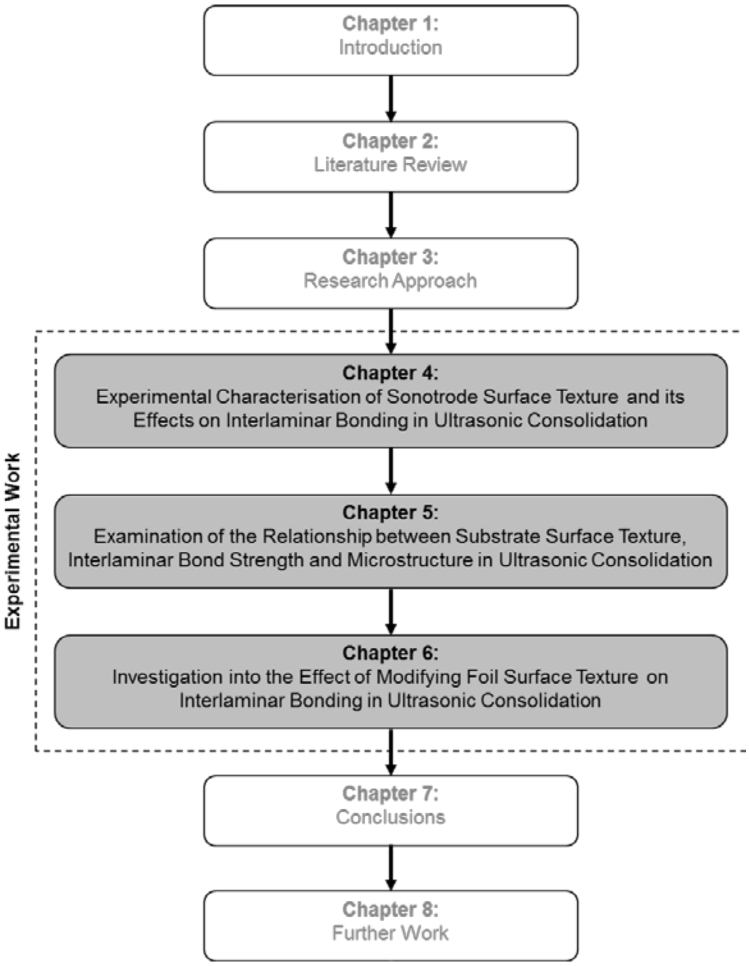

Figure 3-1: Overall thesis organisation, highlighting experimental work.

Chapter 4:

An analysis of the effects of **sonotrode surface texture** on substrate surface roughness, and interlaminar bond strength. A statistical approach was used to quantify the significance of different sonotrode surface textures under a range of UC processing conditions.

Chapter 5:

An examination of the relationship between **substrate surface texture** parameters, interlaminar bond strength and microstructure in UC. A direct comparison of UC samples fabricated by different sonotrodes under the same processing conditions.

Chapter 6:

An investigation into the effects of **foil surface texture modification** on interlaminar bonding in UC. A comparison of the interlaminar bond strength and failure mode (brittle or ductile) and the microstructure of samples fabricated using pre-textured foils compared to those made with standard stock foil.

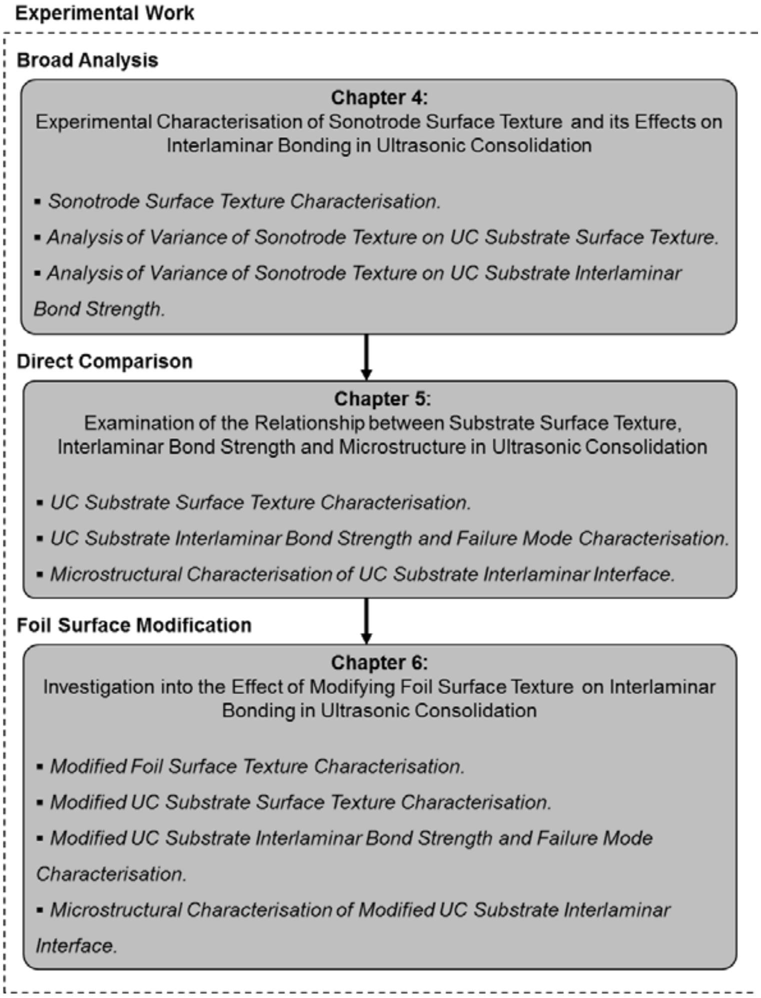

Figure 3-2: Thesis organisation, detailing experimental work.

4 Experimental Characterisation of Sonotrode Surface Texture and its Effects on Interlaminar Bonding in Ultrasonic Consolidation

This chapter is the first of three experimental chapters (Figure 4-1) devised to contribute to the Research Objectives stated within Chapter 3: Research Approach.

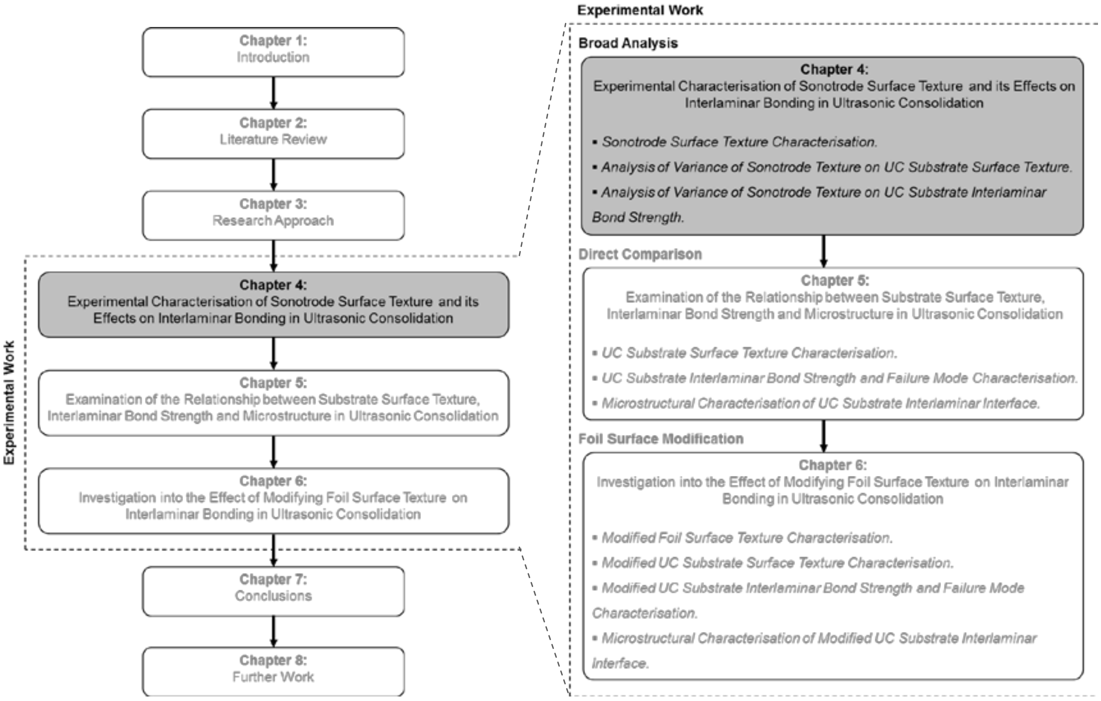

Figure 4-1: Thesis organisation, highlighting Chapter 4.

The focus of this chapter is the first Research Objective, "*to establish if the extent to which the sonotrode weld surface texture is imparted onto the substrate surface during UC is dependent upon the operating parameters*". The following Research Factors are also addressed:

I. Characterise the weld surface texture of different sonotrodes.

II. Characterise the substrate surface texture and determination of the degree of texture transfer from contact with each different sonotrode over a broad range of UC processing conditions.

III. Experimentally measure of interlaminar bond strength and characterise of the failure mode of UC samples manufactured by each different sonotrode over a broad range of UC processing conditions.

This chapter describes the methodology used to measure sonotrode and UC substrate surface textures using white light interferometery and the fabrication of samples with the Alpha 2 UC machine for bond strength measurement through peel test analysis. The results are analysed and a discussion of the pertinent findings is presented. Areas which were consequently found to warrant more detailed examination are identified as the focus of the next experimental chapter.

4.1 Experimental Methodology

4.1.1 Sonotrode Surface Texture Characterisation

The 1st research objective was to characterise the weld surface texture of different sonotrodes. This section presents the methodology used to measure the weld surface of three EDM textured sonotrodes with white light interferometery in order to characterise and compare their textures prior to the fabrication of UC parts. Sonotrode surface measurements were also taken after a number of UC samples were fabricated to identify any change in texture as a result of wear on the sonotrode.

4.1.1.1 Sonotrode Surface Texture Measurement

Sonotrodes with low, medium and high relative roughness surface textures, henceforth referred to as sonotrode A, B and C, were selected to fulfil the 1st technical objective, to "*characterise the weld surface texture of different sonotrodes*". These three tool steel 20kHz full wave seam weld sonotrodes were used in the fabrication of UC sample parts. The weld surface of all the sonotrodes was 38.5mm wide and 50.0mm in diameter (Figure 4-2 and Figure 4-3) and textured via EDM. The weld surface of Sonotrode A and B were standard off-the-shelf textures supplied by the manufacturer, American Technology, Inc., while Sonotrode C was textured by TNT EDM, Inc., Michigan, USA.

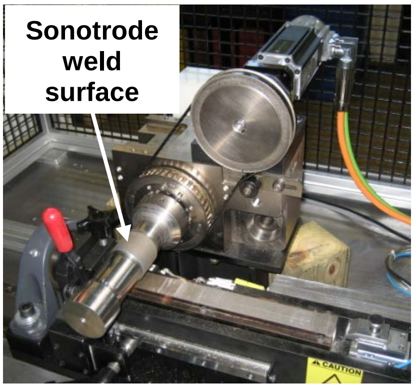

Figure 4-2: Sonotrode fitted in the Alpha 2 UC machine.

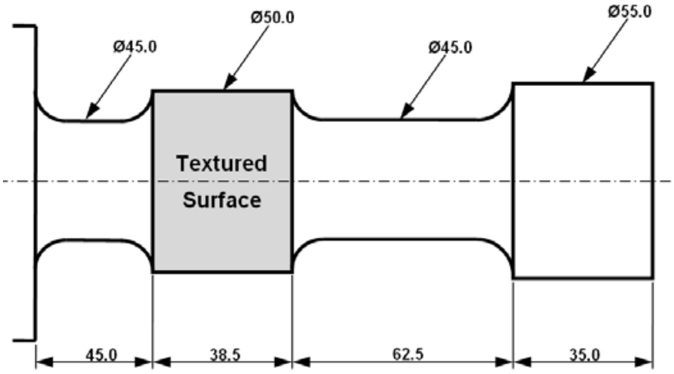

Figure 4-3: Schematic of sonotrode highlighting the textured weld surface (dimensions in mm) (Kong 2005).

The weld surface of each sonotrode was measured using white light interferometery to characterise their surface texture prior to UC sample fabrication. Preliminary metrology testing had shown a high degree of variation in surface texture parameters across the surface of individual sonotrodes and therefore multiple areas were analysed. For each sonotrode the surface texture was measured in twelve different locations across the weld surface using a Zygo NewView 5000 white light interferometer (Figure 4-4). The convention of using twelve measurement locations was adopted from Michigan Metrology, LLC, Michigan, USA, who had previously undertaken sonotrode surface texture analysis for the UC machine supplier, Solidica Inc. The weld surface was arbitrarily divided into equal quadrants and three measurements were taken randomly across the contact surface within each quadrant to ensure the whole area was assessed (Figure 4-5).

Figure 4-4: Photograph of the Zygo NewView^{TM} 5000 white light interferometer used to measure the sonotrode weld surface texture.

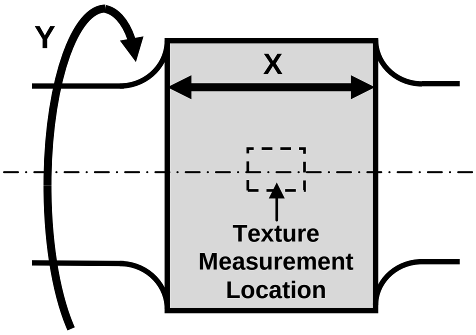

Figure 4-5: Diagram of sonotrode illustrating a texture measurement location, plane of oscillation (X) and direction of rotation (Y).

Table 4-1: Zygo NewView^{TM} 5000 measurement parameters for sonotrode A, B and C (Zygo Corporation 2002).

Parameter	Sonotrode		
	A	B	C
Objective Lens	Mirau x10		
Zoom Setting	x1		
System Magnification	x10		
Measurement Array Size (pixels)	640 x 480 at 30 Hz		
Vertical Resolution (nm)	0.1		
Lateral Resolution (µm)	1.18		
Field of View (mm)	0.70 x 0.53		
Stitched Image Overlap (%)	25		
No. of Images	4 (2x2)	9 (3x3)	
Total Stitched Image Size (mm)	1.21 x 0.91	1.75 x 1.33	
Scan Length (µm)	100	150	

The white light interferometer measurement variables used are shown in Table 4-1. Different setup parameters were required for the measurement of each sonotrode due to the variation in distribution and amplitude of their surface texture features. Each individual measurement of the first sonotrode, A, was made up of four individual scans stitched together resulting in a 1.10mm^2 measurement area. The sonotrodes with rougher surface textures, B and C, required a larger measurement area of 2.33mm^2, made up from nine scans stitched together, in order to capture the surface features completely. These sonotrodes also required an extended scan length due to the amplitude of their surface features.

The 3D surface scan data, acquired from the white light interferometery measurements, was stored as .DAT files and processed using Talymap Platinum software, version 5, Taylor Hobson, Ltd. All the files were processed using a common template. For each data file any non-measured points, arising from large vertical step heights between measured points or locations of high brightness during data collection, were filled based on a smooth shape calculated from surrounding data points. Form error, due to the curvature of the sonotrode surface, was removed using a polynomial filter (Figure 4-6).

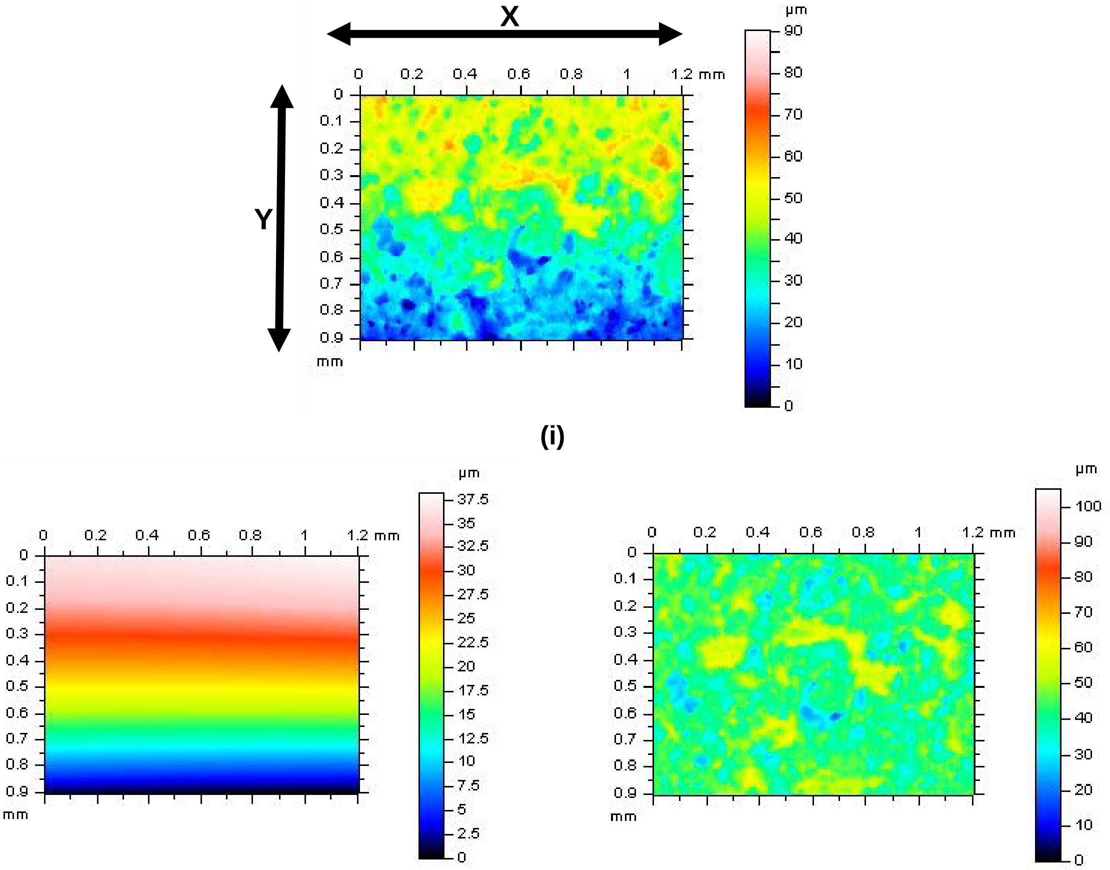

(i)

(ii)

(iii)

Figure 4-6: Pseudo-colour images illustrating the curvature of the sonotrode surface (i), the cylindrical form error removed from the raw data (ii) and the filtered surface with the form error removed (iii).

A number of surface texture parameters (Table 4-2) were calculated for each measurement area (these were selected based on their suitability as discussed in Appendix 4.1). The majority of parameters were based on the ISO 25178: ‘Surface texture analysis parameters’, with additional parameters calculated according to EUR 15178N:

‘The development of methods for the characterisation of roughness in three dimensions’ report. The average surface texture parameters for each sonotrode were calculated.

Table 4-2: ISO 25178 Surface texture analysis parameters (*EUR 15178N) (See Appendix 4.1 for equations and additional detail).

Parameter		**Description**
Amplitude Parameters		
S_a	Average Roughness	Average of surface height deviations from the best fitting plane.
S_q	Root Mean Square Roughness	Average of surface height deviations from the best fitting plane squared.
Ssk	Skewness	+ve Ssk Surface dominated by peaks. -ve Ssk Surface dominated by valleys.
Sku	Kurtosis	Sku > 3 Extreme surface peaks or valleys. Sku = 3 Normally distributed surface texture features. Sku < 3 Slowly varying surface texture.
Topological Characterisation Parameters		
Sds*	Density of Summits	Number of peaks / summits per unit area of the surface.
Ssc*	Mean Summit Curvature	Average principal curvature of all peaks / summits across the surface.
Spectral Analysis Parameters		
Str	Texture Aspect Ratio	Str = 1 Spatially isotropic surface texture. Str = 0 Totally unidirectional surface texture.
Sal	Auto-Correlation Length	Distance between areas of surface texture which are statistically different.
Std	Texture Direction	Angular measurement describing the predominant surface texture direction.
Volume Parameters		
Vmp	Peak Material Voulme	Material volume of surface peaks (top 10%)
Vmc	Core Material Volume	Volume of core material between peaks and valleys (Mid 10-80%).
Vvc	Core Void Volume	Void volume between peaks and valleys (Mid 10-80%).
Vvv	Pit Void Volume	Volume of surface valleys / voids. (Bottom 20%)
Bearing Ratio Parameter		
Sdr	Developed Interfacial Ratio	Fraction of additional surface area due to texture.

4.1.1.2 Sonotrode Surface Texture Wear Measurement

After the UC test samples were fabricated the weld surface texture of each sonotrode was measured again, in accordance with the method previously detailed, to identify any changes in the surface texture.

4.1.2 Analysis of Variance of Sonotrode Texture on UC Substrate Surface Texture

This section presents the initial experimental approach used to fulfil the second technical objective; to "*characterise the substrate surface texture and determine the degree of texture transfer from contact with each different sonotrode under a broad range of UC processing conditions*". Analysis of Variance (ANOVA) is a statistical study used to determine whether observed variation among sample means is statistically significant (Moore & McCabe, 1993). In this instance ANOVA was used to establish if the variation in S_a of UC samples was the result of natural variation or due to differences caused by changing process parameters, including sonotrode S_a, oscillation amplitude, weld speed and weld force.

ANOVA is an established statistical method for determining the relationships between control parameters and response variables and has been used in a number of studies within the field of UC research to understand the effects of process parameters on bond formation. Janaki Ram et al. (2006) and Kulakov & Rack (2009) have utilised ANOVA to establish the influence of UC process parameters on LWD. Hopkins et al. (2012) also adopted ANOVA to determine the statistical significance of UC operating parameters on the mechanical properties of finished UC parts. In these cases statistically significant variations in the chosen response variables were examined to define the relative significance of UC process parameters with the intention of identifying the optimum conditions for bond formation. Similarly, ANOVA was used to examine the relative significance of substrate surface texture and bond strength within this investigation.

The Alpha 2 UC machine was used to manufacture the UC samples from each of the three sonotrodes and white light interferometery was used to measure the S_a of the parts produced.

4.1.2.1 Ultrasonic Consolidation Sample Fabrication

All UC test samples were manufactured on the Alpha 2 UC machine (Figure 2-16) using Al3003-H18 foil (Table 4-3). Al3003-H18 is a widely available commercial grade alloy used in domestic appliances and car trims. This particular material was chosen to enable comparison of results with previous UC research using Al3003-H18 on similar UC equipment (Kong et al. 2004a)(Kong et al. 2004b)(Kong 2005)(Kong & Soar 2005a)(Li & Soar 2009a).

Table 4-3: Composition and mechanical properties of aluminium alloy 3003 (Kong 2005).

Material Property	**Al3003-H18**
Composition (% weight)	97.0 Al 1.5 Mn 0.7 Fe 0.6 Si 0.2 Cu
Tensile Strength (MPa)	205
Yield Strength (MPa)	190
Elongation at Break (%)	4
Hardness (HB)	50

Three sets of UC test samples were fabricated by sonotrodes A, B and C using the process parameters listed in Table 4-4. In order to quantify the effect of UC process parameters on UC sample S_a an ANOVA of four factors at three levels was undertaken.

Table 4-4: ANOVA parameter level values of each factor for all sonotrodes.

Factors	**Level**					
	I	**II**	**III**	**I**	**II**	**III**
Sonotrode	A			B & C		
Oscillation Amplitude (µm)	15	20	21	14	17	20
Weld Speed (mm/s)	20	40	60	20	30	40
Weld Force (N)	1200	1400	1600	1200	1400	1600

The factors of oscillation amplitude, weld speed and weld force at high, medium and low levels were investigated, resulting in 27 process parameter combinations for each sonotrode. Preliminary testing highlighted that the range of process parameters at which sonotrode C could successfully consolidate foils was less than that of sonotrode A and it was not possible to achieve an acceptable level of bonding at oscillation amplitudes above 20µm and weld speeds of more than 40mm/s, at room temperature, using the Alpha 2 UC machine. Different level values were chosen for each sonotrode to ensure their effect was evaluated over what had proven to be the individual sonotrodes effective operating range. In order to verify the absence of variation three replicates for each combination were produced. Previous research has shown that the roughness of the sonotrode weld surface texture deteriorates during operation (Li & Soar 2009a) and therefore the samples were fabricated in a random order and the residual error was analysed to minimise the impact of sonotrode wear on the validity of the statistical analysis.

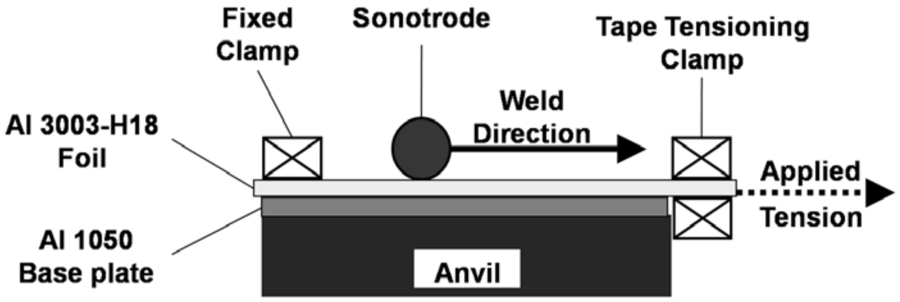

Figure 4-7: Diagram of test sample production on the Alpha 2 UC machine.

For the first set of samples the Alpha 2 UC machine was set up with sonotrode A. An Al1050 base plate, approximately 200mm in length which acted as the initial surface to which the first consolidated foil layer was bonded to, was placed on the anvil with Al3003-H18 foils, 25mm wide and 100µm thick, on top. The start end of both the base plate and foil were held in place using the fixed clamp and the end of the foil was secured by the tape tensioning clamp (Figure 4-7).

The appropriate oscillation amplitude, weld speed and weld force, as specified by the ANOVA experimental plan (Table 4-4), were set and the Alpha 2 UC machine ultrasonically consolidated a 150mm length of foil to the base plate. The specific length was chosen so that the samples would comply with the peel testing standard (BS EN 2243-2:1991) used in subsequent substrate bond strength measurements. The process was repeated and two more foils were consolidated to complete an individual test sample. Test samples for all the process parameter combinations for the first sonotrode were produced. The Alpha 2 UC machine sonotrode was replaced with sonotrode B and C to repeat the procedure to produce the second and third batch of test samples.

High build temperature has been identified as a significant factor in increasing bond quality (George & Stucker 2006)(Janaki Ram et al. 2006b) in UC and therefore the anvil temperature was monitored during processing to ensure that all the samples were manufactured at 25˚C ± 5. This investigation was part of a wider study examining the embedding capabilities of UC (as part of the SMUC project) and as some components are temperature-sensitive, for example electronics modules or SMA fibres, room temperature consolidation was chosen for UC sample so that the results could be applied across the study.

4.1.2.2 Substrate Surface Texture Measurement

All the test samples produced were measured using white light interferometery to characterise their S_a. For each UC sample the surface texture was measured in four different locations across the weld surface (Figure 4-8) using a Zygo NewView 5000 white light interferometer.

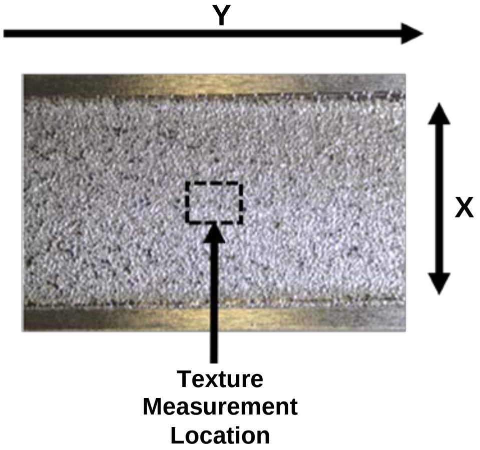

Figure 4-8: Photograph of a UC sample illustrating a texture measurement location, indication plane of sonotrode oscillation (X) and direction of sonotrode rotation (Y).

Identical measurement variables to those used for the sonotrode texture measurement were adopted (Table 4-1), allowing for the larger measurement area and scan length for samples fabricated by sonotrodes B and C. The data files were processed using the same template as used in the sonotrode texture measurement and the surface S_a for each measurement location was determined.

4.1.2.3 Analysis of Variance of Substrate Surface Texture

The ANOVA of process parameters on UC sample average S_a was designed to test the null hypothesis that varying the UC processing parameters had no statistically significant effect on the resultant average S_a of the sample surface. When the substrate surface texture measurements were collated, the sum of squares, SS, of each factor was determined by the sum of the deviations, x, from the population mean, $\bar{x}$, squared (where N is the number of groups within the factor). The sum of squares for each factor was divided by the degrees of freedom, df (N-1), for that factor to give the mean square value, MS (Equation 2-1).

Equation 4-1: $$MS = \frac{SS}{df} = \frac{\sum(x - \bar{x})^2}{N - 1}$$ (Moore & McCabe 1993).

Equation 4-2: $$F - Ratio = \frac{MS_{Factor}}{MS_{Residual\ Error}}$$ (Moore & McCabe 1993).

The F-test determines if the effect of an individual factor was significant compared to the general variation seen across the whole population. The F-Ratio (Equation 4-2) was calculated by dividing the mean square value of a factor, MS_{Factor}, by the mean square of the residual errors, $MS_{Residual\ Error}$.

The probability that a factor fulfils the null hypothesis, and therefore has no statistically significant effect on the resultant S_a of the UC sample, was determined by that factors P-value (from lookup tables). The factors with a P-value of less than 0.05, those that have a less than 5% probability of fulfilling the null hypothesis, can be said to have a statistically significant effect on the UC sample S_a with a 95% confidence level (Moore & McCabe 1993). It should be noted that one-way ANOVA assumes the effect of individual variables are not interdependent and therefore does not account for more complex interactions of process parameters on the response variable. A multi-variate ANOVA would need to be undertaken in order to characterise the interdependent relationships of process parameters and their effect on substrate surface texture and that is outside the scope of this investigation.

The S_a measurement data, along with the parent sonotrode and fabrication processes parameters were input into Statgraphics, version, 5.0 StatPoint Technologies, Inc., in order to determine the ANOVA of substrate surface texture. Statgraphics is a general use PC statistics package capable of performing a range of statistical functions, including ANOVA. This specific software was utilised in this research due to the availability of existing licenses at Loughborough University and its ease of use.

4.1.3 Analysis of Variance of Sonotrode Texture on UC Substrate Interlaminar Bond Strength

This section presents the approach used to contribute to the third Research Factor; to "*experimentally measure the interlaminar bond strength and characterise the failure mode of UC samples manufactured by each of the different sonotrodes*". This was achieved by experimentally measuring the interlaminar bond strength, through peel test analysis, of UC samples produced by each different sonotrode under a range of processing conditions.

The methodology of the substrate bond strength ANOVA is elucidated with a view to establish if the variation in interlaminar bond strength of UC samples was the result of natural variation or due to differences caused by changing process parameters, including sonotrode S_a, oscillation amplitude, weld speed and weld force.

4.1.3.1 Substrate Bond Strength Measurement

Surface texture measurement by white light interferometery is a non-destructive testing method, therefore the UC test samples fabricated by sonotrodes A, B and C used in section 4.1.2 (Analysis of Variance of Sonotrode Texture on Substrate Surface Texture) were also used as UC sample bond strength test pieces. The same four factor, three level ANOVA (Table 4-4) approach was used in order to quantify the effect of UC process parameters on substrate bond strength.

Peel test analysis is an established method of measuring interlaminar weld strength in UC (Friel et al. 2010)(Kong et al. 2003)(Kong et al. 2004a)(Kong et al. 2005) and was used, in this case, to compare the weld strength of samples produced by sonotrodes A, B and C. All UC test samples were peel tested according to BS EN 2243-2:1991, the British Standard used to determine the strength of adhesives in metal to metal peel tests, to establish the average resistance to peeling on the contact points within the weld interface (Kong 2005).

After the surface texture of the UC samples from all the sonotrodes had been measured they were peel tested. Each sample was placed in the peel test apparatus that was attached to a Lloyds Instruments LRX tensile testing machine (Figure 4-9). The uppermost foil layer, at the start end of the weld, was clamped into place. A pull to break test with preload of 0.5N was used and the tensile load was applied at 50 mm/min to the top foil. The load, time and extension data was recorded for each sample, until the load dropped to below 10% of the maximum recorded value. The maximum resistance to the peeling load for each sample was recorded.

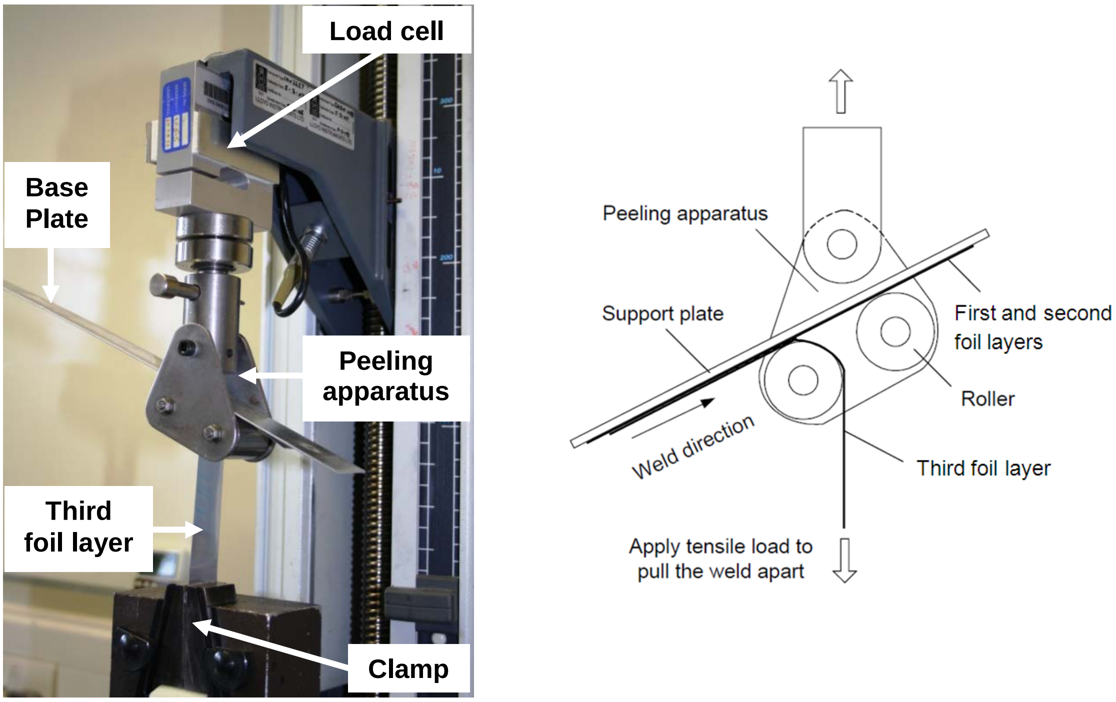

(i) (ii)

Figure 4-9: Lloyds Instruments LRX tensile testing machine set up for peel testing (i) and diagram of peel testing apparatus (ii) (Kong et al. 2004a).

4.1.3.2 Analysis of Variance of Substrate Bond Strength

The same approach was used in the initial ANOVA described in section 4.1.2.3. In this instance the ANOVA tested the null hypothesis that varying the UC processing parameters had no statistically significant effect on the resultant interlaminar bond strength of UC samples.

The maximum peel load data, along with the parent sonotrode and fabrication processes parameters were input into Statgraphics, version, 5.0 StatPoint Technologies, Inc., in order to determine the ANOVA of substrate bond strength.

4.2 Results

4.2.1 Sonotrode Surface Texture Characterisation

4.2.1.1 Sonotrode Surface Texture Measurement

(i) (ii) (iii)

Figure 4-10: Photograph of sonotrode A (i), B (ii) and C (iii).

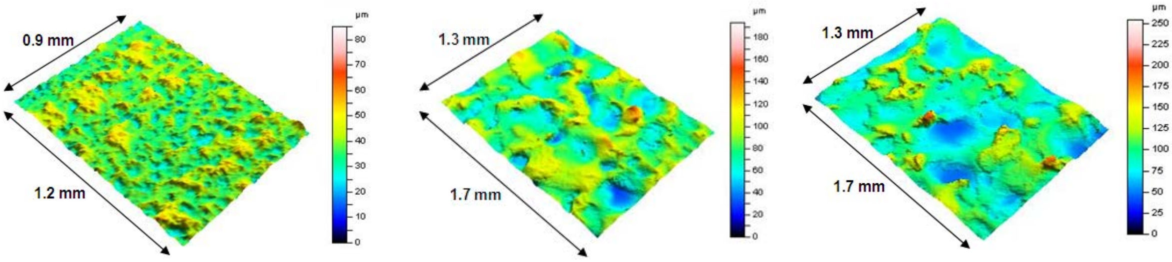

(i) (ii) (iii)

Figure 4-11: 3D pseudo-color image of the surface of sonotrode A (i), B (ii) and C (iii).

Table 4-5: Average surface texture analysis results for sonotrode A, B and C.

Surface Texture Parameters	**Sonotrode**					
	A		**B**		**C**	
	Av.	**σ**	**Av.**	**σ**	**Av.**	**σ**
S_a (μm)	**4.97**	0.60	**14.79**	0.98	**18.87**	1.27
S_q (μm)	**6.40**	0.58	**18.58**	1.05	**23.70**	1.53
Ssk	**-0.172**	0.26	**-0.252**	0.22	**0.398**	0.22
Sku	**3.27**	0.41	**3.06**	0.35	**3.32**	0.56
Sds (1/mm^2)	**39034**	841	**38046**	1308	**36693**	2419
Ssc (1/mm)	**1.14**	0.05	**1.13**	0.07	**1.61**	0.51
Str (s = 0.2)	**0.899**	0.03	**0.796**	0.10	**0.754**	0.10
Sal* (μm)	**29.3**	3.2	**159.0**	22.6	**184.2**	22.1
Std (°)	**71.8**	48.37	**68.32**	48.05	**94.7**	34.83
Vmp (μm^3/μm^2)**	**0.286**	0.057	**0.731**	0.125	**1.339**	0.271
Vmc (μm^3/μm^2)**	**5.47**	0.94	**16.90**	1.54	**21.24**	1.79
Vvc (μm^3/μm^2)**	**7.54**	0.68	**21.43**	1.29	**30.27**	1.94
Vvv (μm^3/μm^2)**	**0.872**	0.108	**2.381**	0.340	**2.161**	0.275
Sdr (%)	**49.39**	3.90	**120.59**	13.24	**207.89**	168.62

** s = 0.2*

***p = 10%, q =80%*

4.2.1.2 Sonotrode Surface Texture Wear Measurement

Table 4-6: Percentage change in surface texture measurements for sonotrode A, B and C after approximately 300 layers (significant variation is highlighted).

Texture Parameter	Change in Sonotrode Surface Texture Parameters (%)		
	A	B	C
Sa (µm)	-7.0	0.6	-3.6
Sq (µm)	-7.6	0.7	-4.9
Sku	10.9	1.6	-7.8
Ssk	-216.7	-6.1	-54.9
Sds (1/mm2)	4.6	2.7	6.2
Ssc (1/mm)	6.6	0.4	-18.1
Str*	-1.3	-9.4	1.6
Sal* (µm)	-6.0	-0.6	5.5
Std (°)	2.2	6.5	-28.8
Vmp (µm^3/µm^2)**	-27.1	5.9	-15.3
Vmc (µm^3/µm^2)**	-5.2	0.5	-3.6
Vvc (µm^3/µm^2)**	-14.3	0.4	-7.4
Vvv (µm^3/µm^2)**	-0.5	0.3	3.7
Sdr (%)	16.4	9.7	28.7

** s = 0.2*
***p = 10%, q =80%*

4.2.2 Analysis of Variance of Sonotrode Texture on Substrate Surface Texture

4.2.2.1 The Effect of Process Parameters on UC Substrate Average Roughness

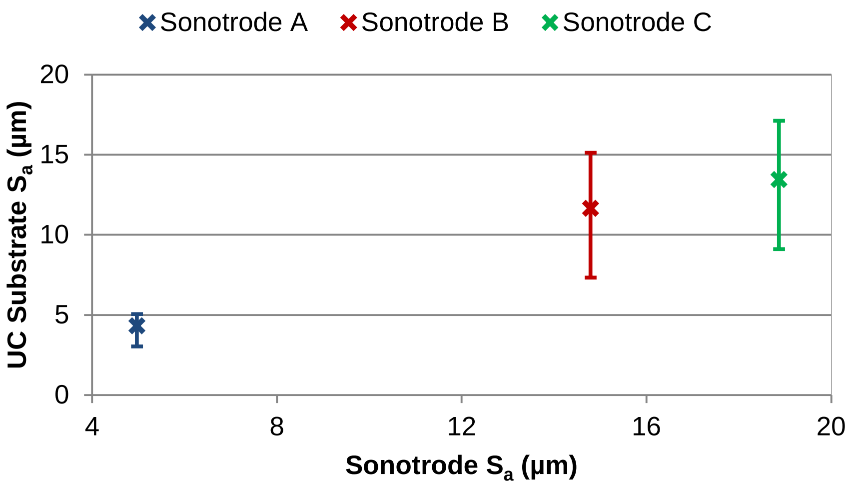

Figure 4-12: Graph to show the mean and range of UC substrate S_a processed with sonotrodes A, B and C.

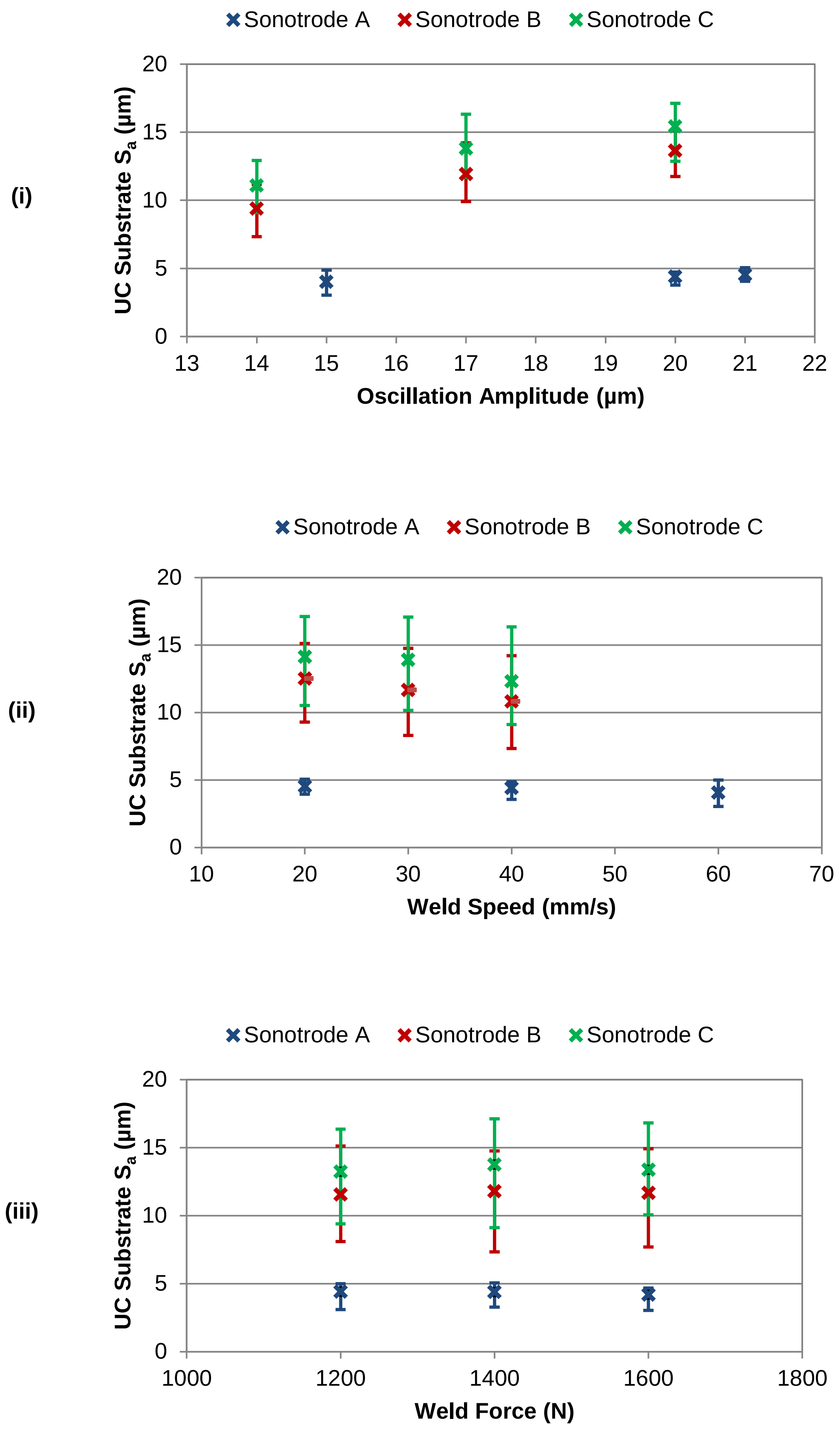

Figure 4-13: Graph to show the mean and range of UC substrate S_a processed with sonotrodes A, B and C at different (i) amplitudes, (ii) weld speeds and (iii) weld forces.

4.2.2.2 Analysis of Variance for UC Substrate Average Roughness Data

Table 4-7: ANOVA of UC process parameters on UC substrate surface S_a (statistically significant variation is highlighted).

Factors	Sum of Squares	Degrees of freedom	Mean Square	F-Ratio	P-Value
Sonotrode S_a	1639.92	2	819.959	1450.53	0.0000
Oscillation Amplitude	510.426	4	127.606	225.74	0.0000
Weld Speed	66.2098	3	22.0699	39.04	0.0000
Weld Force	3.06402	2	1.53201	2.71	0.0686
Residual Error	130.58	231	0.565283		
Total (Corrected)	4498.04	242			

4.2.2.3 Surface Roughness Residual Errors

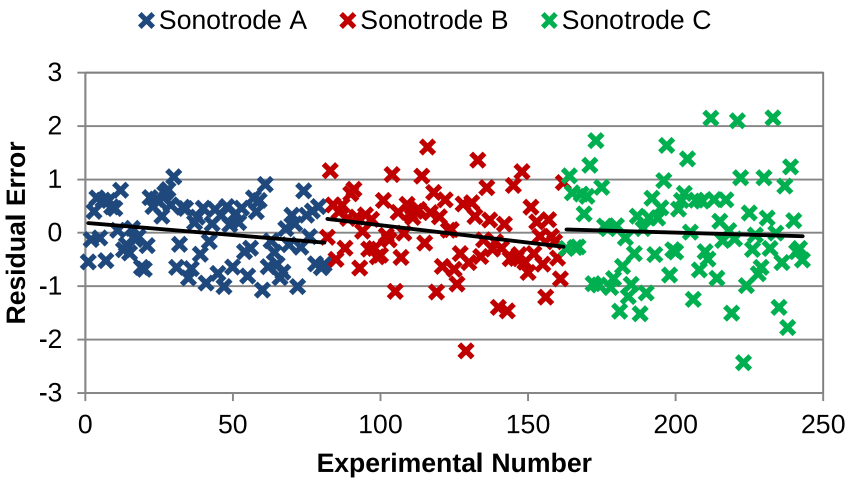

Figure 4-14: Graph to show residuals against experimental number for UC samples produced by sonotrodes A, B and C.

4.2.3 Analysis of Variance of Sonotrode Texture on Substrate Bond Strength

4.2.3.1 The Effect of Process Parameters on UC Sample Bond Strength

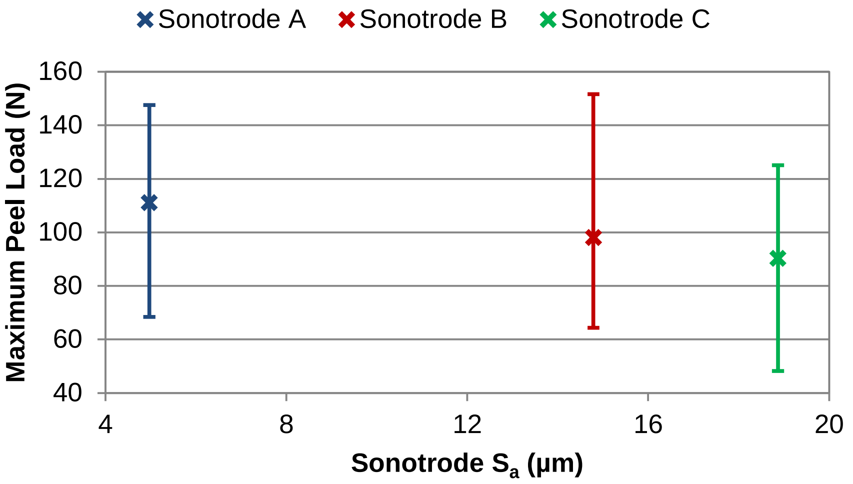

Figure 4-15: Graph to show the mean and range of maximum peel load for UC samples processed with sonotrodes A, B and C.

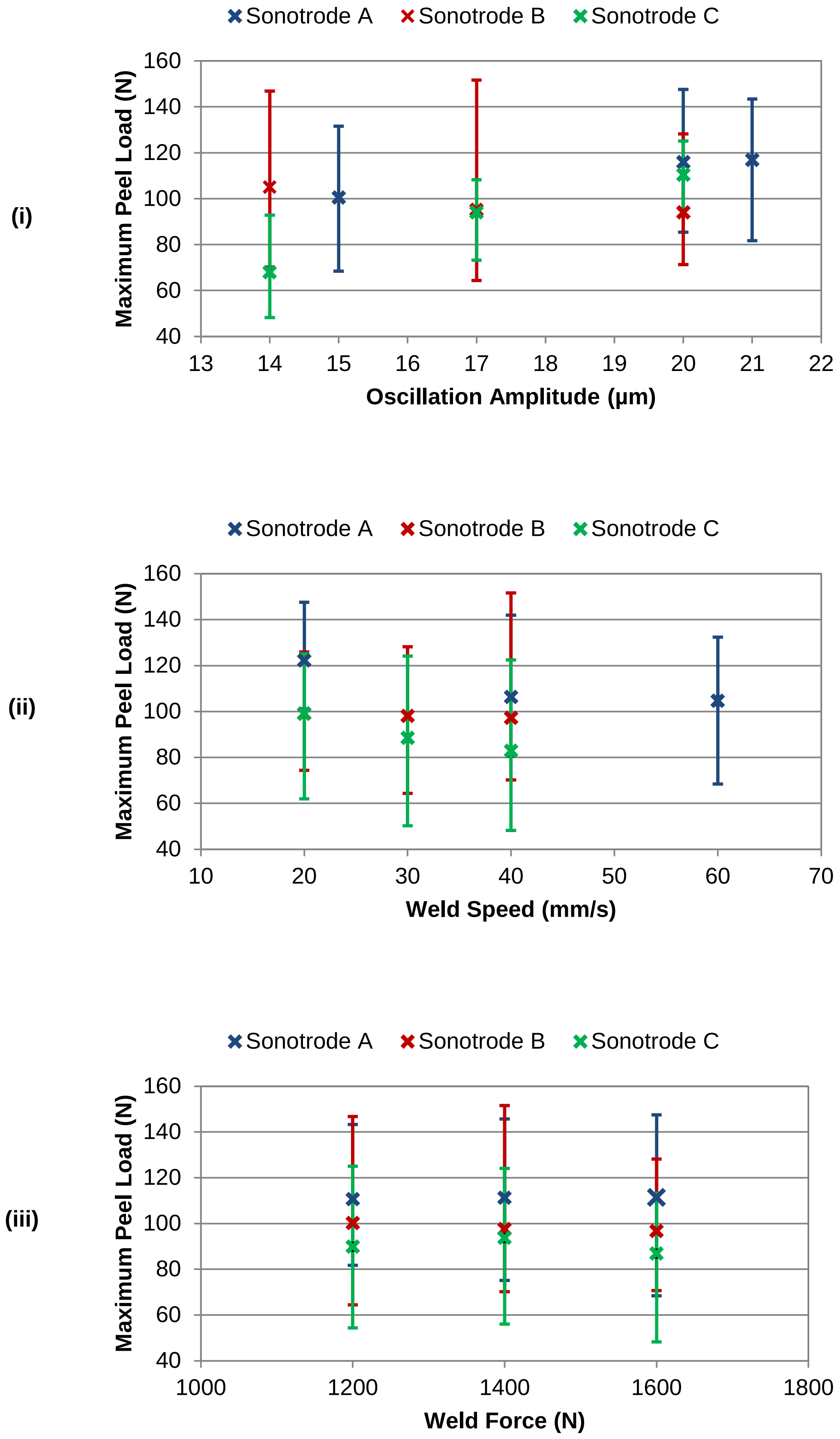

Figure 4-16: Graph to show the mean and range of maximum peel load for UC samples processed with sonotrodes A, B and C at different amplitudes (i), weld speeds (ii) and weld forces (iii).

4.2.3.2 Analysis of Variance for Interlaminar Peel Strength Data

Table 4-8: ANOVA of UC process parameters on interlaminar peel strength in UC samples (statistically significant variation is highlighted).

Factors	Sum of Squares	Degrees of freedom	Mean Square	F-Ratio	P-Value
Sonotrode S_a	6510.21	2	3255.11	11.68	0.0000
Oscillation Amplitude	10748	4	2687.01	9.64	0.0000
Weld Speed	6693.1	3	2231.03	8	0.0000
Weld Force	313.393	2	156.697	0.56	0.5708
Residual Error	62156.9	223	278.73		
Total (Corrected)	96771.4	234			

4.2.3.3 Bond Strength Residual Errors

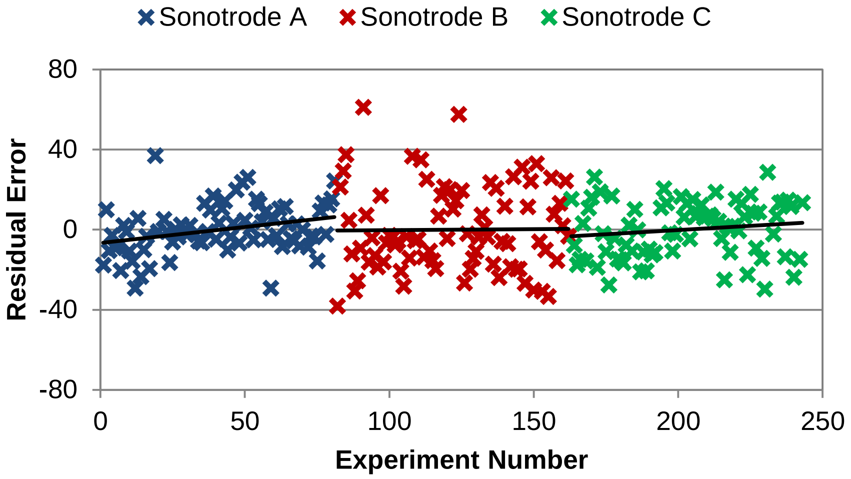

Figure 4-17: Graph to show residuals against experimental number for UC samples produced by sonotrodes A, B and C.

4.2.4 A comparison of Surface Roughness and Interlaminar Peel Strength

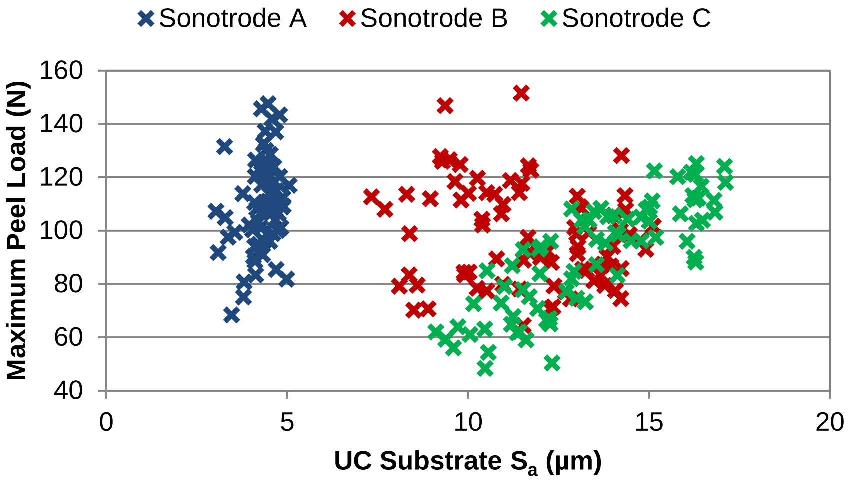

Figure 4-18: Graph to show the relationship between UC substrate S_a and interlaminar peel strength for UC samples produced by sonotrodes A, B and C.

4.3 Discussion

4.3.1 Sonotrode Surface Texture Characterisation

From visual inspection of the weld surface textures of sonotrodes A-C (Figure 4-10) it was apparent their weld surface textures were quite different. The 3D representation of sonotrode A's surface (Figure 4-11i) showed an apparently random distribution of peaks and troughs across the surface. The 3D representation of sonotrode C (Figure 4-11iii) illustrated a less dense population of peaks and valleys whose height range was more than double that of sonotrode A. The peaks in sonotrode C were isolated and significantly higher than the surrounding material while the valleys appeared more shallow with a more gentle transition over a larger area. The intermediate surface of sonotrode B (Figure 4-11ii) contained features that were higher in magnitude than sonotrode A, but lower in magnitude than sonotrode C, with a density of features in-between the two extremes.

4.3.1.1 Amplitude Parameters

The S_a and S_q parameters both confirmed that the amplitude of features on the weld surface of sonotrode C were the highest, at 18.87µm, followed by sonotrode B, 14.79µm and Sonotrode A was the lowest, at 4.97µm (Table 4-5). The standard deviation of these measurements correlated to their magnitude; there was more variation across the weld surface of the sonotrodes with rougher surfaces, C and B, while the texture was more consistent across the less rough weld surface of sonotrode A.

In previous research Li & Soar (2009a) stated that sonotrodes with lower amplitude surface roughness's used in the fabrication of UC parts result in poor interlaminar bonding. It was suggested that a lower level of mechanical coupling between the sonotrode and foil surfaces, due to the low peak amplitudes and limited mechanical interlocking between foil and sonotrode, causes slip between the sonotrode and foil (Figure 4-19). To achieve strong, nascent material bonding in UC the foil surface oxide layer must be broken up in order to bring the base material into direct contact (2.3.3.5) and less relative motion of mating surfaces during bonding could result in a reduced breakup of the oxide layer and weaker interlaminar bonding.

It should also be considered that sonotrodes with high amplitude surface textures impart high amplitude defects onto the surface of the foils they consolidate (Kulakov & Rack 2010). Sonotrode induced surface texture transfer could form deep surface valleys which result in parabola shaped defects in subsequently deposited foil layers and reduced interlaminar weld strength (Janaki Ram et al. 2006b).

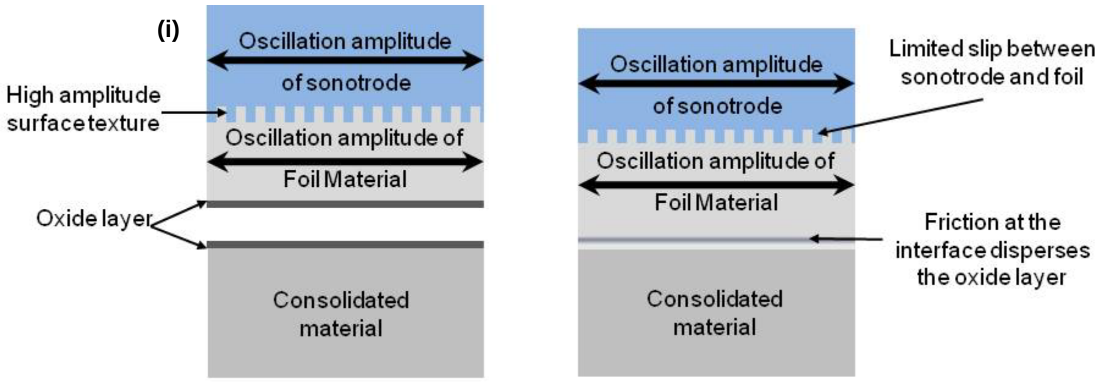

Before Processing **During Processing**

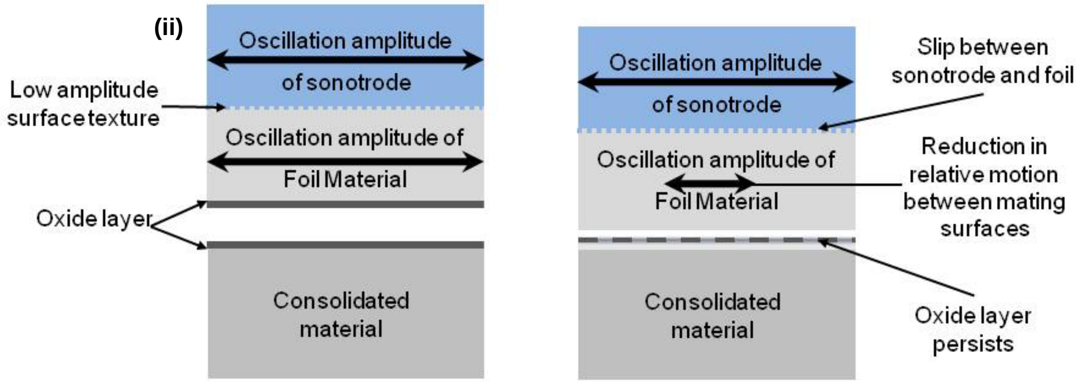

Figure 4-19: The potential effect of high (i) and low (ii) amplitude sonotrode surface textures on oxide layer dispersal prior to (left) and during (right) UC.

The average value of Ssk for sonotrode A and B showed a slight negative skew, of -0.172 and -0.252 respectively, which indicated that the surfaces were dominated by valleys. Conversely, the average Ssk for sonotrode C was distinctly positive and hence the surface texture appeared to be dominated by peaks. The 3D surface image of sonotrode C (Figure 4-11iii) showed the presence of extreme high peaks across the surface with the majority of the surface dominated by troughs. EDM textured surfaces tend to be empty and open as they are formed by overlapping craters (Bleys et al.2006), so it would be expected that the sonotrode surfaces would have a negative Ssk. The fact that Ssk can be significantly affected by extreme values, as explained in the review of surface texture parameters (Appendix 4.1), could explain the positive skew value returned for sonotrode C.

Sonotrode A and C had a similar level of Sku over the critical value of 3.00, A with a value of 3.27 and C with a value of 3.32, indicating the presence of more distinct peaks and/or valleys across their surface texture (Figure 4-20i). The lower Sku of sonotrode B, at 3.06, was more likely to consist of a more slowly varying texture (Figure 4-20ii). The higher level of Sku exhibited by sonotrode A and C would have, in theory, produced higher stress concentrations where the sharper sonotrode peaks were in contact with the foil surface.

The subsequent increased penetration and mechanical interlocking between foil and sonotrode might better maintain the relative motion between the foil and base material, resulting in better interlaminar bonding through atomic forces across nascent material.

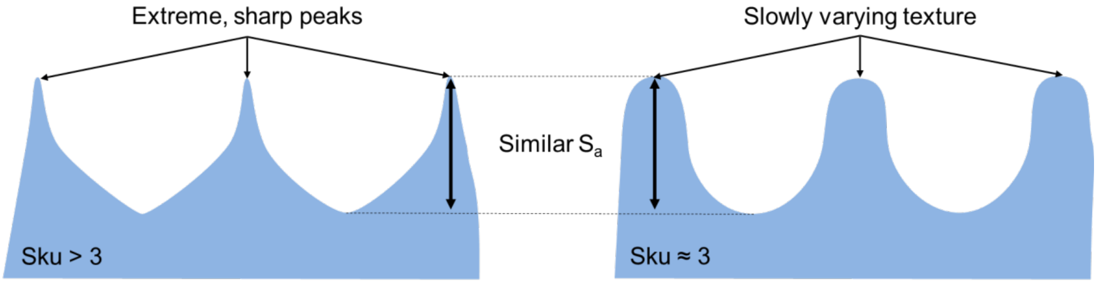

(i) (ii)

Figure 4-20: Diagram illustrating the difference between two surface textures dominated by valleys with similar amplitude features, but high (i) and low (ii) Sku.

The values of standard deviation for Ssk and Sku of all the sonotrodes were relatively high, signifying that these values were not wholly consistent across all the measurements taken and that there is significant texture variation over the sonotrode surfaces.

4.3.1.2 Topological Characterisation Parameters

The average Sds of sonotrodes decreased as the sonotrode S_a increased; sonotrode A had the highest Sds of 39034 peaks/mm^2, while sonotrode C had the lowest at 36693 peaks/mm^2 (Table 4-5). In theory, a lower Sds on the sonotrode surface, as was seen in sonotrode C, would result in higher local contact stresses, as the applied weld force was distributed over a smaller number of peaks, while a lower Sds as was seen in sonotrode A, would correspond to a lower localised contact stresses, as the applied weld force was distributed over a higher number of peaks.

There was a large variation across all the Sds measurements, with the standard deviation increasing as Sds decreased. The standard deviation in the Sds of sonotrode surface C was significantly higher than that of sonotrode A, with almost 3 times the variation across the measurements of sonotrode C. In practice this could have caused similar variation in bond inconsistency in UC as the weld force was distributed unevenly across the sonotrode weld surface (Li & Soar 2009a).

The Ssc of sonotrode C, at 1.6 peaks/mm was slightly higher than that of sonotrode A and B, at 1.1 peaks/mm. The lower level of curvature of sonotrode A and B equated to “gentle” peaks with a larger radius than the greater curvature and sharper peaks of sonotrode C (Figure 4-21). The curvature of the summit peaks affected the contact mechanics between the sonotrode and foil during UC bonding and the incidence of smooth, more curved, peaks increased the contact area, resulting in lower local stress at contact points as weld force was distributed across a larger area between mating surfaces.

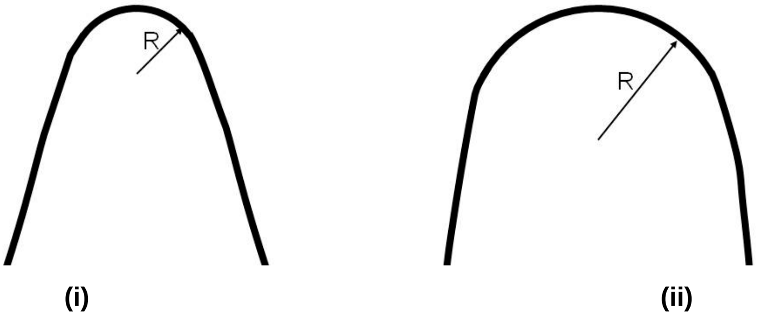

Figure 4-21: Diagram illustrating the difference between two summits with high (i) and low (ii) Ssc (where R is the summit radius).

4.3.1.3 Spectral Analysis Parameters

The Str was relatively high for all the sonotrodes, indicating a high level of surface isotropy. The surface texture of sonotrode A was 90% isotropic, sonotrode B was less so at 80%, while sonotrode C showed an even lower level of texture orientation of 75% (Table 4-5). These results corresponded with the description of EDM surface topography (Bleys et al. 2006) as isotropic due to the nature of the process as the surface was textured by randomly overlapping craters. The Str was more than 0.5 for all the sonotrode surfaces, therefore in this case the texture direction, Std, was disregarded.

When analysing the texture of a surface it was important that a large enough area of the surface was measured so that any calculations of surface texture parameters could be trusted to give an accurate representation of that surface. As previously mentioned in chapter 4.1.1, Sonotrode Surface Texture Characterisation Methodology, larger areas of sonotrode B and C surface were measured in an attempt to fully capture the surface features. The Sal represents the distance between areas of the surface which were statistically different and hence were used to confirm that an adequate area of the sonotrode weld surface textures had been measured. The Sal for sonotrode A is 29.3µm, sonotrode B has a larger Sal of 159.0µm, while sonotrode C had the largest Sal of 184.2µm (Figure 4-22), this meant that the weld surface of sonotrode A was made up of a number of short wavelength components, while sonotrode B and C consisted of longer wavelength spectral components, quantifying what was seen in Figure 4-11. These Sal values confirm that the individual measurement areas, 1.10mm^2 for sonotrode A and 2.33mm^2 for sonotrodes B and C, were significantly large enough to wholly capture a number of surface features.

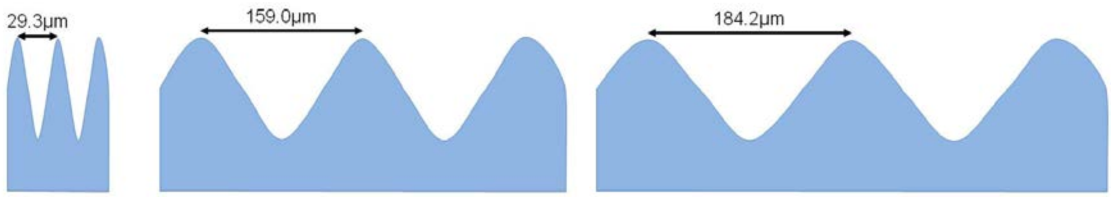

(i) (ii) (ii)

Figure 4-22: Diagram illustrating the average Sal of sonotrode A (i), B (ii) and C (iii).

As seen within the Sds measurements, the lower density of features on the sonotrode surface could corresponded to higher local contact stresses, as seen in sonotrode C with a larger Sal, while a lower density of features, as seen in sonotrode A with a smaller Sal, would correspond to lower local contact stresses.

4.3.1.4 Volume Parameters

Table 4-5 presents the surface texture parameters which characterise the relative Vmp, Vvv, Vmc, and Vvc of the sonotrode weld surface textures (Figure 4-23). It should be noted that there was a relatively large degree of variation in the volume measurement parameters, but that general trends in the results could still be considered.

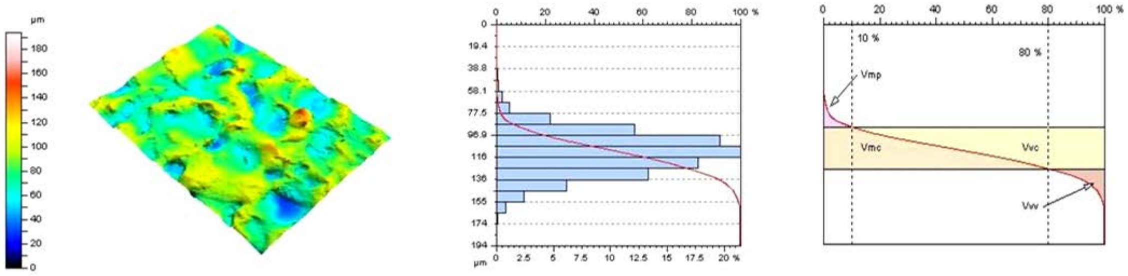

(i) (ii) (ii)

Figure 4-23: Example surface texture measurement of sonotrode B (i) showing the depth distribution and Abbott-Firestone curve (ii) and volume parameters (iii).

The measurement of a relatively small volume of material within the top 10%, Vmp, of all three sonotrodes supported the previous assertion that there were a small number of extreme peaks which protruded above the bulk of the material. These extreme peaks would have been the first points of contact when the sonotrode engaged with the foil's surface during UC. The high weld force spread over the low contact area of isolated peaks would have likely led to deformation of the softer UC foil material and an increase in contact area as more peaks came into contact with the foil material. There was also a relatively small void volume within the bottom 20%, Vvv, of the sonotrodes weld surface which indicated that there were a small number of steep-sided crevices on the sonotrode surfaces.

The Vmp, Vmc and Vvc measurements correlated to the magnitude of the S_a measurement; there was more peak material, core material and core void volume in the sonotrode with the roughest surface, C, than those with less rough surfaces, sonotrode B and A. In agreement with the Ssk measurements, the Vvv of sonotrode B was larger than that of sonotrode A or C and therefore appeared to exhibit the largest void volume.

The volume parameters for all the sonotrodes showed that the surface texture void volume was larger than that of the material volume. This adheres to the previously described characteristic EDM surface topography (Bleys,et al. 2006) as empty and open in nature and supports the conclusion that their surfaces were dominated by voids

For all sonotrodes the ratio of material volume to void volume for the mid 70% of the texture was similar, where the void volume was 1.4 times that of the material volume for sonotrode A and C and 1.3 for sonotrode B. Therefore, in terms of volume, the sonotrode weld surface textures were more dominated by troughs than peaks (Figure 4-25: Diagram showing the effects of sonotrode wear; before (i) and after a period of operation (ii).). This result was in contradiction with the positive values of skew obtained for sonotrode C, however, the volume characterisation method disregards the extreme peaks and troughs included in the measurement of skew which can distort results, and is therefore a more credible result.

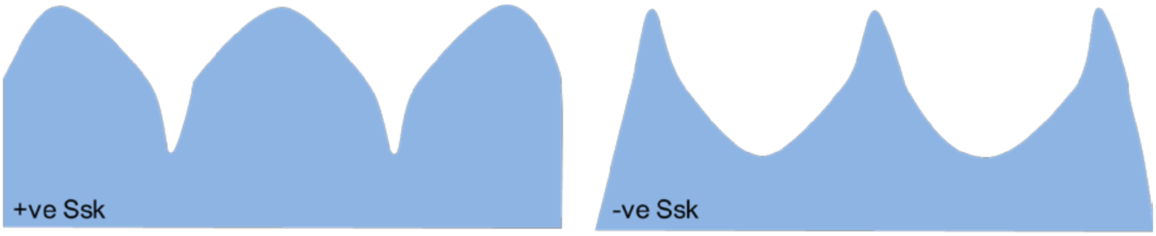

(i) **(ii)**

Figure 4-24: Comparison of surfaces dominated by peak material (i) and those whose surface are dominated by voids (ii).

4.3.1.5 Bearing Ratio Parameters

The Sdr of the sonotrode A weld surface showed an increase of 50% in surface area as a result of the surface texture (Table 4-5). The increase was generally consistent over all the measurements taken as the standard deviation was only 3.9%. The Sdr of sonotrode B’s weld surface showed a 121% increase in surface area as a result of the surface texture, with a larger standard deviation of 13%. The Sdr value was significantly higher for sonotrode C, which saw a 208% increase in surface area due to surface texture. However, the variation in developed interfacial ratio over the surface of sonotrode C was large, with Sdr measurements ranging from 60% to 660% across the sonotrode surface.

From analysis of the individual measurements, where higher developed interfacial ratio values occurred, it became apparent that these values corresponded to the highest summit density measurements (b3, c2, c3 and d2 for sonotrode C) which exhibited a similar level of significant variation.

Sonotrode A and B both exhibited a higher Sds than sonotrode C, but did not have such large developed Sdr values. This was because while the number of features per unit area may have been higher in A and B, the height of these features was not. This was shown by the lower average roughness value for sonotrode A of 4.97µm and B of 14.97µm, compared to sonotrode C, which had a S_a value of 18.87µm.

4.3.1.6 Sonotrode Texture Wear Measurement

In order to identify any changes in weld texture as a result of wear, the surface of sonotrode A, B and C were measured after they had processed approximately 300 foil layers at room temperature over a period of two days. Table 4-6 showed the percentage change in parameters for all three sonotrodes.

While some small changes in the weld surface texture of the sonotrodes may have occurred over this small period of operation, it was difficult to identify these changes outside of the inherent variation of the EDM-textured surfaces and the spatial resolution of the white light interferometer. Only potentially significant changes in textures, where the percentage change exceeded the measurement variation, were identified within this analysis and the potential explanations for these changes were discussed.

There was no significant change in the sonotrode weld surface texture of sonotrode B during the test period. The only significant change observed in the weld surface texture of sonotrode C was a slight decrease in core void volume, Vvc. This reduction in void volume could have been the result of material adhesion and build up in sonotrode cavities or a reduction in peak amplitude as a result of impact and abrasion, both previously identified changes in sonotrode texture that occur over time (Figure 4-25) (Li & Soar 2009a). However, no other significant changes were identified to support this theory and the change could have been the result of the original EDM-texture surface variation.

A significant change in the Ssk of sonotrode A was observed as the degree of negative skew increased. The change in surface texture correlated to the wearing down of surface asperities over time, due to impact and abrasion during operation, resulting in a surface texture that became more dominated by valleys (Figure 4-25).

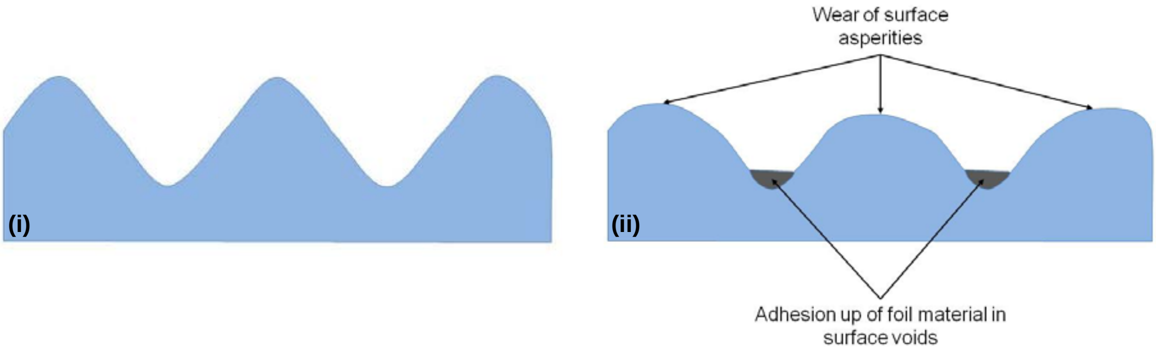

Figure 4-25: Diagram showing the effects of sonotrode wear; before (i) and after a period of operation (ii).

There was also an increased Ssc across sonotrode A's weld surface texture which supported the previously stated assumption that contact between the sonotrode surface asperities and the foil material during bonding blunts asperity peaks, increasing the radius of curvature of individual summits. The Sds of sonotrode A was also seen to increase. Individual summits were defined as any point above all 8 nearest neighbours above the mean plane. It could be assumed that the highest, extreme peaks were the first to be worn down during sonotrode operation. The abrasion and reduction in height of these peaks would have meant that other, lower amplitude surface variations would have been reclassified as peaks within the new surface texture landscape. The increase in both Sds and Ssc would have meant a reduction in local contact stresses over operation time, as the contact area increased while the applied force remained constant. Again, these results supported the previous research by Li & Soar (2009a) that, sonotrode wear can be a significant factor in interlaminar bonding in UC and should be monitored.

A decrease in Vmp, and Vvc was also seen in the texture wear measurement results for sonotrode A. A decrease in peak volume would have been expected as the asperity peaks were worn down through abrasion and impact. As previously noted with sonotrode C, a decrease in core volume could be due to the build-up of foil material within the sonotrode surface cavities.

4.3.2 Analysis of Variance of Sonotrode Texture on Substrate Surface Texture

4.3.2.1 The Effect of Process Parameters on UC Sample Average Roughness

During UC the upper surface of the foil that was due to be bonded came into contact with the rough surface of the sonotrode. The asperity peaks of the sonotrodes rough texture plastically deformed the upper foil surface under the applied weld force. Mechanical coupling between the foil and sonotrode caused the foil to move in plane with the sonotrode at the same oscillation amplitude. The relative motion of the mating surfaces was thought to have generated shear stress at the interface which, along with the compressive and tensile force of the sonotrode, initiated the breakup of the oxide layer on the underside of the foil and the upper surface of the previously consolidated material (as described by the contact-bond process described in section 2.3.3.5 Atomic Forces Across Nascent Material within the Literature Review). The brittle oxide was broken up and plastic flow induced in the material, nascent material extruded through the gaps in the fractured oxide layer and contact points were formed. These contact points were broken and reformed, increasing the weld density, as the relative motion between the foil and previously consolidated material continued (Figure 2-35 and Figure 2-36)

Sonotrode Surface Roughness

The UC samples were fabricated by three different sonotrodes under a range of processing conditions and their surface roughness measurements varied over a large range of values. Figure 4-12 showed that the average roughness of UC samples increased as the average roughness of the sonotrode used to fabricate those samples increased. Samples produced by sonotrode A, with an S_a of 5.0µm exhibited the lowest average surface roughness, with values ranging from 3.0µm to 5.1µm. Samples manufactured using sonotrode B, which had an S_a of 14.8 µm, had a higher average roughness, which varied more considerably between 7.3µm up to 15.1µm. Samples manufactured using sonotrode C, which had an S_a of 18.9µm, had the highest average roughness over a similar range as those samples from sonotrode B of 9.1µm up to 17.1µm. The results indicated that the sonotrodes impart a similar or reduced magnitude version of their surface roughness onto the upper surface of the UC samples they produced.

When the sonotrode came into contact with the foil substrate an imprint of that sonotrode’s texture would have been imparted onto its upper surface (Friel et al. 2010). The upper surface of the foil was plastically deformed as the relatively hard sonotrode surface asperities plastically deformed the foil surface and the substrate material was displaced and forced into the sonotrodes surface cavities, resulting in an inverted version of the sonotrode being transferred to the sample surface (Figure 4-26). In the case of sonotrode B and C the weld surface cavities were deeper and hence might not have been completely filled with plastically deformed material during processing, resulting in areas of the foil that appeared to remain unaltered by the sonotrode. An imperfect texture transfer would have resulted in a foil surface with lower amplitude peaks with flat summits, resulting in a lower average roughness, as was seen in the majority of samples from sonotrode B and C. In samples from sonotrode A only a small number of surface cavities would be sufficiently deep so as to not come into contact with the foil material and hence a smaller reduction in average roughness could be expected (Figure 4-26ii).

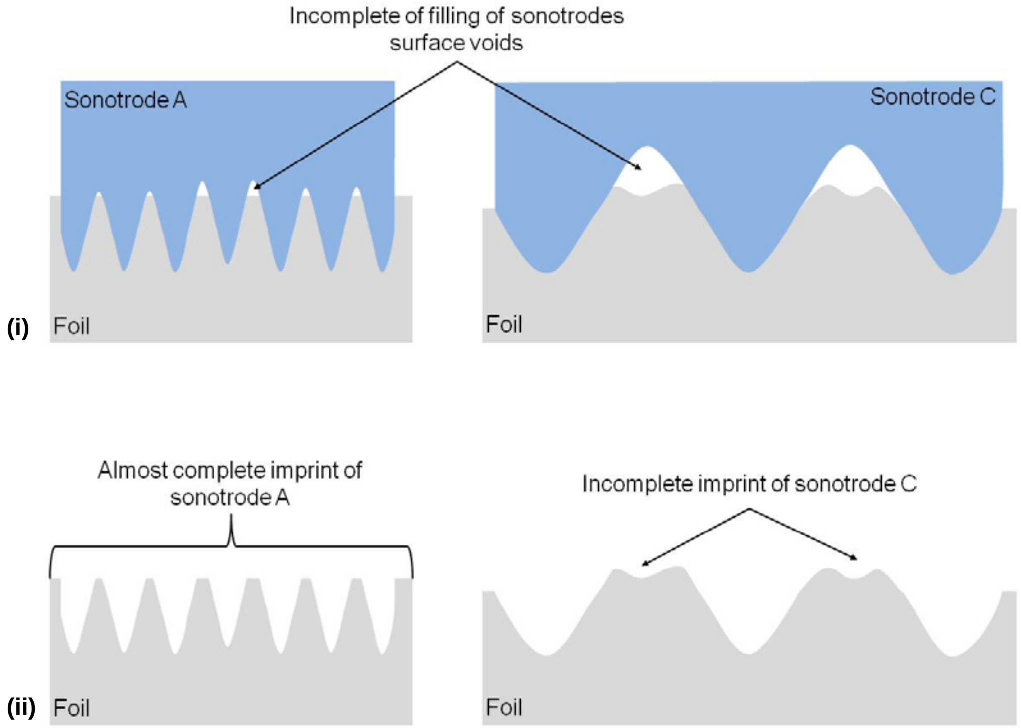

Figure 4-26: Diagram to illustrate plastic deformation of the foil material by sonotrodes A (left) and C (right) during processing (i) and the partially imprinted surface texture that remains on the foil surface after processing (ii).

The sonotrode texture characterisation results (Table 4-5) showed that there was more variation in the consistency of sonotrode average roughness measurements as the amplitude of those roughness measurements increased. Kulakov & Rack (2010) stated that the exact nature of the texture transfer between the sonotrode and upper foil surface in UC was dependent upon the process parameters used; the extent to which the foil surface was plastically deformed was dependent upon the applied weld force, the sonotrodes amplitude of oscillation, which determined the shear stress in the direction of sonotrode motion and the weld speed which affected the compressive and tensile stresses within the foil as the sonotrode rotated forward and the foil material was plastically deformed and displaced. These results (Figure 4-12) agreed with the Kulakov’s research and further suggested that the variation in texture transfer achieved due to changes in process parameters was also significantly dependent upon the original sonotrode surface texture; as the surface roughness of the sonotrode increased the range of UC sample surface textures that were produced under different processing conditions increased.

Oscillation Amplitude

Figure 4-13i showed that the S_a of UC samples increased as oscillation amplitude increased for UC samples produced by all sonotrodes, and that the increase was more substantial in the samples fabricated by the rougher sonotrodes B and C.

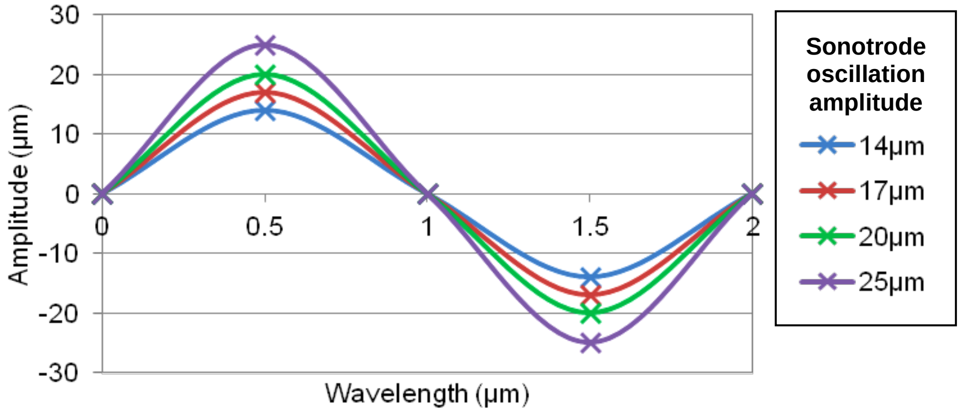

Figure 4-27: The effect of increasing oscillation amplitude for a sonotrode operating at a constant wavelength.

The data (Figure 4-13i) illustrated that UC sample surface roughness increased as oscillation amplitude increased. Figure 4-27 illustrates the theoretical increase in lateral motion that occurs when the oscillation amplitude of the sonotrode increases for a given weld speed (see Chapter 4 Appendix 4.4) for calculation of wavelength from weld speed).

According to the surface effect (section 2.3.4.1), the increased magnitude of cyclic shear stresses from the additional lateral motion would have generated increased interface temperatures as a result of increased friction and deformational heating. The temperature increase would have affected a reduction in the flow stress of the interface material and the resulting increased plastic flow would have increased the degree of foil material forced into the sonotrode cavities and penetration of the sonotrode asperity peaks into the foil material. The volume effect (2.3.4.2) would have attributed the increased ultrasonic energy per unit area to acoustic softening causing the reduction in flow stress, and resulting increased sample surface roughness, at higher sonotrode oscillation amplitudes. The Bauschinger effect (2.3.4.3) would account for the increased plastic deformation through the high frequency cyclic-mechanical softening, where increasing strain further reduced the material flow stress during the reversed-loading conditions.

Any slip between the foil and sonotrode during the final stages of consolidation, resulting in overlapping of the surface textures imparted onto the substrate surface through the additional lateral movement of the sonotrode seen at higher amplitudes could also explain why a higher average roughness was seen at higher oscillation amplitudes in UC.

Weld Speed

Figure 4-13ii shows the average roughness of UC samples decreased as weld speed increased for samples produced by all sonotrodes and that the decrease was also more substantial in the samples fabricated by the rougher sonotrodes, B and C.

The results in Figure 4-13ii showed that a decrease in UC sample surface roughness was seen as weld speed increased. The surface effect theory would accredit the change in sample surface roughness to an increased shear force per unit area affecting a decrease in material yield strength as a result of heating due to friction and deformation. The more complete texture transfer between foil surface and sonotrodes is the product of increasing foil surface plastic flow under these conditions. As seen with increasing amplitude, the higher ultrasonic energy per unit area associated with lower weld speeds could have been attributed to acoustic softening under the volume effect theory. Lower weld speeds were closer to true axial cyclic loading, therefore the greater reduction in material flow stress could have been explained by the additional softening of the Bauschinger effect.

Weld Force

The effect of weld force on UC sample average roughness appeared to have been limited, irrespective of the sonotrode used. Figure 4-13iii showed that there was a small decrease in the average roughness of UC samples produced by sonotrode A as the weld force increased, while UC samples produced by sonotrode B and C showed a minimal reduction in surface roughness as the weld force increased.

While the trends seen in surface roughness for varying oscillation amplitude and weld speed were the same for both sonotrodes, the relationship between weld force and UC sample surface roughness appeared to differ. Increasing weld force could have limited the oscillation of the sonotrode resulting in a smaller oscillation amplitude than was expected. As small oscillation amplitudes have been shown to equate to lower surface roughness’s, this phenomenon could have accounted for the decreased surface roughness seen in samples under increasing weld force in sonotrode A samples. The lower surface roughness which occurred in sonotrode samples fabricated at lower weld forces could have been due to the fact that less upper foil surface plastic deformation occurred resulting in imperfect texture transfer as the sonotrode engaged at a lower pressure over the surface.

Overall, the S_a parameter was a useful method of comparison between parent sonotrode and sample, as it did not take into account positive and negative skew of the texture, allowing the direct comparison of inverted surface textures. It could have been assumed that the UC samples would also exhibit other surface texture characteristics similar to those of their parent sonotrode. This topic is examined more thoroughly in the following experimental chapter.

Previous research (Janaki Ram et al. 2006a)(Kong et al. 2004a) into the effects of amplitude and weld speed saw similar trends in LWD as those seen here in average surface roughness. LWD increased with increasing amplitude and decreased with increasing weld speed. The results suggested a correlation between LWD and UC sample surface roughness, but this relationship cannot be confirmed without further experimentation.

4.3.2.2 Analysis of Variance for Sample Average Roughness Data

The ANOVA of S_a for UC samples produced (Table 4-7) stated that changes in the operating parameters of sonotrode S_a, oscillation amplitude, and weld speed had a statistically significant effect on the S_a of UC sample surfaces. Sonotrode S_a has the most significant effect on sample surface average roughness, followed by oscillation amplitude and weld speed. The P-value for weld force falls outside the specified confidence limit of 95% and hence in this instance the statistical significance of weld force could not be confirmed.

The ANOVA confirmed what was observed in the preliminary analysis; the effect of weld force on UC sample S_a was limited, while there are distinct relationships between the operating parameters of sonotrode surface roughness, oscillation amplitude, weld speed and the resulting sample S_a.

4.3.2.3 Surface Roughness Residual Errors

An increase in the residual error was seen in the ANOVA as the sonotrode surface roughness increased, from sonotrode A to C (Figure 4-14). This trend correlated with the previous results of initial sonotrode characterisation where it was established that there was more variation in the consistency of sonotrode S_a measurements for the rougher sonotrodes B and C.

The gradient of the trend in residual error for all sonotrode samples was slightly negative. This trend could be correlated to a small decrease in sonotrode S_a due to abrasion of surface asperities or the build-up of material within the sonotrode surface cavities. While the effect of wear on sonotrode surface texture was previously identified as being most apparent in sonotrode A (section 4.3.1.6) the trend in residual error for this ANOVA was most apparent for sonotrode B.

4.3.3 Analysis of Variance of Sonotrode Texture on Substrate Bond Strength

4.3.3.1 The Effect of Process Parameters on UC Sample Bond Strength

Sonotrode Surface Roughness

The UC samples were fabricated by three different sonotrodes under a range of processing conditions and their maximum peel load measurements varied over a large range of values. Those produced by sonotrode A, with a S_a of 5.0µm, had the mean highest peel strength overall, with a range of 68.4N to 147.5N. Samples manufactured using sonotrode B, which had a S_a of 14.8 µm, had a lower average peel strength of between 64.4N and 151.6N. Samples manufactured using sonotrode C, which had a S_a of 18.9µm, had the lowest overall peel strength of between 48.3N and 125.1N. All sonotrodes showed a similar degree of spread in their results, displaying a large range in the maximum peel loads, attributable to variation in other process parameters.

Figure 4-15 shows that the maximum peel load of UC samples decreased as the S_a of the sonotrode used to fabricate the samples increased. A certain level of sonotrode surface texture was necessary for high strength bonding in UC (Li & Soar 2009a). Below a threshold level of surface roughness there is insufficient energy transmission between the sonotrode and the foil during consolidation (Figure 4-19). Slippage between the foil and sonotrode could cause insufficient relative motion between the foil and base material. Low interfacial shear forces means that the breakup of surface oxides and plastic flow is limited, resulting in weak interlaminar bonding. In the case of these results it was apparent that all the sonotrodes were above that threshold value as none of the samples displayed the tell-tale crinkling and poor bonding associated with this condition.

The previous results (Figure 4-12) have already shown that S_a of UC samples increased as the S_a of the sonotrode used to fabricate the samples increased. The work of Friel et al. (2010) has shown that sonotrodes with a high S_a produce UC parts with more interlaminar voids, than those from sonotrodes with a smoother surface texture. It has also been established that interlaminar porosity reduces mechanical properties of parts (Janaki Ram et al. 2006a)(Kong et al. 2005) and the lower density of contact points corresponds with a reduction in peel strength.

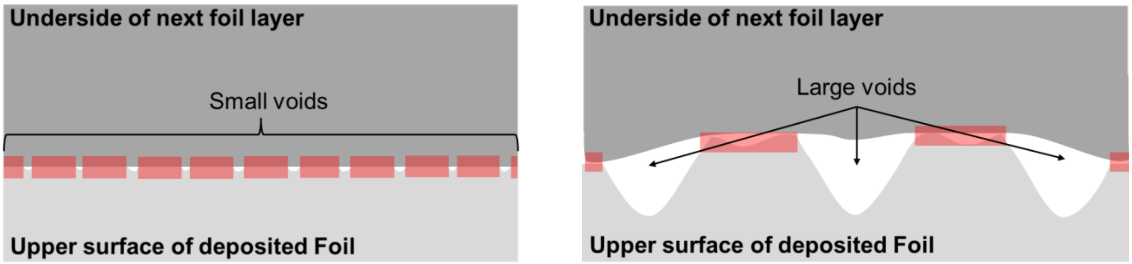

(i) (ii)

Figure 4-28: Diagram to show the incomplete contact and difference in interlaminar void size during consolidation of subsequent layers using a low roughness (i) and high roughness (ii) sonotrode (highlighting areas of direct contact between layers in red).

The reduction in maximum peel load seen in samples fabricated by the rougher sonotrodes could have been the result of incomplete contact between mating surfaces during consolidation due to this high sonotrode induced roughness on the upper surface of the material (Figure 4-28). The surface texture of sonotrode B and C (Figure 4-28ii) was less densely populated by higher amplitude asperities than sonotrode A (Figure 4-28i). The corresponding high amplitude of the asperities imparted onto the foil surface by the rougher sonotrodes during processing may have been sufficiently large so that fewer surface asperities were brought into intimate contact with the subsequent layer. The lower density of asperities meant that fewer contact points were initiated and grown during consolidation, leading to a smaller number of contact points and lower bond strength overall. Within the deeper surface voids areas of oxide layer would remain intact in the absence of direct contact and relative motion between the mating surfaces. In order to fill these voids a higher degree of plastic deformation and flow would have been required to achieve 100% consolidation than in lower roughness surfaces with shallower voids.

Friction theory (Bowden & Tabor 1974) states that the effect of the surface roughness on the coefficient of friction was modest and only discernable at very high surface roughness (actual values were not stated), therefore the relative differences in thermal effects due to frictional heating from the different sonotrode roughness's could be expected to be proportional. Heat generated by friction between the mating surfaces during UC is thought to contribute to the surface effect (2.3.4.1), which is one of the theoretical mechanisms through which bonding is facilitated. Differences in sonotrode and sample S_a could have an impact on the magnitude of the surface effect and hence the extent of plastic deformation, although the effect might be modest.

Oscillation Amplitude

Figure 4-16i showed that the peel strength of UC samples increased as oscillation amplitude increased for UC samples produced by sonotrodes A and C. These results agreed with previous research (Kong et al. 2005) into the effects of amplitude peeling load, where peeling load was seen to have increased with increasing amplitude. Kong stated that the increased oscillation amplitude affects higher oscillating shear forces and higher dynamic interfacial stresses. The energy input per unit area of ultrasonic energy and heat generated by friction at the interface would be higher as a result of the increased oscillation amplitude. Increased acoustic softening (volume effect) and the thermal effects of friction and deformation (surface effects) may have reduced the yield strength of individual contact points, increasing the degree of deformation and plastic flow further. The action of the Bauschinger effect could also account for reduced flow stress during higher amplitude processing in UC where increasing strain further reduced the material flow stress during the reversed-loading conditions. Irrespective of the mechanism, the increased plastic deformation of contact points increased the breakup of surface oxides, enabling more intimate contact of atomically clean metal surfaces required for bond formation by atomic forces across nascent material.

While the surface, volume and Bauschinger effect all theoretically acted to facilitate plastic deformation, in opposition to these mechanisms the UC interface material may have also undergone cold working. As the oscillation amplitude increased the extent of plastic deformation and work hardening would have increased. The resulting increased yield strength of the interface contact points also correlates to the observed increased peel load measurements.

The weld strength of samples fabricated by the rougher sonotrode C was lower at smaller amplitudes than the smoother sonotrodes A and B. This could be attributed to higher magnitude sonotrode induced roughness, where the higher surface peaks of samples processed with sonotrode C reduced the degree of intimate contact and the deeper surface voids required a higher degree of plastic deformation to fill. The increased shear stress, as a result of increasing amplitude, increased the magnitude of plastic deformation, increasing the area of contact points, enabling additional breakup of surface oxides and reducing the size of interlaminar voids.

The trends in increased maximum peel load seen at higher amplitudes in sonotrode A and C also correlated with increased average surface roughness of the UC samples (Figure 4-13i and Figure 4-16i). The peel strength of UC samples produced by sonotrode B decreased slightly as oscillation amplitude increased, in contrast to the other results. At this stage in the experimentation the reason for the difference in the relationship between sonotrode B S_a and changes in oscillation amplitude was unknown. The change in sonotrode was the only controlled change in the processing conditions and therefore the potential effect of surface texture parameters, other than S_a, were examined in the following experimental chapter.

Weld Speed

Figure 4-16ii showed the peel strength of UC samples decreased as weld speed increased for sample produced by all sonotrodes, but that the decrease was more significant in the samples fabricated by sonotrode A and C. These results agree with previously published research into the effect of weld speed on interlaminar bond strength (Kong et al. 2005). As seen in the case of increasing oscillation amplitude, lower weld speeds would have increased the ultrasonic energy input per unit area (volume effect), the interfacial shear stresses thereby increasing the heat generated by friction and deformation (surface effect) and the strain per unit area (Bauschinger effect). These factors would have increased interlaminar plastic flow, increasing the contact point density. Again, the opposing effects of increased work hardening through additional plastic deformation per unit area at lower weld speeds would have increased the yield strength of individual interface contact points, correlating to the increased peel load measurements.

Sonotrode induced roughness and the characteristic increased interlaminar porosity of the rougher sonotrode samples would have accounted for by the lower peel strengths seen in samples from sonotrode B and C. The limited effect of weld speed on the peel strength of samples fabricated by sonotrode B was also unknown and was considered in the following experimental chapter.

Weld Force

The effect of weld force on UC sample peel strength for all sonotrodes appeared to be limited (Figure 4-16iii) and the difference in bond strength of samples fabricated by the different samples was characterised in the previous discussion of Figure 4-15.

4.3.3.2 Analysis of Variance for Interlaminar Peel Strength Data

The ANOVA of interlaminar peel strength for samples produced (Table 4-8) stated that changes in the operating parameters of sonotrode S_a, oscillation amplitude, and weld speed had a statistically significant effect on the bond strength of UC samples. Sonotrode

S_a had the most significant effect on sample bond strength, followed by oscillation amplitude and weld speed. The P-value for weld force fell outside the specified confidence limit of 95% and hence the statistical significance of weld force could not be confirmed.
The ANOVA confirmed what was observed in the preliminary analysis; the effect of weld force on UC sample interlaminar peel strength was limited, while there were distinct relationships between the operating parameters of sonotrode S_a, oscillation amplitude, weld speed and the resulting sample bond strength.

4.3.3.3 Bond Strength Residual Errors

A relatively high level of the residual errors was seen in the ANOVA of sonotrodes A to C (Figure 4-14). The spread was to be expected as it correlated with the fact that there is often a large variation in the bond strength as measured by peel testing (Kong, Soar, & Dickens 2004).

The gradient of the trend in residual error for all sonotrode samples was slightly positive. This trend could have been correlated to a small decrease in sonotrode surface roughness due to abrasion of surface asperities or the build-up material within the sonotrode surface cavities. The effect of wear on sonotrode surface texture was previously identified as being most apparent in sonotrode A (section 4.3.1.6) and the trend in residual error for this ANOVA was also most apparent in sonotrode A. A reduction in sonotrode roughness as a result of wear would also reduce the subsequent sonotrode induced roughness onto the surface of the UC samples. The reduction in sample S_a, which would have been accompanied by a decrease in interlaminar porosity, accounted for the overall increase in peel strength over time.

4.3.4 A comparison of Surface Roughness and Interlaminar Peel Strength

The previous discussion had considered the relationship between UC sample S_a and interlaminar bond strength with other process parameters separately. Figure 4-18 illustrated the direct relationship between UC sample S_a and the maximum peel load over the entire range of processing parameters.

There appeared to be little correlation between the S_a and interlaminar peel strength with UC samples fabricated by sonotrode A and B. For sonotrode C, the interlaminar bond strength increased as the sample S_a increased. This was in direct contrast to the previous discussion (4.3.3.1 Sonotrode Surface Roughness), and previously accepted belief (Janaki Ram et al. 2006b), that UC samples produced by rougher sonotrodes had lower interlaminar peel strength as a result of their increased interlaminar porosity from sonotrode texture transfer.

The UC samples with a higher S_a are thought to have experienced a higher degree of texture transfer between sonotrode C (Figure 4-29i), while those with a lower S_a were thought to have experienced a lesser degree of texture transfer (Figure 4-29ii) (Kulakov & Rack 2010). As a result of the increased depth of sonotrode penetration during processing, the higher S_a samples may have undergone more plastic deformation than those with a lower S_a and work hardening at this stage.

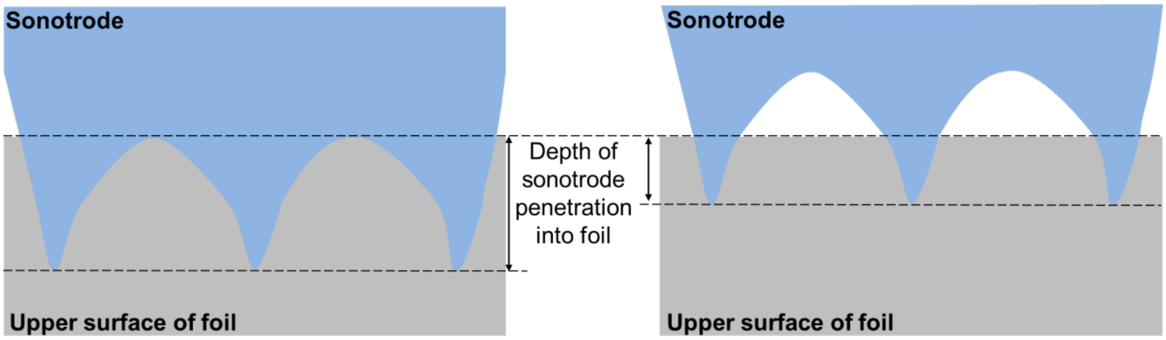

(i) **(ii)**

Figure 4-29: Diagram illustrating the theoretical effects of 100% (i) and 50% (ii) texture transfer between the sonotrode and foil surface during UC.

During the deposition of subsequent foils, the applied normal force would have been distributed across individual points where the asperity tips were in contact with the underside of the upper foil (Figure 4-30). The individual contact points of higher S_a surfaces would have theoretically been subject to an increased force per unit area, due to their smaller contact area. These contact points might then have experienced even more plastic deformation and work hardening during the contact bond process, ultimately increasing the strength of the bonds. The higher pressures across the individual contact points of higher S_a samples might also have better facilitated the break-up of surface oxide layers, further enabling the formation and expansion of individual contact points during the contact bond process.

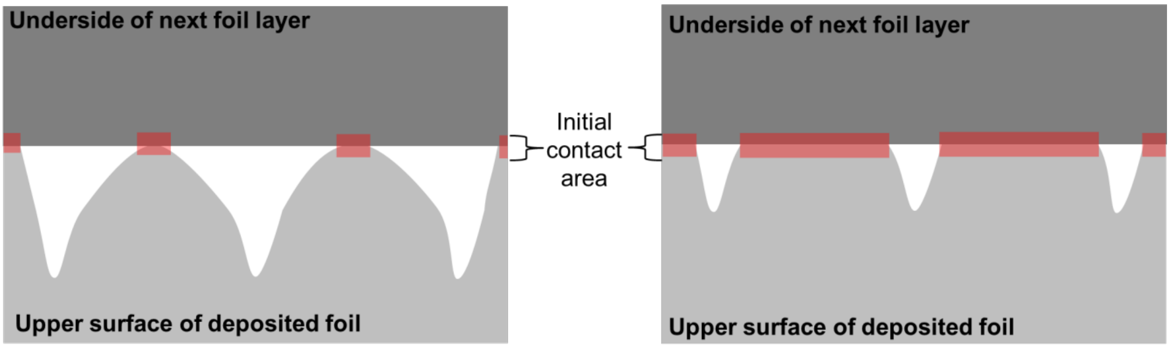

(i) **(ii)**

Figure 4-30: Diagram illustrating the theoretical effects of 100% (i) and 50% (ii) sonotrode texture transfer on the UC sample surface during the deposition of the next foil layers.

During UC, the contact of asperity tips are the initiation point for interlaminar bonding and there were initially less individual interlaminar contact points made during the consolidation of samples fabricated by sonotrodes B and C. However, it could have been the case that these fewer contact points could have been stronger as a result of their deformation history, as attributed to the change in peel strength seen in sonotrodes C as S_a increased. The extent of plastic deformation and work hardening within foils subject to UC cannot be determined without further analysis and hence microstructural examination was undertaken to examine these factors, detailed within the following experimental chapter.

The nature of surface texture transfer between sonotrode and the size, shape and distribution of UC sample surface asperities cannot be confirmed without more detailed surface texture characterisation. According to the proposed explanation the Ssk and Ssc of the surface of the UC sample surface were crucial. The following experimental chapter fully characterised the UC sample surface texture to further examine the validity of the proposed theory.

As previously identified in the discussion, the relationship between sonotrode B and the other processing parameters was less pronounced than with sonotrode A and C. The same was also true of the relationship between UC sample surface roughness and maximum peel load, where a direct relationship was indeterminate. The results appeared in clusters, and some of the data points correlated with the trend seen in sonotrode C results. Through the ANOVA of sonotrode texture on substrate bond strength discussion it became apparent that the deviation in results of sonotrode B compared to the other sonotrodes may have been the result of surface texture parameters other than average surface roughness and therefore the possibility is examined in the following experimental chapter.

4.4 Summary Review

The weld surface of sonotrode A was made up of short wavelength components, while sonotrode C consists of longer wavelength spectral components. Both sonotrodes exhibited distinct peaks and troughs across their surface, but these features were larger in amplitude and less dense in sonotrode C than in sonotrode A. The weld surface texture of sonotrode B contains features of intermediate amplitude and density with a more slowly varying texture in comparison to the other sonotrodes. All sonotrodes appeared to have a surface texture whose volume was dominated by valleys and were isotropic in nature with no distinct texture direction.

The sonotrode surface texture characterisation showed that is important to consider a number of parameters, other than the traditional measurement of S_a, as these parameters could potentially effect the interlaminar bonding of the samples they produced. Changes in sonotrode wear over the period of operation were minimal. There was some evidence of foil adhesion in sonotrode surface cavities and peak wear for sonotrode A.

The sonotrodes were found to impart a similar or reduced magnitude version of their S_a onto the surface of the UC samples they produced and a greater reduction in texture transfer was seen with the rougher sonotrodes.

The operating parameters of sonotrode S_a, oscillation amplitude, and weld speed had a statistically significant effect on the S_a of UC sample while the effect of weld force was limited. The effect of sonotrode S_a was the most significant factor influencing UC sample S_a and as the sonotrode S_a increased, the range of UC sample surface textures that can be produced under different processing conditions increased.

The operating parameters of sonotrode S_a, oscillation amplitude, and weld speed also had a statistically significant effect on UC sample bond strength with the examined range. The effect of sonotrode S_a was the most significant factor and the effect of weld force was, again, limited. UC samples produced by the sonotrode with the lowest S_a exhibited the highest peel strength overall and as the sonotrode S_a increased, the peel strength decreased, irrespective of other processing conditions.

Differences in the relationship between bond strength and changes in oscillation amplitude and weld speed were seen in samples produced by sonotrode B introducing the possibility that surface texture parameters, other than S_a, may have a bearing on interlaminar bonding in UC. Examining the direct relationship between UC sample S_a and interlaminar bond strength supported the theory that interlaminar bonding was more complex and not only dependent upon the number of interface contact points, but that the degree of deformation and strength of those contact points might also have been significant.

5 The Effect of Substrate Surface Texture on Interlaminar Bonding in Ultrasonic Consolidation

The second experimental chapter (Figure 4-1) was conceived to examine the second Research Objective *"to investigate how interlaminar microstructure and bond strength in UC is dependent upon sonotrode weld surface texture".*

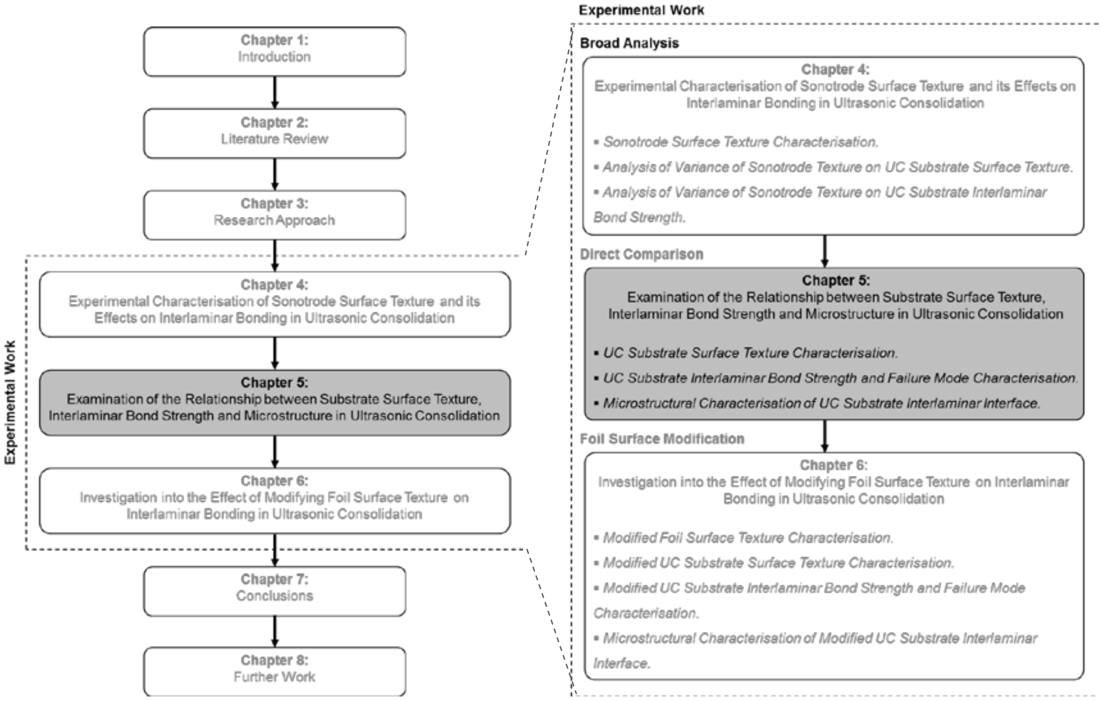

Figure 5-1: Thesis organisation, highlighting Chapter 5.

The following Research Factors are addressed within the chapter:

II. Characterise the substrate surface texture and determine the degree of texture transfer from contact with each different sonotrode over a broad range of UC processing conditions.

III. Experimentally measure the interlaminar bond strength and characterise the failure mode of UC samples manufactured by each of the different sonotrode over a broad range of UC processing conditions.

IV. Experimentally measure the linear weld density and characterise the interlaminar microstructure of UC samples manufactured by each of the different sonotrodes.

Research Factors II and III were partially addressed within the previous chapter, where the S_a and maximum interlaminar peel strength of UC samples fabricated over a broad of range of processing conditions were analysed. It was assumed that the texture transfer between the sonotrode and UC sample surface were similar in nature. It was also proposed that the variation in the results of sonotrode B compared to the other sonotrodes may have been the result of differences in surface texture parameters other than S_a. The

UC samples fabricated for the ANOVA in Chapter 4 were re-examined in more detail within this chapter and the validity of previous assumptions were tested.

More detailed surface texture characterisation of selected samples, fabricated by the three different sonotrodes under otherwise identical processing conditions, was undertaken and the results were compared with the parent sonotrode surface. The relative peel strength and failure mode of these samples under peeling load was examined and a direct comparison of each sample’s interlaminar microstructure is presented. The nature and incidence of interlaminar voids was examined by optical microscopy and quantified through LWD measurements. The interlaminar microstructure was characterised in greater detail using FIB microscopy.

5.1 Experimental Methodology

5.1.1 Substrate Surface Texture Characterisation

A selection of the UC samples originally produced for the ANOVA in Chapter 4 were chosen for more detailed surface texture characterisation. Three samples from each of the three sonotrodes, fabricated under the processing conditions listed in Table 5-1, were identified and their corresponding surface texture data was collated. These particular fabrication parameters were chosen as they were common to samples produced by all three sonotrodes and were in the mid-range of the Alpha 2 UC machine’s operating window.

Table 5-1: UC sample fabrication parameters

Oscillation Amplitude (µm)	Weld Speed (mm/s)	Weld Force (N)
20	40	1400

The surface texture data collected from the analysis in the previous chapter (4.1.2.2) was used to characterise these selected UC samples, adopting the same surface texture analysis parameters (Table 4-2) used in the characterisation of the three sonotrodes

5.1.2 Substrate Bond Strength and Failure Mode Characterisation

The peel test analysis data for the UC samples chosen for direct comparison, specified in the previous section (Table 5-1), was identified and collated.

5.1.3 Microstructural Characterisation of Substrate Interlaminar Interface

5.1.3.1 Linear Weld Density Measurement

Cross-sections of the weld interface were examined in order to determine average LWD of samples fabricated by all three sonotrodes. Three cross-sectional areas for each of the three samples from sonotrodes A, B and C were analysed; twenty-seven microscopy sample cross-sections were prepared in total.

Each UC test sample was sectioned using a cutting disk at three locations along the weld, perpendicular to the direction of travel of the sonotrode (Figure 5-2i). The sections were mounted in KonductoMet, a carbon-filled phenolic thermoset mounting compound from Buehler GmbH, and ground with 240, 400, 600, 800, 1200 grit silicon carbide paper. The samples were polished at 5 and 1µm with diamond paste for 5 minutes each and finally with 0.1µm colloidal silica for 10 minutes. To avoid contamination the samples were washed with soapy water and rinsed with deionised water after every preparation stage. After the final polishing stage the samples were rinsed with methanol and blow-dried using a warm air blower (Figure 5-2ii).

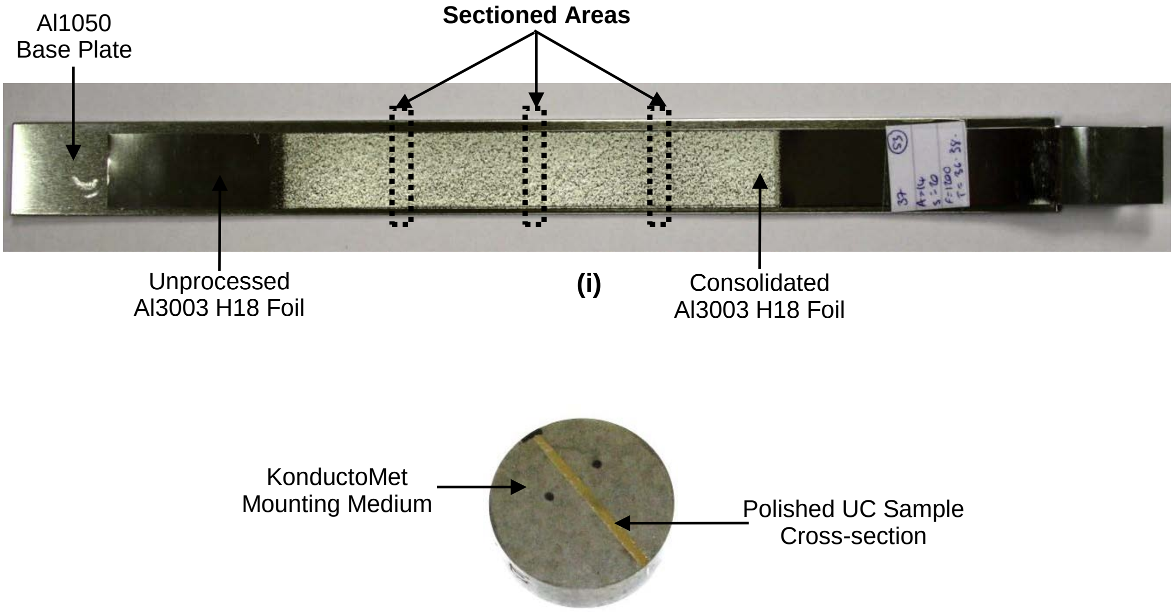

(ii)

Figure 5-2: Example of sectioning locations across the weld surface of a UC sample (i) and a mounted cross-section of a sample, polished in preparation for microscopic analysis (ii).

The polished cross-section samples prepared for microscopy were examined optically using an Olympus BX60M optical light microscope with an Olympus ×20 lens and five images across the width of each cross-section (Figure 4-8) were captured using a

QImaging Micropublisher 3.3MP camera and processed using Image Pro Plus software version 7, Media Cybernetics, Inc.

Figure 5-3: Diagram of UC sample cross-section illustrating a typical imaging area and the LWD measurement location.

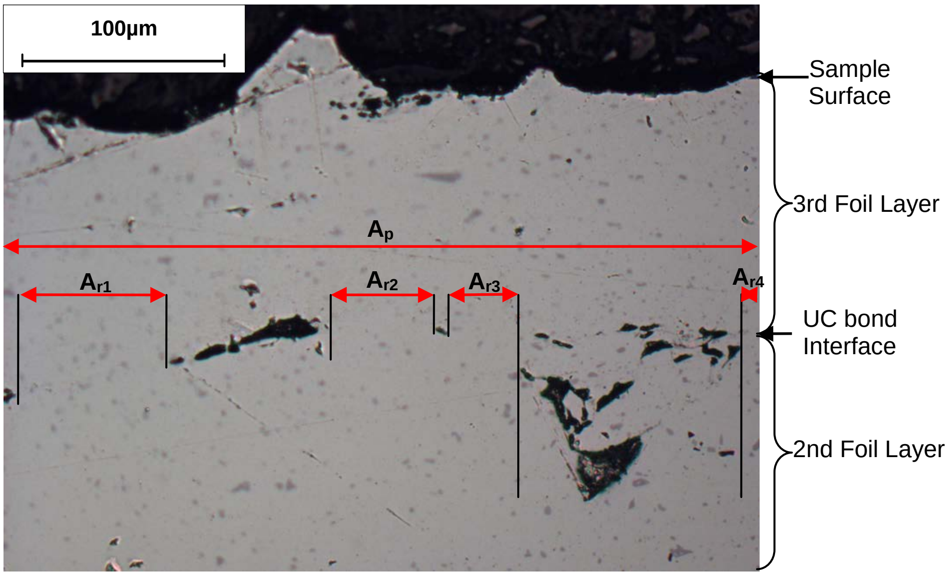

Figure 5-4: Example of an optical micrograph of the interlaminar microstructure of UC sample illustrating the LWD measurement method (A_r = real contact area and A_p = apparent contact area.

LWD is the percentage of the total interlaminar interface that appears to be fully bonded (2.3.3.4). The total width of the optical measurement area, referred to as the apparent weld region A_p, along the interface between the second and third layer of the UC sample was measured (Figure 5-4). The sum of areas along the interface which appear to be metallically bonded, referred to as the real contact area A_r, were also measured.

Equation 5-1:

$$LWD = \frac{A_r}{A_p} \times 100\%$$

(Kong et al. 2005)

The LWD for each optical micrograph was calculated (Equation 5-1) and the average LWD for samples from sonotrode A, B and C was determined.

5.1.3.2 Grain Size Calculation

In order to examine the nature of oxide dispersal and identify any changes in microstructure induced by the different sonotrode textures the UC samples were analysed using FIB. FIB micrographs can be used to measure the orientation and size of grains, representing different crystal lattice orientations as different levels of contrast. Additional microstructure detail, including the presence and density of dislocation, could have been seen through TEM but due to the added complexity of sample preparation and larger time scales require for the procedure in this case FIB was adopted (Canovic et al. 2008)(Johnson 2008).

The particular FIB analysis approach utilised within this investigation required samples of a high quality polished finish in order to produce viable images and the best quality sample from each sonotrode was selected for imaging. The Nova 600 NanoLab, Ultra High Resolution (UHR) Field Emission Gun (FEG) – Dual Beam (DB) Scanning Electron Microscope (SEM) / Focussed Ion Beam (FIB) machine, FEI Company^{TM}, Hillsboro Oregon, USA, (Figure 5-5) at the Loughborough Materials Characterisation Centre (LMCC), Loughborough University, was used to capture the FIB micrograph's of the UC samples.

Figure 5-5: Nova 600 NanoLab, UHR FEG- DB SEM/FIB machine used to capture the FIB micrographs.

Images were captured from the following characterisation areas (Figure 5-6):

- **Horizontal Characterisation Area**: to examine the effect of different sonotrode surface textures on the interlaminar microstructure of UC samples. Approximately seven overlapping FIB micrographs were captured along the interface between the second and third layer of the UC sample.
- **Vertical Characterisation Area**: to examine the effect of different sonotrode surface textures on the microstructure throughout the bulk of a UC sample's material. Overlapping FIB micrographs were captured from the UC sample surface across two foil layers down to the interface between first and second foil layer.
- **Foil Surface Characterisation Area**: to examine the effect of different sonotrode-induced roughness's on the microstructure of UC samples. Approximately four overlapping FIB micrographs were captured along the upper surface of the UC sample.

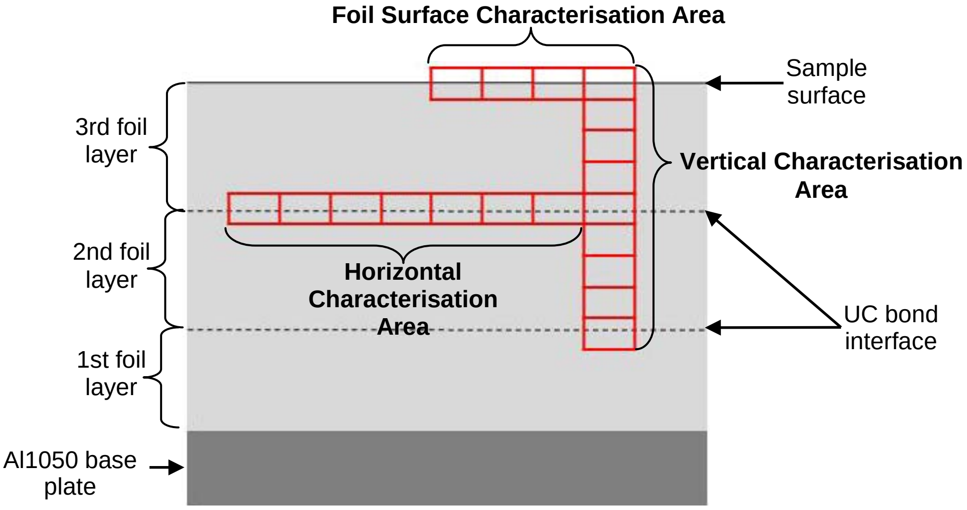

(i)

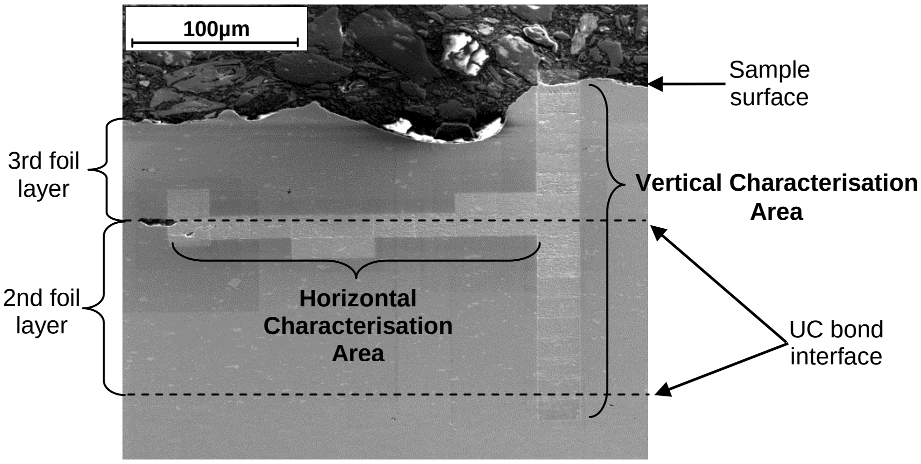

(ii)

Figure 5-6: Diagram of the UC sample cross-section illustrating the location of the different characterisation areas (i) SEM micrograph of a FIB-imaged sample illustrating the horizontal and vertical characterisation areas (ii).

Two sets of FIB micrographs for each of the characterisation areas were collected from the samples from sonotrode A, B and C. To limit the subjective selection of characterisation areas the method of sampling randomisation described by Higginson & Sellars (2003) was adopted. It was necessary to locate a 'typical' area of the weld interface as the correct location for measurement for preliminary image collection, however, subsequent images were 'sight unseen' and simply adjacent to the initial image. All the FIB micrographs were collected at x5000 magnification with a beam current of 500pA and 2.7 minute image acquisition time, measuring 25.6μm x 22.1μm.

Once all the individual FIB micrographs had been captured they were assembled, using Microsoft PowerPoint, to create an overview of the characterisation areas for samples from each sonotrode (Figure 5-7).

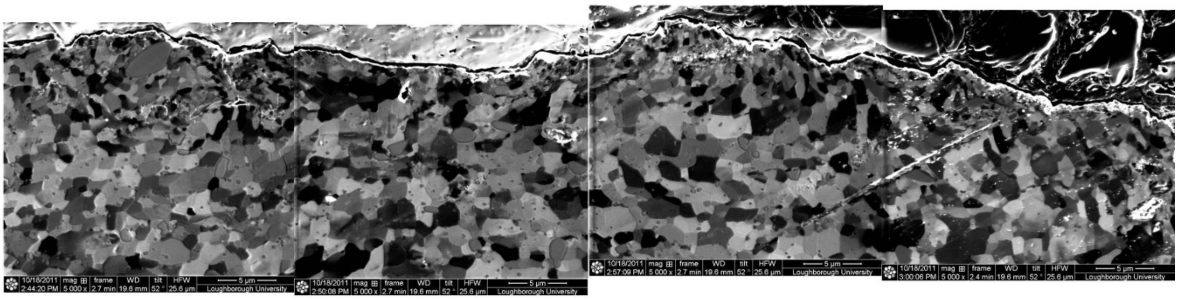

Figure 5-7: Example of FIB micrographs assembled to create an overview of the foil surface characterisation area.

The effect of different sonotrode surface textures on the microstructure within the vertical characterisation area of individual samples was quantified by measuring the grain size and shape throughout the foil layers. Each consolidated foil layer was divided into regions, 5μm deep regions within the vicinity of the interface and 15μm deep regions towards the midpoint of the layer (Figure 5-8), and the average sub-grain size, $\bar{L}$, in the vertical and horizontal directions was calculated using the linear intercepts method (Equation 5-2) where intercept points, x, were counted as all of the specific points at which a sub-grain boundary crossed a measurement traverse of length, L, at a given magnification, M.

Equation 5-2: (Higginson & Sellars 2003, p. 36)

$$\bar{L} = \frac{\sum L}{M \times \sum x}$$

The product of the vertical and horizontal measurements was used to calculate the average grain size for each foil layer region. The change in grain orientation and identification of equiaxed grains was determined by the ratio of vertical to horizontal grain size measurements within individual regions.

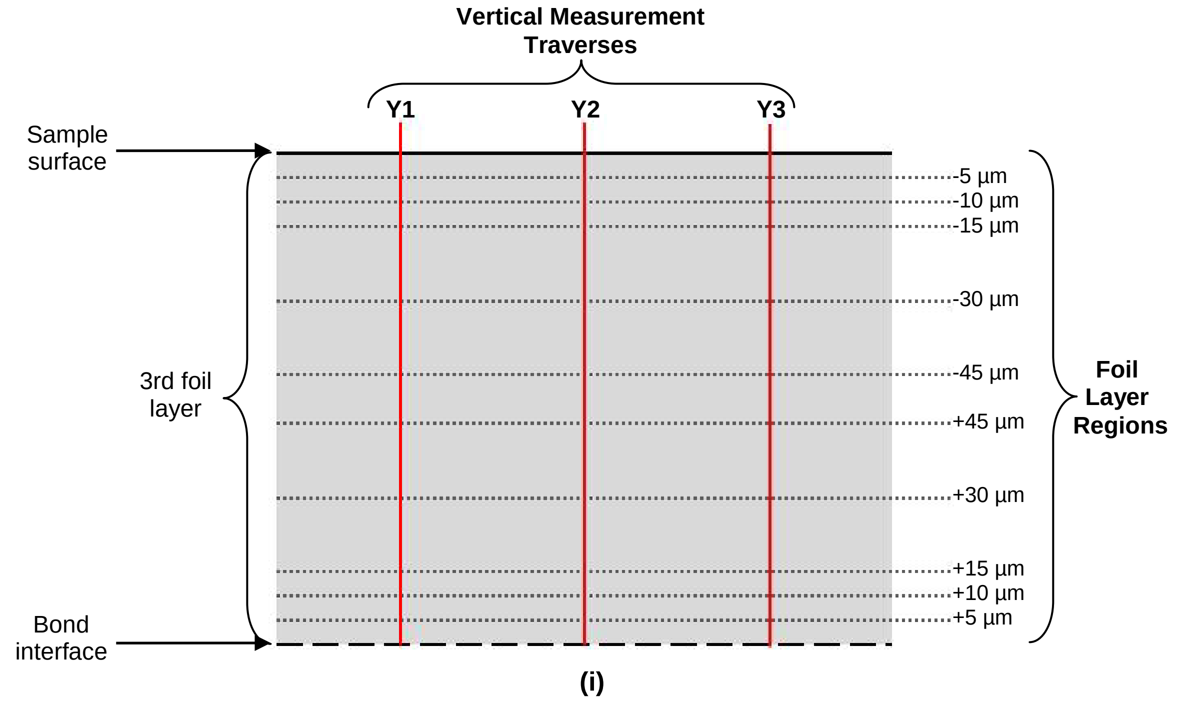

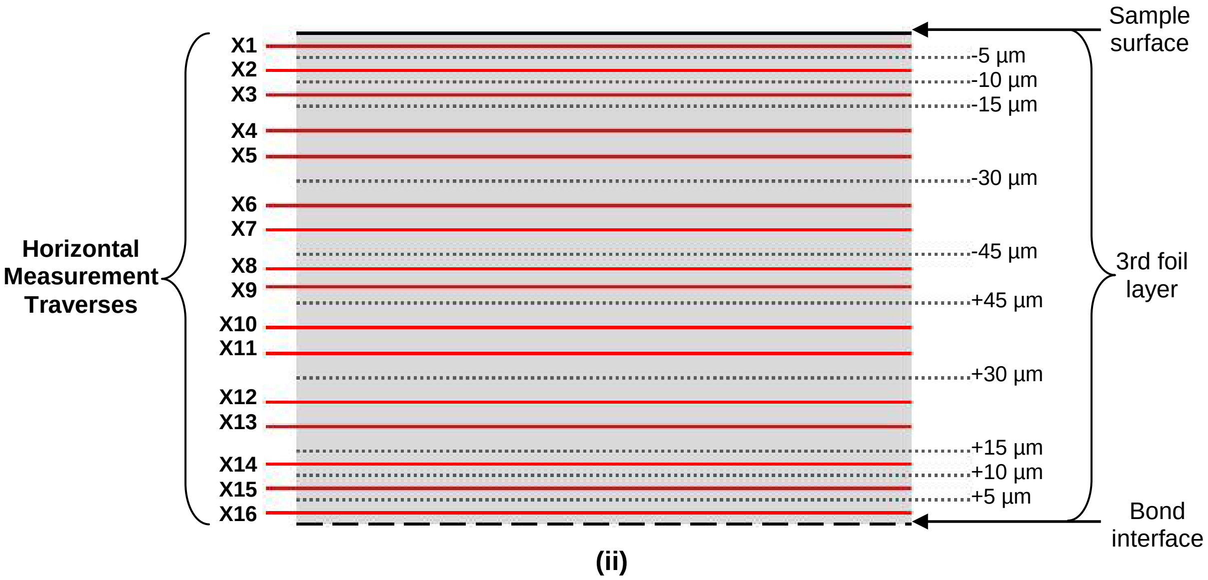

Figure 5-8: Diagram illustrating the grain boundary measurement locations in the vertical (i) and horizontal (ii) directions within the 3rd foil layer.

5.2 Results

5.2.1 Substrate Surface Texture Characterisation

(i) (ii) (iii)

Figure 5-9: Photograph of samples fabricated by sonotrode A (i), B (ii) and C (iii).

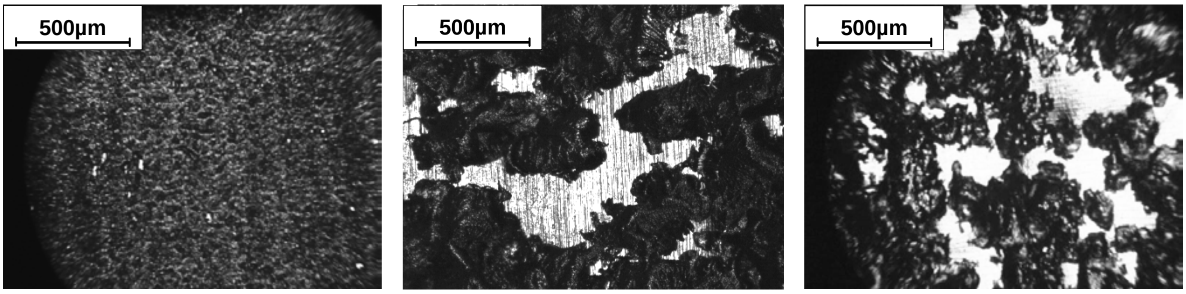

(i) (ii) (iii)

Figure 5-10: Optical micrographs of sample surfaces fabricated sonotrode A (i), B (ii) and C (iii).

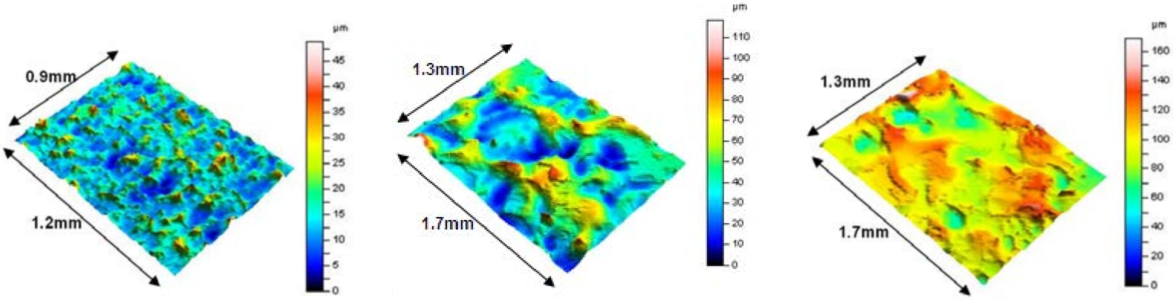

(i) (ii) (iii)

Figure 5-11: 3D pseudo-colour image of sample surfaces fabricated by sonotrode A (i), B (ii) and C (iii).

Table 5-2: Average surface texture analysis results for samples from sonotrode A, B and C.

Surface Texture Parameters	Sample Measurements					
	A		B		C	
	Av.	σ	Av.	σ	Av.	σ
S_a (µm)	4.48	0.67	12.80	0.74	14.47	2.58
S_q (µm)	5.87	0.75	16.59	1.30	18.76	2.81
Sku	3.88	0.55	3.73	1.19	3.86	1.32
Ssk	0.416	0.322	0.250	0.520	-0.303	0.281
Sds ($1/mm^2$)	36329	1592	35055	1207	30952	2890
Ssc (1/mm)	0.976	0.043	0.710	0.023	0.845	0.094
Str (s = 0.2)	0.787	0.122	0.720	0.155	0.789	0.093
Sal* (mm)	28.99	2.63	159.42	16.8	71.05	9.72
Vmp ($\mu m^3/\mu m^2$)**	0.394	0.062	1.000	0.421	0.821	0.180
Vmc ($\mu m^3/\mu m^2$)**	4.79	0.87	14.28	0.66	16.05	3.24
Vvc ($\mu m^3/\mu m^2$)**	7.28	1.37	20.13	2.12	20.97	3.72
Vvv ($\mu m^3/\mu m^2$)**	0.630	0.130	1.78	0.292	2.586	0.485
Sdr (%)	35.58	3.03	32.05	5.72	58.81	12.43

** s = 0.2*
***p = 10%, q =80%*

Table 5-3: Percentage difference between surface texture measurements for samples A, B and C and the original sonotrode (significant variation, which exceeds that of the measurement variation is highlighted).

Texture Parameter	Change in Sonotrode Surface Texture Parameters (%)		
	A	B	C
S_a (µm)	-9.9	-13.5	-23.3
S_q (µm)	-8.3	-10.7	-20.8
Sku	18.7	21.9	16.3
Ssk	341.9	199.2	-176.1
Sds (1/mm2)	-6.9	-7.9	-15.6
Ssc (1/mm)	-14.4	-37.2	-47.5
Str*	-12.5	-9.5	4.6
Sal* (µm)	-1.0	0.3	-61.4
Vmp ($\mu m^3/\mu m^2$)**	37.8	36.8	-38.7
Vmc ($\mu m^3/\mu m^2$)**	-12.4	-15.5	-24.4
Vvc ($\mu m^3/\mu m^2$)**	-3.4	-6.1	-30.7
Vvv ($\mu m^3/\mu m^2$)**	-27.8	-25.2	19.7
Sdr (%)	-28.0	-73.4	-71.7

** s = 0.2*
***p = 10%, q =80%*

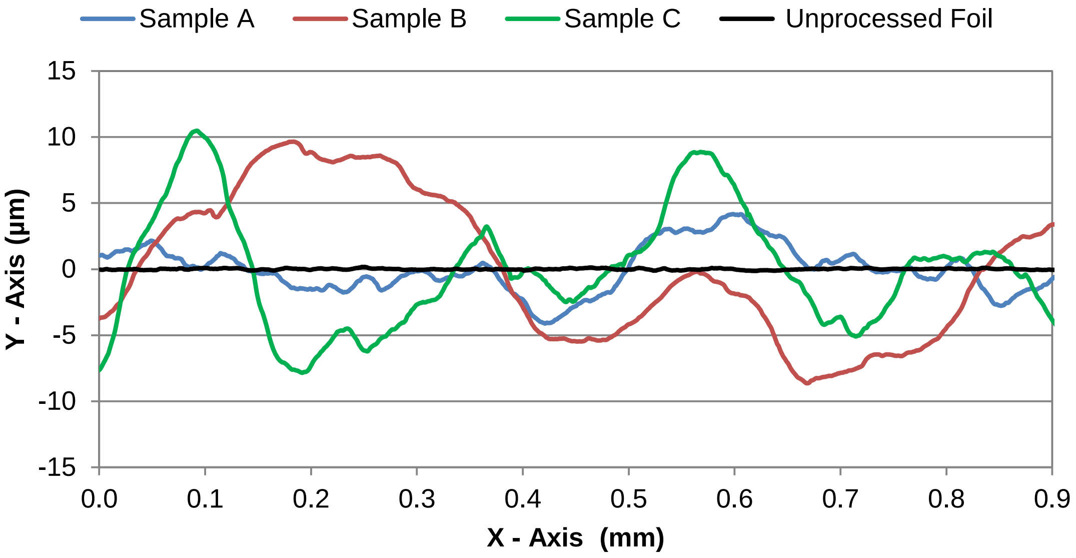

Figure 5-12: Example 2D surface profiles of a plain unprocessed foil and samples fabricated by sonotrode A, B and C.

5.2.2 Substrate Bond Strength and Failure Mode Characterisation

Table 5-4: Maximum peeling load and extension of samples from sonotrode A, B and C.

Sonotrode Sample	Sample S_a (µm)		Maximum Peeling Load (N)		Extension at Maximum Peeling Load (mm)	
	$\bar{x}$	σ	$\bar{x}$	σ	$\bar{x}$	σ
A	4.48	0.22	97.6	17.3	7.35	0.1
B	12.80	0.40	85.5	13.2	9.78	3.7
C	14.47	0.88	108.5	12.4	4.40	1.2

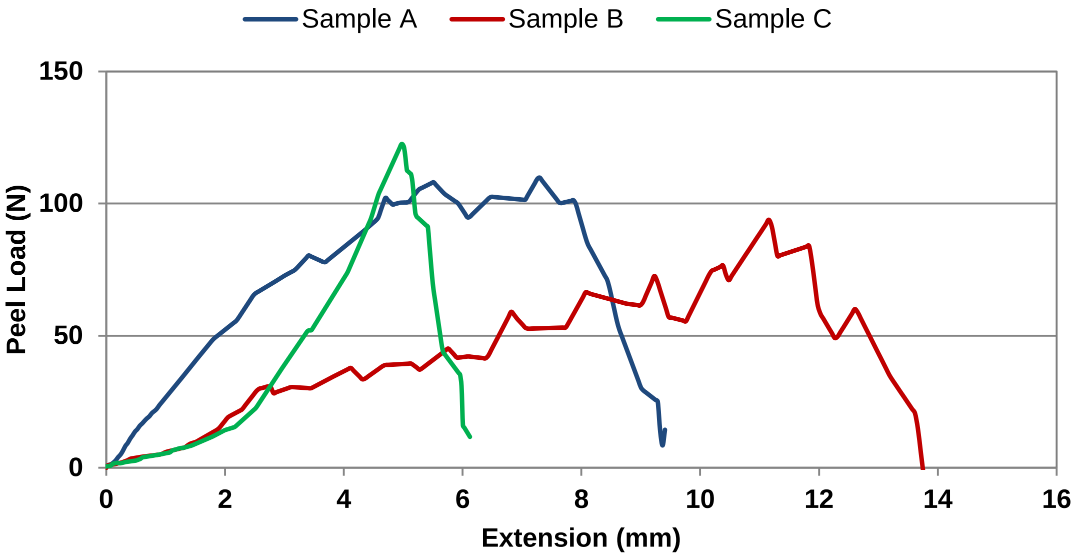

Figure 5-13: Characteristic peeling load-extension graph for samples fabricated by sonotrode A, B and C

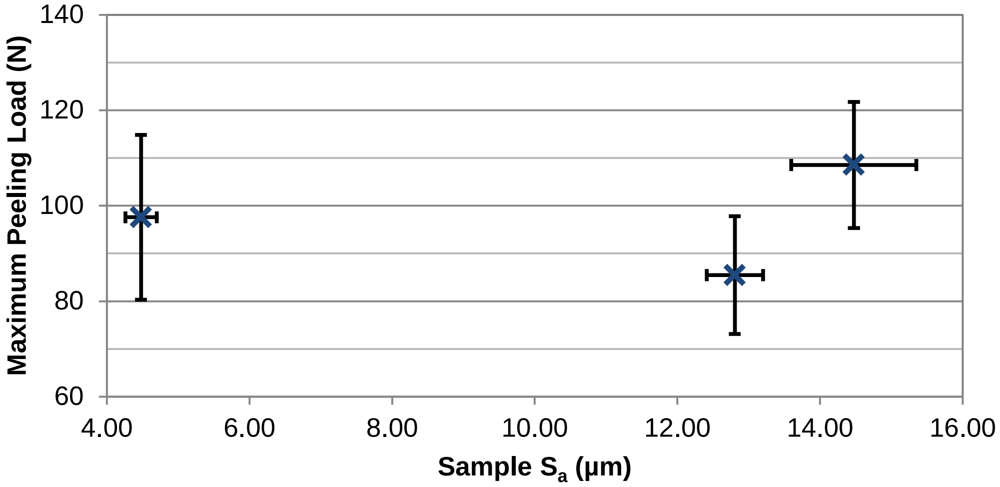

Figure 5-14: The relationship between the maximum peeling load and S_a of UC samples.

5.2.3 Microstructural Characterisation of Substrate Interlaminar Interface

5.2.3.1 Optical Microscopy and Linear Weld Density Measurement

Table 5-5: LWD of samples from sonotrode A, B and C.

Sonotrode Sample	Sample S_a (µm)		LWD (%)	
	$\bar{x}$	σ	$\bar{x}$	σ
A	4.48	0.22	66.3	11.1
B	12.80	0.40	79.4	3.7
C	14.47	0.88	45.5	9.7

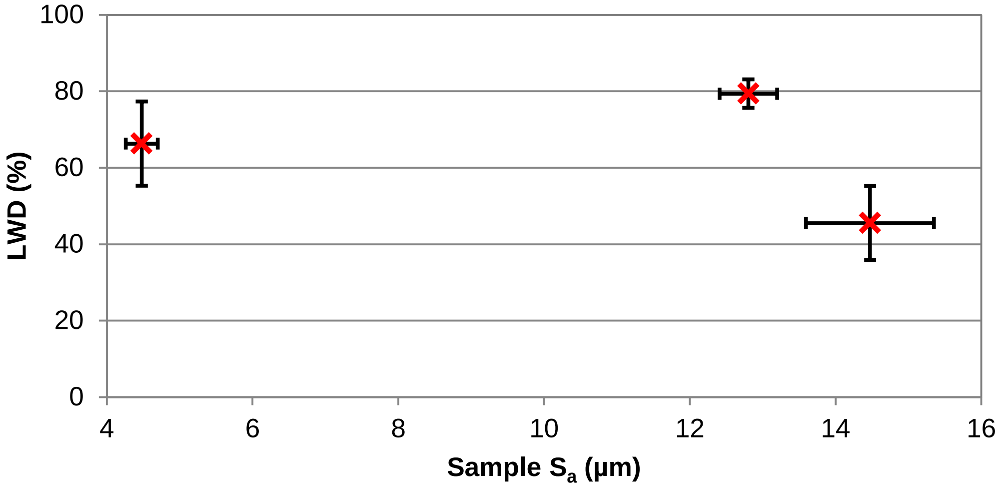

Figure 5-15: The relationship between the LWD and S_a of UC samples.

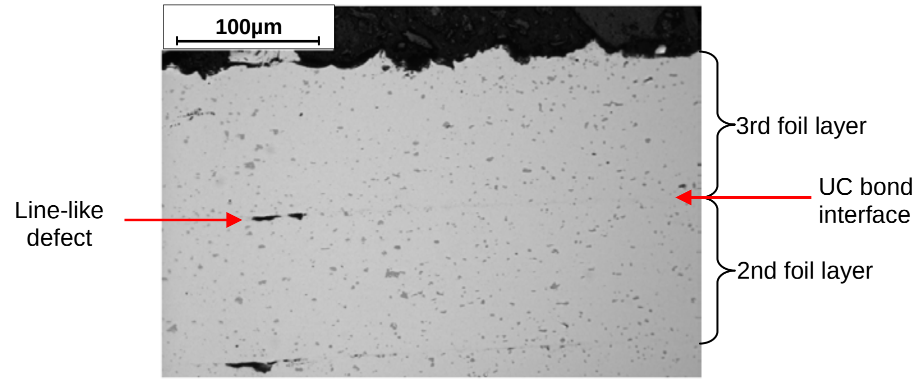

(i)

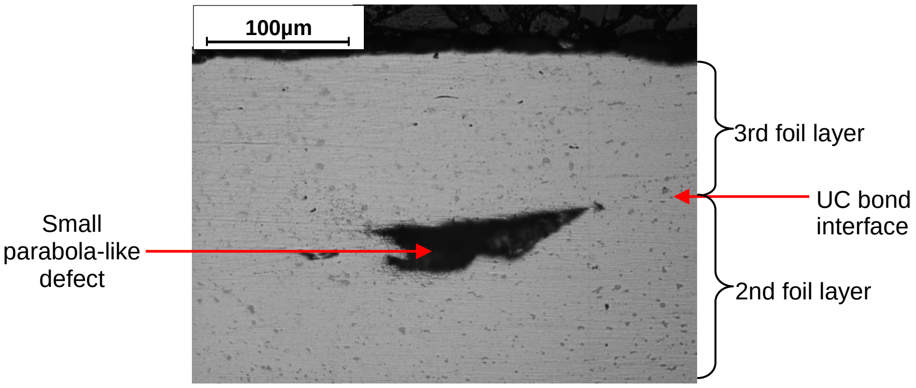

(ii)

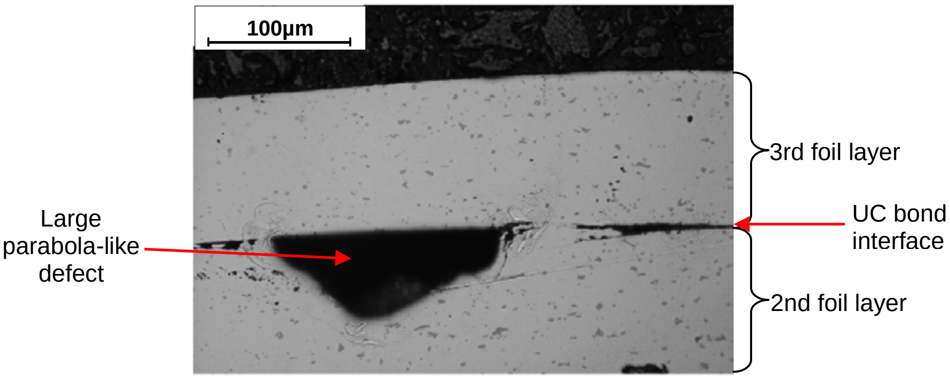

(iii)

Figure 5-16: Optical micrographs of the interlaminar microstructure of UC samples fabricated by sonotrode A (i), B (ii) and C (iii).

5.2.3.2 Focussed Ion Beam Analysis

5.2.3.2.1 Foil Surface Microstructure

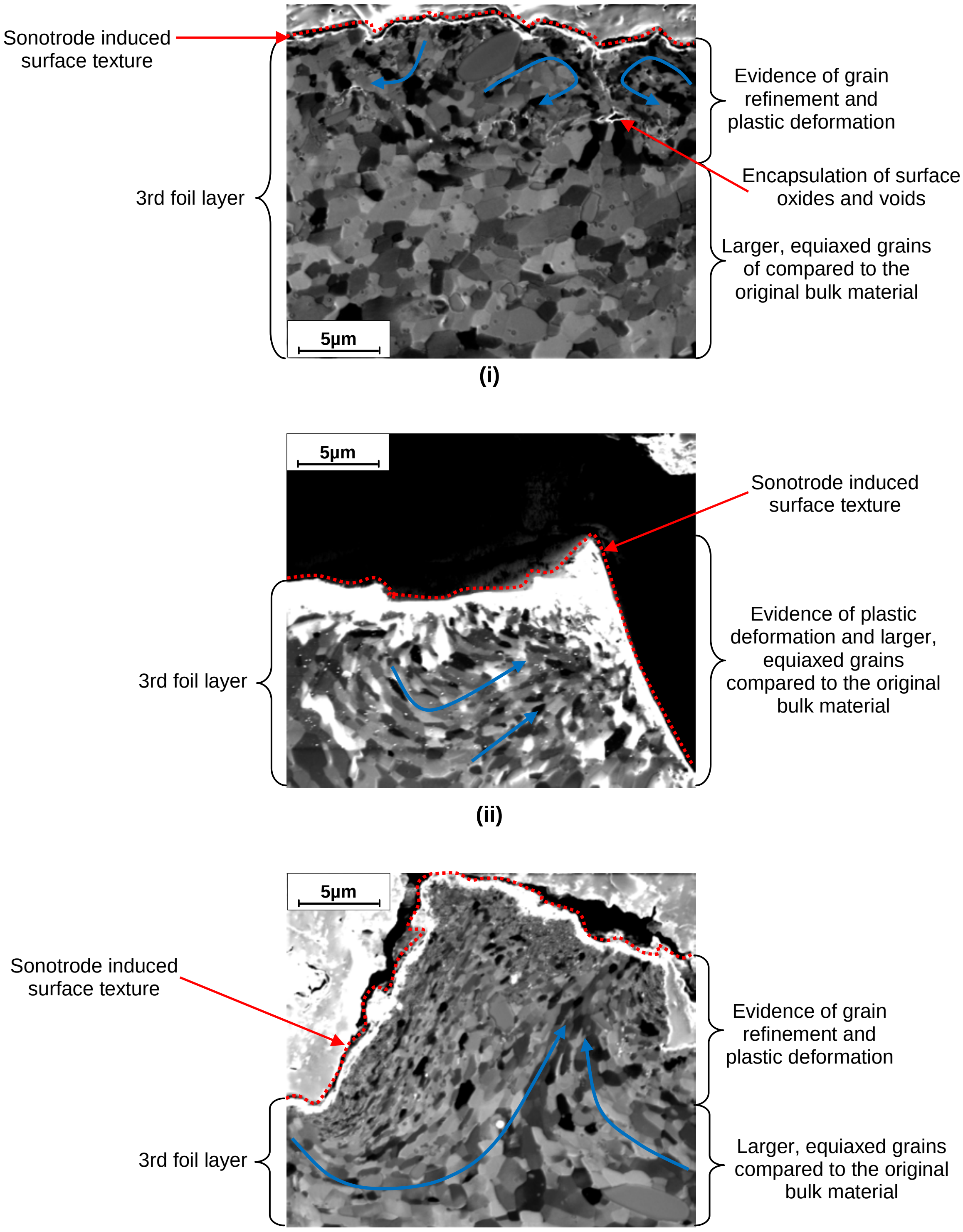

(i)

(ii)

(iii)

Figure 5-17: FIB micrograph's of the surface microstructure of UC samples fabricated by sonotrode A (i), B (ii) and C (iii), illustrating the effects of sonotrode induced texture, and evidence of plastic deformation (blue arrows), grain refinement and recovery.

5.2.3.2.2 Interlaminar Interface Microstructure

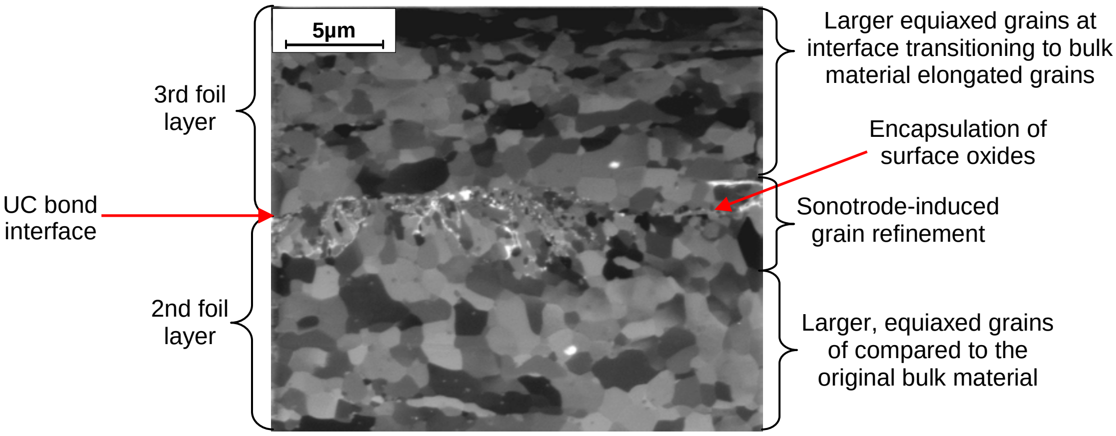

Figure 5-18: FIB micrograph's of the interlaminar microstructure of UC samples fabricated by sonotrode A.

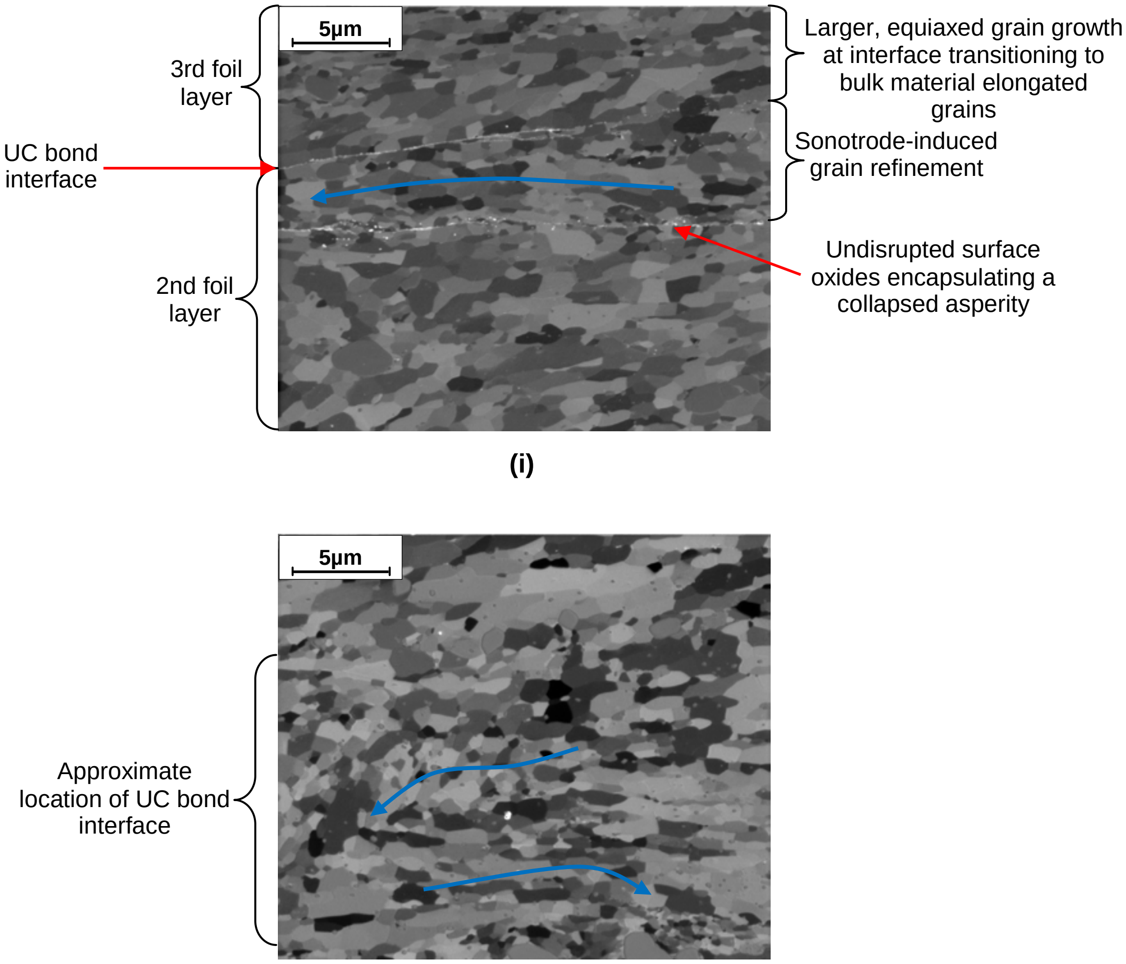

(i)

(ii)

Figure 5-19: FIB micrograph's of the interlaminar microstructure of UC samples fabricated by sonotrode B illustrating the collapse of surface asperities (i) and absence of oxide layer (ii) around the bond interface location of sample B (evidence of apparent plastic flow direction is indicated by blue arrows).

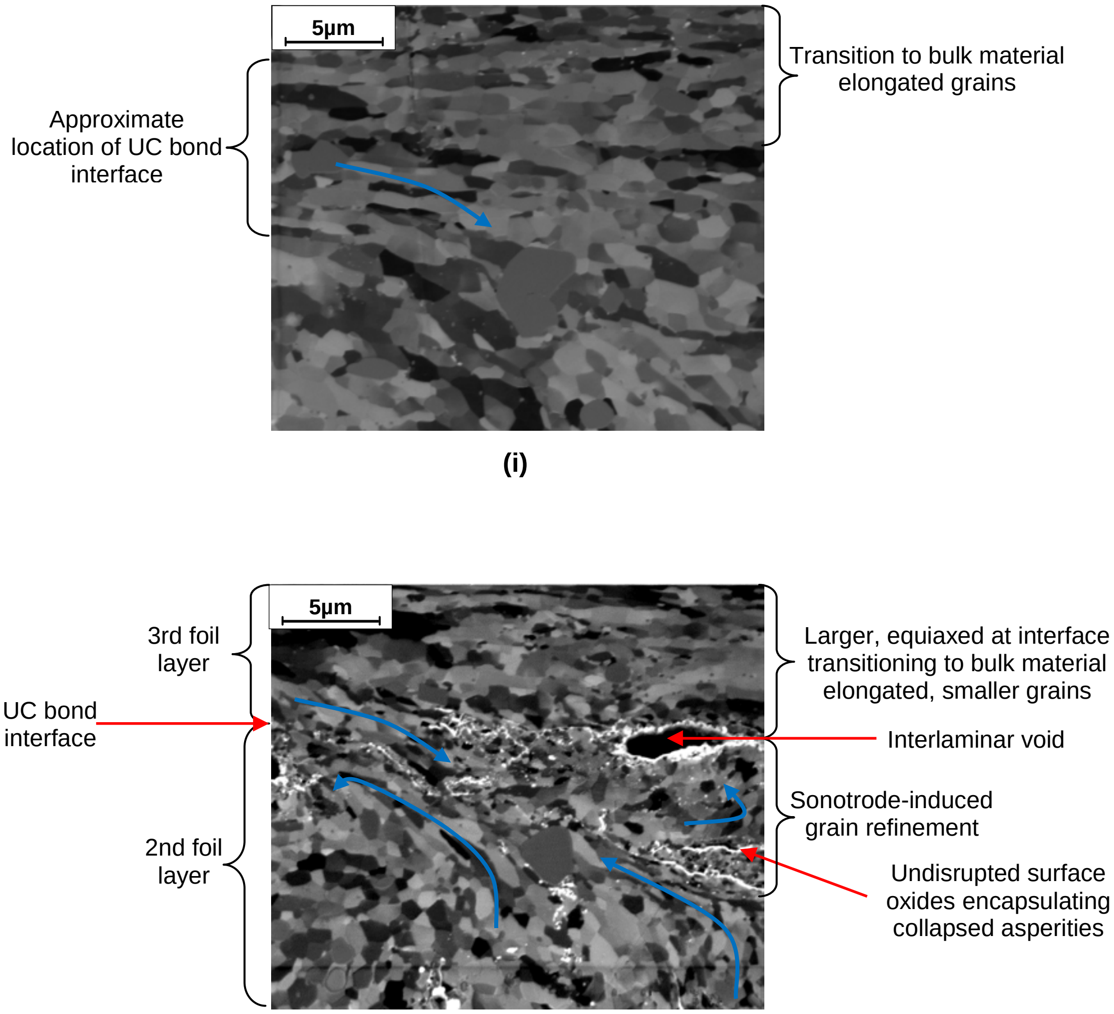

(i)

(ii)

Figure 5-20: FIB micrograph's of the interlaminar microstructure of UC samples fabricated by sonotrode C illustrating the absence of oxide layer (i) and the persistence of the surface oxide layer (ii) in different areas across the bond interface location of sample C (evidence of apparent plastic flow direction is indicated by blue arrows).

5.2.3.2.3 Grain Morphology Measurements

Table 5-6: Maximum surface and interface grain size and aspect ratios for samples from sonotrode A, B and C.

Sonotrode Sample	Maximum Surface Grain Size (µm)	Maximum Surface Grain Aspect Ratio (Y/X)	Maximum Interface Grain Size (µm)	Maximum Interface Grain Aspect Ratio (Y/X)
A	1.224	0.90	0.950	0.80
B	0.709	0.71	0.786	0.63
C	0.699	1.10	0.699	0.78

5.2.3.2.4 Grain Size Measurements

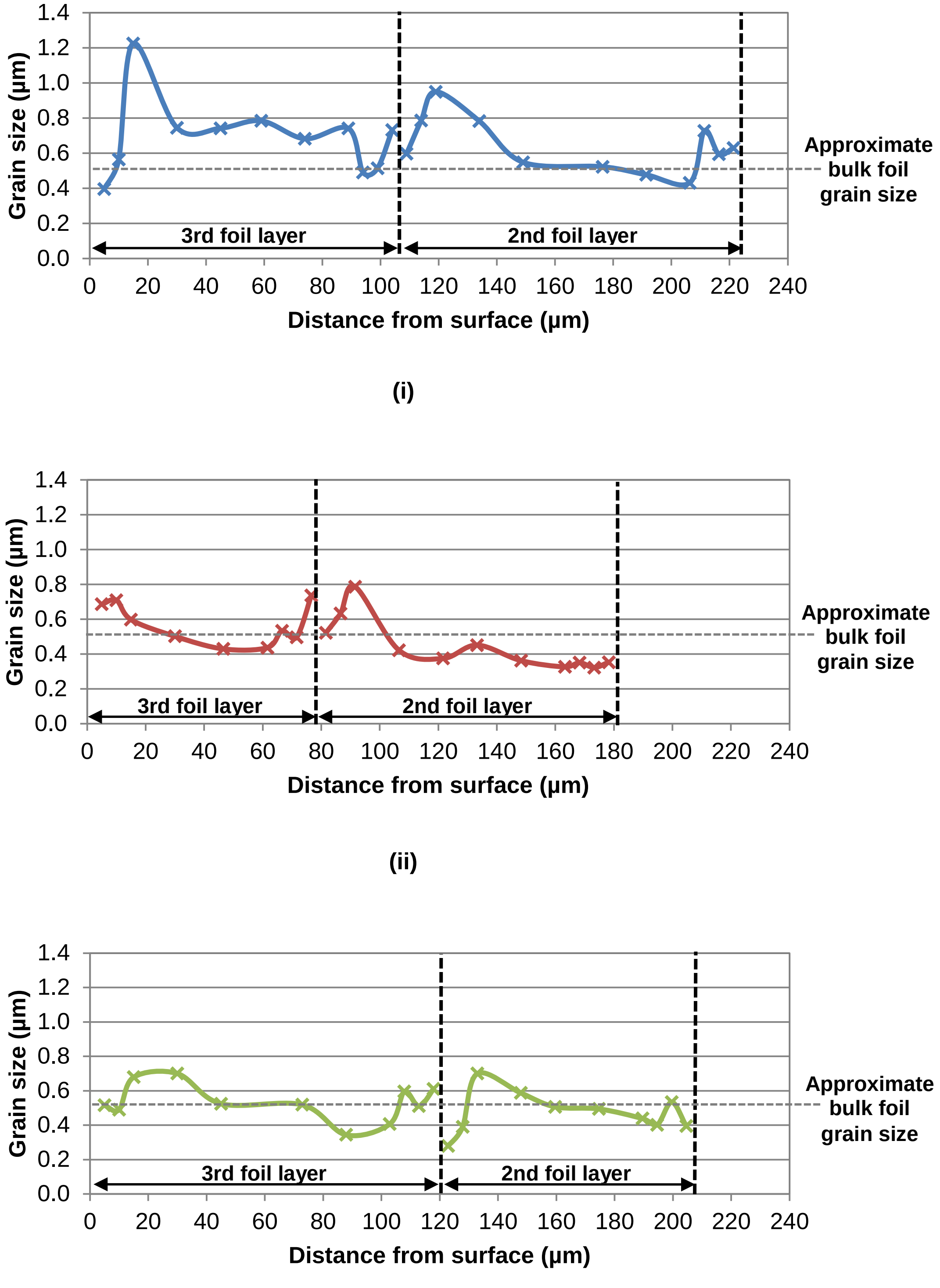

(i)

(ii)

(iii)

Figure 5-21: Graph to show the change in grain size in relation to distance from foil interface for samples from sonotrode A (i), B (ii) and C (iii).

5.2.3.2.5 Grain Aspect Ratio Measurements

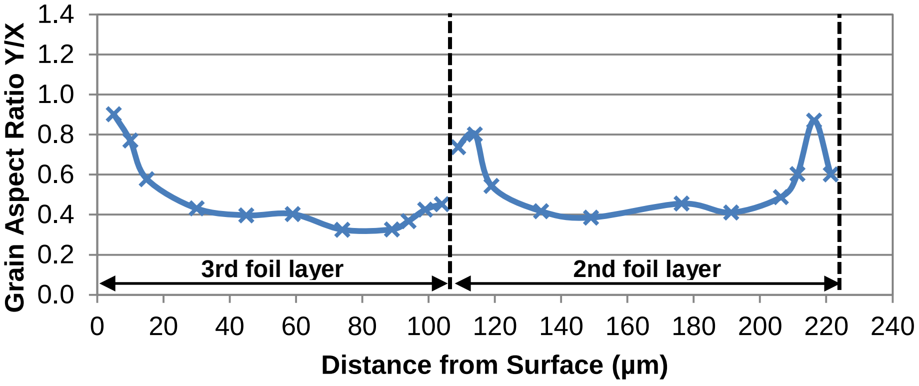

(i)

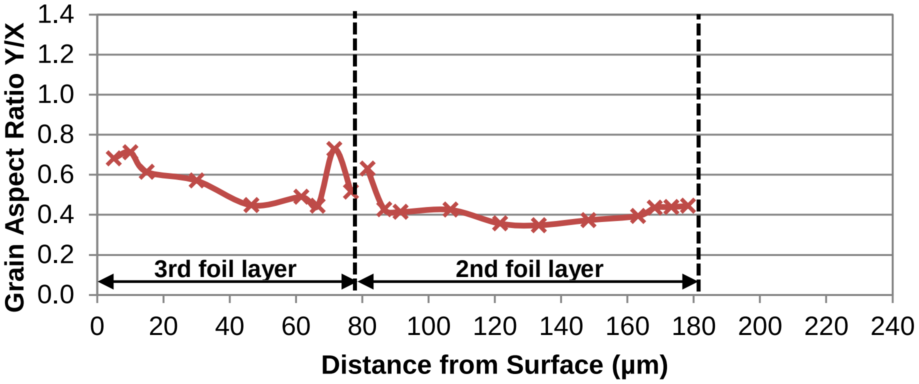

(ii)

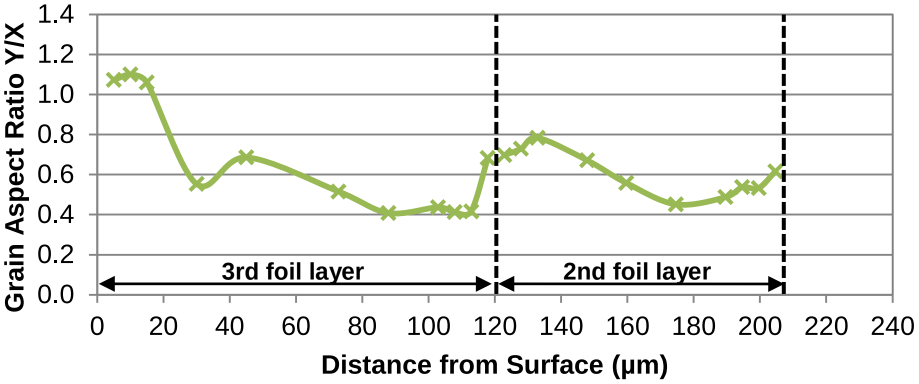

(iii)

Figure 5-22: Graph to show the change in grain aspect ratio in relation to distance from foil interface for samples from sonotrode A (i), B (ii) and C (iii).

5.3 Discussion

5.3.1 Substrate Surface Texture Characterisation

From visual inspection of the UC samples (Figure 5-9) it was apparent that, like their parent sonotrodes, the surface textures were quite different to each other. The UC samples (Figure 5-11) demonstrated similar surface characteristics to the surface texture of the sonotrode used in their manufacture (Figure 4-11). The peaks and troughs on the surface of the UC samples were, again, randomly distributed, with the surface composition of sonotrode A samples consisting of densely packed distinct small peaks and troughs, and the sonotrode C samples composed of peaks and troughs which were more spread out and of higher magnitude. The surface of UC samples fabricated by sonotrode B exhibited intermediate surface characteristics.

As discussed in the previous chapter, it was expected that the surface of the samples would reveal an inversely-textured, reduced amplitude version of the original sonotrode texture and through visual inspection this appeared to be the case. The samples fabricated by sonotrode A were relatively smooth and matte in appearance, while the samples produced by sonotrode B and C were rougher to the touch with bright, reflective areas (Figure 5-10). The bright, reflective areas within the rougher sonotrodes corresponded to areas of the foil which had not been plastically deformed by contact with the sonotrode during the UC and remain in their original, as-rolled state (Friel et al. 2010). These unprocessed foil areas were larger and more common in samples from sonotrode B and C as the weld surface cavities were deeper and hence the voids were not completely filled with plastically deformed material during processing.

5.3.1.1 Amplitude Parameters

As with the original sonotrodes the S_a and S_q parameters both showed that the amplitude of features on sample C were the highest, at 14.47µm, followed by sample B, 12.80µm and that the average height of the features on the surface of sample A was the lowest, at 4.48µm (Table 5-2). The standard deviation of these measurements also appeared to correlate to the magnitude of the S_a measurement; there was more variation in texture across the surface of samples with rougher surfaces, C, while the texture was more consistent in samples with a less rough surface, A.

The S_a of sonotrode A samples was 9.9% less than the roughness of the sonotrode itself, which fell within the measured variation of sonotrode A, while the samples B and C were 13.5 and 23.3% less rough than their parent sonotrode, a more significant decrease in S_a

(Table 4-6). This more significant reduction in the amplitude of surface features correlated to the hypothesis that these samples had not experienced adequate plastic deformation, through contact with the rougher sonotrode during fabrication, to sufficiently fill the deeper asperity cavities of the sonotrode (Figure 4-26). This resulted in samples with lower flatter surface peaks. The effect of areas of unprocessed foil on the surface on UC samples has been identified in previous work (Friel et al. 2010), where larger areas of unprocessed foils corresponded with higher interlaminar void volume with an expected reduction in mechanical properties.

Like their parent sonotrodes, all samples had a Sku over the critical value of 3, indicating the presence of more distinct peaks and/or valleys across their surface texture (Table 5-2). Samples A and C had a similar level of Sku, A with a value of 3.88 and C with a value of 3.86, while sample B had a slightly lower Sku of 3.76 and hence the surface consisted of a slightly more slowly varying texture (Figure 5-12). The level of all the samples Sku was higher than their original sonotrode texture by between 16 and 22% (Table 4-6). It had already been established that the Sku of sonotrode B was lower than sonotrode A and C, and therefore the lower Sku value of sample B was to be expected.

The Ssk for sample A and B showed a positive Ssk, of 0.416 and 0.250 respectively, which indicated that their surfaces were dominated by peaks. Conversely, the average Ssk for sample C was -0.303 and therefore the surface texture was dominated by valleys (Table 5-2). Theoretically the Ssk of each of the samples would be equal and opposite to the original sonotrode weld surface texture, as the sonotrode-induced roughness imparts a similar, opposite imprint of its surface onto the foil surface during processing. Sample B was close to the theoretical complete reversal of Ssk, while sample A saw an increase in the magnitude of Ssk and sample C saw a small reduction (Table 4-6). It has already been shown that there was a reduction in the sonotrode-imparted sample S_a due to insufficient plastic flow during consolidation and this could have accounted for the reduction in valley depth and hence smaller negative Ssk seen in sample C.

5.3.1.2 Topological Characterisation Parameters

The Sds of the samples decreased as the S_a increased; sample A had the highest Sds of 36329 peaks/mm^2, while sample C had the lowest at 330952 peaks/mm^2 (Table 5-2). In UC, a lower Sds on the sample surface (i), as seen in sample C, would correspond to higher local contact stresses during the consolidation of subsequent layers, as the applied weld force was distributed over a smaller number of peaks, while a lower Sds (ii), as seen in sample A, would correspond to lower local contact stresses, as the applied weld force was distributed over a larger number of peaks (Figure 4-28).

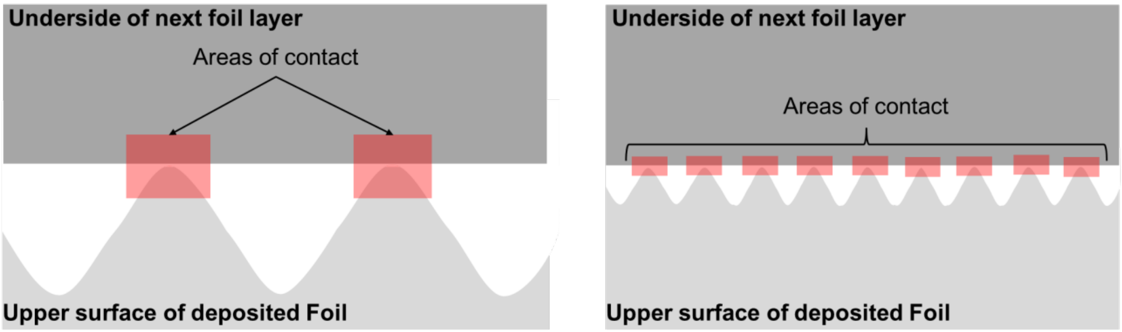

(i) (ii)

Figure 5-23: Diagram to show the applied weld force distribution over different contact areas in samples with low (i) and high (ii) Sds.

Reduction in sample Sds compared to the original sonotrode increased as the S_a increased, indicating a higher degree of surface texture loss at higher S_a's (Table 4-6), in line with the previous results. It should be recalled from the previous chapter that there was often a large variation in sonotrode Sds measurements and this was also true from the sample measurements.

The Ssc of sample A, at 0.976 peaks/mm was slightly larger than that of sample C, 0.845 peaks/mm (Table 5-2), while sample B had a smaller Ssc of 0.710 peaks/mm (Figure 5-12). The radius of curvature in sample B was larger (Figure 4-21iii) in contrast to the smaller radius peaks of sample A and C (Figure 4-21i-ii). It could be predicted that the Ssc could effect the contact mechanics during UC bonding, where smooth, more curved, peaks increase the contact area between the upper surface of the sample and underside of the next plain foil layer during consolidation. Lower local stresses might be seen at the contact points as the weld force was distributed across a larger area between the mating surfaces.

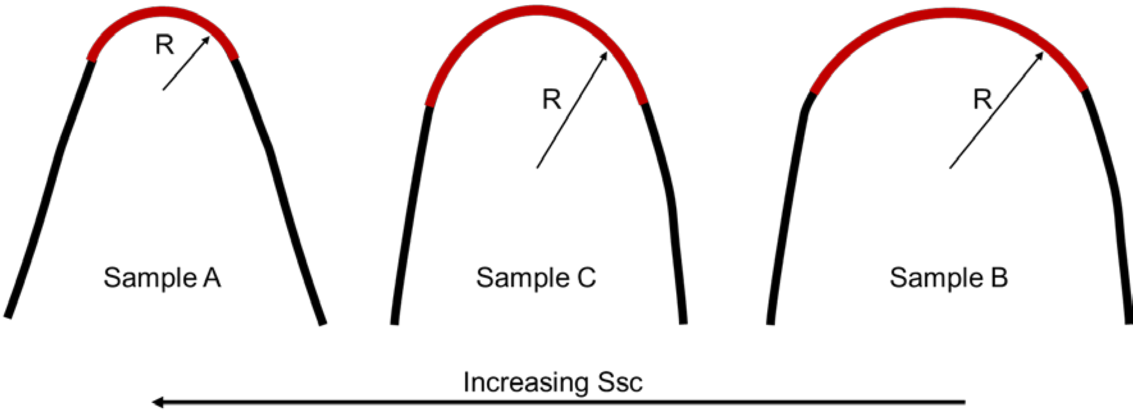

(i) (ii) (iii)

Figure 5-24: Diagram illustrating the difference in peak radius with larger (i), intermediate (ii) and smaller (iii) Ssc (where R is the summit radius).

A decrease in Ssc was seen across all the samples and a higher degree of curvature loss was seen in samples with high S_a. This appeared to be the result of incomplete texture transfer within sonotrode cavities, where insufficient plastic flow during processing leads to partially filled voids and subsequently foil surfaces with flatter peaks (Table 4-6).

According to the solid-state joining mechanism of atomic forces across nascent material (2.3.3.5), dispersal of surface oxides to generate atomically clean surfaces and plastic deformation to bring the mating surfaces into close contact, are required for bonding in UC. The higher interlaminar contact stresses, generated as a result of higher Ssc in sample A and lower Sds in sample C, could be expected to affect a higher degree of oxide break-up and plastic deformation as a result of their topology and contact with the underside of the deposited foil.

5.3.1.3 Spectral Analysis Parameters

The surface texture of sample A was 78.7% isotropic, sample C was less so at 78.9%, while sample B showed a lower level of texture orientation of 72.0% (Table 5-2). As seen in the original sonotrode surface, the Str was relatively high for all samples. A small reduction in isotropy was seen in sample A, compared to the corresponding sonotrode value (Table 4 6), which indicated that a small degree of slip between sonotrode and foil during the relative motion of UC processing may have introduced a degree of texture orientation into the foil surface.

The Sal for sample A was 28.99µm, sample C had a larger Sal of 71.05µm, while sample B had the largest Sal of 159.42µm, this meant that the weld surface of sample A was made up of a number of short wavelength components, while sample B and C consisted of longer wavelength spectral components, quantifying what can be seen in Figure 5-12. The lower density of features on the sample surface, as identified in sample B could have corresponded to a higher local contact stress at individual contact points, but this could be counteracted by the lower Sku and higher Ssc value of sample B which indicated that these less dense contact points would have a relatively larger contact area. Lower density features, as seen in sample A with a smaller Sal, could have corresponded to lower local contact stress occurring at a higher frequency.

A large reduction, of over 60% in Sal, was seen in sample C, indicating a significant loss of individual features over the surface compared to the original sonotrode texture, while there was a negligible change in sample A and B. This data, along with the other substrate surface texture characterisation parameters, continued to indicate that a significant reduction in surface feature amplitude occurred during processing with sonotrode C, due to its larger magnitude components.

5.3.1.4 Volume Parameters

The extreme peaks, in the top 10% of Vmp, would have been the first points of contact when the underside of the plain foil came into contact with the sample surface during UC. The applied weld force would have been spread over the small peak contact areas leading to the deformation of the softer, unprocessed, foil material. The contact area would have increased as more peaks came into contact with the foil material. The void volume in the bottom 20%, Vvv, of the sample surface was the area furthest away from contact with the underside of the plain foil during consolidation and a significant amount of plastic deformation would have been required to disrupt the persistent oxide layer and fill the void to achieve 100% LWD.

The Vvv, Vmc and Vvc measurements correlated to the magnitude of the S_a measurement; there was a larger Vvv, Vmc and Vvc in the sample with the roughest surface, C, than those with less rough surfaces, samples B and A. However, the Vmp of sample B was larger than that of sonotrode C.

The volume parameters for all the samples showed that the surface texture void volume was larger than that of the material volume, even in sample A where a high degree of positive skew was previously reported. The sensitivity of the Ssk parameter and its vulnerability to the effect of extreme values had been discussed in the previous chapter and hence the volume parameters were useful as an alternative method of evaluating the nature of the sample surface. In all samples the void volume was larger than material volume, indicating that the surface texture of the samples were dominated by valleys and not peaks. The ratio of material volume to void volume for the mid 70% of the texture was similar for all samples. For sample A the void volume was 1.5 times that of the material volume, 1.4 for sample B and for sample C the ratio was 1.3. This ratio was also similar to that of the original sonotrode surfaces. Therefore, in terms of volume, the sample surfaces were more dominated by valleys than peaks. This result was in contradiction with the positive values of skew obtained for sonotrode C, as the core volume characterisation method disregarded extreme peaks and troughs included in the measurement of skew.

While considering the extreme Vmp and Vvv measurements the results corresponded to the changes in Ssk. As the sample was effectively an imprint of the original sonotrode surface texture the sonotrode Vvv was equivalent to the sample Vmp and vice versa. The increase in peak material volume and decrease in Vvv for samples A and B corresponded to the change from negative to positive Ssk of the surface, while the opposite was seen in sample C.

5.3.1.5 Bearing Ratio Parameters

The Sdr of sample A was 36%, 32% for sample B and 59% for sample C, therefore the additional surface area due to texture of the sample C was the highest. Samples A and B both exhibited higher Sds values than sample C, but did not have such a large developed Sdr's. This could have been because while the number of features per unit area may have been higher in A and B, the height of these features was not, as seen in the lower S_a values of these samples. Sample B had a lower developed interfacial ratio than sample A, despite the larger number of summits per unit area and higher S_a value. This was because sample B had slowly varying smooth surface texture, also seen in its lower Sku, Ssc and 2D profile (Figure 5-12).

The surface of all the samples exhibited a lower developed interfacial ratio than the original sonotrode value. The Sdr for sample A was 28% lower than that of its sonotrode, sample B was 73% lower while for sample C, the Sdr was 72% lower than the developed interfacial ratio of sonotrode C. The reduction in Sdr seen in samples B and C corresponded with the lower S_a values as well as a reduction in peak density of the sample surface due to incomplete surface texture transfer as a result of limited plastic deformation.

5.3.2 Substrate Bond Strength and Failure Mode Characterisation

According to Kong et al. (2004a), peel testing is a method of describing the effectiveness of interlaminar bonding in UC through the failure of contact points within a weld interface, where individual contact points fail at different loads. Maximum peeling load occurs at the point when the bulk material fails in preference to individual contact points and highlights the deterioration in interlaminar material properties. Samples with poorly developed low strength contact points experience a high level of extension or complete delamination of the foil layer.

The results showed that differences in UC sample surface texture affected the load-extension characteristics of UC samples during peel testing. The samples produced by sonotrode C had the highest peel strength overall of 108.5N, samples manufactured using sonotrode B, had the lowest average peel strength of 85.5N, while samples manufactured using sonotrode A had an intermediate peel strength of 97.6N (Table 5-4). All samples showed a similar degree of spread in their results, with a standard deviation of between

12 and 17N. This degree of variation in measured maximum peel load was to be expected, as previous research (Kong et al. 2004a) has also shown a significant level of spread in peel testing results. The results did not indicate a proportional relationship between sample S_a and maximum peel load under these processing conditions. However, in the absence of other processing variables it is possible that the combined interaction of surface texture parameters, including the shape and amplitude of surface features which may effect the break-up of surface oxides and proximity of interface surfaces as discussed in the previous section, might have an impact on the peel characteristics of UC samples.

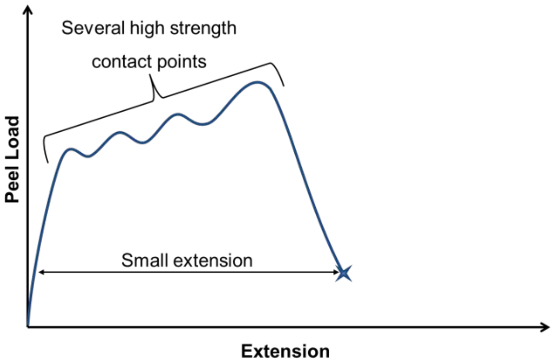

Figure 5-25: Diagrams illustrating the different bond strength and failure mode characteristics of sample A.

It is important to note not only the maximum peeling load of each sample, but the load-extension characteristics of these samples (Figure 5-13). The interface of sample A appeared to be made up of several high strength contact points, corresponding to small sub-peaks in peel load as the extension increased (Figure 5-25).

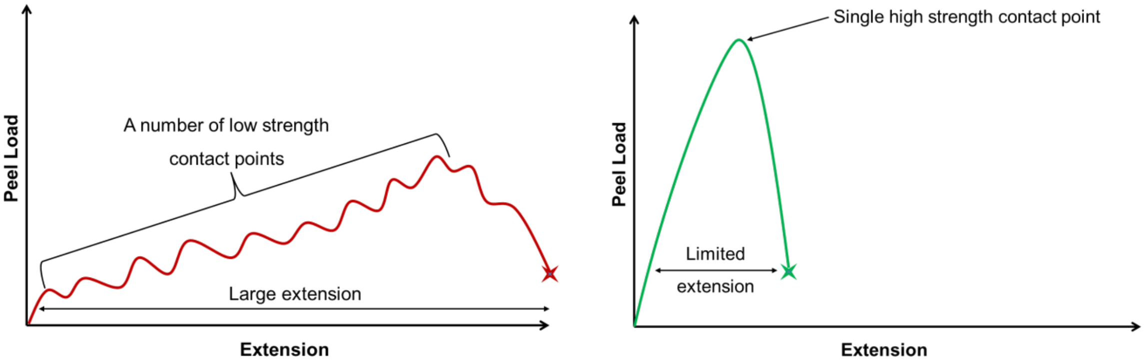

(i) (ii)

Figure 5-26: Diagrams illustrating the bond strength and failure mode characteristics of samples B (i) and C (ii).

Sample B appeared to be made up of a large number of lower strength contact points with a significant degree of extension before the maximum peel load was achieved (Figure 5-26i). The peel characteristics of sample C was that of an individual high strength contact point with limited extension (Figure 5-26ii). The rougher surface of sample C appeared to form higher strength, but brittle bonds, while samples A and B exhibited ductile failure characteristics at a lower maximum peeling load.

Previous investigations into the nature of failure of UC parts under peeling load have shown that the highest weld strengths occur in UC parts fabricated at high oscillation amplitudes and that the nature of failure was more brittle in nature, while the failure mode of parts manufactured at lower amplitudes were more ductile (Friel et al. 2010). It could be postulated that the rougher texture of sonotrode C ensured that a high level of mechanical coupling between the sonotrode and the upper surface of the foil occurred during the consolidation of individual layers of sample C. This resulted in the more efficient transmission of the oscillation amplitude of the sonotrode into relative motion between the foil and base material. Unprocessed areas of foil seen in the upper surface of sample C (Figure 5-10iii) might not have been present if a significant amount of slip between sonotrode and foil had occurred during processing.

The high average roughness of the upper surface of previously consolidated material, onto which subsequent layers of sample C were consolidated, would also have had an impact on the bond strength. The higher Sku, lower density of peaks across the surface of sample C would mean that the applied weld force was distributed across fewer contact initiation points, increasing the level of plastic deformation and work hardening at each location. The resulting bonds would have high weld strength but be brittle in nature, as seen in the sample C. This theory agrees with previous research which has shown that UC samples with a rough surface texture result in a higher level of grain refinement at the weld interface (Johnson 2008), where grain refinement was associated with work hardening and more brittle material properties.

A less rough sonotrode surface texture, in this case sonotrode A, may have been less efficient in transferring the oscillation amplitude of the sonotrode into the relative motion of the foil due to a lower level of mechanical coupling and a degree of slip between the sonotrode and upper surface of the foil. The lower amplitude, more densely populated features of the surface of the sample would result in more numerous contact initiation points but with a lower forces distribution during consolidation. Less plastic deformation and work hardening during processing could account for the lower weld strength seen over multiple contact points seen in the samples from sonotrode A. Previous research (Johnson 2008) has shown that UC samples with a polished interlaminar mating surfaces that no grain refinement and limited oxide distribution occurs at the interface, inferring that a degree of interlaminar surface roughness is required in order to disrupt the surface oxide layer and achieve metallic bonding in UC.

As with sample C, the areas of unprocessed foil seen in the upper surface of sample B (Figure 5-10ii) indicate that there was limited slip between sonotrode and foil during processing. The transmission of the ultrasonic oscillation into relative motion between the foil and consolidated substrate material is necessary to disrupt the surface oxide and initiate plastic deformation to bring the surfaces into contact to achieve bonding (Figure 5-27). We might therefore assume that there was an adequate level of mechanical coupling between the sonotrode and foil during consolidation.

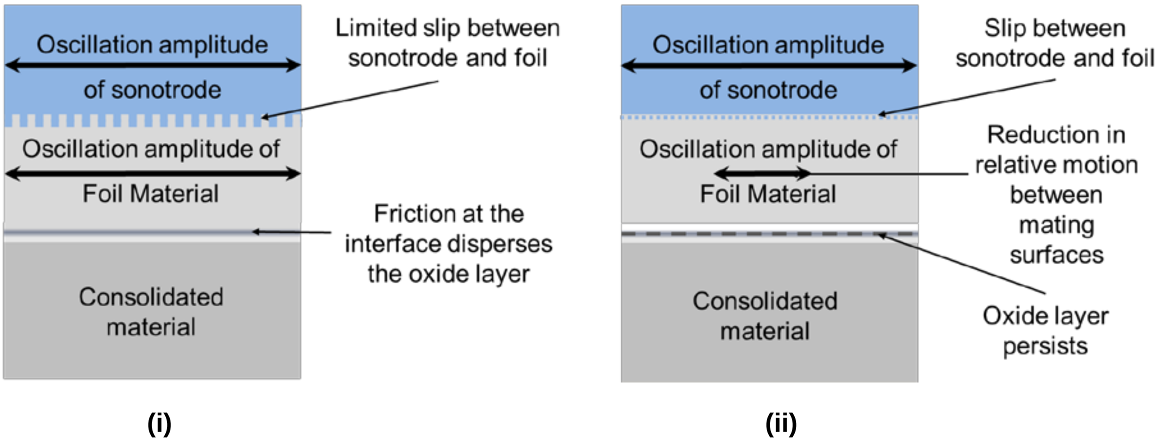

Figure 5-27: Diagram illustrating effect of a high (i) and low (ii) level of transmission of the oscillation amplitude of the sonotrode.

Compared to sample A, the surface features of sample B were higher in amplitude and less densely populated and it might be expected that this would result in a higher peel load measurement. However, the nature of the surface of sample B was such that the area of individual contact points was large, due to the large peak radius, and therefore for a given applied weld force the resulting contact pressure was lower. Less plastic deformation and work hardening during processing could account for the lower weld strengths seen in samples from sonotrode B.

5.3.3 Microstructural Characterisation of Substrate Interlaminar Interface

5.3.3.1 Optical Microscopy and Linear Weld Density Measurement

Examination of the weld interface of samples fabricated using the rougher sonotrode, C, showed the highest incidence of interlaminar voids with a LWD of 45.5% (Table 5-5). Samples produced by sonotrode A had a higher LWD of 66.3% and the LWD of samples from sonotrode B were the highest at 79.4%. As well as exhibiting a lower level of interlaminar bonding, the nature of the voids and imperfections in sample C were different to those seen in sample A. Janaki Ram et al. (2006b) identified three types of defects commonly found within the bond interface in UC parts; line-like, parabola-like and point-like defects and that most UC parts contain these defects to some extent. It was noted that line-like defects were commonly found in parts with a low LWD, parabola-like defects were found in parts with a medium LWD and that point-like defects were most common in parts with a high LWD. The results obtained in this research contradict these claims. In sample A, with a medium LWD of 66.3%, the defects seen were predominantly line-like, while in samples B and C, both high and low weld densities, the defects were predominantly parabola-like. This contradiction could be due to the influence that sonotrode texture had on the formation of interlaminar defects, which was not examined in the original research.

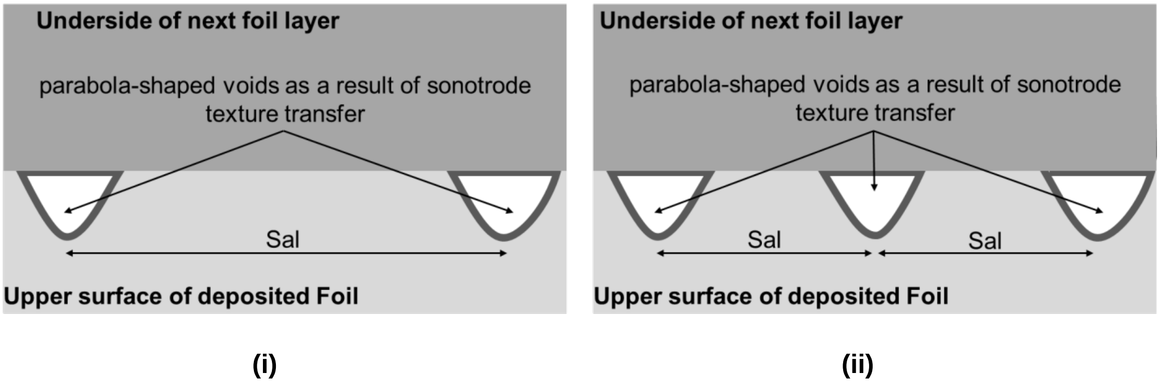

Figure 5-28: Diagram illustrating the differences in void distribution between sample B (i) and sample C (ii).

The parabola-like unbonded areas along the UC weld interface of sample B and C (Figure 5-16) appeared to be the result of sonotrode induced roughness effects, where the magnitude of the texture imparted onto the foil surface by the parent sonotrode during UC was sufficiently large that subsequent layers could not be brought into adequate intimate contact, by the applied normal force or plastic deformation, in order to fill the surface voids and minimise interlaminar porosity. While the parabola-like interlaminar voids in sample B were similar in size to those seen in sample C, due to the similar average roughness values, it was the higher frequency of voids that resulted in the lower LWD measurement of sample C. This can be represented by the lower autocorrelation length, Sal, seen in sample C compared to that of sample B (Figure 5-28).

The line-like defects seen in sample A (Figure 5-16i) appeared to be due to the insufficient plastic deformation and break up of the oxide layer during UC. While there were no large defects along the interface of sample A there was evidence of the persistent, unbroken oxide layer along the interface where metallic bonding had not been established, which was represented by the low LWD Measurement (Figure 5-29). The presence of defects and the medium to low level of LWD observed in the samples was undesirable. None of the sonotrodes produce samples with a LWD of over 80%, however that is not to say that a higher level of LWD density could not be achieved with an alternative sonotrode texture or through variation in other operating parameters.

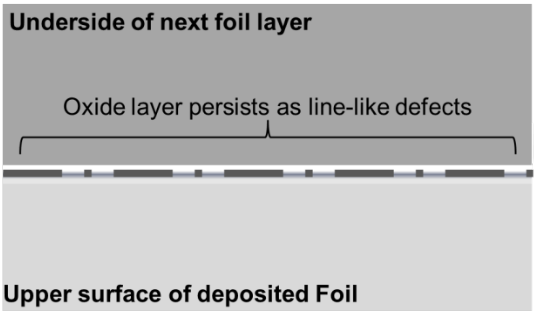

Figure 5-29: Diagram illustrating the characteristic line-like defects of sample A.

The relationship between sample surface roughness and LWD was the complete inverse of that seen between surface roughness and maximum peel load, where sample C had the highest resistance to peel load and sample B the lowest. Previous research had shown some, but not complete, correlation between linear weld density and peel strength (Kong, Soar, & Dickens, 2004) and therefore it should be clarified that these results showed that a low linear weld density did not necessarily indicate poor bond strength as is sometimes assumed.

It was important to note that the LWD measurements taken within the sample batches varied considerably, as could be seen in the high levels of standard deviation in the results. This was thought to be due to the inherent limitations of the linear weld density measurement method. The sample preparation procedure was time consuming and only a small fraction of the actual weld interface could be examined using the LWD method, 7.4% per microscopy sample (Appendix 5.2). The accuracy of the measurements were dependent on the quality of the sample preparation, where scratches, surface contamination or the use of strong chemical etchants can lead to an overestimation in void density, while insufficient polishing could disguise a persistent oxide layer leading to an underestimation of surface defects. During void measurement the definition of voids was also found to be subjective and could vary between operators. Figure 5-30 shows that the perceived bonded area, and hence LWD measurement, can appear to vary depending on the operators selection of brightness and contrast.

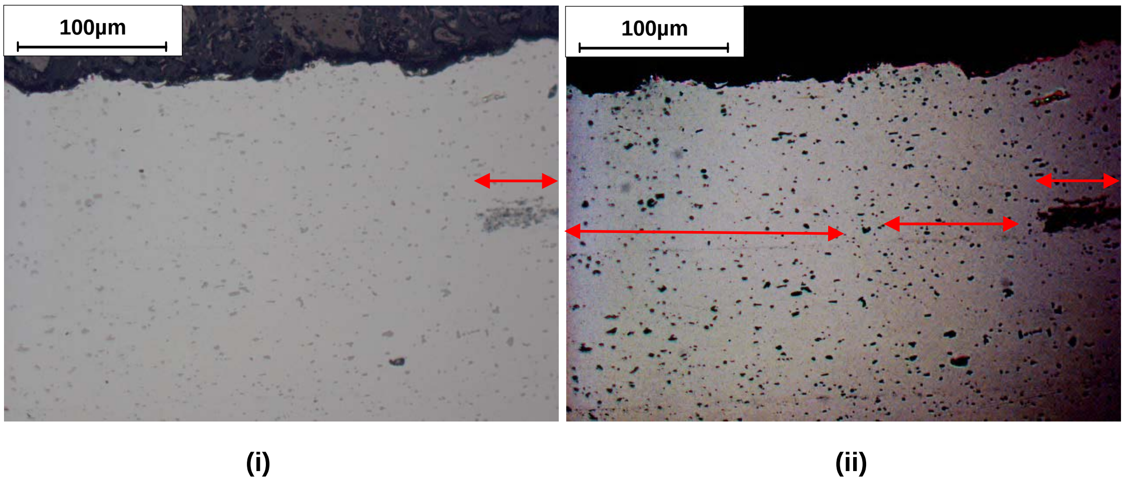

Figure 5-30: A normal (i) and high contrast versions of the same optical micrograph, highlighting the fact that evidence of the oxide layer, and hence measured LWD, can be dependent upon the operators preferred imaging parameters (unbonded areas are highlighted by the red arrows).

5.3.3.2 Focussed Ion Beam Analysis

In order to characterise the effect of the different sonotrode surface textures on UC sample microstructure the results from the FIB analysis were considered in two stages. Initially the effect of direct contact with the sonotrode on the subsurface microstructure of UC samples was considered, with the images collected from the foil surface characterisation area and vertical characterisation images from the third foil layer (Appendix 5.2). Secondly the effect of UC sample surface texture on the interlaminar microstructure was examined, with images collected from the horizontal characterisation area and vertical characterisation images from the second foil layer (Appendix 5.2). The analysis was sub-divided so that the effect of sonotrode surface texture and foil surface interaction at each stage of ultrasonic consolidation could be considered separately.

5.3.3.2.1 Foil Surface Microstructure Characterisation

Table 5-7 summarises the general changes in subsurface grain morphology identified within the samples.

As shown in Figure 5-17i, sample A’s surface exhibited the expected high frequency, low amplitude, peaks and troughs previously detailed in the sample surface texture characterisation results. The surface of sample C (Figure 5-17iii) showed sharp, higher, amplitude peaks at wider spacing than in sample A, as previously identified in the characterisation results. Sample B’s surface (Figure 5-17ii) appeared to be composed of a flat summit and a flat trough separated by a steep slope. The spacing of surface features of sample B were such that it would require significantly more surface imaging to truly capture the surface texture.

Table 5-7: Changes in subsurface grain morphology for samples from sonotrode A, B and C.

Sample	Changes in Grain Morphology
A	▪ Some nano-scale grain refinement around surface features. ▪ Significant equiaxed sub-grain growth. ▪ Transition to rolled grain morphology.
B	▪ Some nano-scale grain refinement around surface features. ▪ Some sub-grain growth, a degree of the original rolled morphology remains. ▪ Transition to rolled grain morphology.
C	▪ Significant nano-scale grain refinement around surface features. ▪ Some equiaxed sub-grain growth. ▪ Slow transition to rolled grain morphology.

The typical microstructure of the Al3003-H18 foil, prior to processing consists of 0.5µm grains elongated along the rolling direction (Figure 2-46) (Dehoff & Babu, 2010). Examination of the microstructure in the vicinity of the foil surface revealed a thin layer of grain refinement along the surface of all samples, with additional significant refinement around areas of apparent deformation and plastic flow.

Within sample A (Figure 5-17i) a fine grained structure can be seen around surface valleys, which corresponded to areas where sonotrode peaks had penetrated and plastically deformed the sample surface during processing. Grain refinement could also be seen within surface peaks, which correlated to areas where the foil material was plastically deformed and extruded into sonotrode surface cavities during processing. A small region of grain refinement was seen in sample B around the steep transition along the interface consistent with plastic deformation and flow due to sonotrode interactions (Figure 5-17ii). Sample C showed large areas of grain refinement and plastic flow within the surface peak material (Figure 5-17iii). The shape and orientation of the larger grains within these peaks illustrated the general flow of material as a result of the foil material extruding into the sonotrode surface cavities upon contact with the sonotrode surface. A degree of grain orientation, highlighting plastic deformation and the material flow direction, was evident across all the sample surfaces.

Low temperature heavy deformation can result in significant microstructure refinement (Valiev et al. 2000). The UC sample surfaces were plastically deformed under compressive and cyclic shear stress as a result of contact with the sonotrode surface during processing. Deformation is expected to have been achieved through the generation and movement of lattice dislocations (Guy & Hren 1974). The grain refinement observed at the UC sample surface was thought to be the result of sub-grain division due to dislocation pile-up during plastic deformation (Johnson 2008) or CDRX (2.3.6) (Gourdet & Montheillet 2003)(Siddiq & Sayed 2012). Strain energy stored within the crystal lattice during plastic deformation, in the form of dislocations, provides a driving force for grain-boundary migration ("Grain-boundary migration" 1972), which could account for the fact that the level of grain refinement within the UC samples appeared to correlate with the apparent degree of sonotrode-induced deformation experienced by the material.

The smaller, nano-scale, refined grains visible at the sample surface may equate to an increase in material hardness, according to the Hall-Petch relationship (Equation 2-1), where the yield stress of a material increases as its grain size decreases. An increase in surface hardness after sonotrode induced surface deformation could have implications with respect to interactions with consolidation of the subsequent layer.

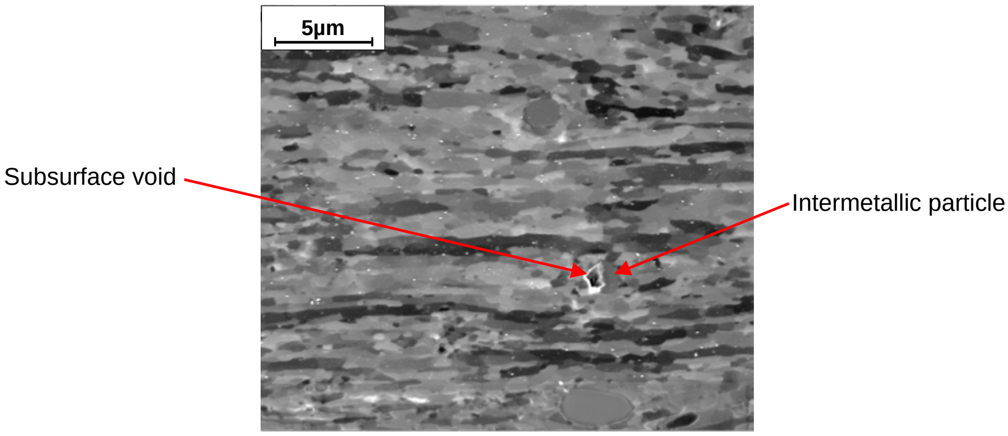

Figure 5-31: FIB micrograph of a subsurface void (~60µm below the surface) within the bulk material of a UC sample fabricated by sonotrode C.

The encapsulation of surface oxides and voids just below the surface of sample A (Figure 5-17i) may have become embedded as a result of direct contact with the sonotrode. The presence of voids was less evident in samples B and C, although this may have been due to the increased spacing of their surface features. This phenomena could have implications with regards to the presence of weld defects and limited oxide dispersion during consolidation of subsequent layers in sample A. Subsurface voids, apparently beyond the limit of direct contact with the sonotrode, were evident in samples processed by all sonotrodes. It was not known if these voids, commonly in the vicinity of intermetallic particles, were the result of UC process interactions or pre-existing defects in the foil (Figure 5-31).

Alongside areas of grain refinement, equiaxed increase in sub-grain size was also seen. Beyond the surface grain refinement, larger grains were seen within the subsurface material, a maximum grain size of 1.2µm approximately 15µm from the surface was observed in sample A (Figure 5-21i). The grain size transitioned back to that of the standard bulk material approximately 30µm from the surface (Figure 5-32). The maximum grain size measured in sample B and C was approximately 0.7µm, significantly less than in sample A (Figure 5-21ii and iii). The grain size in sample B quickly transitioned back to the bulk grain size within 30µm, while the transition in sample C was longer, occurring 45µm from the sample surface.

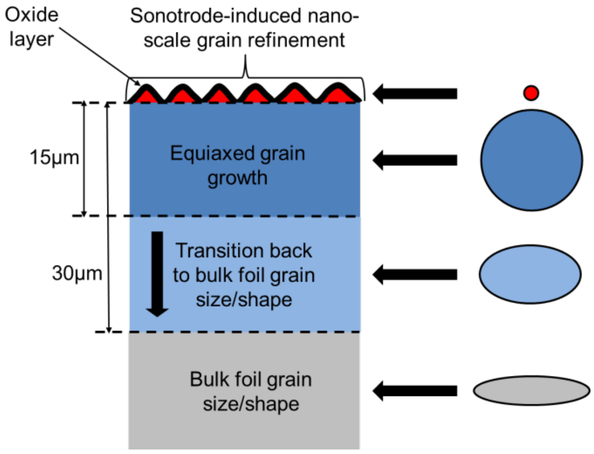

Figure 5-32: Diagram of the subsurface microstructure of samples from sonotrode A, illustrating the change in grain morphology.

The largest subsurface grains of sample A were almost equiaxed at the surface, with an aspect ratio approaching 1, reverting back to a flatter, elongated shape further from the surface (Figure 5-22i). The bulk grain size aspect ratio, of around 0.4, was also measured approximately 30µm from the sample surface. The effect of sonotrode A's interaction with the sample appeared to extend up to a depth of 30µm into the foil (Figure 5-32). Equiaxed sub-grain growth was also seen in sample C (Figure 5-22iii) with a similar transition to the bulk grain size aspect ratio. A degree of elongation in the rolling direction of grains within the microstructure of sample B remained, even within close proximity to the sample surface (Figure 5-22ii).

As described in the literature review (2.3.6), dynamic recovery by sub-grain rotation is a potential mechanism for subsurface sub-grain growth in UC (Sojiphan et al. 2010)(Sriraman et al. 2010a)(Sriraman et al. 2010b)(Sriraman et al. 2011). Sub-grain growth is thought to occur through the migration of dislocations and grain boundaries in order to increase grain size, where the driving force is to reduce the stored strain energy within grains by reducing the surface area to volume ratio ("Grain-boundary migration" 1972)(Guy & Hren 1974). Therefore the degree of sonotrode induced plastic deformation could be equivalent to the observed increase in sub-grain size within the sample grain morphology. The reduction in grain size away from the sample surface was thought to correspond with the extent of plastic deformation, diminishing as the distance from the sonotrode contact surface increased (Figure 5-33).

Another theory is that grain growth can occur during UC as a result of sub-grain boundary dissolution, when dislocation annihilation occurs under the repeated reverse straining conditions of the Bauschinger effect (2.3.4.3) (Higginson & Sellars 2002). In this case the reduction in grain size away from the sample surface would have also corresponded with the extent of sonotrode induced plastic deformation, where the dislocation density and the probability of annihilation would have diminished as the distance from the sonotrode contact surface increased (Figure 5-33).

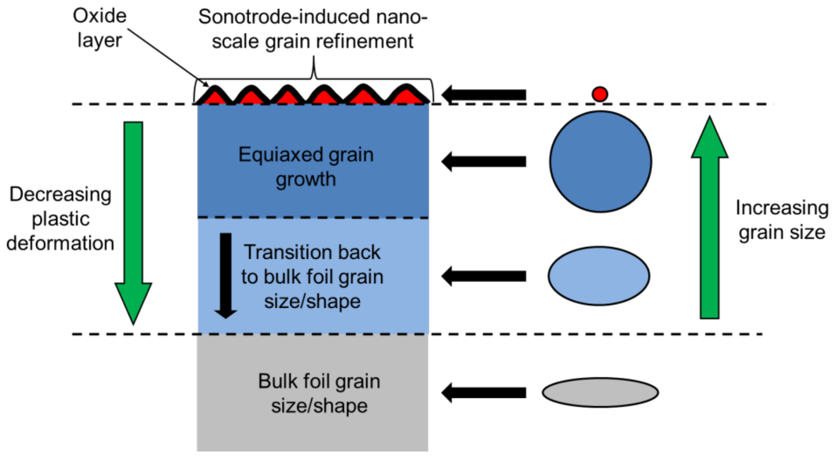

Figure 5-33: Diagram of the subsurface microstructure and grain morphology of UC samples, highlighting the negative correlation between plastic deformation and sub-grain size.

The additional transition depth from the surface of sample C before the microstructure reverted back to that of the bulk material was thought to correspond with the higher amplitude of the surface features, penetrating deeper into the foil material.

Thermal and acoustic energy, generated by surface and volume effects (2.3.4.1 and 2.3.4.2) (Kong et al. 2005), could also have provided energy to drive the increase in sub-grain size (Hayes & Shyne 1969)(Yoshida & Ohsone 1981). The dissipation of energy from the sample surface into the bulk material also corresponded to the grain size transition observed within the sample grain morphology.

It has already been proposed that the extent to which the sonotrode plastically deformed the sample surface would have been expected to have an effect on the resultant grain morphology, irrespective of the mechanism by which the sub-grain growth had occurred. It was, therefore, important to consider any variation in the deformation mechanics of sonotrode interaction with the sample surface. The effects of on the foil sample surface as a result of contact with the sonotrode were evaluated for each sample in a simplified model of the cross-sectional area (Figure 5-34).

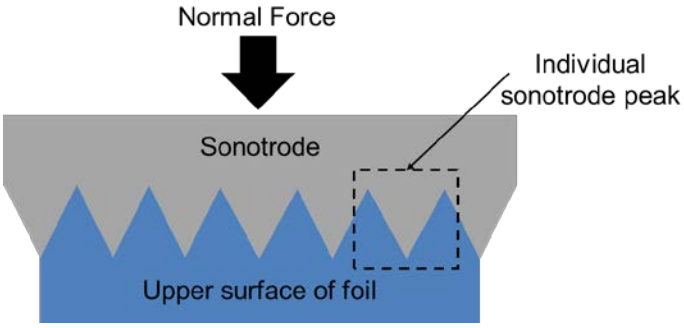

Figure 5-34: Diagram of the contact between the sonotrode and foil during UC, highlighting one sonotrode peak.

Initially the extent of plastic deformation generated within the foil surface through sonotrode contact was considered. It was assumed that the degree of plastic deformation was proportional to the volume of material displaced by the sonotrode peaks under the applied normal force. Sample B and C were thought to be subject to significantly higher levels of normal deformation due to the nature of their surface feature distribution. Sample A was thought to have experienced comparatively lower normal distribution as a result of its lower amplitude features (Figure 5-35, relative values and example calculations are shown in Appendix 5.5).

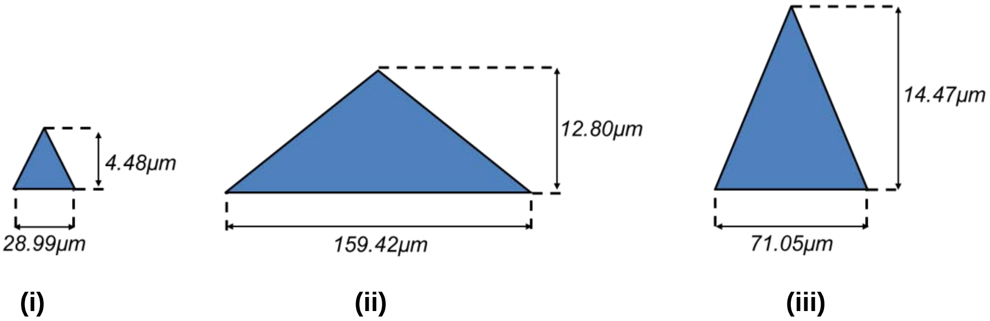

Figure 5-35: Diagram illustrating the transferred peak geometry texture on the surface of sample A (i), B (ii) and C (iii), based on the sample surface texture parameters S_a and Sal (Table 5-2).

The increased sub-grain growth measure in sample A appeared to correlate with the lower normal deformation experienced by the foil during contact with sonotrode A and the lower increase in sub-grain size experienced by sample B and C appeared to correlate with the higher level of normal deformation experienced by the foil during contact with sonotrode B and C (Figure 5-36).

The greater the extent of sonotrode induced deformation under the normal force, the higher the degree of recovery that would be required before an increase in sub-grain growth, relative to the original morphology, would be observed. It was thought that the lower normal deformation of sample A meant that there were less lattice defects to recover prior to sub-grain growth and hence a higher magnitude of grain size increase was seen. The higher normal deformation of sample B and C meant that there were more lattice defects to recover prior to sub-grain growth and therefore a smaller increase in size was observed.

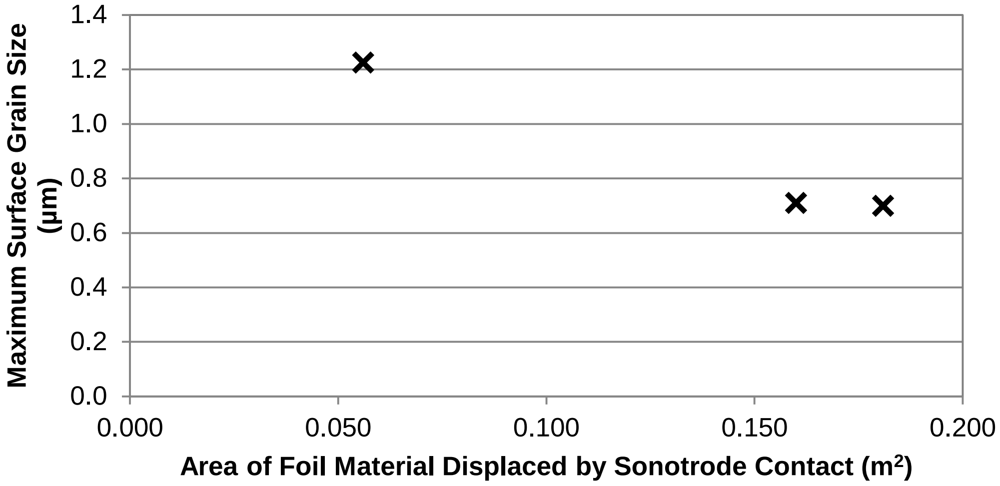

Figure 5-36: Graph to show estimated area of foil material displaced by sonotrode contact against measured maximum surface sub-grain size.

5.3.3.2.2 Interlaminar Interface Characterisation

Characteristic images Figure 5-18 to Figure 5-20 were used to represent the interlaminar interface of each of the samples (a composite of all images collected from the horizontal characterisation area can be found in Appendix 5.2).

Examination of the interlaminar bond interface of sample A showed evidence of the surface oxide layer along the length on the measured area. The oxide was sparse in some locations and more persistent in others. The topology of the interface appeared slightly flatter than the surface texture (Figure 5-17i) but with similar areas of grain refinement around areas of apparent deformation and plastic flow to those identified in the foil surface characterisation of sample A.

The presence and thickness of the surface oxide layer within the interlaminar interface of sample B varied along the length of the interface. In some locations (Figure 5-19i) the oxide was persistent and thick, particularly in the vicinity of large voids, while in other locations along the interface (Figure 5-19ii) the oxide appeared completely dispersed. The interface areas where the oxide layer remains possibly corresponds with the flat valleys or troughs of the surface texture. In these areas the high dynamic interfacial forces of bonding in UC appear to have had limited effect on breaking up the oxide layer between two relatively smooth surfaces.

The dispersion of the oxide layer within the interface sample C was also sporadic in nature (Figure 5-20i) and exhibited similar oxide dispersion characteristics to those identified in sample A, but on a larger scale. The depth of encapsulated oxides and interlaminar voids in sample C (Figure 5-20ii) was significantly deeper than those in sample A, this related back to the surface texture characterisation discussion where the nature of sample A and C were identified as similar in their more sharply varying nature.

It was assumed that the difference between the foil surface characterisation region, discussed in the previous section, and the interlaminar interface region were a result of interface interactions during the consolidation of the third foil layer.

There was no evidence of sub-grain size increase below the UC bond interface above that which was observed in the surface characterisation measurements. Grain size measurements below the interface of sample A (Figure 5-21i) showed a slightly reduced maximum sub-grain size of 1µm, compared to that of 1.2µm recorded along the upper surface of the foil. Similar grain size was seen at the interface of samples B and C compared to the measurements at the surface. The grain aspect ratio measurements (Figure 5-22) showed than that the subsurface grains of all the samples were no longer equiaxed.

The reduction in sub-grain size of sample A and the difference in aspect ratio of all samples subsurface grains compared to those of the subsurface interface could have been the result of compression at the interface caused during by the addition of the third foil layer during processing (Figure 5-37). The distance from the interface for the grain size to transition back to the standard bulk material size of the second foil was approximately 30µm, the same as seen in the surface of sample A.

An increase in the size and aspect ratio of sub-grains within the 5 to 15µm above the interlaminar interface between the second and third foil layer was seen in all the samples (Figure 5-21 and Figure 5-22). A similar increase was also seen above the interface of the first and second foil layer in samples A and C. Changes in grain morphology above the interface was not evident above interlaminar voids, where the original sub-grains structure appeared to remain unmodified (Figure 5-38).

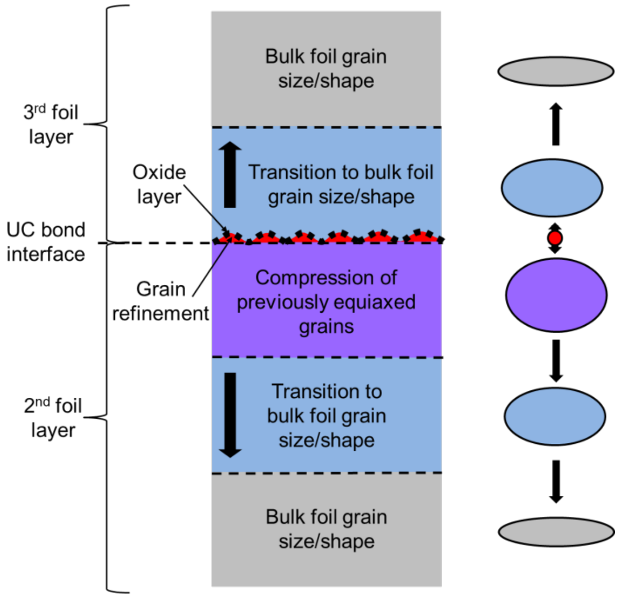

Figure 5-37: Diagram of the interface microstructure of samples illustrating the change in grain morphology.

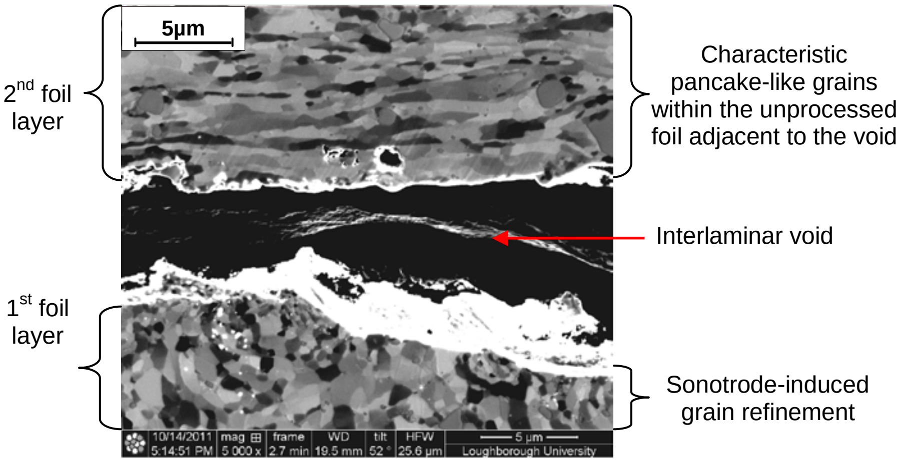

Figure 5-38: FIB micrograph of the unprocessed foil microstructure surrounding an interlaminar void within a UC sample fabricated by sonotrode B.

The theoretical increase in foil surface hardness, as a result of sonotrode induced surface deformation indicated by the presence refined grains, was suggested within the surface characterisation area discussion. The predicted difference in the relative hardness between 0.5µm pancake-like grains on the underside of the unprocessed foil (Dehoff & Babu, 2010)(third foil layer) and the nano-scale refined grains of the sample surface (second foil layer) was thought to be responsible in sub-grain growth above the interface during consolidation.

Similar to the relationship between sonotrode and foil surface discussed in the previous section, the harder surface of the second foil layer would have deformed the relatively softer underside of the unprocessed foil during processing (Figure 5-39). The thermal and acoustic energy, generated through the surface and volume effects (2.3.4.1 and 2.3.4.2) (Kong et al. 2005), could have provided energy to drive an increase in sub-grain size within the underside of the third foil layer. Equally, growth through sub-grain boundary dissolution as a result of the Bauschinger effect (2.3.4.3) (Higginson & Sellars 2002) could have accounted for the sub-grain growth observed above the interface.

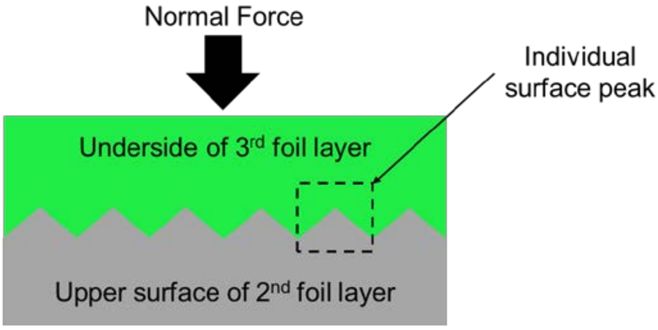

Figure 5-39: Diagram of the contact between the underside of the 3rd foil layer and the upper surface of the 2nd foil layer during UC, highlighting one foil surface peak.

It is important to appreciate that a degree of variability was seen within the grain size measurements for a number of reasons. The sampling size was limited to two vertical characterisation profiles per sample, due to the expense and the time taken for the DBFIB-imaging process as well as the limited availability of the equipment. An established and commonly adopted approach to grain size measurement (Higginson & Sellars 2003), the linear intercept method of measuring grain size was limited to characterising the grain size in two-dimensions, while the grains themselves are three-dimensional features and the choice of measurement spacing can significantly affect the accuracy and resolution of the results. In some cases it was difficult to locate the exact interface location due to complete dispersal of the surface oxide layer and hence the exact distance from the interface of grain size measurements was difficult to determine. Overall, these identified limitations were equally applicable to all of the measurements taken and therefore should be considered as a basis for comparison as opposed to absolute measurement values.

5.3.3.2.3 The Ultrasonic Consolidation Process

Based on the results within the chapter a theoretical model of the UC process was developed. The model is an updated version of the current understanding of the UC process, incorporating the findings of the current investigation. The aim of the model was to illustrate the effect of sonotrode weld surface texture on the interlaminar microstructure in UC with a view to optimising the interlaminar bonding.

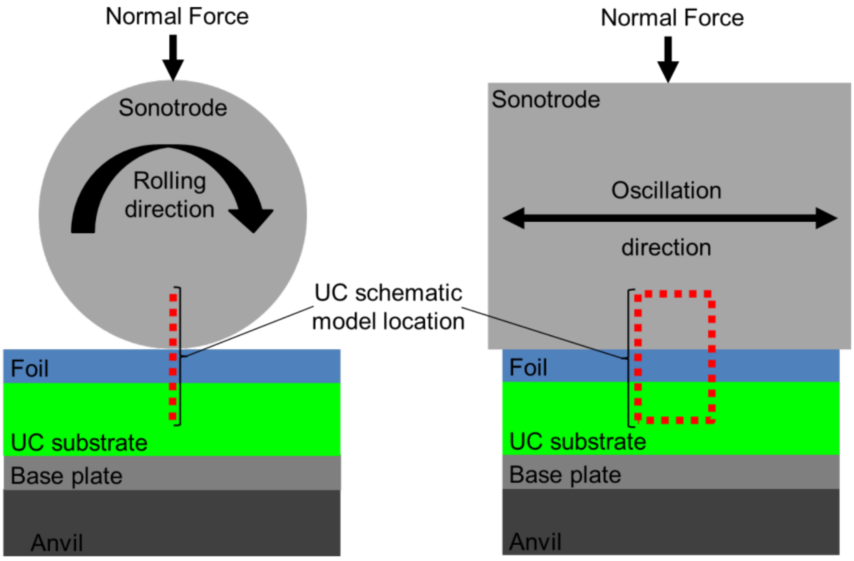

(i) **(ii)**

Figure 5-40: Diagram of the perpendicular (i) and cross-section (ii) view of the Alpha 2 UC machine setup, highlighting the relative location of the schematic model featured in figures 5-42 – 5-45.

Figure 5-40 illustrates an overview of the experimental setup of the Alpha 2 UC machine, highlighting the focus of the model. The model breaks down the UC process into three distinct stages:

1. **Normal deformation** through sonotrode and UC substrate surface contact.
2. **Contact point formation** under frictional sliding conditions.
3. **Recovery** under pure stick conditions.

In practice the stages most likely occur progressively with some level of overlap simultaneously but are described separately for clarity. Stages 2 and 3 are based on the finite element modelling of Pal & Stucker (2011) and have been developed to incorporate the experimental findings of the investigation.

Stage 1: Normal deformation

During the UC process normal deformation occurs in two locations. Firstly on the upper surface of the foil as the result of contact with the sonotrode weld surface texture and to a lesser degree along the lower surface of the foil through contact with the surface of the previously consolidated layer, the UC substrate surface (Figure 5-41). Plastic deformation at both locations is generated where the peaks of the sonotrode and substrate surface contact the foil layer under the applied weld force.

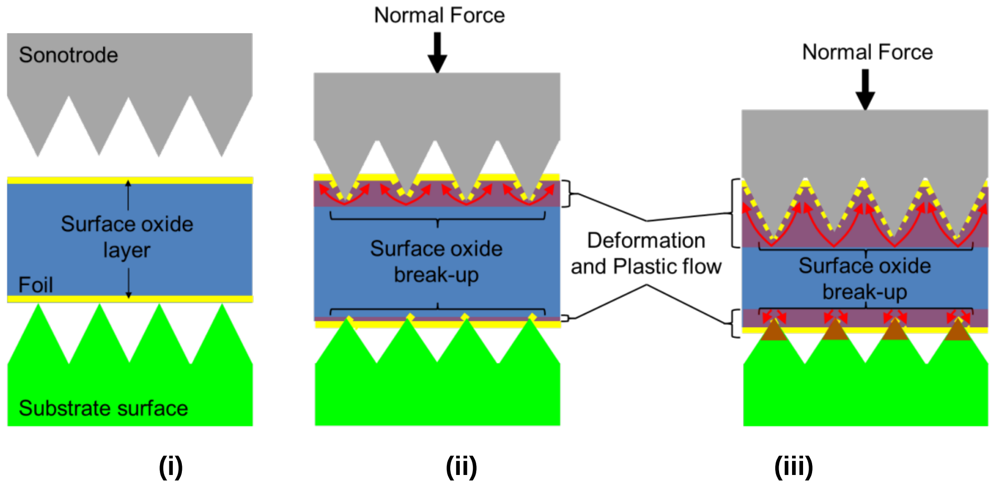

Figure 5-41: Schematic of UC illustrating prior to contact with the sonotrode (i), during initial contact (ii) and after complete engagement of the sonotrode (iii).

The extent of the plastic deformation at the upper foil surface is thought to be proportional to the volume of material displace by the sonotrode surface peaks, therefore a sonotrode with a relatively large peak volume will induce more plastic deformation, in the form of dislocations at a microscopic scale, during contact with the foil than a sonotrode with a smaller peak volume. The amplitude of sonotrode surface peaks is also thought to influence the depth of deformation effects on the material microstructure, where a sonotrode with a larger S_a would induce microstructural deformation deeper into the foil than once with a smaller S_a.

The lesser degree of deformation along the underside of the foil is due to a smaller difference in hardness between the contacting surfaces and potential compression of the substrate surface topology under the applied weld force.

Prior to sonotrode contact the foil is coated with a continuous oxide (Figure 5-41i) which is fractured and can become embedded in the foil material as a result of the normal deformation.

Stage 2: Contact point formation

As a result of the normal deformation, mechanical coupling between the sonotrode and foil surface is established and with the foil is subject to ultrasonic oscillation in-line with the sonotrode and relative to the substrate surface. At this stage frictional sliding occurs between the underside of the foil and the upper surface of the substrate surface (Figure 5-42). The relative motion of these surfaces disrupts the oxide coating of both surfaces (Figure 5-42i). The contact of nascent material establishes metallurgical bonds and the area of contact points between the layers develop (Figure 5-42ii).

The area, frequency and height of the contact points developed during the bonding process appears to be related to the topology of the substrate surface texture and therefore also directly related to the sonotrode induced normal deformation of during consolidation of the previous layer. For example:

- Substrate surfaces with a smaller feature spacing have more locations from which to initiate contact points while surfaces with larger feature spacing have less locations from which contact points can be initiated.
- Substrate surfaces with higher amplitude peak require a higher level of deformation and plastic flow in order to fill sonotrode induce valleys and reduce interlaminar porosity, while less plastic flow is necessary for surfaces with a smaller peak height.
- Substrate surfaces with smaller peak volumes and a more sharply varying texture might be expected to penetrate into the underside of the foil under higher contact pressure while the foil might be more likely to deform and conform to the shape of substrate surfaces with a more slowly varying texture.

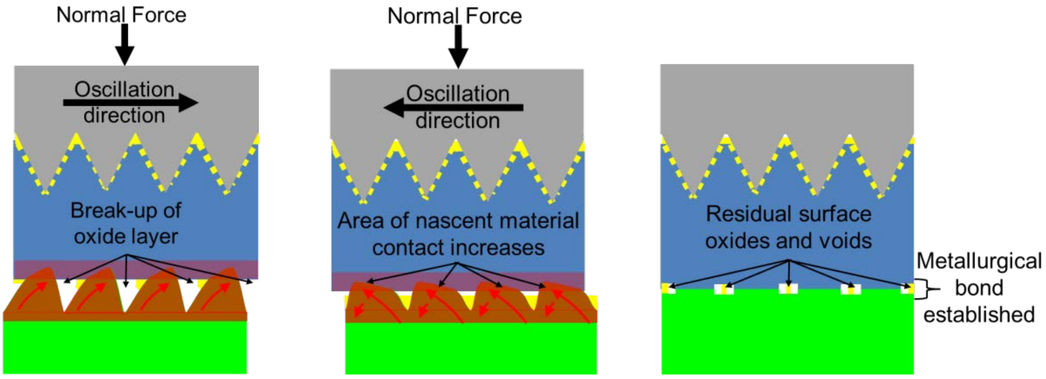

(i) (ii) (iii)

Figure 5-42: Schematic of UC frictional sliding conditions as contact points are initiated and developed (i - iii).

Deformation continues under the relative motion of the oscillations and a degree of frictional heating, known as the surface effect, occurs at the interface, enabling further break–up of the oxide layer and closer contact between the mating surfaces. The contact-bond process continues under the oscillating conditions as the contact area increases and becomes sufficient to inhibit further relative motion (Figure 5-42iii).

Stage 3: Recovery

Once pure stick conditions have been established between the foil and previously consolidated substrate surface, the process of recovery under the influence of the volume and/or Bauschinger effect is initiated. While effectively constrained by the sonotrode and the substrate surface the continued foil oscillations can be thought to be subject to acoustic softening and/or cyclic mechanical softening at both the upper and lower surface (Figure 5-43).

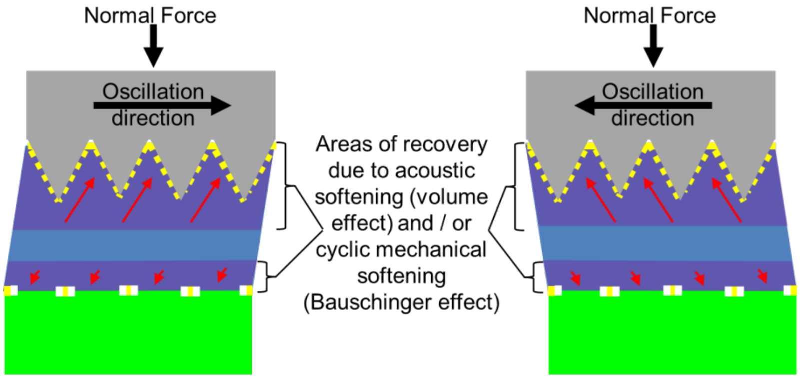

(i) **(ii)**

Figure 5-43: Schematic of UC under pure stick conditions as recovery occurs under the volume and/or Bauschinger effect (i - ii).

Both softening phenomena are thought to reduce the flow stress of the foil surface material and bring the mating surfaces into closer contact, reducing the interlaminar porosity. Acoustic energy from the volume effect could also have provided energy to drive the recovery of microstructural dislocations and subsequent grain the growth. Equally, the recovery of dislocations and increase in sub-grain size through sub-grain boundary dissolution could occur as a result of the Bauschinger effect.

Evidence from this and previous research is not sufficient to confirm the validity of either softening phenomena or to establish the metallurgical restoration mechanisms that are at work. However, the evidence remains that the greater the extent of previous deformation experienced by the sub-surface foil material, the lesser the resultant increase in grain size observed.

5.3.3.2.4 Microstructural Characterisation of UC Substrate

A general microstructural characterisation of a cross-section through the model is illustrated in Figure 5-44. Variations in grain morphology that may occur as the result of sonotrode surface texture variation are discussed.

The height of the sonotrode weld surface texture features is reflected in the depth of the sonotrode-induced nano-scale grain refinement on the upper surface of the 3rd foil layer and to a lesser degree at the bond interface. This is followed by a region of equiaxed sub-grain growth, where the increase in grain size is inversely proportional to the level of deformation induced by the sonotrode surface weld texture.

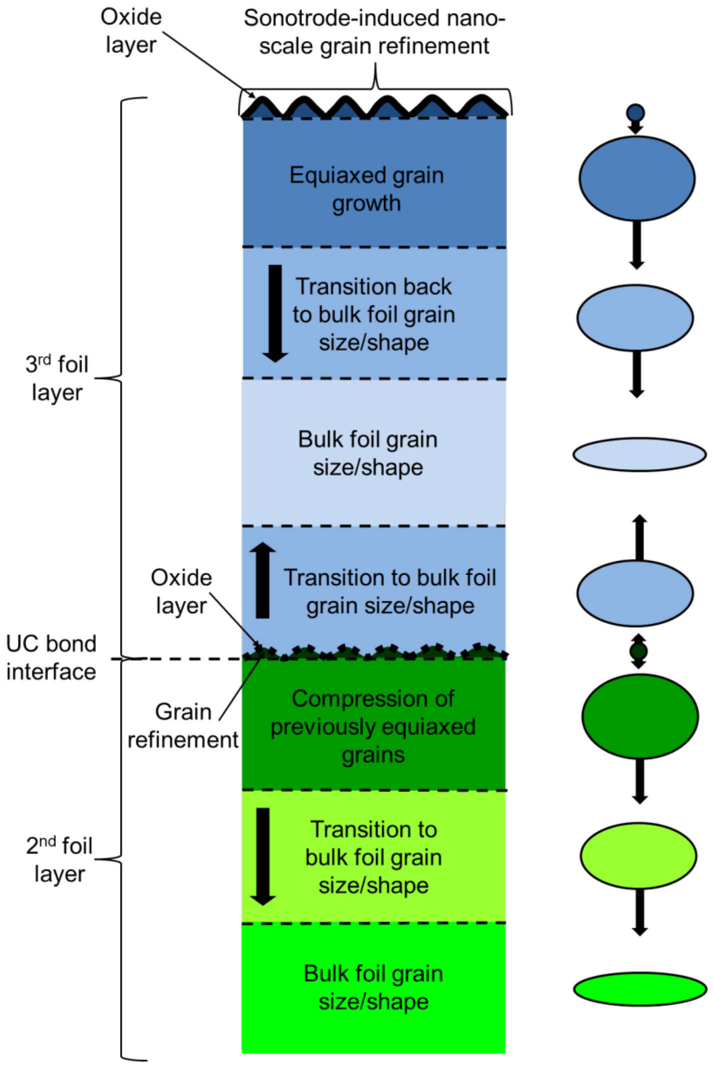

Figure 5-44: Diagram of the microstructure of a UC sample cross-section showing the difference in grain morphology throughout.

A region where the grain morphology transitions from the area of equiaxed sub-grain growth back to that of the bulk foil is seen, where the depth of transition is proportional to the amplitude of the sonotrode weld surface texture.

Above the weld interface a smaller region of modified grain morphology can be observed which transitions back to that of the bulk material into the foil above over less depth than seen at the upper surface of the foil.

While surface oxides were evident in all areas where bonding has not occurred, the incidence of persistent surface oxide in areas which were in contact appeared to be related to magnitude of the sonotrode-induced substrate surface texture, where less interlaminar surface oxides were seen in samples with higher amplitude surface features.

Below the bond interface the grain morphology echoes that seen in the third foil layer but with evidence of compression as a result on subsequent foil deposition.

5.4 Summary Review

The aim of this chapter was to test the second Research Objective "*to investigate how interlaminar microstructure and bond strength in UC is dependent upon sonotrode weld surface texture*" and the surface texture characterisation, bond strength and failure mode analysis and detailed microstructural characterisation of the UC substrate interlaminar interface results supported the proposition.

The surface texture characterisation results upheld the previous assertion that sonotrodes were found to impart a similar or reduced magnitude version of all their surface texture parameters onto the surface of the UC samples they produced. The greater reduction in texture transfer observed with the rougher sonotrodes was attributed to the increased degree of plastic deformation required to fill the deeper cavities during contact with rougher sonotrodes during processing.

The previous chapter proposed that the differences in the relationship between bond strength and changes in oscillation amplitude and weld speed seen in samples produced by sonotrode B were the result of differences in surface texture parameters rather than average surface roughness, S_a. The detailed surface texture characterisation of samples produced by sonotrode B has shown a degree of variation between sample B and the samples produced by the other sonotrodes. Samples produced by sonotrode B appear to have had a smooth slowly varying texture, lower Sku, Ssc and Str, and lower frequency feature spacing, with higher Sal. Samples A and C had a more sharp peaked texture, with higher Sku, Ssc and Str, higher frequency feature spacing, and lower Sal; in proportion to their S_a.

Examination of bond strength and failure mode analysis of samples fabricated by each sonotrode highlighted the differences in how UC sample surface texture affected the load-extension characteristics of UC samples during peel testing. These differences appeared to be dependent upon the surface area and density of individual contact points as well as the amplitude of surface features.

The experimentation also drew attention to that the fact that low LWD measurements do not necessarily equate to low bond strength and that sonotrode texture appeared to be a critical variable in the formation of interlaminar defects under otherwise identical processing conditions.

High magnification analysis of all the samples indicated that the degree of sonotrode induced deformation experienced by the material corresponded with the subsequent proportion of sub-grain growth. The theory of the surface, volume and Bauschinger effects were all used to evaluate the observed microstructural changes and variation.

FIB imaging results also indicated that a significant degree of the observed microstructural changes occurred as a result of sonotrode-foil interactions and not as a result of the relative motion of the surfaces during consolidation. However, the relative motion at the interface remains key to ensuring the breakup of the surface oxide layer and initiate sub-grain growth in the underside of the newly consolidated foil.

6 The Effect of Substrate Surface Texture Modification on Interlaminar Bonding in Ultrasonic Consolidation

The previous experimental chapters focussed on the significance of the sonotrode and substrate surface texture on interlaminar bonding in UC. The third experimental chapter (Figure 4-1) focuses on the final Research Objective *“to understand how modifying the surface texture of stock foil prior to manufacture can be used to modify interlaminar bonding in UC”*.

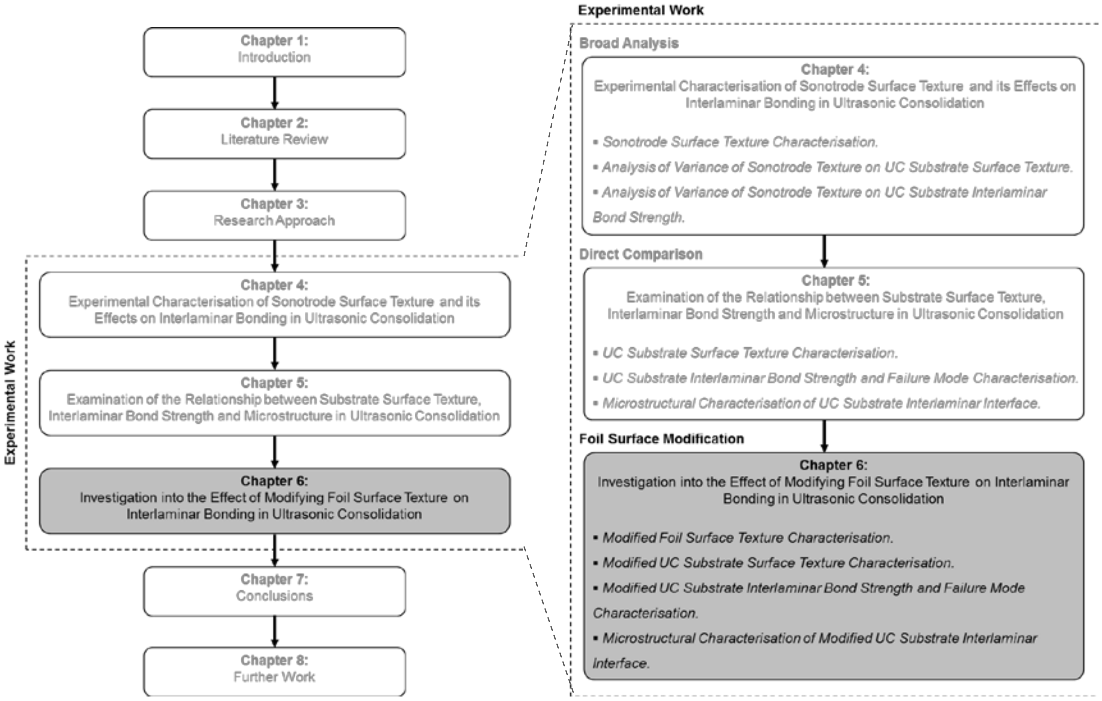

Figure 6-1: Thesis organisation, highlighting Chapter 6.

The following Research Factors are addressed within the chapter:

V. Investigate texturing methods that could be applied to foils used in the manufacture of UC samples.

VI. Evaluate the extent to which pre-textured foils affect interlaminar bond strength and microstructure in UC.

The chapter describes the foil surface modification and characterisation methodology adopted to fulfil Research Factor 5. The effect of the foil surface modification is evaluated through substrate bond strength measurement and microstructural characterisation of the modified substrate interlaminar interface in order to fulfil Research Factor 6 and test the final Research Objective.

6.1 Experimental Methodology

6.1.1 Foil Surface Modification

In order to modify the stock foil surface texture the unprocessed foil was plastically deformed through mechanical means by rolling sonotrode B over the foil surface without the ultrasonics engaged. The aim was to texture the surface of the foil with an equal and opposite version of the UC sample surface texture. Sonotrode B was chosen because of its intermediate surface roughness, in comparison to sonotrode A and C.

In order to modify each foil the Alpha 2 UC machine was set with a Al 1050 base plate and Al 3003-H18 foil in the standard processing configuration (Figure 4-7) with the appropriate weld speed and weld force were selected (Table 6-1). The sonotrode was then applied to the foil surface and traversed the length of the anvil in the absence of any ultrasonic oscillation. The foils were rolled without the ultrasonics engaged as the initiation of ultrasonic excitation at this stage would have bonded the foil to underlying base plate, rendering it unsuitable for subsequent consolidation.

Table 6-1: Processing conditions for each of the modified foil samples.

Foil Sample Number	Weld Speed (mm/s)	Weld Force (N)	Number of Passes
T1	40	1400	1
T2	40	1400	2
T3	40	1400	3
T4	40	2000	1
T5	10	1400	1
T6	10	1400	2
T7	10	1400	3

In some cases the foils were subject to multiple passes from the sonotrode in order to achieve different surface texture characteristics. All the foils were processed at room temperature. Four foils were textured under the same processing conditions for each test condition which were later used to produce the UC samples.

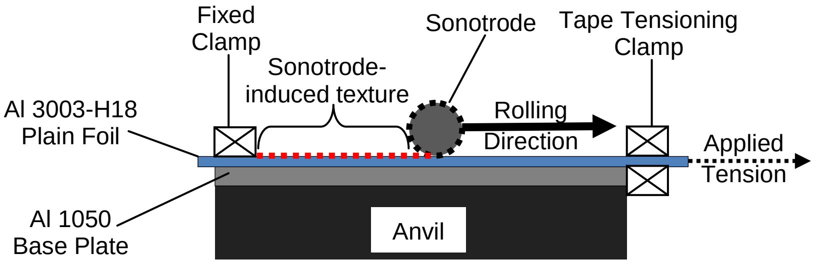

Figure 6-2: Diagram of foil sample texture modification set up using the Alpha 2 UC machine.

The process was repeated for all the foil processing parameter combinations (Table 6-1) to produce all the modified foil samples. The foils were rolled at relatively slow (10mm/s) and fast (40mm/s) weld speeds and at high (2000N) and low (1400N) weld forces in order to produce a range of modified foil surface textures.

6.1.2 Modified Foil Surface Texture Characterisation

In order to establish the nature of the surface modification imparted onto the foils by the sonotrode a foil from each set of processing conditions was measured using white light interferometery and compared to the original foil (Figure 6-3 and Figure 6-4).

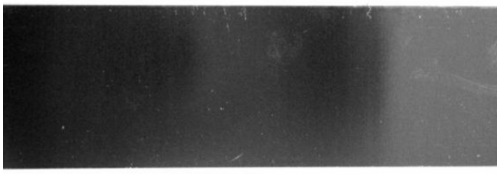

Figure 6-3: Stock Al3003-H18 foil.

Figure 6-4: Modified Al3003-H18 foil textured by sonotrode rolling.

For each modified foil the texture was measured in four different locations along the length of the surface using the Zygo NewView 5000 white light interferometer. Measurement variables similar to those used for the sonotrode and UC sample texture measurement in previous chapters, but shorter in scan length, were adopted (Table 4-1). The data files were processed using the same template as used in the sonotrode texture measurement (4.1.1) and the surface texture analysis parameters for each foil-texture modified sample was determined.

Table 6-2: Zygo NewView™ 5000 measurement parameters for sonotrode A, B and C (Zygo Corporation 2002).

Parameter	Setting
Objective Lens	Mirau 10 X
Zoom Setting	X 1
System Magnification	X 10
Measurement Array Size (pixels)	640 x 480 at 30 Hz
Vertical Resolution (nm)	0.1
Lateral Resolution (µm)	1.18
Field of View (mm)	0.70 x 0.53
Stitched Image Overlap (%)	25
No. of Images	9 (3x3)
Total Stitched Image Size (mm)	1.75 x 1.33
Scan Length (µm)	50

6.1.3 Ultrasonic Consolidation Sample Fabrication

The base of all the UC test samples were manufactured on the Alpha 2 UC machine at Loughborough University using stock, unprocessed Al 3003-H18 foil. The first two layers of all the samples were fabricated using sonotrode B under the processing conditions listed in Table 5-1. For each sample the length of the consolidated area was 150mm in order to comply with the BS EN 2243-2:1991 peel test requirements.

Table 6-3: UC sample fabrication parameters

Oscillation Amplitude (μm)	Weld Speed (mm/s)	Weld Force (N)
20	40	1400

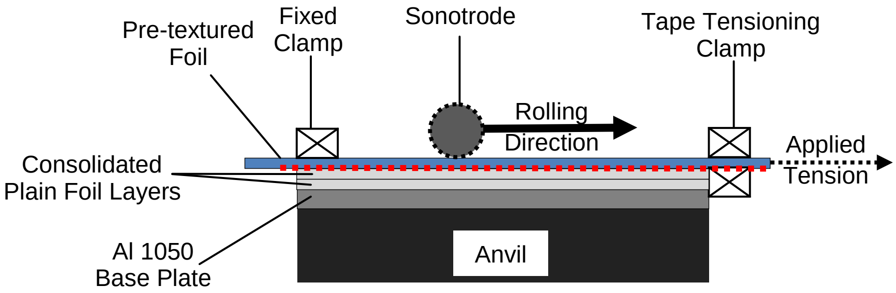

Figure 6-5: Diagram of foil-texture modified UC sample fabrication, illustrating the consolidation of the modified foil on top of the base UC sample using the Alpha 2 UC machine.

The pre-textured foil was placed on the base sample, with the textured surface on the underside in contact with the previously consolidated layers, and clamped into position (Figure 6-5). The modified foil layer was then consolidated into place under the previously stated processing conditions to complete an individual test sample. Three replicate UC samples for each of the seven texture-modified foil variants (T1-7) were fabricated. All the samples were manufactured at room temperature and the anvil temperature was monitored during processing to ensure that all the samples were manufactured at 25˚C ± 5.

6.1.4 Modified Substrate Surface Texture Characterisation

An identical surface texture measurement method and data processing procedure to that used in the previous experimental chapters was adopted to collect the data from the foil-texture modified UC samples. The surface texture analysis parameters from the sonotrode characterisation (Chapter 4) and direct comparison UC samples (Chapter 5) were used to characterise these UC samples (4.1.1).

6.1.5 Modified Foil Sample Bond Strength Measurement and Failure Mode Characterisation

The bond strength of each UC sample was measured using peel test analysis method, as described fully in Chapter 4’s Methodology (4.1.3.1) and the load extension data was recorded in order to characterise the nature of the bond failure in each case.

6.1.6 Microstructural Characterisation of Modified Foil Sample Interlaminar Interface

6.1.6.1 Optical Microscopy and Linear Weld Density Measurement

The same method for measuring LWD was used as detailed in the previous chapter (5.1.3.1). One UC sample from each of the seven different foil modification variations (T1 - T7) was randomly selected. The average LWD for each foil-texture modified UC sample was calculated.

6.2 Results

6.2.1 Modified Foil Surface Texture Characterisation

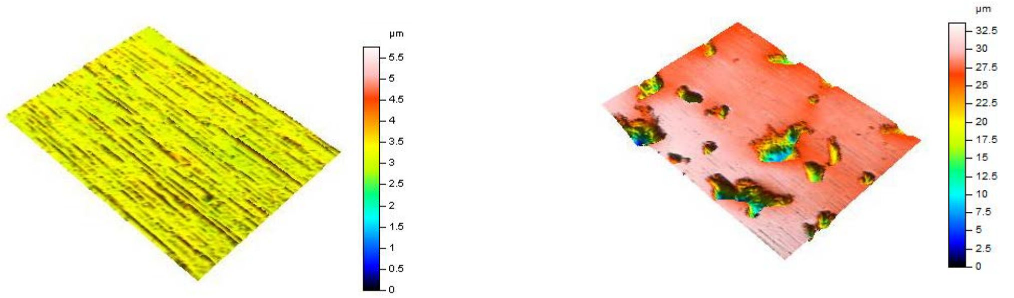
T0 **T4**

Figure 6-6: 3D pseudo-colour image of unprocessed stock Al3003-H18 Foil (T0) and foil modified by rolling with a weld force of 2000N at 40mm/s (T4).

Number of Passes	**Weld Speed (mm/s)**	
	10	**40**
1	**T5** 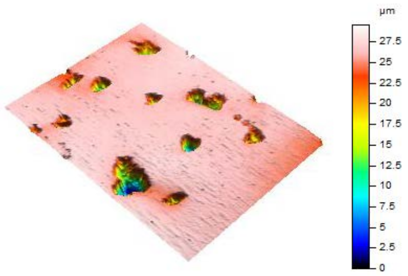	**T1** 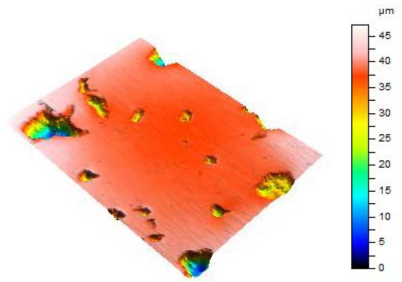
2	**T6** 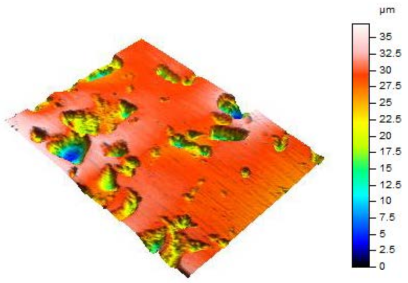	**T2** 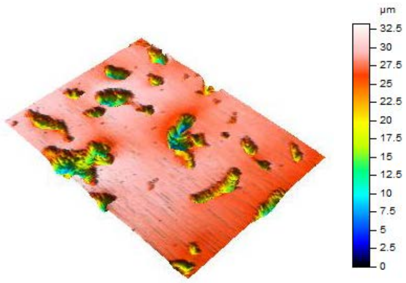
3	**T7** 	**T3** 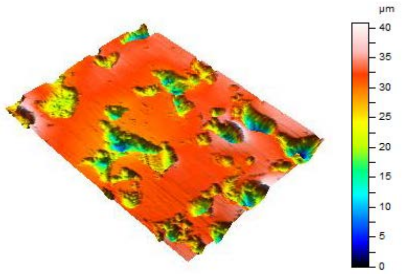

Figure 6-7: 3D pseudo-colour image of foils modified by rolling at different weld speeds and multiple passes under a weld force of 1400N.

Table 6-4: Average surface texture analysis parameters for modified foils

	Foil Measurements													
	T1		**T2**		**T3**		**T4**		**T5**		**T6**		**T7**	
	Av.	**σ**	**Av.**	**σ**	**Av.**	**σ**	**Av.**	**σ**	**Av.**	**σ**	**Av.**	**σ**	**Av.**	**σ**
S_a (μm)	1.84	0.56	2.27	0.42	3.62	0.47	2.39	0.75	1.34	0.20	3.31	0.97	3.69	0.25
S_q (μm)	3.65	0.97	3.68	0.46	5.12	0.61	3.84	1.39	3.16	0.61	5.20	1.29	5.27	0.22
Sku	22.26	6.43	12.66	4.86	6.26	1.29	19.49	10.11	32.47	8.35	12.92	3.78	8.57	2.37
Ssk	-3.922	0.662	-2.784	0.632	-1.634	0.317	-3.668	1.008	-4.769	0.499	-2.544	0.366	-1.994	0.296
Sds (1/mm^2)	50920	5850	48755	4554	45928	3708	45438	2407	50534	8440	47609	4827	47591	4133
Ssc (1/mm)	0.29	0.08	0.31	0.04	0.43	0.05	0.30	0.04	0.26	0.02	0.40	0.08	0.41	0.08
Sal* (μm)	126.7	14.1	111.0	22.7	136.8	30.1	127.0	10.7	112.3	20.9	138.1	11.7	123.0	9.8
Str (s = 0.2)	0.667	0.111	0.799	0.030	0.738	0.122	0.581	0.211	0.662	0.148	0.781	0.049	0.829	0.062
Vmp (μm^3/μm^2)**	0.086	0.050	0.078	0.036	0.154	0.043	0.044	0.022	0.044	0.036	0.154	0.030	0.130	0.005
Vmc (μm^3/μm^2)**	0.94	0.41	1.33	0.53	3.60	0.69	1.21	0.36	0.76	0.12	2.67	1.06	3.64	0.61
Vvc (μm^3/μm^2)**	1.37	0.65	1.52	0.35	3.46	0.81	1.42	0.56	1.03	0.40	2.89	0.73	3.42	0.35
Vvv (μm^3/μm^2)**	0.885	0.242	1.052	0.169	1.173	0.176	1.177	0.378	0.629	0.092	1.286	0.335	1.197	0.070
Sdr (%)	4.82	0.95	6.57	0.63	9.33	0.64	6.31	1.69	4.28	0.30	7.94	1.97	9.87	2.00

** s = 0.2*

***p = 10%, q =80%*

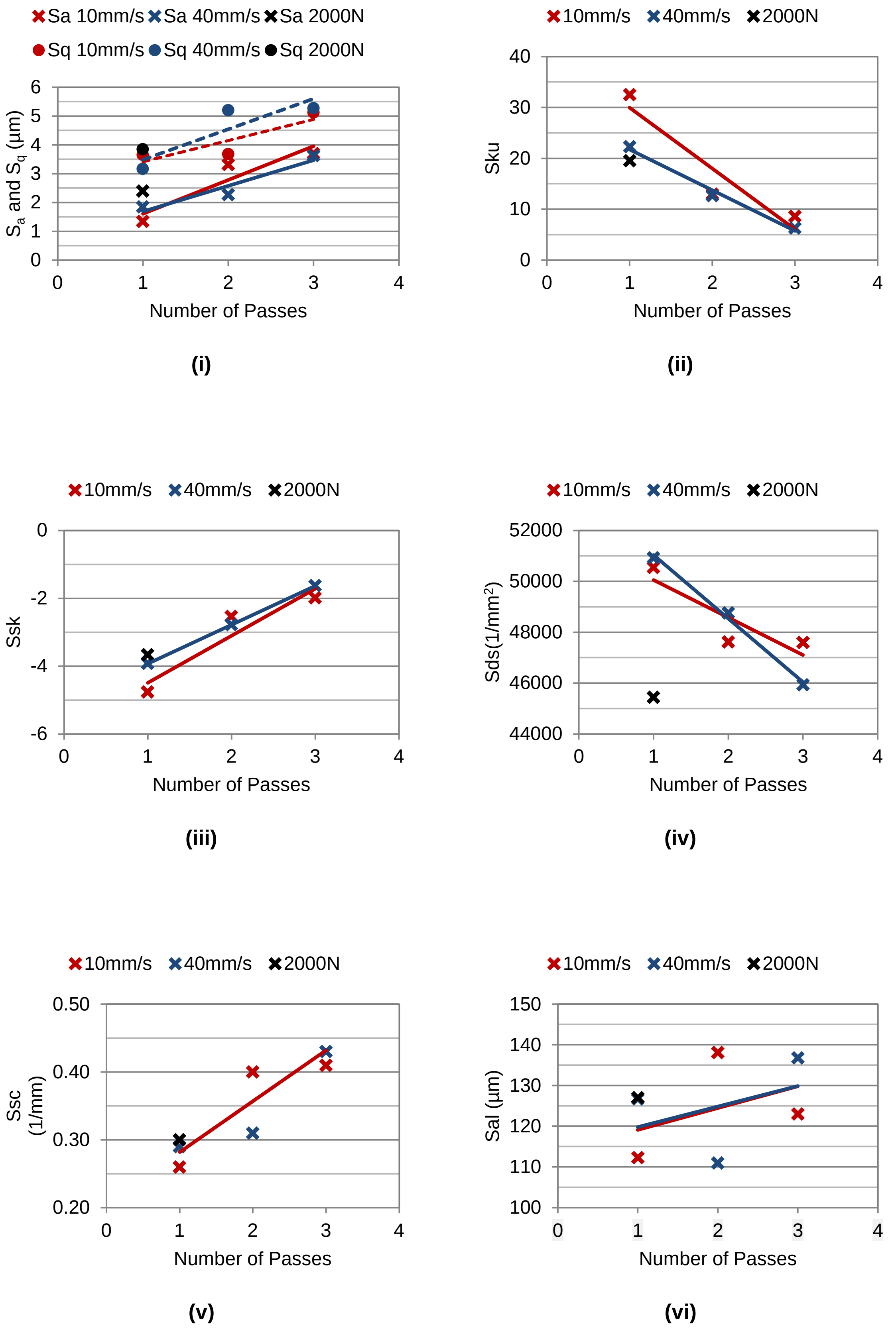

Figure 6-8: Graph to show trends in S_a and S_q (i), Sku (ii), Ssk (iii), Sds (iv), Ssc (v), and Sal (vi) values for modified foils based on their processing conditions.

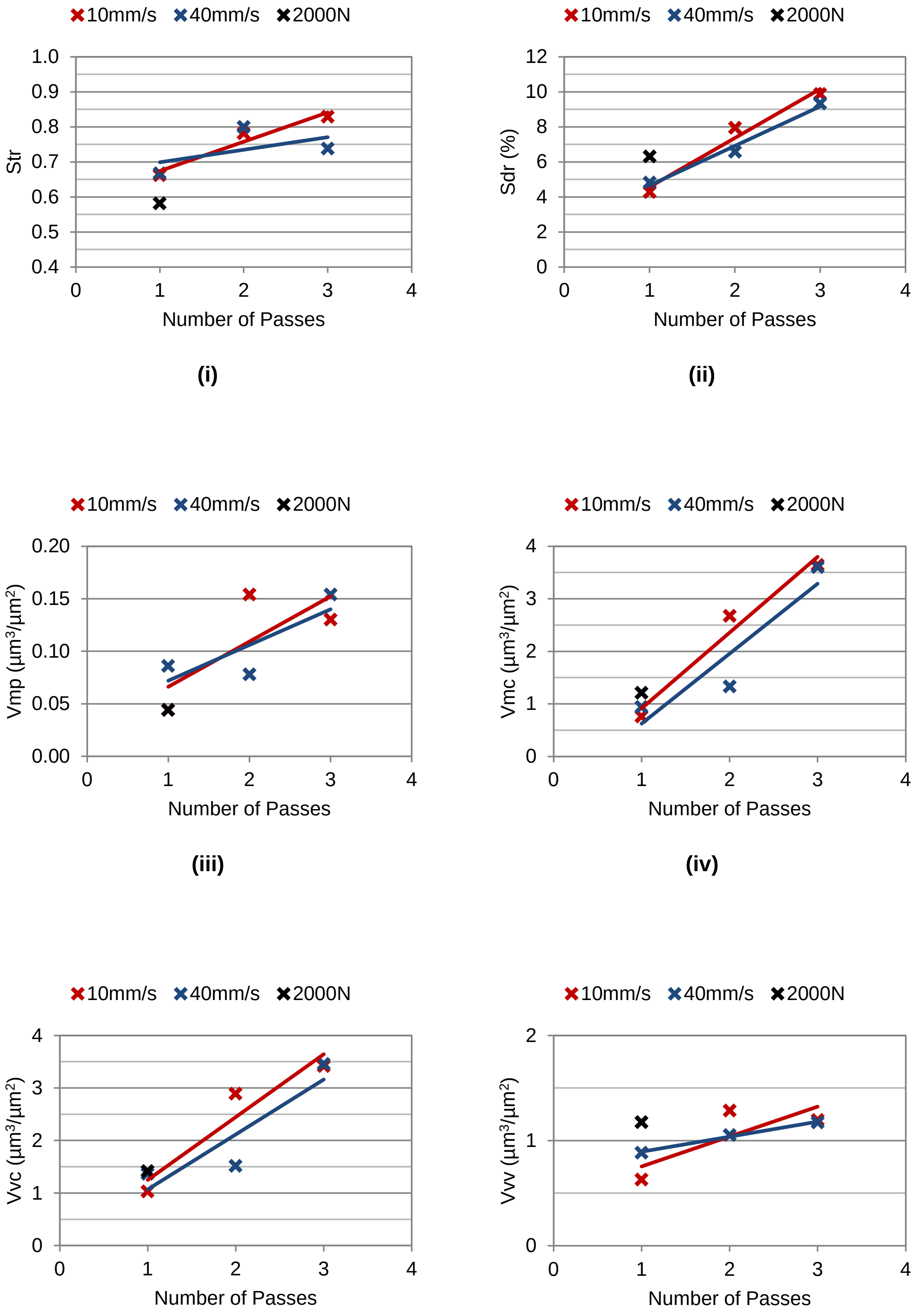

(i) **(ii)**

(iii) **(iv)**

(v) **(vi)**

Figure 6-9: Graph to show trends in str (i), sdr (ii), Vmp (iii), Vmc (iv), Vvc (v) and Vvv (vi) values for modified foils based on their processing conditions.

6.2.2 Modified Foil Sample Surface Texture Characterisation

Table 6-5: Average surface texture analysis parameters for modified foil samples

Surface Texture Parameters	Sample Measurements															
	Sample B / T0		T1		T2		T3		T4		T5		T6		T7	
	Av.	σ	Av.	σ	Av.	σ	Av.	σ	Av.	Av.	σ	σ	Av.	σ	Av.	σ
S_a (μm)	12.80	0.74	11.59	1.00	11.41	1.81	10.83	1.55	11.58	11.51	1.45	0.90	11.53	0.88	11.51	1.45
S_q (μm)	16.59	1.30	15.04	1.18	14.81	2.05	14.06	1.85	14.93	14.79	1.60	1.13	14.91	1.11	14.79	1.60
Sku	3.73	1.19	3.51	0.43	3.71	0.49	3.65	0.83	3.53	3.39	0.31	0.47	3.58	0.52	3.39	0.31
Ssk	0.250	0.520	-0.004	0.304	-0.081	0.350	-0.103	0.232	-0.024	0.068	0.274	0.313	0.020	0.232	0.068	0.274
Sds (1/mm^2)	35055	1207	36556	1362	36405	1413	36262	1409	35785	36221	1375	1361	36021	1592	36221	1375
Ssc (1/mm)	0.71	0.023	0.72	0.04	0.70	0.03	0.69	0.03	0.69	0.72	0.02	0.03	0.71	0.03	0.72	0.02
Str (s = 0.2)	0.720	0.155	0.730	0.143	0.700	0.147	0.786	0.123	0.794	0.770	0.096	0.161	0.735	0.104	0.770	0.096
Sal* (μm)	159.4	16.8	148.1	17.2	146.8	12.6	153.8	13.7	148.6	141.8	11.6	13.74	152.33	26.39	141.8	11.6
Vmp (μm^3/μm^2)**	1.000	0.421	0.860	0.114	0.818	0.212	0.787	0.120	0.813	0.819	0.078	0.095	0.878	0.134	0.819	0.078
Vmc (μm^3/μm^2)**	14.28	0.66	12.92	1.18	12.84	1.89	12.27	2.06	13.29	13.00	1.59	1.06	12.94	1.10	13.00	1.59
Vvc (μm^3/μm^2)**	20.13	2.12	17.45	1.47	17.27	3.48	16.13	2.39	17.53	17.68	2.38	2.24	17.23	1.92	17.68	2.38
Vvv (μm^3/μm^2)**	1.780	0.292	1.867	0.379	1.795	0.243	1.756	0.223	1.753	1.731	0.273	0.322	1.778	0.272	1.731	0.273
Sdr (%)	32.05	5.72	32.99	3.07	32.97	3.98	29.29	2.72	32.81	33.35	3.15	3.13	31.96	3.90	33.35	3.15

** s = 0.2*
***p = 10%, q =80%*

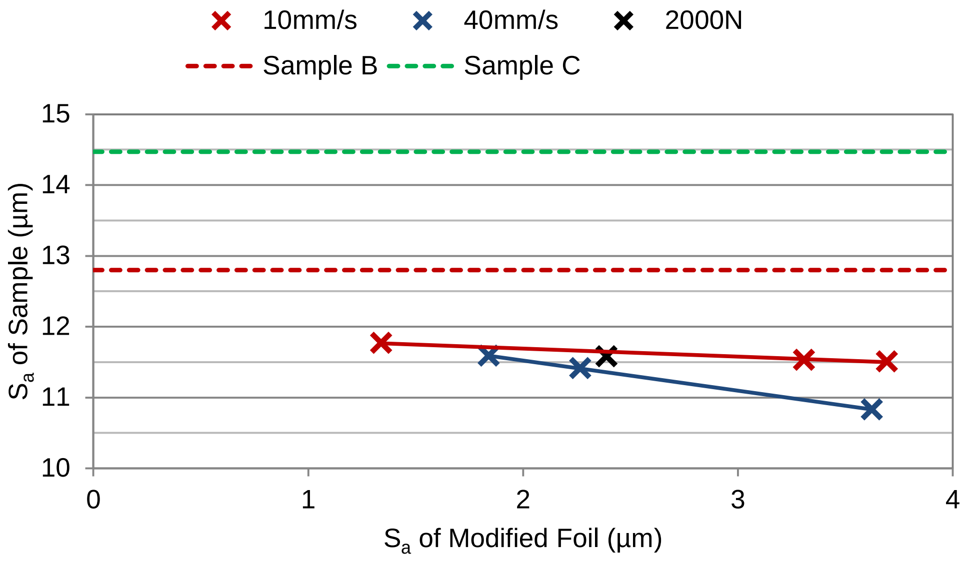

Figure 6-10: Graph to show S_a of the samples fabricated using modified foils under different foil modification processing conditions (the S_a of unmodified sample B and C from the previous chapter are shown for comparison).

6.2.3 Modified Foil Sample Bond Strength Measurement and Failure Mode Characterisation

Table 6-6: Average maximum peeling load for modified foil samples, T1-7, compared with the unmodified sample B, T0.

Foil Sample Number	Weld Speed (mm/s)	Weld Force (N)	Number of Passes	Maximum Peeling Load (N)	
				$\bar{x}$	σ
B / T0	-	-	-	85.47	13.2
T1	40	1400	1	85.67	2.64
T2	40	1400	2	89.43	0.86
T3	40	1400	3	92.44	10.17
T4	40	2000	1	88.83	4.71
T5	10	1400	1	88.62	2.67
T6	10	1400	2	95.88	14.12
T7	10	1400	3	93.87	4.93

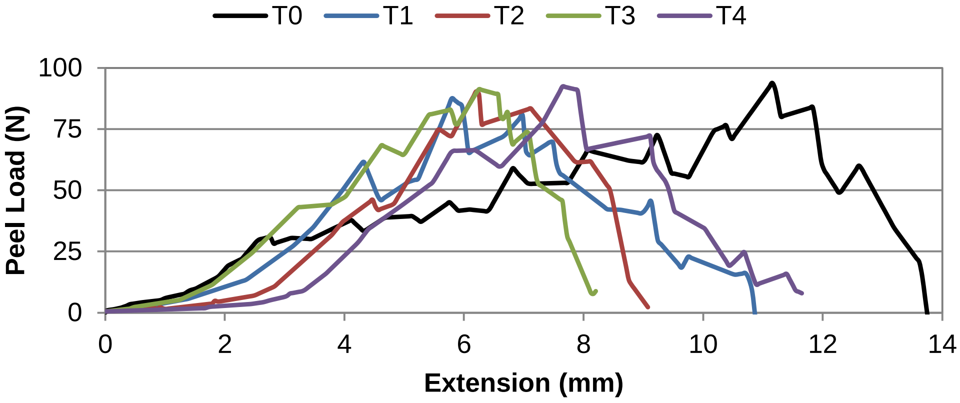

(i)

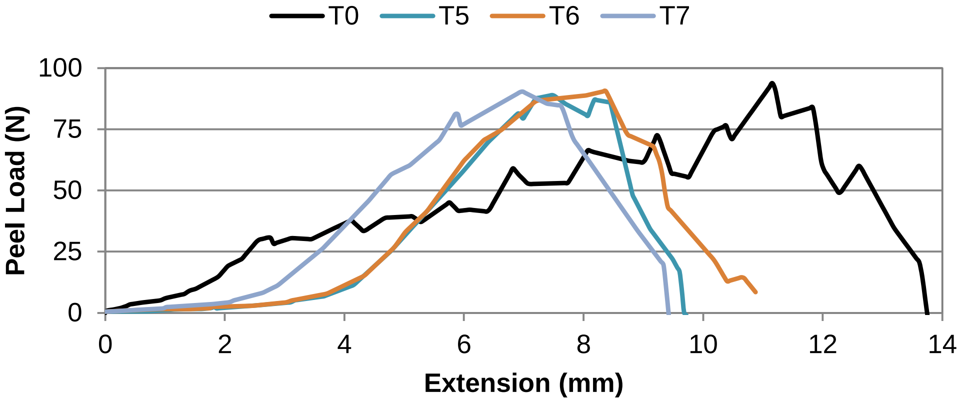

(ii)

Figure 6-11: Characteristic peeling load-extension graph for foil samples modified at a weld speed of 40mm/s (i) and 10mm/s (ii) compared with the unmodified sample B, T0.

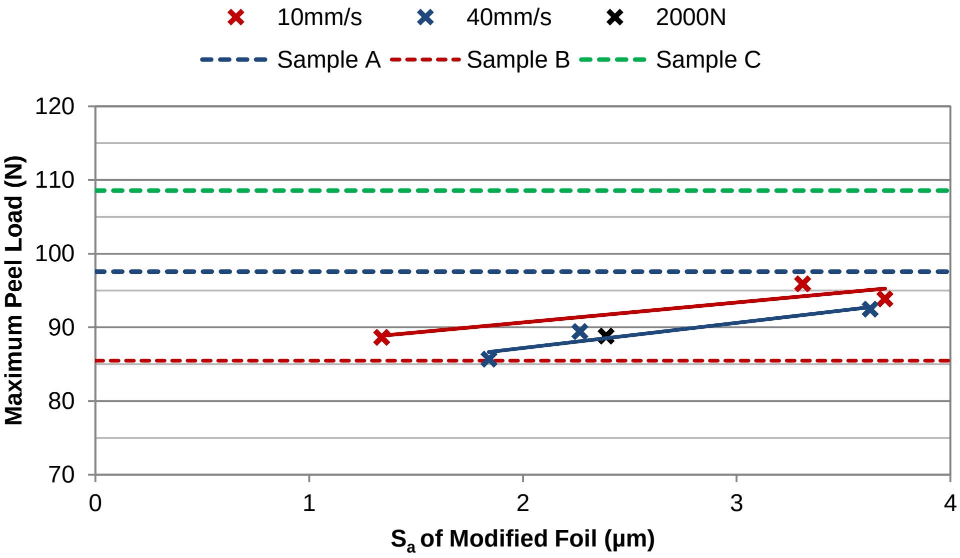

Figure 6-12: Graph to show the maximum peeling load for foil modified samples based on the S_a of the pre-textured foil (the maximum peeling load of unmodified samples A, B and C from the previous chapter are shown for comparison).

6.2.4 Microstructural Characterisation of Modified Foil Sample Interlaminar Interface

Table 6-7: Average LWD for modified foil samples, T1-7, compared with the unmodified sample B, T0.

Foil Sample Number	Weld Speed (mm/s)	Weld Force (N)	Number of Passes	LWD (%)	
				$\bar{x}$	σ
B /T0	-	-	-	79.4	3.7
T1	40	1400	1	62.1	18.5
T2	40	1400	2	54.6	3.9
T3	40	1400	3	55.9	9.1
T4	40	2000	1	46.6	9.3
T5	10	1400	1	54.4	8.8
T6	10	1400	2	75.3	5.9
T7	10	1400	3	60.3	16.7

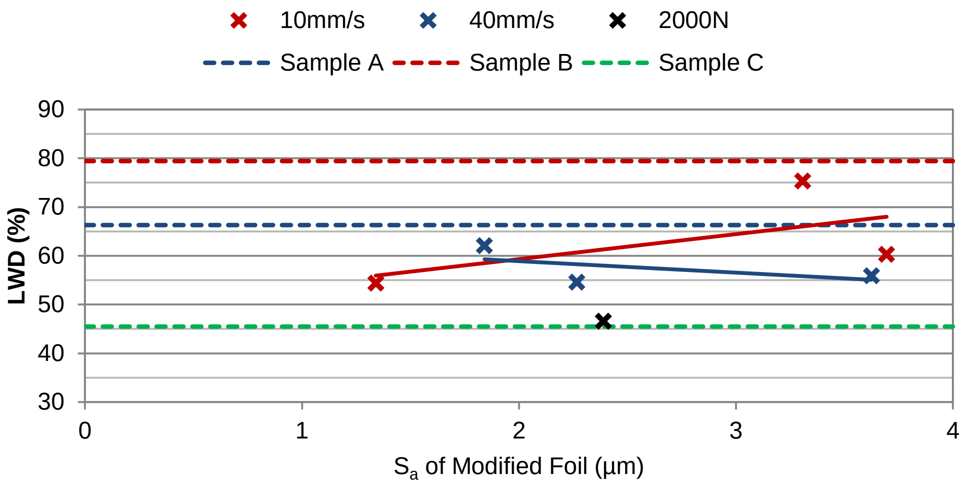

Figure 6-13: Graph to show the LWD for foil modified samples based on the S_a of the pre-textured foil (the LWD of unmodified samples A, B and C from the previous chapter are shown for comparison).

6.3 Discussion

6.3.1 The Effect of Foil Surface Modification on Foil Surface Texture

The surface texture of the stock Al3003-H18 foil was formed through contact with rolling stands during the final rolling procedure (Plouraboue & Boehm 1999). The stock foil (Figure 6-6, T0) appears to be composed of a series of very low amplitude ridges, aligned in the original rolling direction with a S_a of 0.16µm.

The fine ridges from the plain stock foil could still be seen in the areas of unprocessed foil in modified foils T1-7 after texturing with the sonotrode (Figure 6-6, T4, and Figure 6-7). The surface of the foil T1, modified using a single pass at a weld speed of 40mm/s, was composed of irregular shaped cavities at a range of depths. These surface features were formed through contact with the sonotrode surface, where the sonotrode peaks had plastically deformed areas of the original foil surface. As the number of modification passes applied increased, T2 and T3, the frequency of these surface features increased and the spacing between them decreased, reducing the surface area of the foil that remained flat and unprocessed. Foil samples modified by the sonotrode at a slower weld speed of 10mm/s, T5-7, showed similar surface properties. Modifying the foils at 40mm/s using an increased weld force of 2000N, T4, appeared to result in a surface composed of deeper cavities. The increased pressure applied by individual surface peaks in contact with the foil during processing resulted in a higher degree of plastic deformation as the sonotrode surface texture penetrated deeper into the foil surface (Figure 5-26).

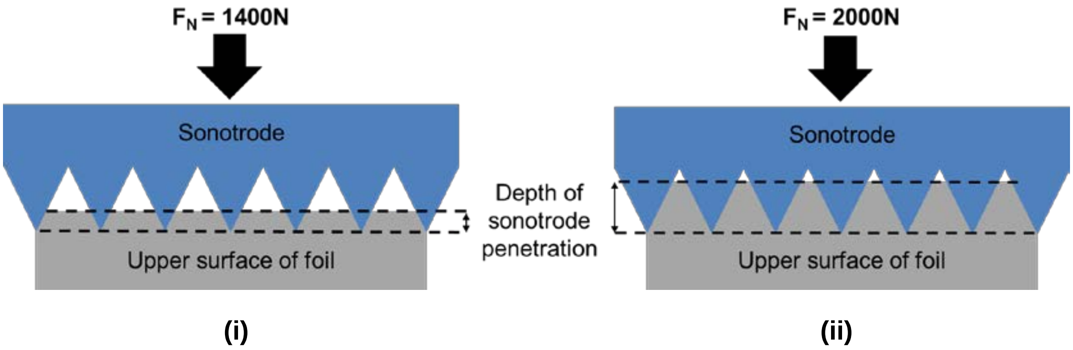

Figure 6-14: Diagram illustrating the difference in sonotrode penetration depth for foil modified at 1400N (i) and 2000N (ii).

In order to quantify the effects of the different foil modification techniques of weld speed, weld force and number of passes applied to foils prior to UC the surface texture analysis parameters for modified foils were measured (Table 6-4).

Both the S_a and S_q of the modified foils increased as the number of sonotrode passes increased (Figure 6-8i). Similar increases in surface roughness were observed when the foils were processed at both weld speeds. The increase measured S_a was thought to be the result of an increased number of surface voids. An increase in the applied weld force corresponded to a further small increase in the roughness of the foils as the depth of the cavities imparted into the foil increased. The S_a and S_q values of all the modified foils, S_a = 1.34 to 3.69µm and S_q = 3.16 to 5.27µm, were significantly less than the values measured across the weld surface of sonotrode B and the sample B / T0 in the previous chapters.

The degree of Sku of the modified foils decreased as the number of sonotrode passes increased (Figure 6-8ii). A high Sku value indicates extreme surface features, in this case deep troughs. An increase in the number of sonotrode passes resulted in an increased in the number of these deep surface cavities and hence the surface features appeared less extreme. The affect of the weld speed and weld force at which the foils were processed on did not appear to have a significant on Sku. As the number passes increased to three the Sku of the foils, 6.26 at 40mm/s, began to approach the Sku value of the parent sonotrode B, 3.06, and sample B/ T0, 3.73.

All the modified foils exhibited negative Ssk, ranging from -1.63 to -4.77. The degree of negative Ssk decreased as the number of sonotrode passes increased (Figure 6-8iii). At first this appeared counter-intuitive as the surface did not appear to become less dominated by valleys, as the number of surface deformation features increased. However it was considered that the material could have deformed as a result of contact with the sonotrode and was displaced, hence a degree of bulging in the surface material adjacent to areas of deformation experienced a decrease in the extent of negative skew (Figure 6-15). It is also important to remember that the value of Ssk is calculated by measuring deviations from the S_q and, as we have already seen, this S_q value increases as the number of passes increases and hence a decreased degree of variation from this value is reported. The modified foils are negatively skewed, similar to sonotrode B, Ssk = -0.25, and opposite to sample B / T0, Ssk = 0.25.

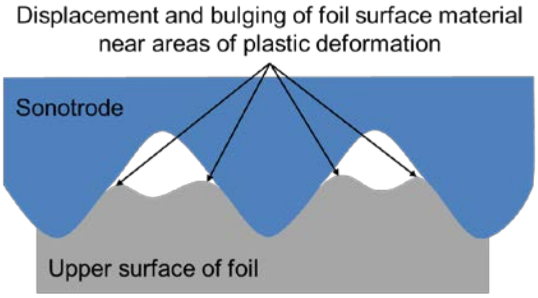

Figure 6-15: Diagram illustrating the decrease in negative Ssk due to material displacement.

The density of summits, Sds, of the modified foils ranges from 45438 to 50920 1/mm^2 and are significantly higher than the values measured for sonotrode B, 38046 1/mm^2, and sample B / T0, 35055 1/mm^2. In this case the segmentation used to define individual summits measures the density of the small amplitude ridges of the unprocessed stock foil; hence a very large measurement density was calculated. The density of these numerous summits decreased as the number of passes and applied weld force used during modification increased (Figure 6-7iv). The decrease in density corresponded to the increase in number of individual surface cavities where the foil had been deformed.

The Ssc values, which range from 0.26 to 0.43 1/mm across the modified foils, were significantly lower than the Ssc of sonotrode B and sample B / T0, 1.13 and 0.71 1/mm respectively. The Ssc of the modified foils were less curved as the majority of their surface was composed of flat unprocessed material, unlike the distinct peaks seen in sonotrode and UC samples surfaces. The Ssc of modified foils increased as the number of passes applied increased; the effect of applied weld force and processing weld speed appeared to be negligible (Figure 6-7v). The increase could have been the result of the higher level of deformation, where an increasing degree of curvature and bulging across the foil surface was introduced where material was displaced as a result of the plastic deformation and protruded from the area adjacent to the deformation location.

The Sal of the modified foils ranged from 111.0 to 138.1µm and the length increased as the number of passes applied increased (Figure 6-8f). It should be noted that the measurements themselves were very distributed, with standard deviations of up to 30.1µm in one case, but a general trend was still evident. As with the values of Ssk these results initially appeared counter-intuitive as the spacing of the surface features did not decrease as the degree of surface deformation increased. Once again it was important to recall how the Sal was calculated; the threshold value by which the distance between statistically different areas of the surface were calculated was based on the surface peaks, irrespective of the valley components. It was previously noted that the increased degree of plastic deformation was accompanied by an increase in the material displaced and extruded from the cavities around a given deformation location and that the frequency of these surface protuberances increased.

The modified foils exhibited a range of Str values, ranging from 0.58 to 0.83, with some foil samples exhibiting similar ratios to that of sonotrode B and sample B / T0, 0.80 and 0.72 respectively. The degree of isotropy increased as the number of sonotrode passes increased (Figure 6-9i), irrespective of weld speed. A higher degree of directionality appeared in surface of foils modified with a single pass, indicating the same degree of directionality in the higher amplitude peaks of sonotrode B used for processing. The random nature of the distribution of peak/foil interaction and surface deformation experienced during multiple passes increased the isotropy of the surface texture of modified foils. An increase in the applied weld force appeared to reduce the level of isotropy within modified foils. The sonotrode surface peaks penetrated deeper into the surface of the foil during processing, causing an increase in the number of lower amplitude peaks in contact with the foil at a higher weld force and therefore decreasing the degree of directionality evident in those higher amplitude peaks (Figure 6-16).

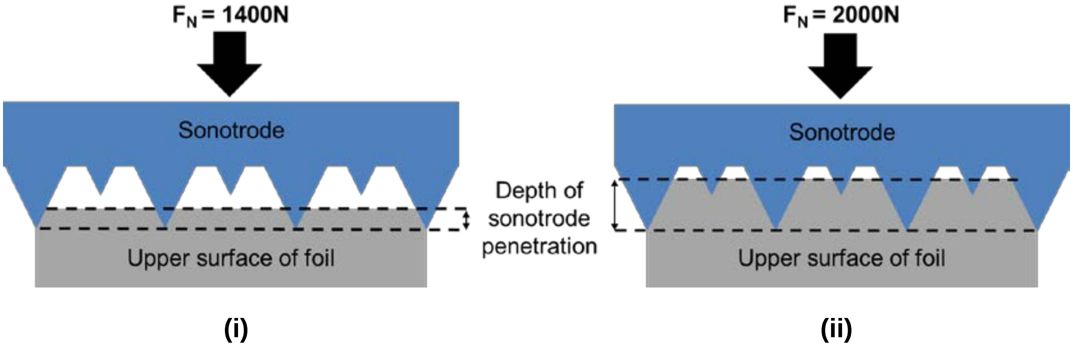

Figure 6-16: Diagram illustrating the increasing number of low amplitude sonotrode surface peaks that come into contact with the foil surface under increasing normal force from 1400N (i) to 2000N (ii).

The Sdr of modified foils increased as the applied weld force and number of passes increased, irrespective of weld speed. While nowhere near the Sdr of sonotrode B, 120.6%, and sample B / T0, 32.1%, the range in Sdr of the foils was between 3.8 and 9.6%. The change in the nature of the foil, as a result of sonotrode interaction, was primarily to deform the flat surface. A number of voids were produced as a result of the plastic deformation of the material under the application of the sonotrode surface peaks. Unlike UC, by rolling the foils with the sonotrode without the influence of ultrasonic oscillation, there was a minimal increase in the peak properties of the foil surface and the material did not sufficiently deform the foil material to fill the sonotrode surface cavities in the absence of the surface, volume and Bauchinger effects. A higher degree of surface deformation, deeper surface voids in the case of higher weld force and a higher frequency of voids in the case of multiple passes, from the original foil surface correlated with the observed increase in the developed interfacial ratio of the modified foils.

The Vmp of the modified foils increased as the number of passes increased; weld speed and weld force did not appear to have any significant effect on the relationship (Figure 6-9iii). The increased degree of plastic deformation across samples exposed to multiple passes resulted in a small increase in the material displaced and extruded from the cavity around the deformation locations which correlated to the small increase in Vmp seen in the results. It should also be noted that the peak material volume was determined as the volume of material contained by the top 10% of the surface and is a method of comparing samples of the same average roughness. In this case, however, there is a distinct increase in the total height and hence volume of material which is examined to produce this measurement. As the average feature height increased the volume of material contained within this upper 10% of material would have also increased. The foil peak material volume of the modified foils ranged from 0.04 to 0.15$\mu m^3/\mu m^2$, all significantly lower than sample B / T0 , 1.00$\mu m^3/\mu m^2$. The Vmc of the modified foils increased from 0.76 to 3.64 $\mu m^3/\mu m^2$ as the number of passes increased; over time the Vvc was also seen to increase by a similar extent, from 1.03 to 3.46$\mu m^3/\mu m^2$ (Figure 6-9iv-v). The equivalent increase in material and volume parameters was in line with the previous statement that as the depth of the foil samples increased, due to additional plastic deformation from multiple passes, the volume of material which was examined to produce the volume parameter also increased, thereby increasing the magnitude of the measurements. The Vvv increased as the number of sonotrode passes increased (Figure 6-9vi). The Vvv of modified foils also increased when processed at a higher weld force. The additional passes and higher weld pressure equated to an increase in the overall void volume, where increased void depth and frequency through an increase in the total plastic deformation of the foil surface.

The reduction in these volume parameters, and the majority of other surface texture parameters, compared to the larger volume parameters recorded in the previous chapter by UC-processed sample B / T0’s surface were attributed to the absence of the surface, volume and Bauschinger effects during surface rolling and limited extrusion of the foil material into the sonotrode surface cavities during foil modification.

6.3.2 The Effect of Foil Surface Modification on Substrate Surface Texture

Surface texture measurement of the UC samples fabricated using the pre-textured foils revealed that their S_a was less than that of reference sample B / T0, fabricated using stock foil. The S_a of modified foil samples ranged from 10.33 to 11.77µm in comparison to sonotrode B, 14.79µm, and sample B / T0, 12.80µm. The reduction in surface texture transfer between sonotrode B for the standard sample B / T0 was 13.5%, while the worst case reduction in texture transfer of the modified samples was a loss of 26.9%, for sample T3 processed at 40mm/s, weld force of 1400N and three sonotrode passes. As noted in the previous chapter, incomplete surface texture transfer between the sonotrode and UC samples was attributed to limited plastic flow during contact between the sonotrode and upper foil surface during consolidation. Insufficient plastic deformation of the foil material and incomplete filling of the sonotrode surface cavities resulted in flat areas of unprocessed foil surface, apparently untouched by the sonotrode surface. The observed reduction in plastic deformation of pre-textured foils could be attributed to the fact that these foils have already been work hardened during the foil modification process. The pre-textured foils were already plastically deformed prior to consolidation and therefore were more resistant to plastic deformation during consolidation than the unmodified stock foil used to fabricate T0 / sample B.

Smaller variation in the extent to which surface texture was transferred to the upper surface of the modified foils after consolidation was also apparent in the results. The sample surface texture decreased as the modified foil surface texture increased (Figure 6-10). This appeared to be related to the extent of plastic deformation during foil modification, where multiple passes and processing at lower weld speeds caused an increase in the degree of work hardening of the foil and hence a higher resistance to further deformation through contact with the sonotrode and a reduction in sample S_a after consolidation.

It was important to note that the standard deviation of foil modified sample S_a measurements were quite substantial, between 0.88 and 1.81µm, however a strong correlation to the general trend in all the results was observed.

Other than S_a, the other measured surface texture parameters exhibited characteristics similar to the unmodified sample B / T0.

6.3.3 The Effect of Foil Surface Modification on Substrate Bond Strength

Preliminary analysis of the characteristic peeling load-extension graph for foil modified UC samples (Figure 6-11) revealed a similar magnitude maximum peel strengths across all the samples. The characteristic peel profiles of foils pre-processed at a weld speed of 40mm/s,T1-4, (Figure 6-11i) were composed of numerous, distinct sub-peaks like those seen in sample B / T0, while samples prepared at 10mm/s, T5-7, (Figure 6-11ii) exhibited a smoother extension profile more reminiscent of sample C from the previous chapter.

The range of peel loads ranged from 85.67N for sample T1, processed at 40mm/s under a weld force of 1400N and one sonotrode passes, to 95.88N for sample T6, processed at 10mm/s with weld force of 1400N and two sonotrode passes (Table 6-6). The average maximum peel load of all the pre-textured foil samples were slightly higher than the unmodified sample B / T0, samples T1,2, 4 and 5 were within 5N, while samples T3, 6 and 7 had peel strengths approaching the higher peel strength of sample A from the previous chapter (Figure 6-12).

The maximum peel load of the modified samples increased as the S_a of the pre-textured foil used in their fabrication increased. The previous discussion section proposed that modified foil S_a was proportional to the degree of plastic deformation and work hardening experienced by the foil during texturing, therefore it could be concluded that samples whose foils have undergone the most pre-process deformation demonstrated a higher resistance to peeling after consolidation. The foils modified at lower weld speeds, higher weld force and an increasing number of sonotrode passes exhibited higher peel strengths than those processed at higher weld speeds, lower weld forces and with a lower number of sonotrode passes.

It could be theorised that contact between the rougher surfaces of the modified foil surfaces would have generated greater dynamic interfacial forces at the weld interface during consolidation as a result of the surface effect. Frictional forces generated at the UC weld interface are dependent on two factors; adhesion and deformation. The deformation force is the force required to “plow” a path across the surface of the softer materials by the asperities on the harder surface (Bowden & Tabor, 1974)(Moore, 1975).

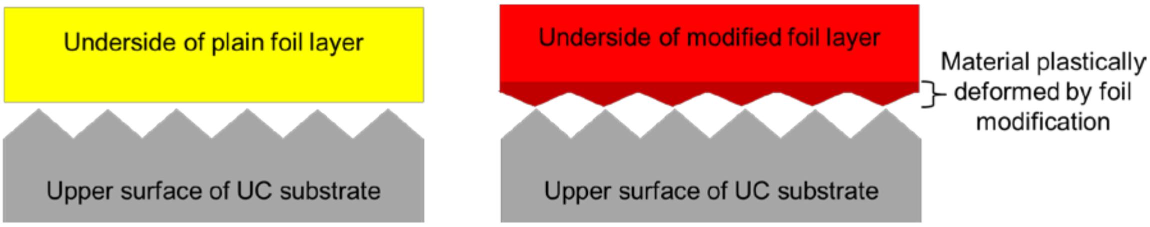

(i) **(ii)**

Figure 6-17: Diagram illustrating contact between upper surface of UC substrate and the underside of the plain (i) and modified foil layer (ii).

During consolidation of standard UC samples, such as sample B / T0 (Figure 6-17i), there was a difference in hardness between the upper surface of the substrate, whose surface had been work hardened through contact with sonotrode surface, and the underside of the stock Al3003-H18 foil. The increased surface hardness of the modified foils (Figure 6-17ii) would have reduced the difference in hardness between the two foils surfaces and hence increased the deformation and frictional forces generated during the fabrication of foil modified UC samples. The increase in thermal energy generated as a result of the increased friction could have increased the amount of plastic flow at the interface, facilitating the breakup of the surface oxide layers and bringing the surfaces into intimate contact to achieve bonding.

In the previous chapter the higher peel strength of sample C, despite its low LWD, was attributed to the higher level of plastic deformation from contact with sonotrode C. The increase in surface deformation meant that even though the area of contact was lower the strength of individual contact points was high enough to increase the overall resistance to peeling. The additional plastic deformation of foils through pre-consolidation modification might also have accounted for their increased maximum peel load. The similarity in the peel-extension characteristics of samples fabricated from foils modified at 10mm/s T5-7, subject to a higher degree of deformation while processed at lower speeds, to sample C added weight to the proposition (Figure 6-18).

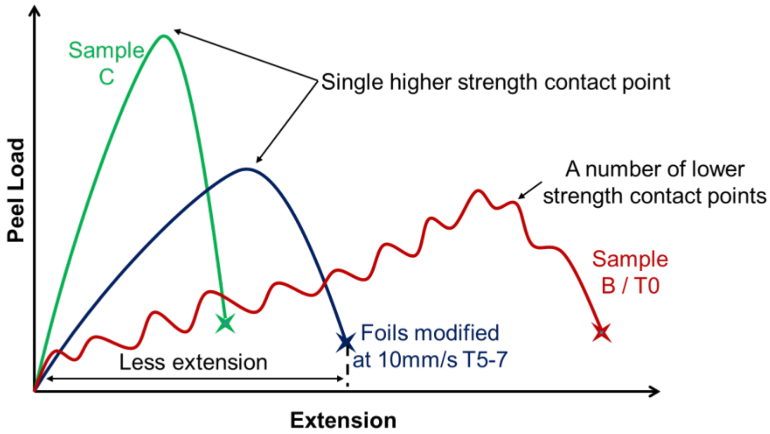

Figure 6-18: Graph illustrating similarities in peeling load-extension characteristics of UC samples made from foils modified at lower speeds and the reference samples from sonotrode B (T0) and C.

The foil surface microstructure characterisation discussion in the previous chapter identified the fact that contact with the sonotrode sometimes appeared to result in the encapsulation of surface oxides and voids below the substrate surface. It is possible that this may have also occurred along the surface of the foils during the modification process. The introduction of further encapsulated voids and surface could have inhibited bonding, reducing the weld density and potentially adversely effecting the mechanical properties of the resulting parts. However, the phenomenon did not appear to have adversely effected the sample bond strength in comparison with the standard sample B / T0 in this case.

6.3.4 The Effect of Foil Surface Modification on the Microstructure of the Substrate Interlaminar Interface

All the foil modified samples exhibited a lower LWD than the baseline sample B / T0 and higher LWD than unmodified sample C (Figure 6-13). The lowest recorded pre-textured sample LWD measurement was 46.6% from sample T4, modified using a weld speed of 40mm/s, weld force of 2000N and one sonotrode pass. Foil T4 was processed at a higher weld force than the other foils and it appeared that the higher level of localised deformation was less easily recovered than the more distributed deformation imparted through multiple sonotrode passes at lower weld forces. The level of plastic flow between the mating surfaces, promoted by surface, volume and Bauschinger effects during UC, was insufficient to fill the sonotrode induced interlaminar voids.

A small reduction in the LWD of foil modified samples processed at 40mm/s was seen as the average foil S_a increases. As the roughness of the foil increased the degree of plastic deformation required to fill the surface voids of that foil surface and bring the two foils into complete contact during consolidation also increased. It may be the case that an increase in work hardening corresponded to the increased amplitude of surface valleys and peaks as a result of the higher level of plastic deformation. Consequently the degree of interlaminar plastic flow generated during the UC process became increasingly insufficient to fill the interlaminar voids and hence a reduction in LWD was observed.

In contrast to the samples modified at higher weld speeds, an increase in the LWD of foil modified samples processed at 10mm/s was seen as the S_a of the foil surface increased. While the foil S_a increased in line with the level of plastic deformation and work hardening for samples processed at lower speeds, in this instance the level of plastic flow generated during the UC process appeared to increasingly fill the interlaminar voids, improving the LWD of samples. A potential explanation for the change in relationship between S_a and LWD was that foils modified at lower weld speeds were subject to additional plastic deformation, where the longer dwell time increased the amount of work hardening within the foil surface material. The increased relative hardness of mating surfaces, along with the higher average S_a, caused an increased resistance to interfacial motion, thereby increasing the amount of heat generated as a result of friction at the interface. This additional thermal energy generated could have increased the level of plastic flow generated at the weld interface, increasing the LWD measurements.

6.4 Summary Review

The aim of this chapter was to fulfil the outstanding Research Factors. The focus of research Factor V was to investigate a texturing method that can be applied to unprocessed foils used in the manufacture of UC samples. This was achieved by rolling sonotrode B over the stock foil without the ultrasonics engaged, thereby plastically deforming the surface. A range of modified foil surface textures were achieved by rolling the foils at two different weld speeds and weld forces and applying a number of sonotrode passes. The nature of the modified foil surface texture was measured by white light interferometry and characterised through a number of surface texture parameters.

While the original intention was to texture the surface of the foil with an equal and opposite version of the UC sample surface texture the foil surface texture, the modification process was unable to achieve sufficiently rough surfaces to mimic the surface texture sample B using this method. The discovery highlighted the influence of the surface, volume and Bauschinger effects generated by friction and ultrasonic oscillations during UC and the fact that they appeared to increase the level of plastic deformation at the foil surface as well as the weld interface during consolidation.

The amplitude and distribution of surface features increased as the number of sonotrode passes applied increased and an increase in void depth was seen in samples processed at a higher weld force. The modification weld speed did not appear to have a considerable effect on the surface texture of the foils. In all cases some areas of the foil surface remained unprocessed after the modification procedure and a small increase in peak material occurred around deformation locations as a result of displaced material.

The purpose of Research Factor VI was to evaluate the extent to which pre-textured foils affect interlaminar bond strength and microstructure in UC. This was measured by changes in resistance to peeling and LWD measurements of samples fabricated using the modified foils.

Foil modification weld speed appeared to have the most significant effect on interlaminar bonding. UC samples fabricated using foils processed at lower weld speeds exhibited a greater resistance to peeling and an increased linear weld density compared to those made using foils modified at higher weld speeds. This relationship was thought to be a result of the increased level of microstructural deformation and work hardening experienced by the foils processed at lower speeds.

The number of sonotrode passes applied during foil modification was also seen to affect UC sample properties. Applying additional passes increased the deformation area and hence the amount of work hardening of the foil surface was thought to increase, which accounts for the recorded higher peel strengths of samples made with these foils. The effect of additional sonotrode passes on LWD was dependent on the sonotrode weld speed and the relationship appears to be effected by the work hardening and frictional forces generated at the weld interface.

Foils modified at a higher weld force resulted in a slight increase in peel load and a large reduction in LWD. The higher level of localised plastic deformation appeared to offer an increased resistance to peeling but the plastic deformation during consolidation was insufficient to fill the sonotrode induce surface voids. These findings were similar to the results seen in sample C in the previous chapter.

The findings show that the level of plastic deformation, and the assumption of associated work hardening, of modified foils prior to consolidation was crucial to the bonding process in UC, echoing the importance of this factor identified in the previous chapter.

The aim of this chapter was to test the final Research Objective that modifying the surface texture of stock foil prior to manufacture can be used to modify interlaminar bonding in UC and the results and discussion of the experimentation detailed within this chapter have fully supported this proposition.

7 Conclusions

The purpose of the investigation was to test the proposed Research Objectives (Chapter 3). Within this chapter, conclusions drawn from the research are presented in the context of the aspects of the Objectives that they addressed.

The first Research Objective was *“to establish if the extent to which the sonotrode weld surface texture is imparted onto to the substrate surface during UC is dependent upon the operating parameters*”. This objective was researched in Chapter 4.

A significant expansion of the existing body of knowledge was achieved through a systematic analysis of the S_a transfer between the sonotrode and the UC substrate surface over a range of different operating conditions. The independent effects of some operating parameters had previously been investigated over a smaller range in other research (Johnson, 2008) (Friel et al. 2010) (Kulakov & Rack, 2010), but the more comprehensive findings of this investigation can be used to substantiate and expand upon the aforementioned work.

Through statistical analysis, sonotrode weld surface S_a was identified as the most significant factor in determining the resulting substrate surface S_a in UC. Sonotrode oscillation amplitude and weld speed also appeared to be statistically significant, while the impact of variations in weld force did not appear to have a measurable effect within the examined range. The degree of plastic deformation required to ensure a complete imprint of the sonotrode weld surface texture emerged as a key factor for S_a transfer in UC.

No published research has previously considered the impact of sonotrode surface texture beyond S_a. The extensive comparison between sonotrode and UC substrate surface texture undertaken in the course of this research has uniquely revealed the extent to which sonotrode surface texture characteristics are transferred to the samples they produce. The relationship was identified through the careful selection and analysis of a number of surface texture parameters (S_a, S_q, Ssk, Sku, Sds, Ssc, Str, Sal, Std, Vmp, Vmc, Vvc, Vvv, Sdr).

The results have shown that UC substrate surface texture can be manipulated through carefully variation of operating conditions, most notably sonotrode weld surface texture.

In order to quantify the effect of the established sonotrode texture transfer, the second Research Objective was “*to investigate how interlaminar microstructure and bond strength in UC is dependent upon sonotrode weld surface texture*”. The results from Chapter 4 and

5 identified the complex relationship between sonotrode weld surface texture parameters and interlaminar porosity, microstructure and bond strength for one set of process parameters.

It was found that the characteristic amplitude, feature spacing and kurtosis of the sonotrode weld surface texture are factors that significantly effected interlaminar porosity and bond strength in UC; increasing S_a, Sku and decreasing Sal corresponded to higher interlaminar porosity and bond strength. The results challenge the prevalent view within the UC research area that lower interlaminar porosity always corresponds with high bond strength.

Evidence of metallurgical recovery was observed along the interlaminar bond interface of the UC samples and the mechanism of recovery was attributed to the volume and / or Bauschinger effect; however the validity of either phenomenon could not be confirmed by the results of the present investigation. As a result of this research a relationship between the magnitude of recovery within the UC interlaminar microstructure and the level of foil surface plastic deformation induced by different sonotrode textures was proposed. Evidence of a lower level of recovery was observed in samples that were subject to a greater extent of sonotrode-induced deformation. This prospective relationship warrants further consideration with regards to developing the understanding of how interlaminar bonding is achieved in UC.

The investigation has shown that sonotrode weld surface texture significantly influences interlaminar porosity, bond strength and microstructure in UC and is therefore a crucial factor that should be considered in an attempt to optimise interlaminar bonding in UC. Therefore it is advised that sonotrode weld surface texture should be specified when selecting UC operational parameters in order to achieve the required level of interlaminar bond strength and that may this may need to be offset against acceptable levels of porosity for a given application.

The third and final Research Objective was "*to understand how modifying the surface texture of stock foil prior to manufacture could be used to modify interlaminar bonding in UC*". This objective was achieved by the results from Chapter 6 where different levels of foil modification were shown to affect a change in interlaminar porosity and bond strength compared to UC samples fabricated under similar conditions using unmodified stock foil.
The increase in both interlaminar bond strength and porosity as a result of different levels foil modification was attributed to an increased resistance to plastic flow at the interface. Increasing numbers of lower speed, higher force sonotrode rolling passes without the

ultrasonic engaged were associated with increased foil surface work hardening and higher levels interlaminar friction due to the predicted increased foil surface hardness were also assumed.

The results provided proof of the principle that foil surface modification effects interlaminar bonding in UC which may encourage additional investigation of this approach to optimisation of interlaminar bonding in UC. Further investigation into foil modification should consider the impact of the foil material processing prior to UC, specifically the impact of cold working.

The observed reduction in sonotrode weld surface texture transfer in foils modified by sonotrode rolling without the ultrasonics engaged, compared to UC substrate surface textures fabricated under similar process parameters, supported the theory that some softening phenomena, as a result of ultrasonic excitation, was in action during UC.

A degree of sonotrode weld surface texture degradation was evident after a relatively short period of operation (approximately 300 layers or 45m of foil consolidation). The investigation has shown the importance of regular surface texture wear monitoring with the implications with regards to the choice of sonotrode material and the method of weld surface texturing adopted. The build-up of foil material in surface cavities, particularly in the sonotrodes with lower S_a, was noted and therefore shorter service interval between chemical cleaning of weld surfaces for less rough sonotrodes should be considered.

With respect to the originally stated Research Aim, the investigation has significantly advanced the understanding of how sonotrode weld surface texture, UC substrate surface texture and foil surface texture effect interlaminar bonding in UC. The broader implications of this work from a manufacturing perspective are that more appropriate operating parameters can now be selected to produce UC parts with different properties for a range of different applications in the future.

8 Further Work

Based on the research contained within this thesis there are several areas which have been identified for further investigation. Additional work could be undertaken to further support the validity of the stated conclusions and expand the scope of the research beyond the timescale and budget limitations of the current investigation.

8.1 Examining the Effect of Sonotrode Weld Surface Texture in Different Materials

This investigation examined the effect of sonotrode weld surface texture in Al3003-H18 only and it is suggested that additional testing should be undertaken to establish if the relationships identified within this research are supported across a range of different metals. Not all metals behave identically when subject to plastic deformation and therefore the author believes it advisable to characterise the effect of sonotrode weld surface texture, in a similar manner to the work performed here, on other metals commonly used in UC.

8.2 Further Microstructural Analysis

It was noted in the FIB Analysis of Chapter 5 that the relative magnitude of UC substrate surface texture was sufficiently large that it would require significantly more FIB imaging to capture the characteristic microstructure over a larger area. It was also noted that the microstructure of only two UC sample cross-section for each sonotrode were analysed and while a relevant measurement location was selected there may be other elements which this did not capture.

Additional measurements were not made at the time due to the availability and cost of the FIB analysis procedure. It would be a valid endeavour to collect additional data to support the conclusions of the investigation. Examining oxide dispersal, grain morphology and plastic flow around the bond interface for samples fabricated at different oscillation amplitudes, weld speeds and in samples subject to foil surface modification, could support the research conclusions or reveal further undiscovered phenomena.

TEM analysis has been used to examine the interlaminar interface of UC samples in previous research (Johnson, Interlaminar subgrain refinement in ultrasonic consolidation, 2008). The same techniques could be used to validate the proposition that the observed interlaminar recovery was proportional to the level of sonotrode induced plastic deformation. It would be expected that differences in the subsurface dislocation density of samples fabricated by different sonotrode would correlate with the changes in grain morphology identified within the current investigation. However, it should be noted that there is anecdotal evidence of preparation issues in the production of TEM samples around the interlaminar interface and therefore it should be considered that the analysis technique may be inappropriate The effects of different degrees of sonotrode-induced deformation on the interlaminar microstructure could also be examined by measuring differences in stored energy and grain misorientation through electron backscatter diffraction (EBSD) techniques commonly used in metallography (Higginson & Sellars 2002).

8.3 Alternative Sonotrode Weld Surface Textures

The current investigation was successful at establishing the relationship between sonotrode weld surface texture and interlaminar bonding in UC. It is proposed that the work should be expanded to look at a wider variety of sonotrode weld surface textures.

Based on the findings of this research, the specification of sonotrode weld surface texture can be a more informed decision. Selection of sonotrode weld surface texture, based on a range of surface texture parameters, characterised by surface texture feature shape (Sku, Ssk, Ssc), spacing (Sal) as well as surface roughness (S_a), could be used in future research to further develop the understanding of the established relationship between sonotrode weld surface texture and interlaminar bonding in UC.

8.4 Foil Surface Texture Modification

Investigating the effect of foil surface texture on interlaminar bonding in UC by sonotrode rolling was useful for establishing the existence of a relationship between the two. It could also be worthwhile expanding the investigation to look at a much wider variety of interfacial textures produced by a range of surface texturing techniques and to examine their effect on UC, where optimisation could promote superior interlaminar bonding.

It is not desirable, from a commercial standpoint, to engineer the surface of each layer prior to consolidation; therefore it is also important to consider how foil texture can be achieved on a larger scale. The use of bespoke textured rolling mills during the manufacture of the stock foil, as opposed to the plain mill roll used currently, is a viable foil modification method.

8.5 Analysis of Mechanical Properties

Specification of mechanical properties of UC manufactured materials is an essential requirement to satisfy several potential commercial customers and promote the use of UC for a wider range of applications. Within the investigation the interlaminar bond strength was evaluated through interlaminar peel testing as the limitations of the Alpha 2 UC machine meant that it was complex and inefficient to fabricate standard tensile or shear strength test pieces for mechanical property analysis. Investigating the effect of sonotrode weld surface texture on interlaminar bonding through conventional testing of UC samples could be achieved by repeating some of the research using commercial UC production equipment.

8.6 Non-Destructive Interlaminar Bonding Analysis

The extent to which the current method of examining the interlaminar porosity, LWD, is reliable has been discussed within the current investigation. Accurate LWD measurement is dependent upon skilled preparation of microscopy samples and potentially subjective measurement techniques. The process is also heavily time-consuming, destructive, and only evaluates a small fraction of the interlaminar bond interface of a sample.

While within the scope of this investigation it was established that LWD was not proportional to bond strength, this does not mean that the measurement of interlaminar porosity is therefore redundant. The original intention of the investigation was to identify the capability of UC to produce parts which could exhibit different properties for a range of different applications. It is therefore possible that minimal interlaminar porosity might be a crucial requirement for certain applications. It is possible that interlaminar porosity is one factor which has inhibited the adoption of UC in industry.

Therefore, it is the author’s opinion that a more efficient and thorough method of assessing interlaminar contact area should be developed so that interlaminar porosity can be monitored and minimised. Establishing an alternative method of quantifying interlaminar contact area, particularly a Non-Destructive Testing (NDT) technique, would be a valid area of investigation which could be valid across all branches of UC research. X-ray microtomography (Friel 2011) and pulse-echo ultrasonic testing (Liu et al. 2008) are both potentially promising NDT methods which could be used to determine the area of contact at the bonding interface.

References

Arsenlis, A. & Parks, D.M. (2002) Modelling the evolution of crystallographic dislocation density in crystal plasticity. *Journal of the Mechanics and Physics of Solids*, 50 (9), pp. 1979-2009.

ASM International (n:d) *Crystalline structure subject guide*. [WWW] Available from: http://www.asminternational.org/content/SubjectGuides/sg_crystal_structure_f04.jpg [Accessed 07/02/2012].

Bannantine, J.A., Comer, J.J., & Handrock, J.L. (1990) *Fundamentals of metal fatigue analysis*. Prentice Hall.

Digital Surf (2006) *New 3D parameters and filtration techniques for surface metrology*. [WWW] Available from: http://www.qualitymag.com/QUAL/Home/Files/PDFs/New3DParametersandFiltrationTechniquesforSurfaceMetrology.pdf. [Accessed 05/07/2012].

Bleys, P., Kruth, J.P., Lauwers, B., Schacht, B., Balasubrramanian, V., Froyen, L., & Van Humbeeck, J. (2006) Surface and sub-surface quality of steel after EDM. *Advanced Engineering Materials*, 8 (1-2), pp. 15-25.

Bonetti, E., Pasquini, L., & Sampaolesi, E. (1997) The influence of grain size on the mechanical properties of nanocrystalline aluminium. *Nanostructured Materials*, 9 (1-8), pp. 611-614.

Bowden, F.P., & Tabor, D. (1974) *Friction: an introduction to tribology*. London: Heinemann Educational Books Ltd.

Brandon, D., & Kaplan, W.D. (1997) *Joining processes: an introduction.* Chichester: John Wiley.

Callister, W.D., & Rethwisch, D.G. (2008) *Fundamentals of materials science and engineering : an integrated approach.* 3rd ed. Hoboken, N.J: John Wiley & Sons.

Canovic, S., Jonsson, T., & Halvarsson, M. (2008) Grain contrast imaging in FIB and SEM. *Journal of Physics: Conference Series*, 126 (1), pp. 012054 1 - 4.

Cotterill, P., & Mould, P.R. (1976) *Recrystallization and grain growth in metals*. London: Surrey University Press.

Daniels, H.P. (1965) Ultrasonic Welding. *Ultrasonics*, 3 (4), pp. 190-196.

Dehoff, R.R., & Babu, S.S. (2010) Characterization of interfacial microstructures in 3003 aluminum alloy blocks fabricated by ultrasonic additive manufacturing. *Acta Materialia*, 58 (13), pp. 4305-4315.

Doherty, R., Hughes, D., Humphreys, F., Jonas, J., Jensen, D., Kassner, M., King, W.E., McNelley, T.R., McQueen, H.J. & Rollett, A.D. (1997) Current issues in recrystallization: a review. *Materials Science and Engineering A*, 238 (2), pp. 219-274.

Domack, M.S., & Baughman, J.M. (2005) Development of nickel-titanium graded composition components. *Rapid Prototyping Journal*, 11 (1), pp. 41-51.

Doumanidis, C., & Gao, Y. (2004) Mechanical modeling of ultrasonic welding. *AWS Welding Journal*, 83 (4), pp. 140s-146s.

Fabrisonic LLC. (2012). *Sonic LayerTM 7200.* [WWW] Available from: http://www.fabrisonic.com/sonic_layer_7200.html [Accessed 07/05/2012].

Flood, G. (1997) Ultrasonic energy welds copper to aluminium. *Welding Journal*, 76 (1), pp. 43-45.

Friel, R.J. (2011) *Investigating the effect if ultrasonic consolidation on shape memory alloy fibres*, PhD Thesis. Loughborough University, UK.

Friel, R.J., & Harris, R.A. (2010) A nanometre-scale fibre-to-matrix interface characterization of an ultrasonically consolidated metal matrix composite. *Proceedings of the Institution of Mechanical Engineers, Part L: Journal of Materials: Design and Applications*, 224 (1), pp.31-40.

Friel, R.J., Johnson, K.E., Dickens, P.M., & Harris, R.A. (2010) The effect of interface topography for ultrasonic consolidation of aluminium. *Materials Science & Engineering A*, 527 (16-17), pp. 4474-4483.

Gao, Y., & Doumanidis, C. (2002) Mechanical analysis of ultrasonic bonding for rapid prototyping. *Journal of Manufacturing Science and Engineering*, 124 (2), pp. 426-434.

George, J., & Stucker, B. (2006) Fabrication of lightweight structural panels through ultrasonic consolidation. *Virtual and Physical Prototyping*, 1 (4), pp. 227-241.

Gourdet, S., & Montheillet, F. (2003) A model of continuous dynamic recrystallization. *Acta Materialia*, 51 (9), pp. 2685-2699.

Graff, K. (2009) Ultrasonic additive manufacture / ultrasonic consolidation - past, present and future. *Ultrasonic Additive Manufacturing Technology Symposium*, Edison Welding Institute, Columbus, Ohio, USA, October 20th-21st.

Grain-boundary migration. (1972) *Progress in Materials Science*, 16, pp. 127-130.

Gunduz, I.E., Ando, T., Shattuck, E., Wong, P.Y., & Doumanidis, C.C. (2005) Enhanced diffusion and phase transformations during ultrasonic welding of zinc and aluminium. *Scripta Materiala*, 52 (9), pp. 939-943.

Guy, A.G., & Hren, J.J. (1974) *Elements of physical metallurgy*. 3rd ed. London: Addison-Wesley Publishing Company, Inc.

Hansson, I., & Tholen, A. (1978) Plasticity due to superimposed macrosonic and static strains. *Ultrasonics*, 16 (2), pp. 57-64.

Hansson, S., & Hansson, K.N. (2005) The effect of limited lateral resolution in the measurement of implant surface roughness: A computer simulation. *Journal of Biomedical Materials Research Part A*, 75A (2), pp. 472-477.

Hatamleh, O., Smith, J., Cohen, D., & Bradley, R. (2009) Surface roughness and friction coefficient in peened friction stir welded 2195 aluminum alloy. *Applied Surface Science*, 255 (16), pp. 7414-7426.

Hayes, G.A., & Shyne, J.C. (1969) The influence of ultrasonic energy on kinetic processes in solids. *Institute of Electrical and Electronics Engineers Transactions on sonics and ultrasonics*, 16 (2), pp. 68-75.

Higginson, R.L., & Sellars, C.M. (2003) *Worked examples in quantitative metallography*. Maney Publishing.

Higginson, R.L., & Sellars, S.M. (2002) The effect of strain path reversal during hot rolling on austenitic stainless steel. *Materials Science and Engineering: A*, 338 (1-2), pp. 323-330.

Hopkins, C.D., Wolcott, P.J., Dapino, M.J., Truog, A.G., Babu, S.S, & Fernandez, S.A. (2012) Optimizing ultrasonic additive manufactured al 3003 properties with statistical modelling. *Journal of Engineering Materials and Technology*, 134 (1), pp. 011004 1-6.

Hosford, W.F. (2005) *Physical Metallurgy*. Boca Raton, Florida: CRC Press.

Hu, X., Wei, C., Margolin, H., & Nourbakhsh, S. (1992) The bauschinger effect and the stresses in a strained single crystal. *Scripta Metallurgica et Materialia*, 27, pp. 865-870.

Humphreys, F.J., & Hatherly, M. (1995) *Recrystallization and related annealing phenomena*. 1st ed. Oxford: Pergamon.

Janaki Ram, G.D., Yang, Y., & Stucker, B.E. (2006a) Effect of process parameters on bond formation during ultrasonic consolidation of aluminium alloy 3003. *Journal of Manufacturing Systems*, 25 (3), pp. 221-238.

Janaki Ram, G.D., Yang, Y., George, J., Robinson, C., Stucker, & B.E. (2006b) Improving linear weld density in ultrasonically consolidated parts. *Proceedings of the 17th Solid Freeform Fabrication Symposium*, Austin, TX, USA, pp. 692-708.

Janaki Ram, G.D., Yang, Y., Nylander, C., Aydelotte, B., Stucker, B.E., & Adams, B.L. (2007) Interface microstructures and bond formation in ultrasonic consolidation.

Proceedings of the 18th Solid Freeform Fabrication Symposium, Austin, TX, USA, pp. 266-283.

Johnson, K. (2008) *Interlaminar subgrain refinement in ultrasonic consolidation*. PhD Thesis. Loughborough University, UK.

Johnson, K., Edmonds, H.C., Higginson, R.L., & Harris, R.A. (2011) New discoveries in ultrasonic consolidation nano-structures using emerging analysis techniques. *Proceedings of the Institution of Mechanical Engineers, Part L: Journal of Materials: Design and Applications*, 225 (4), pp. 277-287.

Johnson, K., Higginson, R., Dickens, P., West, G., Gupta, A., & White, D. (2007) Formation of nano-grains during biaxial high frequency fully reversed loading. *Materials Science and Technology - Association for Iron and Steel Industry,* 4, pp. 2618-2629.

Koellhoffer, S., Gillespie, J.W., Advani, S.G., & Bogetti, T.A. (2011) Role of friction on the thermal development in ultrasonically consolidated aluminium foils and composites. *Journal of Materials Processing Technology*, 211 (11), pp. 1864-1877.

Kong, C.Y. (2005). *Investigation of ultrasonic consolidation for embedding active/passive fibers in aluminium matrices*. PhD Thesis. Loughborough University, UK.

Kong, C.Y., & Soar, R.C. (2005a) Method for embedding optical fibers in an aluminium matrix by ultrasonic consolidation. *Applied Optics*, 44 (30), pp. 6325-6333.

Kong, C.Y., & Soar, R.C. (2005b) Fabrication of metal–matrix composites and adaptive composites using ultrasonic consolidation process. *Materials Science and Engineering A*, 412 (1-2), pp. 12-18.

Kong, C.Y., Soar, R.C., & Dickens, P.M. (2003) Characterisation of aluminium alloy 6061 for the ultrasonic consolidation process. *Materials Science and Engineering A*, 363 (1-2), pp. 99-106.

Kong, C.Y., Soar, R.C., & Dickens, P.M. (2004a) Optimum process parameters for ultrasonic consolidation of 3003 aluminium. *Journal of Materials Processing Technology*, 146 (2), pp. 181-187.

Kong, C.Y., Soar, R.C., & Dickens, P.M. (2004b) Ultrasonic consolidation for embedding SMA fibres within aluminium matrices. *Composite Structures*, 66 (1-4), pp. 421-427.

Kong, C.Y., Soar, R.C., & Dickens, P.M. (2005) A model for weld strength in ultrasonically consolidated components. *Proceedings of the Institue of Mechanical Engineers Part C: Journal of Mechanical Engineering Science,* 219 (1), pp. 83-91.

Kreye, H. (1977) Melting phenomena in solid state welding processes. *Welding Journal*, 56, pp. 154-158.

Kulakov, M., & Rack, H.J. (2009) Control of 3003-H18 aluminium in ultrasonic consolidation. *Journal of Engineering Materials and Technology*, 131 (2), pp. 021006.

Kulakov, M., & Rack, H.J. (2010) Surface damage during ultrasonic consolidation of 3003-H18 aluminum. *Rapid Prototyping Journal*, 16 (1), pp. 12 - 19.

Lal, G.K., & Venkata Reddy, N. (2009) *Introduction to engineering plasticity*. Oxford, UK: Alpha Science International Ltd.

Lancaster, J.F. (1987) *Metallurgy of welding*. 4th ed. London: Allen & Unwin.

Langenecker, B. (1966) Effects of ultrasound on deformation characteristics of metals. *Institute of Electrical and Electronics Engineers Transactions on Sonics and Ultrasonics*, 13 (1), pp. 1-8.

Li, D., & Soar, R.C. (2009a) Influence of sonotrode texture on the performance of an ultrasonic consolidation machine and the interfacial bond strength. *Journal of Materials Processing Technology*, 209 (4), pp. 1627-1634.

Li, D., & Soar, R.C. (2009b) Characterization of process for embedding SiC fibers in Al 6061 O matrix through ultrasonic consolidation. *Journal of Engineering Materials Technology*, 131 (2), pp. 021016 1-6.

Liu, J., Li, M., Sheu, S., Karabin, M.E., & Schults, R.W. (2008) Macro- and micro-surface engineering to improve hot roll bonding of aluminum plate and sheet. *Materials Science and Engineering: A*, 479 (1-2), pp. 45–57.

Mariania, E., & Ghassemieh, E. (2010) Microstructure evolution of 6061 O Al alloy during ultrasonic consolidation: An insight from electron backscatter diffraction. *Acta Materialia*, 58 (7), pp. 2492-2503.

Matsuoka, S. (1998) Ultrasonic welding of ceramics/metals using inserts. *Journal of Materials Processing Technology*, 75 (1-3), pp. 259-265.

Messler, R. W. (1999) *Principles of welding: processes, physics, chemistry, and metallurgy*. Chichester: John Wiley.

Michigan Metrology. (2005) *Glossary of surface texture parameters*., Liovania, Michigan, USA: Michigan Metrology.

Moore, D.F. (1975) *Principles and applications of tribology*. 1st ed. Oxford: Pergamon Press Ltd.

Moore, D.S., & McCabe, G.P. (1993) *Introduction to the practice of statistics*. 2nd ed. New York: W.H Freeman and Company.

NDT Resource Centre. (n.d.) Crystal defects: linear defects (dislocations) [WWW] http://www.ndted.org/EducationResources/CommunityCollege/Materials/Graphics/DislocationDirection.gif [Accessed 08/03/2012].

Neppiras, E. A. (1965) Ultrasonic welding of metals. *Ultrasonics*, 3 (3), pp. 128-135.

Orlov, D., Todaka, Y., Umemoto, M., & Tsuji, N. (2009) Role of strain reversal in grain refinement by severe plastic deformation. *Materials Science and Engineering A*, 499 (1-2), pp. 427-433.

Pal, D., & Stucker, B.E. (2011) Dislocation density crystal plasticity based finite element modelling of ultrasonic consolidation. *Proceedings of the 22nd Solid Freeform Fabrication Symposium*, Austin, TX, USA, pp. 375-404.

Plouraboue, F., & Boehm, M. (1999) Multi-scale roughness transfer in cold metal rolling. *Tribology International*, 32 (1), pp. 45-57.

Prieb, V. (1999) *Structural aspects of metal joining, stretching and stamping using ultrasonics*. Berlin, Germany: 1st Memory Alloys GmbH.

Robinson, C.J., Stucker, B., Lopes, A.J., & Wicker, R. (2006) Integration of direct-write (DW) and ultrasonic consolidation (UC) technologies to create advanced structures with embedded electrical circuitry. *Proceedings of the 17th Solid Freeform Fabrication Symposium*, Austin, TX, USA, pp. 60-69.

Schick, D.E., Hahnlen, R.M., Dehoff, R., Collins, P., Babu, S.S., Dapino, M.J., & Lippold, J.C. (2010) Microstructural characterization of bonding interfaces in aluminium 3003 blocks fabricated by ultrasonic additive manufacturing. *Welding Journal*, 89 (5), pp. 105-115.

Schick, D., Babu, S.S., Foster, D.R., Dapino, M., Short, M., & Lippold, J.C. (2011) Transient thermal response in ultrasonic additive manufacturing of aluminum 3003. *Rapid Prototyping Journal*, 17 (5), pp. 369-379.

Siddiq, A., & Gassemieh, E. (2008) Thermomechanical analyses of ultrasonic welding process using thermal and accoustic softening effects. *Mechanics of materials*, 40 (12), pp. 982-1000.

Siddiq, A., & Ghassemieh, E. (2009) Theoretical and FE analysis of ultrasonic welding of Aluminium. *Journal of Manufacturing Science and Engineering*, 131 (4), pp. 041007 1-11.

Siddiq, A., & Sayed, T.E. (2012) A thermomechanical crystal plasticity constitutive model for ultrasonic consolidation. *Computational Materials Science*, 51(1), pp. 241-251.

Siggard, R.J., Madhusoodanan, A.S., Stucker, B., & Eames, B. (2006) Structurally embedded electrical systems using ultrasonic consolidation. *Proceedings of the 17th Solid Freeform Fabrication Symposium,* Austin, TX, USA, pp. 70-83.

Slamova, M., Ocenasek, V., & Vander Voort, G. (2004) Polarized light microscopy: utilization in the investigation of the recrystallization of aluminum alloys. *Materials Characterization*, 52 (3), pp. 165-177.

Sojiphan, K., Sriraman, M.R., & Babu, S.S. (2010) Stability of microstructure in Al3003 builds made by very high power ultrasonic additive manufacturing. *Proceedings of the 21st Solid Freeform Fabrication Symposium*, Austin, TX, USA, pp. 362-371.

Sriraman, M.R., Babu, S.S., & Short, M. (2010a) Bonding characteristics during very high power ultrasonic additive manufacturing of copper. *Scripta Materialia*, 62 (8), pp. 560-563.

Sriraman, M.R., Fujii, H., Gonser, M., Babu, S.S., & Short, M. (2010b) Bond characterization in very high power ultrasonic additive manufacturing. *Proceedings of the 21st Solid Freeform Fabrication Symposium*, Austin, TX. USA, pp. 372-382.

Sriraman, M.R., Gonser, M., Foster, D., Fujii, H.T., Babu, S.S., & Bloss, M. (2012) Thermal transients during processing of 3003 Al-H18 multilayer build by very highpower ultrasonic additive manufacturing. *Metallurgical and Materials Transactions B*, 43 (1), pp. 133-144.

Sriraman, M.R., Gonser, M., Fujii, H.T., Babu, S.S., & Bloss, M. (2011) Thermal transients during processing of materials by very high power ultrasonic additive manufacturing. *Journal of Materials Processing Technology*, 211 (10), pp. 1650-1657.

Stout, K. J., & Blunt, L. (1994) *Three-dimensional surface topography*. 2nd ed. London: Penton Press.

Taylor Hobson Ltd. (n.d.) *A guide to surface texture parameters*. [Pamphlet] Available from: Taylor Hobson, Leicester, UK.

Taylor Hobson Ltd. (2003) *Exploring surface texture: a fundamental guide to the measurement of surface finish*. 4th Edition ed. Leicester, England: Taylor Hobson Ltd.

Thomas, T.R. (1999) *Rough Surfaces*. 2nd Edition ed. London: Imperial College Press.

Tuttle, R.B. (2007) Feasibility study of 316L stainless steel for the ultrasonic consolidation process. *Journal of Manufacturing Processes*, 9 (2), pp. 87-93.

Valiev, R. Z., Islamgaliev, R. K., & Alexandrov, I. V. (2000) Bulk nanostructured materials from severe plastic defromation. *Progress in Materials Science*, 45 (2), pp. 103-189.

Vill, V. I. (1962) *Friction welding of metals.* New York: American Welding Society.

Weare, N.E., Antonevich, J.N., & Monroe, R.E. (1960) Fundamental studies of ultrasonic welding. *Welding Journal*, 39, pp. 331-341.

White, D. (2002a) Ultrasonic consolidation. *Appliance Manufacturer*, 50 (9), pp. 22-23.

White, D.R. (2002b) Object consolidation employing friction joining. *Patent No. 6457629*, United States of America.

White, D.R. (2003) Ultrasonic consolidation of aluminium tooling. *Advanced Materials & Processes*, 161, pp. 64-65.

Whitehouse, D.J. (1994) *Handbook of surface metrology*. Bristol: Institute of Physics Publishing.

Yang, Y., Janaki Ram, G.D., & Stucker, B.E. (2009) Bond formation and fiber embedment during ultrasonic consolidation. *Journal of Materials Processing Technology*, 209 (10), pp. 4915-4924.

Yoshida, I., & Ohsone, H. (1981) Effect of ultrasonic vibration on the metallurgical properties of steel. *Journal de Physique Colloques*, 42 (C5), pp. 1153-1158.

Zhang, C., & Li, L. (2008) A friction-based finite element analysis of ultrasonic consolidation. *Welding Journal*, 87 (7), pp. 187-194.

Zygo Corporation. (2002) *New viewTM 5000 specifications*. [Manual] Available from: Zygo Corporation, Middlefield, CT, USA.

Appendices

Chapter 4 Appendix - 4.1

Surface Metrology

Surface Metrology can be defined as “the measurement of the deviations of a work piece from its intended shape”, i.e. that described by its technical drawing. Surface metrology includes the measurement of features which deviate from the components shape as well as surface texture measurement. The surface texture of a component is dependent upon its structure and the process by which it was manufactured. A surface can be described in terms of roughness, waviness and form and specific surface texture parameters can be used to quantify surface characteristics (Taylor Hobson Ltd.).

The study of surface metrology in three dimensions is referred to as three dimensional (3D) surface measurement, 3D topographic measurement or areal measurement. While surface texture has previously been analysed in two dimensions, as a series of profiles across a components surface, the development of 3D profilometers and 3D non-contact measurement methods has meant that measurement can be evaluated based on the area of a surface, as opposed to a single line scan (Taylor Hobson Ltd.).

At the time of publication the international standardisation of analysis tools for 3D surface texture was still in progress (Digital Surf 2006). Care has been taken to present the most up to date tools and surface measurement parameters that are expected to be implemented in ISO 25178*:* Geometric Product Specifications (GPS) – Surface texture: areal standard.

Surface Texture components

Every surface is can be divided into form, waviness, roughness components based on wavelength (Figure 0-1). The surface form refers to the general shape of a surface, for example the curve of a spherical or cylindrical object, and has the longest wavelength. Surface waviness features are those with a shorter wavelength, for example low frequency undulations as result of material vibrations during processing. Surface roughness characteristics occur at an even shorter wavelength and are generally of the most interest, for example in the analysis of frictional behaviour of mating surfaces and lubrication characteristics (Taylor Hobson Ltd. 2003)(Thomas 1999).

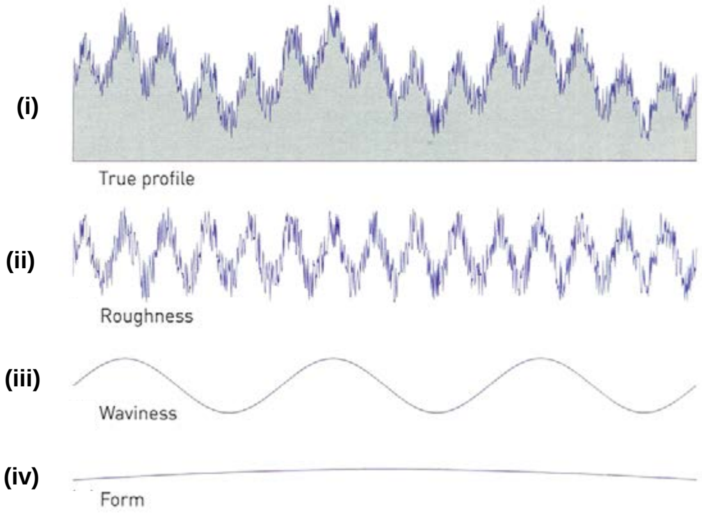

Figure 0-1: A surface (i) is made up of roughness (ii), waviness (iii) and form (iv) components (Taylor Hobson Ltd.).

There is no specific criteria for the range of wavelengths at which these three components occur. DIN 4760 attempted to quantify the relationship by asserting that the form length should by more than 1000 times its amplitude and the length of waviness features must be between 100 and 1000 times their amplitude. In practice the division is normally dependent upon the application for which the surface is being assessed (Thomas 1999).

Surface Lay

Surface lay refers to the directional character of the dominant pattern of a surface as a result of wear or the movements of the tool used to machine that surface (Figure 0-2) (Thomas 1999)(Whitehouse 1994). A surface may be composed of multiple lays as a result of being subject to numerous machining processes or have no apparent lay pattern and therefore appear isotropic.

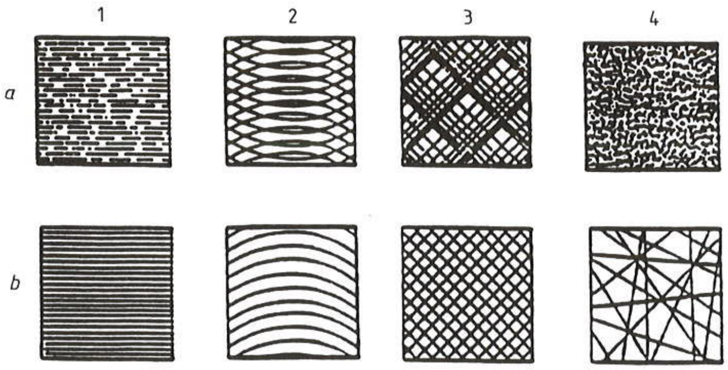

Figure 0-2: Characteristic surface finishes for common machining processes: 1) peripheral grinding, 2) face grinding, 3) honing, 4) lapping for process variations a) and b) (Whitehouse 1994).

Data Processing

The 3D surface texture maps, obtained from instruments such as white light interferometers, show the true texture of the object measured, including form, waviness and roughness components. In some applications it is desirable to analyse the surface texture of components without taking into account on or more of these components. For example, in order to measure the surface roughness of a cylindrical object the primary form of a surface can be mathematically removed by filtering (Figure 0-3) using software such as the TalyMap 3D Analysis Software from Taylor Hobson Ltd.

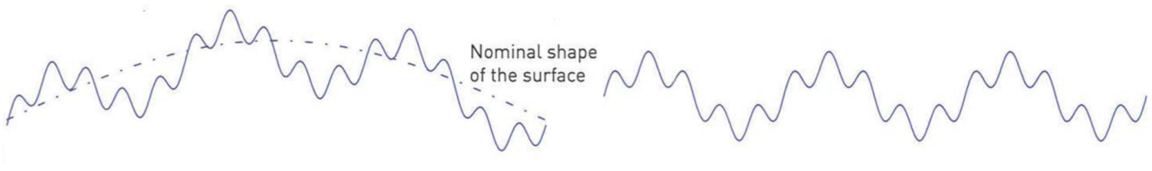

(a) (b)

Figure 0-3: a) Pre-filtered profile with cylindrical form and b) profile with form removed (Taylor Hobson Ltd. 2003).

As with the specification of wavelengths for form, waviness and roughness components, the choice of which filters to apply to a surface is equally subjective. The inappropriate specification of component wavelength and application of filters can mean that important detail is lost and a false measurement of surface texture is obtained.

Surface Texture Parameters

In order to quantify, compare and analyse change in surface textures a number of surface texture parameters are defined in the upcoming ISO 25178 standard.

Amplitude Parameters

Average roughness, S_a, is one of the most commonly used parameters for surface texture measurement. The S_a of a surface is the arithmetic average of the absolute values of the surface height deviations measured from the best fitting plane (Equation 0-1i). Similar to S_a, the root mean square (RMS) roughness of a surface, S_q, is the average of the surface height deviations squared (Equation 0-1ii) (Michigan Metrology).

$$S_a = \iint_a |Z(x,y)|\, dxdy \qquad\qquad S_q = \sqrt{\iint_a \left(Z(x,y)\right)^2 dxdy}$$

(i) **(ii)**

Equation 0-1: Mathematical formula for Average Roughness, S_a (i), and Root Mean Square Roughness, S_q (ii) (Michigan Metrology).

The S_a and S_q parameters can be used as an overall measure of surface texture and are adequate to identify differences in texture characteristics for a given surface type or monitoring changes in surfaces. S_a is more commonly used to measure machined surfaces while S_q is used in the optics industry to determine light scattering characteristics. Both of these parameters are limited in that they are insensitive to peaks and troughs and their relative spacing (Figure 0-4). Surfaces may have the same S_a value but be very different in nature and hence other parameters are needed to fully characterise a surface (Michigan Metrology).

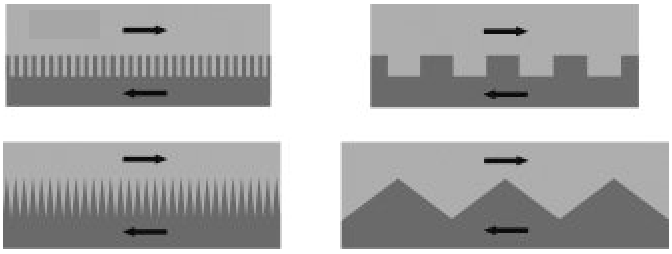

Figure 0-4: Four different rough surfaces in cross-section all with the same average roughness (Hansson & Hansson 2005).

The skew of a surface, Ssk, denotes whether that surface is dominated by peaks or troughs (Figure 0-5). If Ssk>0, the surface texture is dominated by peaks, and if Ssk<0, the surface texture is dominated by valleys. In the calculation of Ssk the RMS height values are cubed (Equation 0-2i) and their polarity is maintained, but this also means that extreme high or low points have a significant affect the Ssk and hence the measurement is not very repeatable. Ssk is useful in predicting lubricant retention, and monitoring wear (Michigan Metrology).

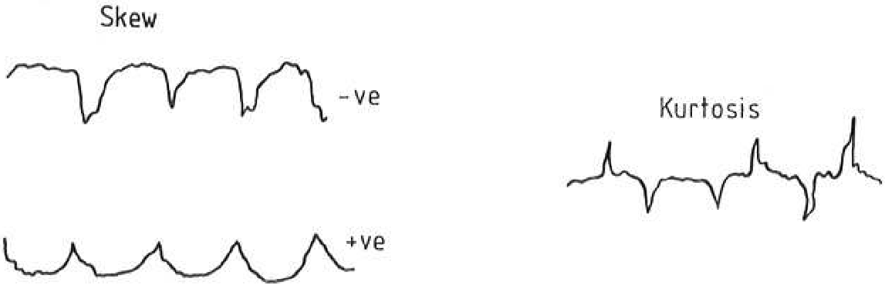

Figure 0-5: Examples of positive and negative skew and kurtosis on a surface (Whitehouse 1994).

Kurtosis, Sku, is a measure of the presence of extreme peaks or valleys within a surfaces texture. A surface with a normally distributed texture would tend to have an Sku of 3. If the Sku value is more than 3, the surface contains extreme peaks or valleys and if the Sku is less than 3, the surface is free from extreme peaks or valleys with a slowly varying texture. Similarly to the Ssk parameter, Sku is vulnerable to extremes and has low repeatability as the Sq parameter is used the power of four (Equation 0-2ii) (Michigan Metrology).

$$Ssk = \frac{1}{S_q^3}\iint_a \left(Z(x,y)\right)^3 dxdy \qquad\qquad Sku = \frac{1}{S_q^4}\iint_a \left(Z(x,y)\right)^4 dxdy$$

(i) **(ii)**

Equation 0-2: Mathematical formula for Skewness, Ssk (i), and Kurtosis, Sku (ii) (Michigan Metrology).

Topological Characterisation Parameters

Topological characterisation parameters analyse the density and nature of surface features in relation to functional requirements (Digital Surf 2006). The Density of Summits, Sds, quantifies the number of summits per unit area of the surface. Summits can be detected on the surface in a process called segmentation. Significant peaks are identified using the Watersheds algorithm, which segments the material surface into significant elements called motifs (Figure 0-6). The summit density of the surface can then be calculated.

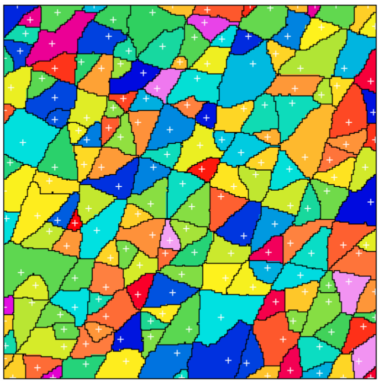

Figure 0-6: Surface segmented into motifs, each peak location is denoted by a cross (Digital Surf 2006).

The Sds value can be used in evaluating the contact stresses in mating surfaces, for example a low Sds values would indicate high local contact stresses. Sds is commonly used in bearing, seal and electronic contact applications (Michigan Metrology).

$$Ssc = \frac{1}{N}\iint_{summit}\left(\frac{\partial^2 Z(x,y)}{\partial x^2}\right) + \left(\frac{\partial^2 Z(x,y)}{\partial y^2}\right) dydx$$

Equation 0-3: Mean summit curvature, Ssc (Michigan Metrology).

Mean summit curvature, Ssc, is the average of the principal curvatures (Equation 0-3) of all summits within the sampling area (Stout & Blunt 1994)

Ssc can be used to determine the relative elastic and plastic deformation of a surface under loading and hence, in the prediction of friction and wear characteristics of surfaces. (Michigan Metrology)

Spectral Analysis Parameters

The presence and degree of texture orientation or lay within a surface can influence that surfaces friction and wear behaviour, hence this parameter is importance in the analysis of surface texture (Hatamleh et al. 2009**.** The isotropy of a surface can be quantified by using the autocorrelation function (ACF) (Digital Surf 2006). The ACF can be used to quantify how similar the texture of a surface at one point is to its surface at a given distance from the original location. To determine the ACF a surface a duplicate surface of relative lateral displacement (Δx,Δy) from that surface, is multiplied with the original surfaces. By integration and normalizing to S_q a measure of the area of overlap between the two functions is determined (Equation 0-4) (Michigan Metrology).

$$ACF(\Delta x, \Delta y) = \frac{\iint_A Z(x,y)Z(x-\Delta x, y-\Delta y)dxdy}{\iint_A Z^2(x,y)dxdy}$$

Equation 0-4: Autocorrelation function, ACF (Digital Surf 2006).

The shape of the central peak on the autocorrelation image of the surface indicates the surface isotropy. A symmetrical central lobe indicates isotropy (Figure 0-7i), while a distinct orientation indicates anisotropy (Figure 0-7ii). The presence of secondary peaks indicates a periodic, or pseudo-periodic, texture (Digital Surf 2006).

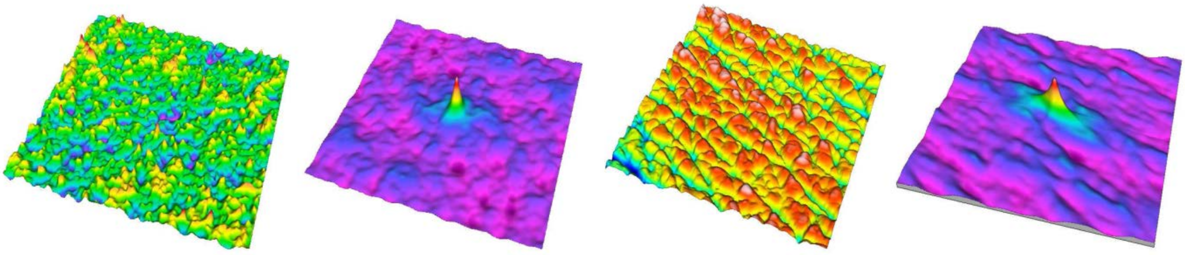
(i) **(ii)**

Figure 0-7: Isotropic surface (i) (left) and autocorrelation image with symmetrical central lobe (right) anisotropic surface (ii) (left) and autocorrelation image with unsymmetrical central lobe (Digital Surf 2006).

The level of isotropy illustrated in the autocorrelation image is quantified by the texture aspect ratio, Str**.** The Str of a surface varies from 0, for a totally unidirectional texture, to 1, for a spatially isotropic texture (Hatamleh et al. 2009). Str is calculated from the ratio of the length of fastest decay ACF in any direction, Rmin, to the length of slowest decay ACF in any direction, Rmax, of the central lobe on the autocorrelation surface at a given threshold value, normally 0.2 (Figure 0-8)(Equation 0-5)(Digital Surf 2006).

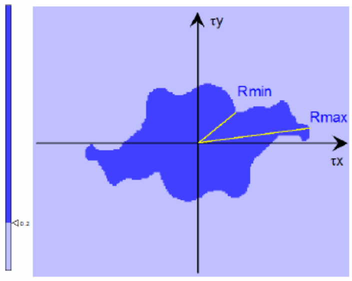

Figure 0-8: Rmin and Rmax measurements from the central lobe of autocorrelation image (threshold = 0.2) (Digital Surf, 2006).

$$Str = \frac{Rmin}{Rmax}$$

Equation 0-5: Texture aspect ratio, Str (Digital Surf 2006).

In surface texture analysis Rmin, the fastest decay autocorrelation length at a given threshold value, is represented by the Sal parameter. Sal represents the distance between areas of the surface which statistically different and can be used to quantify the spectral content of surface, for examples a surface with a large Sal would be made up of long wavelength spectral components (Digital Surf 2006).

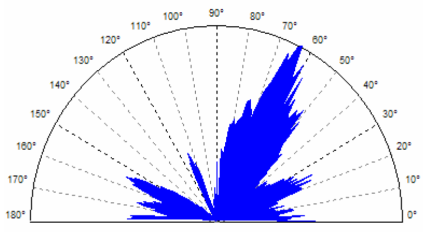

Figure 0-9: An example of a surface polar spectrum of the, with an Std of 64° (Digital Surf 2006).

The texture direction of a surface, Std, is an angular measurement which indicates the predominant direction of surface lay. Std can be determined by integrating the Fourier spectrum in polar coordinates. The polar spectrum represents the power spectrum for different directions along the surface and the angle with the largest power spectrum is the predominant surface direction (Figure 0-9). The Std value is defined in degrees anticlockwise relative to the Y axis. A surface with a Std of 0° has its dominant lay along the Y axis (Digital Surf 2006) (Michigan Metrology).

Std can be used to detect the presence of a preliminary surface modification process, where a lay direction has been imparted onto the surface by a particular machining process. However, it should be noted that if the surface Str value is more than 0.5, the Std value is meaningless as the texture direction is indeterminate (Michigan Metrology) (Stout & Blunt 1994).

Volume Parameters

Volume parameters are used in differentiating surface with similar S_a values and determining the relative dominance of peak structures or valleys within a texture. The functional volume parameters are calculated from the bearing ratio curve (Figure 0-10). The bearing ratio, sometimes referred to as material ratio, Abbott-Firestone curve or Abbott curve, is a plot of the ratio of void to material starting at the highest peak. Consider two parallel planes, parallel to the material surface. The upper plane cuts through the surface where a given fraction of material, p, is above that plane, the lower plane cuts through the surface where a larger fraction of material, q, is above that plane (Whitehouse, 1994). Standard values for the bearing threshold values are p=10% and q=80% (Digital Surf 2006).

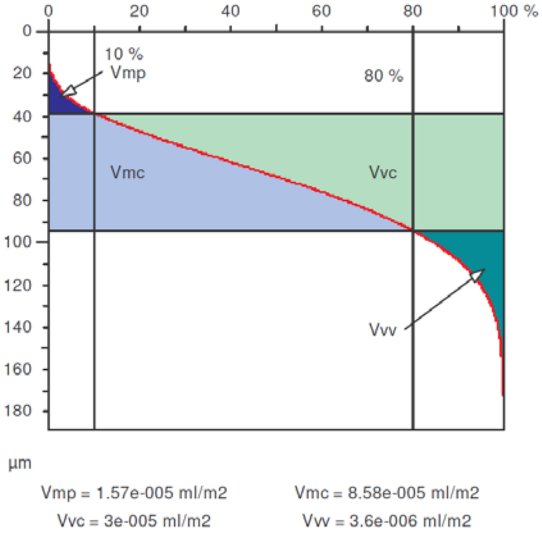

Figure 0-10: Functional volume parameters dervied from Abbott curve with bearing raio thersholds of 10% and 80%)(Digital Surf 2006).

The peak material volume, Vmp, refers to the volume of material within the surface peaks in the 10% bearing area. The core material volume, Vmc, refers to the volume of material between the two bearing threshold values 10% and 80%. The core void volume, Vvc, refers to the void volume between the bearing threshold values 10% and 80%. The valley void volume, Vvv, refers to the volume of the valleys contained above 80% of the bearing area (Digital Surf 2006).

Chapter 4 Appendix - 4.2

Sonotrode A Pre-Process Texture Parameters

Texture Parameter	**Measurement Number**												**Average**	**σ**
	a1	**a2**	**a3**	**b1**	**b2**	**b3**	**c1**	**c2**	**c3**	**d1**	**d2**	**d3**		
Sa (µm)	5.46	5.71	5.88	4.52	5.01	5.65	4.73	4.17	4.02	4.76	4.74	5.02	**4.97**	0.60
Sq (µm)	6.86	7.04	7.19	5.86	6.52	7.12	6.15	5.53	5.49	6.33	6.29	6.40	**6.40**	0.58
Sku	3.18	2.77	2.61	3.23	3.39	2.96	3.18	3.72	4.12	3.42	3.52	3.11	**3.27**	0.41
Ssk	-0.373	-0.429	-0.279	-0.138	-0.474	-0.378	0.288	0.170	0.043	-0.128	0.026	-0.397	**-0.172**	0.256
Sds (1/mm2)	40835	37519	38075	39207	39537	39463	39071	39020	39203	39263	39064	38158	**39034**	841
Ssc (1/mm)	1.15	1.08	1.10	1.23	1.15	1.10	1.20	1.17	1.10	1.14	1.15	1.08	**1.14**	0.05
Str*	0.914	0.917	0.894	0.929	0.951	0.927	0.857	0.864	0.880	0.890	0.894	0.865	**0.899**	0.030
Sal* (µm)	33.0	27.5	28.7	24.9	30.5	32.5	30.2	27.8	26.5	29.9	34.9	24.8	**29.3**	3.2
Std (°)	44.0	95.7	26.5	36.7	20.5	175.8	100.8	20.5	90.0	114.0	36.7	100.7	**71.8**	48.4
Vmp ($\mu m^3/\mu m^2$)**	0.269	0.224	0.214	0.250	0.265	0.221	0.306	0.344	0.359	0.354	0.363	0.269	**0.286**	0.057
Vmc ($\mu m^3/\mu m^2$)**	6.22	6.76	6.91	4.83	5.50	6.40	4.94	4.28	4.08	5.03	5.01	5.69	**5.47**	0.94
Vvc ($\mu m^3/\mu m^2$)**	7.49	7.81	8.56	7.25	7.09	8.41	8.52	6.85	6.47	7.31	7.66	7.04	**7.54**	0.68
Vvv ($\mu m^3/\mu m^2$)**	0.929	0.920	0.856	0.813	1.033	0.994	0.715	0.699	0.758	0.949	0.864	0.934	**0.872**	0.108
Sdr (%)	50.6	44.4	45.9	56.9	50.4	44.5	54.5	52.8	47.6	49.4	48.9	46.8	**49.4**	3.9

_* s = 0.2_
_**p = 10%, q =80%_

Sonotrode B Pre-Process Texture Parameters

Texture Parameter	**Measurement Number**												**Average**	**σ**
	a1	**a2**	**a3**	**b1**	**b2**	**b3**	**c1**	**c2**	**c3**	**d1**	**d2**	**d3**		
Sa (μm)	13.98	15.20	14.59	15.15	15.46	13.29	14.44	14.06	14.39	15.60	14.23	17.06	**14.79**	0.98
Sq (μm)	17.45	18.46	18.95	18.94	19.01	17.55	18.38	17.44	18.51	19.37	17.72	21.14	**18.58**	1.05
Sku	3.04	2.56	3.35	3.12	2.76	3.78	3.48	2.72	3.21	2.97	2.99	2.76	**3.06**	0.35
Ssk	-0.053	-0.254	-0.403	-0.511	-0.180	-0.488	0.293	-0.208	-0.336	-0.331	-0.216	-0.337	**-0.252**	0.216
Sds (1/mm2)	36447	38510	36718	39704	35966	38922	37029	38783	37972	39649	39427	37421	**38046**	1308
Ssc (1/mm)	1.19	1.19	1.17	1.14	1.25	1.14	1.12	1.04	1.01	1.08	1.12	1.08	**1.13**	0.07
Str*	0.717	0.784	0.661	0.908	0.825	0.883	0.667	0.821	0.854	0.645	0.875	0.914	**0.796**	0.100
Sal* (μm)	127.9	151.9	133.2	182.3	132.6	167.6	134.4	164.8	176.3	191.2	183.8	162.0	**159.0**	22.6
Std (°)	26.5	66.0	128.8	114.0	114.0	65.9	43.9	66.0	0.1	143.3	0.1	51.3	**68.3**	48.1
Vmp ($\mu m^3/\mu m^2$)**	0.752	0.631	0.848	0.577	0.739	0.733	1.015	0.569	0.731	0.622	0.760	0.795	**0.731**	0.125
Vmc ($\mu m^3/\mu m^2$)**	16.32	18.47	16.34	17.63	17.59	14.09	15.76	15.80	16.78	17.97	16.00	20.00	**16.90**	1.54
Vvc ($\mu m^3/\mu m^2$)**	20.83	20.88	20.58	20.79	22.79	19.47	23.57	21.32	21.16	23.14	20.07	22.61	**21.43**	1.29
Vvv ($\mu m^3/\mu m^2$)**	1.948	2.039	2.851	2.604	2.252	2.747	1.875	2.220	2.556	2.397	2.238	2.840	**2.381**	0.340
Sdr (%)	129.81	122.66	130.88	135.28	132.87	134.43	106.59	103.99	110.13	96.63	124.63	119.23	**120.59**	13.24

** s = 0.2*
***p = 10%, q =80%*

Sonotrode C Pre-Process Texture Parameters

Texture Parameter	**Measurement Number**												**Average**	**σ**
	a1	**a2**	**a3**	**b1**	**b2**	**b3**	**c1**	**c2**	**c3**	**d1**	**d2**	**d3**		
Sa (µm)	17.63	21.53	19.69	18.77	20.02	17.90	17.45	19.07	17.37	19.57	19.51	17.95	**18.87**	1.27
Sq (µm)	22.35	27.00	24.19	23.13	24.58	22.23	22.15	24.77	22.15	24.76	24.62	22.46	**23.70**	1.53
Sku	3.54	2.80	2.68	2.70	2.96	2.96	3.62	4.50	3.76	3.88	3.10	3.28	**3.32**	0.56
Ssk	0.465	0.203	0.140	0.235	0.105	0.246	0.386	0.804	0.718	0.476	0.450	0.554	**0.398**	0.223
Sds (1/mm2)	35278	32825	36772	33350	36176	40351	36816	39404	39966	35489	38155	35738	**36693**	2419
Ssc (1/mm)	1.24	1.19	1.71	1.09	1.59	2.93	1.43	1.97	1.95	1.21	1.72	1.30	**1.61**	0.51
Str*	0.621	0.582	0.733	0.607	0.740	0.798	0.745	0.852	0.871	0.858	0.827	0.809	**0.754**	0.102
Sal* (µm)	156.4	174.8	173.1	185.5	183.0	166.1	162.7	196.1	213.1	232.4	171.9	195.5	**184.2**	22.1
Std (°)	66.0	123.8	159.5	128.7	95.7	114.0	66.0	66.0	56.2	66.0	66.0	128.8	**94.7**	34.83
Vmp (µm^3/µm^2)**	1.253	1.327	1.011	1.033	1.177	1.003	1.400	1.944	1.519	1.516	1.482	1.401	**1.339**	0.271
Vmc (µm^3/µm^2)**	19.55	24.33	23.74	20.51	22.73	21.20	19.32	20.78	18.64	22.17	22.04	19.89	**21.24**	1.79
Vvc (µm^3/µm^2)**	29.19	35.31	31.08	30.61	29.70	29.07	27.56	29.84	29.39	29.98	32.09	29.42	**30.27**	1.94
Vvv (µm^3/µm^2)**	2.065	2.761	2.177	2.279	2.489	2.065	2.055	2.086	1.736	2.284	2.123	1.818	**2.161**	0.275
Sdr (%)	94.4	89.2	239.0	59.9	153.9	660.0	136.5	312.2	311.8	80.5	252.4	104.8	**207.9**	168.62

** s = 0.2*
***p = 10%, q =80%*

Sonotrode A Post-Process Texture Parameters

Texture Parameter	**Measurement Number**												**Average**	**σ**
	a1	**a2**	**a3**	**b1**	**b2**	**b3**	**c1**	**c2**	**c3**	**d1**	**d2**	**d3**		
Sa (μm)	5.87	5.83	6.01	4.73	4.13	4.44	4.79	4.47	3.47	3.67	4.19	3.90	**4.62**	0.86
Sq (μm)	7.14	7.21	7.37	6.08	5.46	5.60	6.26	5.95	4.61	4.77	5.41	5.07	**5.91**	0.94
Sku	2.52	2.68	2.61	3.50	4.88	3.50	3.36	3.59	5.02	3.85	3.78	4.20	**3.62**	0.81
Ssk	-0.103	-0.287	-0.230	-0.580	-1.184	-0.776	0.299	-0.144	-0.814	-0.746	-0.973	-1.015	**-0.546**	0.449
Sds (1/mm2)	37765	38211	38286	42259	43016	42847	39671	40139	42021	40278	41292	44056	**40820**	2084
Ssc (1/mm)	1.09	1.11	1.13	1.20	1.21	1.18	1.35	1.31	1.32	1.15	1.16	1.34	**1.21**	0.09
Str*	0.858	0.920	0.849	0.908	0.844	0.924	0.829	0.865	0.924	0.963	0.873	0.888	**0.887**	0.040
Sal* (μm)	29.6	28.6	31.4	30.1	25.0	26.4	31.4	28.6	20.5	26.4	26.4	25.8	**27.5**	3.1
Std (°)	114.0	20.5	114.0	143.3	0.1	90.0	12.8	20.5	90.0	66.0	66.0	143.3	**73.4**	50.8
Vmp (μm^3/μm^2)**	0.249	0.231	0.266	0.230	0.136	0.154	0.321	0.288	0.188	0.172	0.133	0.138	**0.209**	0.064
Vmc (μm^3/μm^2)**	6.90	6.87	7.21	5.28	4.48	5.13	4.93	4.63	3.72	4.05	4.72	4.35	**5.19**	1.17
Vvc (μm^3/μm^2)**	8.84	8.54	8.67	6.43	4.77	5.60	8.58	7.25	4.55	4.67	5.00	4.62	**6.46**	1.81
Vvv (μm^3/μm^2)**	0.758	0.893	0.843	0.939	1.043	0.874	0.738	0.880	0.756	0.808	0.979	0.904	**0.868**	0.093
Sdr (%)	47.0	48.9	48.6	56.2	57.7	51.2	71.4	68.5	68.8	52.2	51.5	67.8	**57.5**	9.1

** s = 0.2*
***p = 10%, q =80%*

Sonotrode B Post-Process Texture Parameters

Texture Parameter	Measurement Number												Average	σ
	a1	a2	a3	b1	b2	b3	c1	c2	c3	d1	d2	d3		
Sa (μm)	15.40	14.70	14.49	15.57	15.59	13.28	13.66	13.79	15.03	17.11	14.91	14.97	**14.87**	1.03
Sq (μm)	19.36	18.83	18.23	19.54	19.74	16.61	17.06	18.09	18.87	21.14	18.45	18.50	**18.70**	1.21
Sku	3.56	3.55	2.95	2.91	3.33	2.93	2.96	3.54	2.85	3.10	2.79	2.85	**3.11**	0.30
Ssk	-0.450	-0.397	-0.093	-0.277	-0.291	-0.394	0.029	-0.164	-0.133	-0.614	-0.304	-0.119	**-0.267**	0.180
Sds (1/mm2)	41172	36714	39018	38269	37716	39895	39423	39739	38571	39564	39245	39358	**39057**	1140
Ssc (1/mm)	1.08	1.18	1.09	1.10	1.16	1.21	1.10	1.11	1.14	1.14	1.10	1.16	**1.13**	0.04
Str*	0.442	0.828	0.741	0.546	0.938	0.754	0.684	0.776	0.852	0.808	0.578	0.710	**0.721**	0.141
Sal* (μm)	161.6	146.1	161.4	157.8	174.8	146.9	156.8	155.8	151.8	189.4	137.2	157.3	**158.1**	13.0
Std (°)	133.0	114.0	73.0	0.1	95.7	66.0	66.0	66.0	56.2	100.8	51.2	51.2	**72.8**	34.7
Vmp (μm^3/μm^2)**	0.768	0.800	0.844	0.744	0.837	0.678	0.926	0.946	0.697	0.610	0.687	0.749	**0.774**	0.101
Vmc (μm^3/μm^2)**	18.05	16.39	16.46	18.06	17.55	15.75	15.97	14.86	16.59	19.84	17.02	17.13	**16.97**	1.30
Vvc (μm^3/μm^2)**	21.47	20.71	22.09	22.95	23.17	17.61	20.08	20.77	23.50	22.22	21.29	22.30	**21.51**	1.62
Vvv (μm^3/μm^2)**	2.350	2.683	2.195	2.486	2.438	2.269	1.809	2.517	2.428	3.010	2.419	2.041	**2.387**	0.304
Sdr (%)	147.98	130.42	158.11	143.18	118.60	98.40	127.03	125.60	165.13	146.96	124.91	101.00	**132.28**	20.83

** s = 0.2*
***p = 10%, q =80%*

Sonotrode C Post-Process Texture Parameters

Texture Parameter	**Measurement Number**												**Average**	**σ**
	a1	**a2**	**a3**	**b1**	**b2**	**b3**	**c1**	**c2**	**c3**	**d1**	**d2**	**d3**		
Sa (μm)	19.38	18.34	17.62	17.71	17.91	17.99	15.93	21.16	19.85	17.12	18.53	16.84	**18.20**	1.41
Sq (μm)	23.57	22.16	21.93	21.54	22.18	22.52	20.54	25.59	25.01	21.42	22.57	21.55	**22.55**	1.49
Sku	2.91	2.60	3.14	2.73	2.75	3.09	3.45	2.47	3.23	3.35	2.78	4.15	**3.06**	0.46
Ssk	0.410	0.238	-0.289	-0.017	0.085	-0.148	0.249	0.215	0.232	0.366	0.227	0.587	**0.18**	0.24
Sds (1/mm2)	38171	38655	37969	39416	40124	38138	39380	38310	37872	38971	40435	40301	**38978**	939
Ssc (1/mm)	1.37	1.43	1.35	1.14	1.30	1.05	1.43	1.25	1.45	1.46	1.37	1.25	**1.32**	0.13
Str*	0.843	0.900	0.813	0.732	0.454	0.739	0.751	0.743	0.817	0.809	0.794	0.791	**0.765**	0.110
Sal* (μm)	189.4	189.5	202.1	190.0	172.5	170.1	187.0	203.9	226.3	170.1	235.3	196.7	**194.4**	20.5
Std (°)	90.0	66.0	89.9	20.5	0.2	114.0	114.0	114.0	66.0	8.5	36.7	90.0	**67.5**	41.8
Vmp (μm^3/μm^2)**	1.370	1.020	0.883	0.939	0.963	1.061	1.191	1.085	1.448	1.204	1.024	1.424	**1.134**	0.193
Vmc (μm^3/μm^2)**	21.13	20.77	21.17	20.16	20.57	19.68	17.73	24.05	22.38	19.14	20.70	18.19	**20.47**	1.72
Vvc (μm^3/μm^2)**	30.11	29.15	25.43	25.77	28.17	26.06	25.48	34.09	29.08	27.59	29.13	26.38	**28.04**	2.52
Vvv (μm^3/μm^2)**	1.963	1.888	2.425	2.285	2.294	2.839	2.282	2.245	2.767	1.863	1.985	2.055	**2.241**	0.319
Sdr (%)	303.4	286.3	326.0	237.3	373.4	133.7	208.0	302.5	291.7	236.1	196.4	315.9	**267.6**	66.6

_* s = 0.2_
_**p = 10%, q =80%_

Chapter 4 Appendix - 4.3

Change in Sonotrode A Texture Parameters

Texture Parameter	**Pre-Process Texture Parameters**	**Post-process Texture Parameters**	**Change in Texture Parameters**	**Change in Texture Parameters (%)**
Sa (µm)	4.97	4.62	-0.35	-7.0
Sq (µm)	6.40	5.91	-0.49	-7.6
Sku	3.27	3.62	0.36	10.9
Ssk	-0.172	-0.546	-0.374	-216.7
Sds (1/mm2)	39034	40820	1785	4.6
Ssc (1/mm)	1.14	1.21	0.07	6.6
Str*	0.899	0.887	-0.011	-1.3
Sal* (µm)	29.3	27.5	-1.7	-6.0
Std (°)	71.8	73.4	1.6	2.2
Vmp ($\mu m^3/\mu m^2$)**	0.286	0.209	-0.078	-27.1
Vmc ($\mu m^3/\mu m^2$)**	0.00547	0.00519	-0.00028	-5.2
Vvc ($\mu m^3/\mu m^2$)**	0.00754	0.00646	-0.00108	-14.3
Vvv ($\mu m^3/\mu m^2$)**	0.000872	0.000868	-0.000004	-0.5
Sdr (%)	49.4	57.5	8.1	16.4

Change in Sonotrode B Texture Parameters

Texture Parameter	**Pre-Process Texture Parameters**	**Post-process Texture Parameters**	**Change in Texture Parameters**	**Change in Texture Parameters (%)**
Sa (µm)	14.79	14.87	0.09	0.6
Sq (µm)	18.58	18.70	0.12	0.7
Sku	3.06	3.11	0.05	1.6
Ssk	-0.252	-0.267	-0.015	6.1
Sds (1/mm2)	38046	39057	1011	2.7
Ssc (1/mm)	1.13	1.13	0.00	0.4
Str*	0.796	0.721	-0.075	-9.4
Sal* (µm)	159.0	158.1	-0.9	-0.6
Std (°)	68.3	72.8	4.4	6.5
Vmp ($\mu m^3/\mu m^2$)**	0.731	0.774	0.043	5.9
Vmc ($\mu m^3/\mu m^2$)**	16.90	16.97	0.08	0.5
Vvc ($\mu m^3/\mu m^2$)**	21.43	21.51	0.08	0.4
Vvv ($\mu m^3/\mu m^2$)**	2.381	2.387	0.007	0.3
Sdr (%)	120.59	132.28	11.68	9.7

Change in Sonotrode C Texture Parameters

Texture Parameter	**Pre-Process Texture Parameters**	**Post-process Texture Parameters**	**Change in Texture Parameters**	**Change in Texture Parameters (%)**
Sa (µm)	18.87	18.20	-0.67	-3.6
Sq (µm)	23.70	22.55	-1.15	-4.9
Sku	3.32	3.06	-0.26	-7.8
Ssk	0.398	0.18	-0.219	-54.9
Sds (1/mm2)	36693	38978	2285	6.2
Ssc (1/mm)	1.61	1.32	-0.29	-18.1
Str*	0.754	0.765	0.012	1.6
Sal* (µm)	184.2	194.4	10.2	5.5
Std (°)	94.7	67.5	-27.24	-28.8
Vmp (µm^3/µm^2)**	1.339	1.134	-0.204	-15.3
Vmc (µm^3/µm^2)**	21.24	20.47	-0.77	-3.6
Vvc (µm^3/µm^2)**	30.27	28.04	-2.24	-7.4
Vvv (µm^3/µm^2)**	2.161	2.241	0.079	3.7
Sdr (%)	207.9	267.6	59.7	28.7

** s = 0.2*
***p = 10%, q = 80%*

Chapter 4 Appendix - 4.4

Calculation of Wavelength based on Weld Speed

Weld Speed (mm/s)	Wavelength (µm)
20mm/s	1.0
30mm/s	1.5
40mm/s	2.0
60mm/s	3.0

Example Wavelength Calculation:

Sonotrode Oscillation Frequency = 20000Hz
Weld speed = 40mm/s

20000 oscillations over 40mm in 1 second

20000/40 = 500 oscillations over 1 mm

1/500 = 0.002mm wavelength of oscillation

Wavelength = **2µm**

Chapter 5 Appendix - 5.1

Sonotrode A UC Sample Texture Parameters

Texture Parameter	**Measurement Number**												**Av**	**σ**
	58				**59**				**71**					
	a	**b**	**c**	**d**	**a**	**b**	**c**	**d**	**a**	**b**	**c**	**d**		
S_a (µm)	4.05	3.79	4.84	5.27	4.41	5.73	4.76	3.87	3.59	3.81	4.78	4.85	**4.48**	0.67
S_q (µm)	5.38	5.04	6.40	6.65	5.93	7.14	6.40	5.17	4.84	5.05	6.09	6.33	**5.87**	0.75
Sku	4.68	4.09	3.50	3.36	4.23	2.80	4.24	3.99	4.50	4.15	3.37	3.68	**3.88**	0.55
Ssk	1.088	0.092	0.010	0.582	0.652	0.301	0.611	-0.066	0.308	0.333	0.567	0.515	**0.416**	0.322
Sds (1/mm^2)	38105	36730	36306	35827	37363	34078	36110	37680	38312	37094	33055	35290	**36329**	1592
Ssc (1/mm)	0.978	0.979	0.993	0.964	1.028	1.061	0.973	0.967	0.989	0.928	0.893	0.959	**0.976**	0.043
Str*	0.931	0.791	0.728	0.877	0.844	0.899	0.873	0.579	0.551	0.719	0.809	0.845	**0.787**	0.122
Sal* (µm)	26.69	30.01	34.32	28.89	28.61	27.83	30.76	32.35	29.96	26.58	25.46	26.45	**28.99**	2.63
Std (°)	0.2	20.5	105.1	114.0	66.0	114.0	114.0	14.0	159.5	36.7	16.7	66.0	**68.9**	51.8
Vmp (µm^3/µm^2)**	0.472	0.339	0.388	0.429	0.445	0.366	0.494	0.308	0.346	0.334	0.354	0.450	**0.394**	0.062
Vmc (µm^3/µm^2)**	4.07	4.05	5.30	5.73	4.56	6.61	4.85	4.07	3.73	4.00	5.24	5.23	**4.79**	0.87
Vvc (µm^3/µm^2)**	7.18	5.42	7.19	8.84	7.65	9.51	7.82	5.59	5.37	6.36	8.47	8.00	**7.28**	1.37
Vvv (µm^3/µm^2)**	0.397	0.673	0.892	0.528	0.614	0.652	0.728	0.765	0.629	0.541	0.514	0.624	**0.630**	0.130
Sdr (%)	35.17	33.94	38.06	33.59	39.93	41.53	35.79	34.36	34.89	31.68	31.57	36.41	**35.58**	3.03

_* s = 0.2_
_**p = 10%, q =80%_

Sonotrode B UC Sample Texture Parameters

Texture Parameter	**Measurement Number**												**Av**	**σ**
	21				**69**									
	a	**b**	**c**	**d**	**a**	**b**	**c**	**d**	**a**	**b**	**c**	**d**		
S_a (μm)	13.17	12.86	12.41	13.73	13.37	12.09	12.04	11.90	12.46	14.35	12.58	12.72	**12.80**	0.74
S_q (μm)	16.36	16.76	15.62	17.14	17.55	15.96	15.57	15.24	16.43	20.13	16.20	16.07	**16.59**	1.30
Sku	2.89	3.62	2.85	2.97	4.20	3.56	3.30	3.90	3.90	7.23	3.25	3.02	**3.73**	1.19
Ssk	0.050	0.552	-0.200	0.460	0.658	-0.256	-0.070	0.078	-0.025	1.621	0.004	0.112	**0.25**	0.520
Sds (1/mm^2)	33199	36742	33980	34673	35718	33868	36102	36419	35847	35938	34509	33663	**35055**	1207
Ssc (1/mm)	0.736	0.675	0.709	0.701	0.709	0.690	0.709	0.699	0.740	0.742	0.710	0.749	**0.71**	0.023
Str*	0.770	0.368	0.744	0.505	0.631	0.862	0.780	0.899	0.833	0.666	0.710	0.835	**0.72**	0.155
Sal* (μm)	174.5	176.6	175.5	152.1	182.1	136.8	154.9	154.7	161.5	160.3	125.0	159.3	**159.4**	16.8
Std (°)	143.3	20.5	66.0	0.2	8.5	114.0	114.0	114.0	114.0	36.7	159.5	66.0	**79.73**	54.1
Vmp (μm^3/μm^2)**	0.823	1.146	0.616	0.889	1.356	0.821	0.786	0.801	0.928	2.191	0.840	0.797	**1.00**	0.421
Vmc (μm^3/μm^2)**	14.97	14.98	14.22	15.45	14.45	13.83	13.52	13.32	13.70	13.84	14.62	14.43	**14.28**	0.66
Vvc (μm^3/μm^2)**	20.02	21.71	18.56	23.53	21.17	17.49	18.18	17.70	19.44	23.89	19.43	20.48	**20.13**	2.12
Vvv (μm^3/μm^2)**	1.718	1.430	2.001	1.442	1.607	2.275	2.076	1.772	2.078	1.377	1.930	1.672	**1.78**	0.292
Sdr (%)	29.80	25.40	35.34	24.48	26.68	35.91	28.47	27.88	33.94	37.87	36.01	42.81	**32.05**	5.72

** s = 0.2*
***p = 10%, q =80%*

Sonotrode C UC Sample Texture Parameters

Texture Parameter	**Measurement Number**												**Av**	**σ**
	21				**69**									
	a	**b**	**c**	**d**	**a**	**b**	**c**	**d**	**a**	**b**	**c**	**d**		
S_a (μm)	16.57	11.56	14.14	16.87	17.98	18.77	10.43	13.43	14.73	13.16	13.51	12.52	14.47	2.58
S_q (μm)	21.16	17.87	17.33	22.08	21.98	23.42	13.99	17.71	18.95	17.42	16.65	16.56	18.76	2.81
Sku	3.37	7.56	2.90	4.14	3.04	2.87	4.75	3.98	3.46	4.12	2.65	3.51	3.86	1.32
Ssk	-0.245	-0.281	0.062	-0.632	0.238	-0.133	-0.728	-0.606	-0.442	-0.201	-0.313	-0.352	-0.303	0.281
Sds (1/mm^2)	31756	30319	28403	25718	27142	29846	31748	32479	35019	34651	33753	30590	30952	2890
Ssc (1/mm)	0.827	0.635	0.816	0.872	0.920	0.984	0.753	0.814	0.913	0.913	0.902	0.787	0.845	0.094
Str*	0.605	0.860	0.810	0.882	0.893	0.811	0.659	0.870	0.721	0.749	0.753	0.858	0.789	0.093
Sal* (μm)	93.28	58.63	70.88	65.48	71.38	72.68	59.94	76.62	82.93	67.78	68.55	64.45	71.05	9.72
Std (°)	0.2	66.0	175.7	26.4	143.4	166.0	114.0	171.5	114.0	26.5	0.2	79.2	90.3	66.5
Vmp (μm^3/μm^2)**	0.844	1.099	0.764	0.876	0.981	1.116	0.551	0.772	0.683	0.808	0.569	0.790	0.821	0.180
Vmc (μm^3/μm^2)**	18.13	11.57	16.16	19.35	20.10	21.19	10.98	13.99	16.68	13.93	16.04	14.46	16.05	3.24
Vvc (μm^3/μm^2)**	25.21	18.37	21.07	21.92	27.15	26.06	14.99	17.93	21.78	20.72	19.10	17.35	20.97	3.72
Vvv (μm^3/μm^2)**	2.704	3.206	1.769	3.380	2.195	2.933	2.234	3.023	2.654	2.387	2.095	2.450	2.586	0.485
Sdr (%)	44.21	64.64	47.98	78.27	67.15	80.82	44.38	53.48	57.22	64.86	54.12	48.52	58.81	12.43

** s = 0.2*
***p = 10%, q =80%*

Calculation of LWD measurements as a percentage of the weld interface:

Weld interface width of microscopy samples = 25000µm

Width of weld interface used for individual LWD measurements = 370µm

Number of LWD measurements taken per microscopy samples = 5

$$\frac{(370\ \times 5)}{25000} \times 100 = \mathbf{7.4}\%$$

Chapter 5 Appendix - 5.3

8.6.1.1.1 UC Sample A Surface Characterisation Area

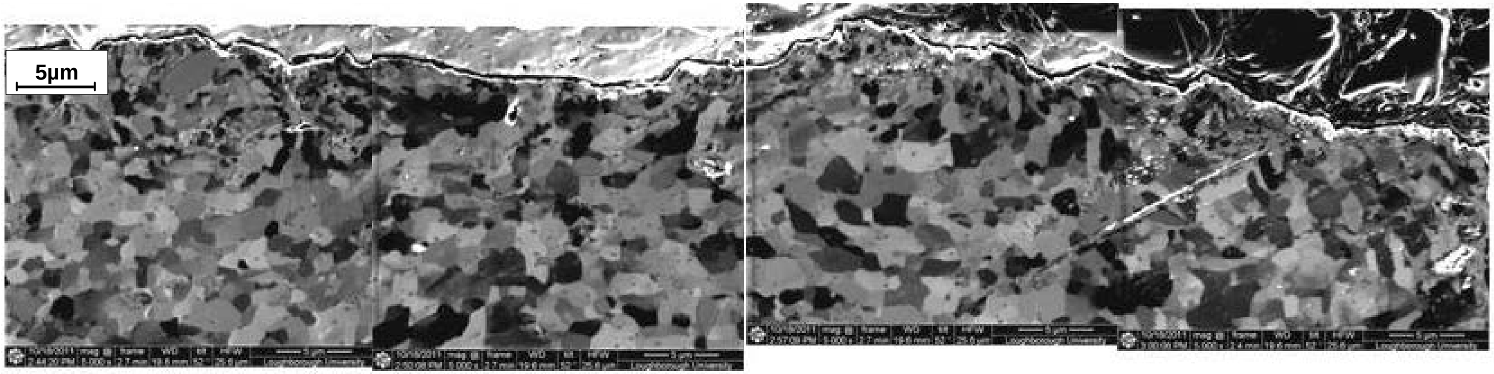

UC Sample B Surface Characterisation Area

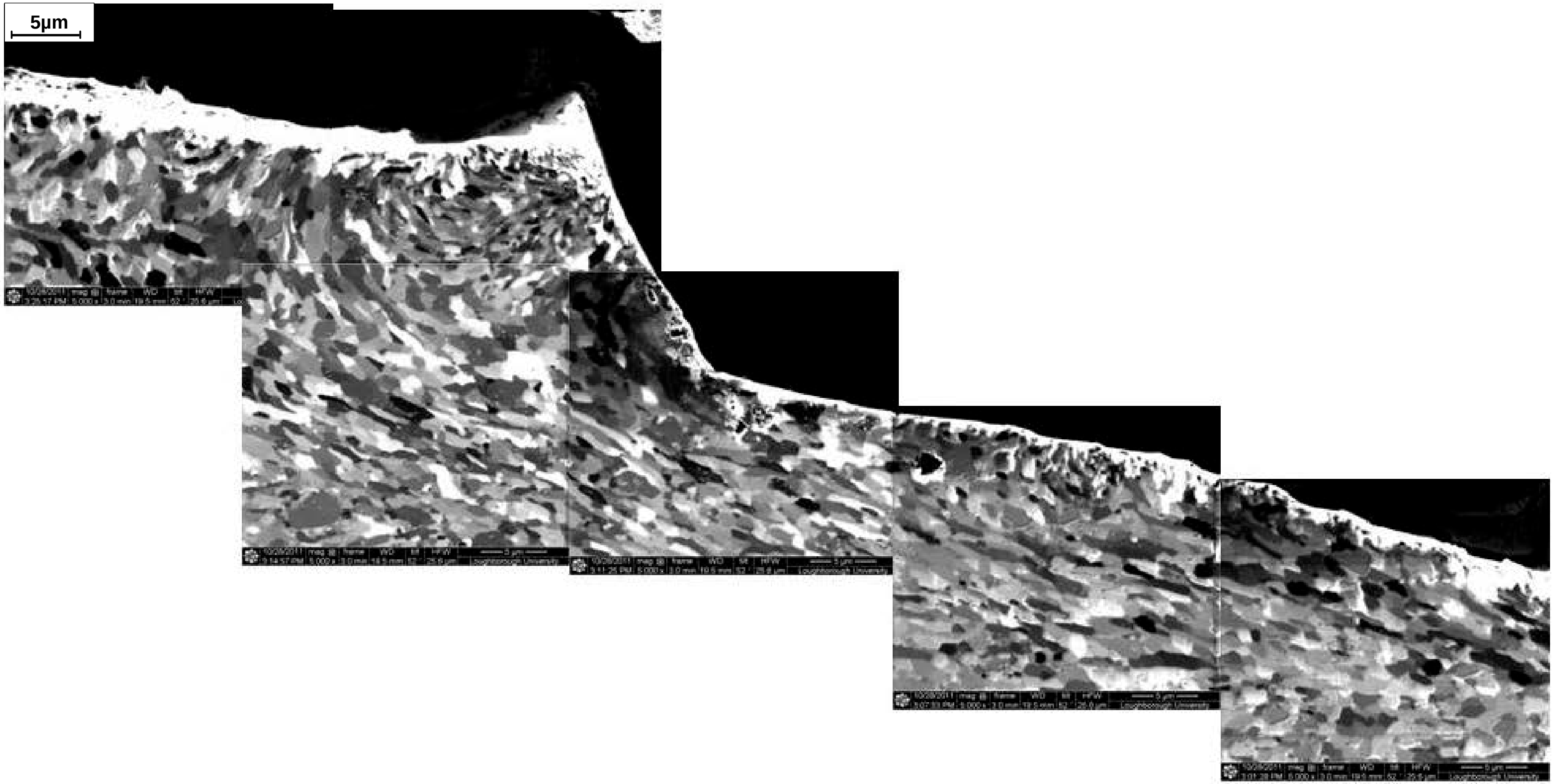

UC Sample C Surface Characterisation Area

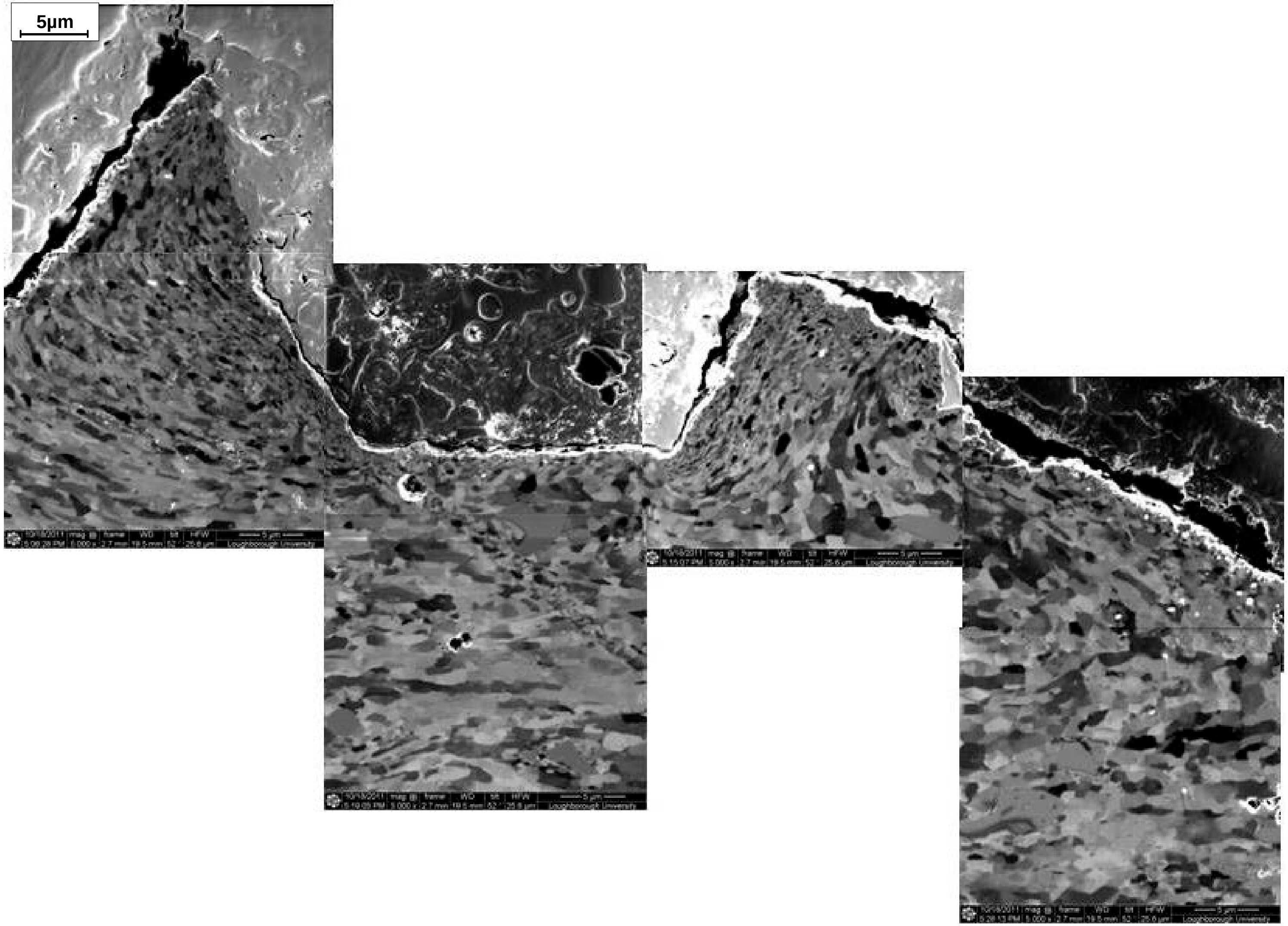

UC Sample A Horizontal Characterisation Area

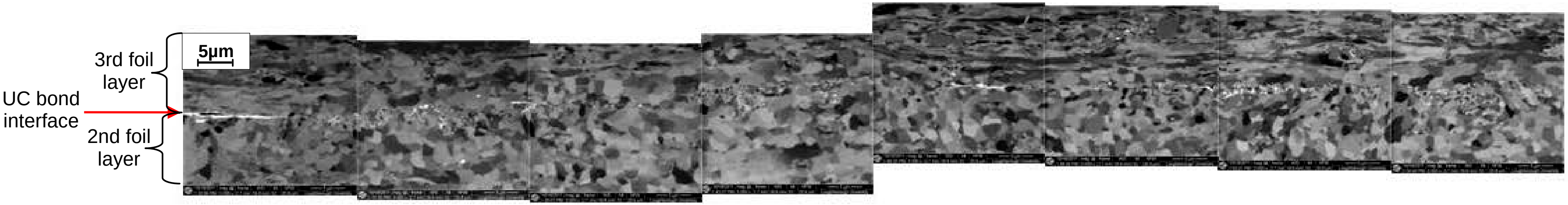

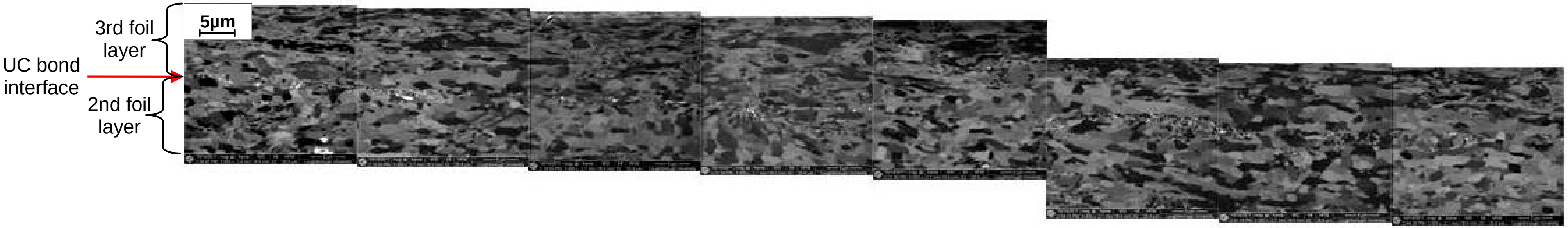

UC Sample B Horizontal Characterisation Area

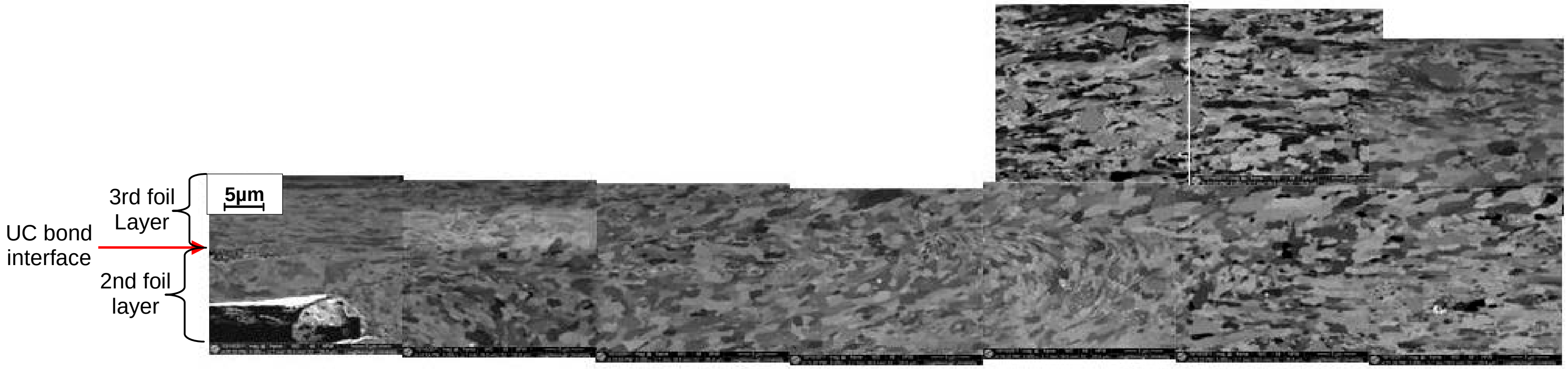

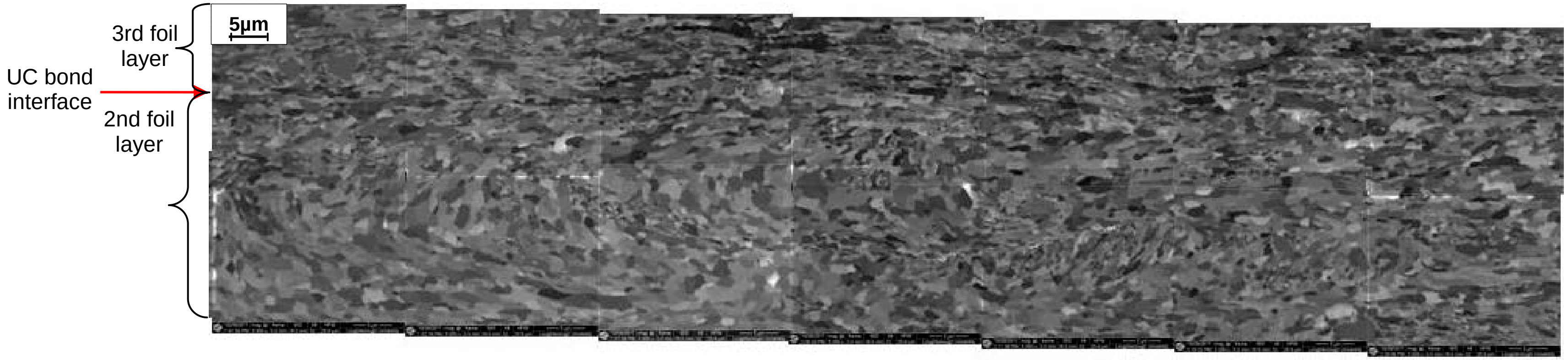

UC Sample C Horizontal Characterisation Area

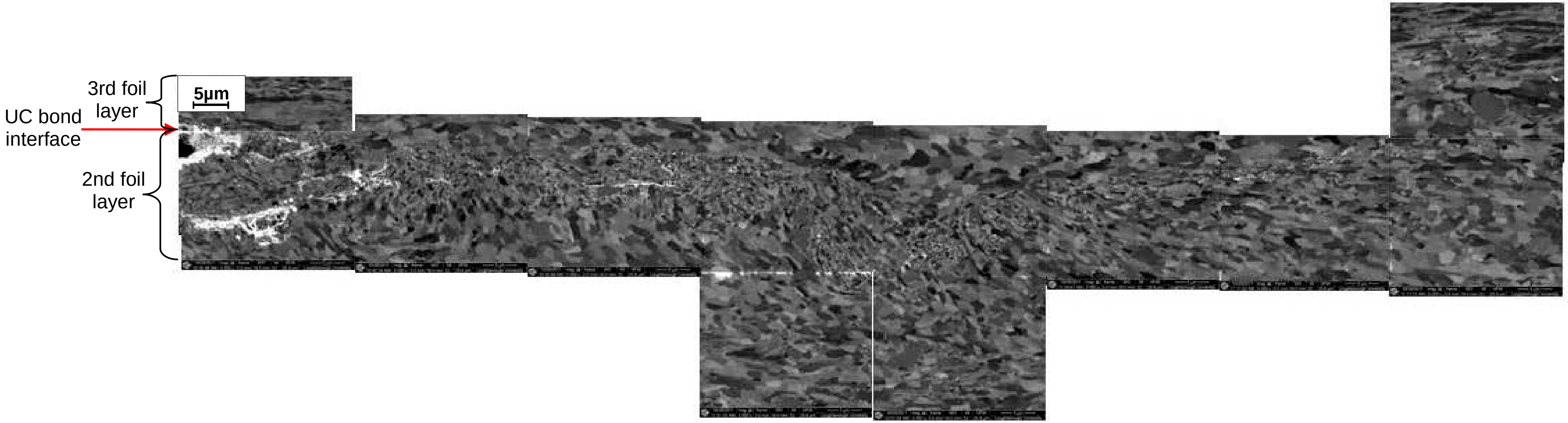

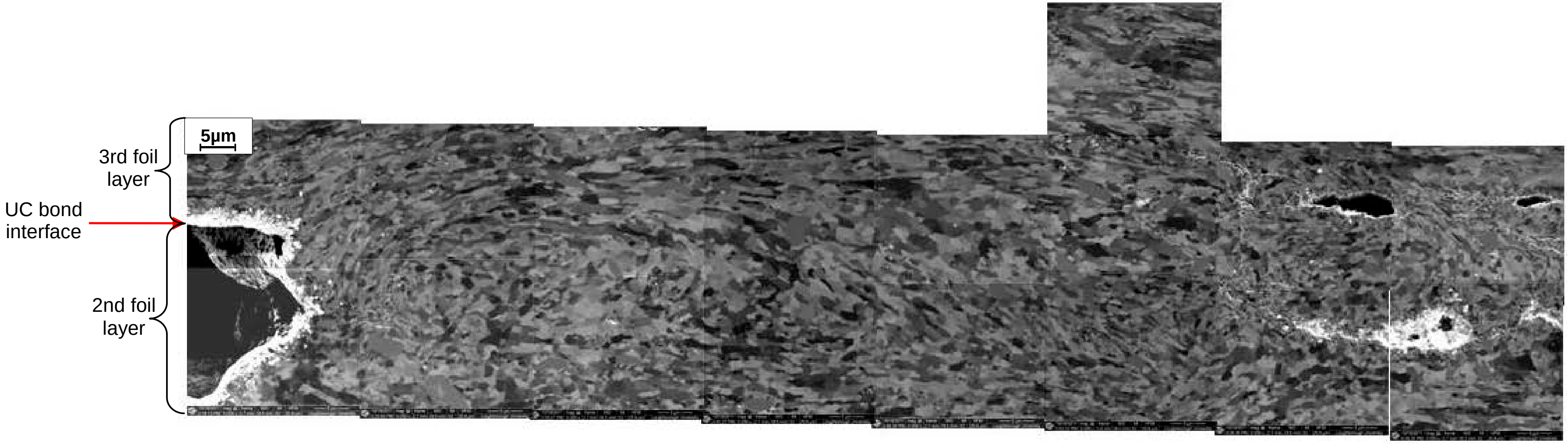

UC Sample A Vertical Characterisation Area

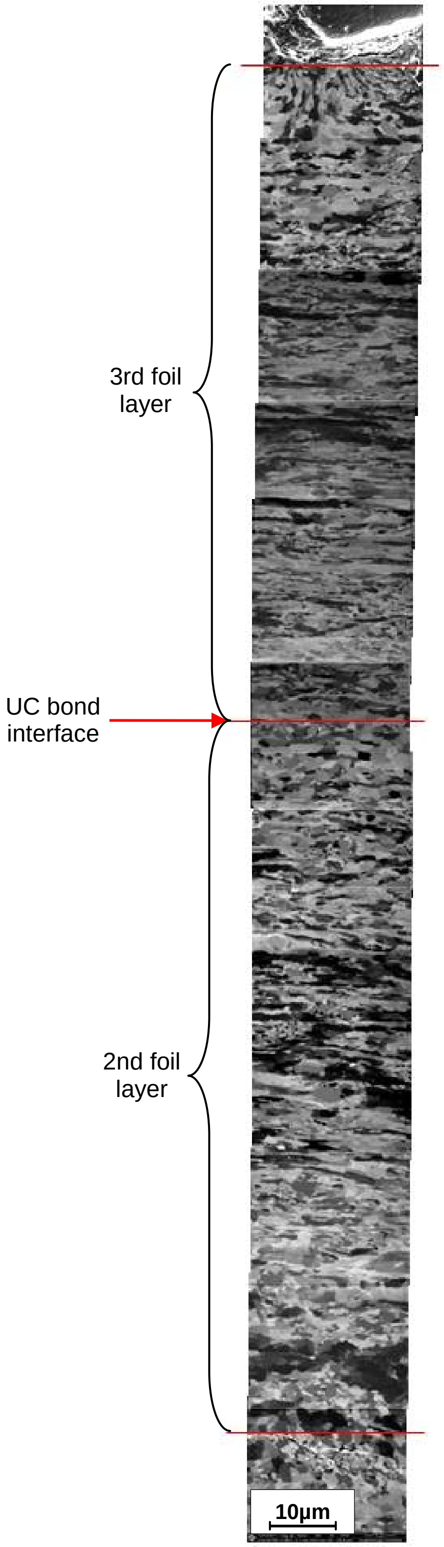

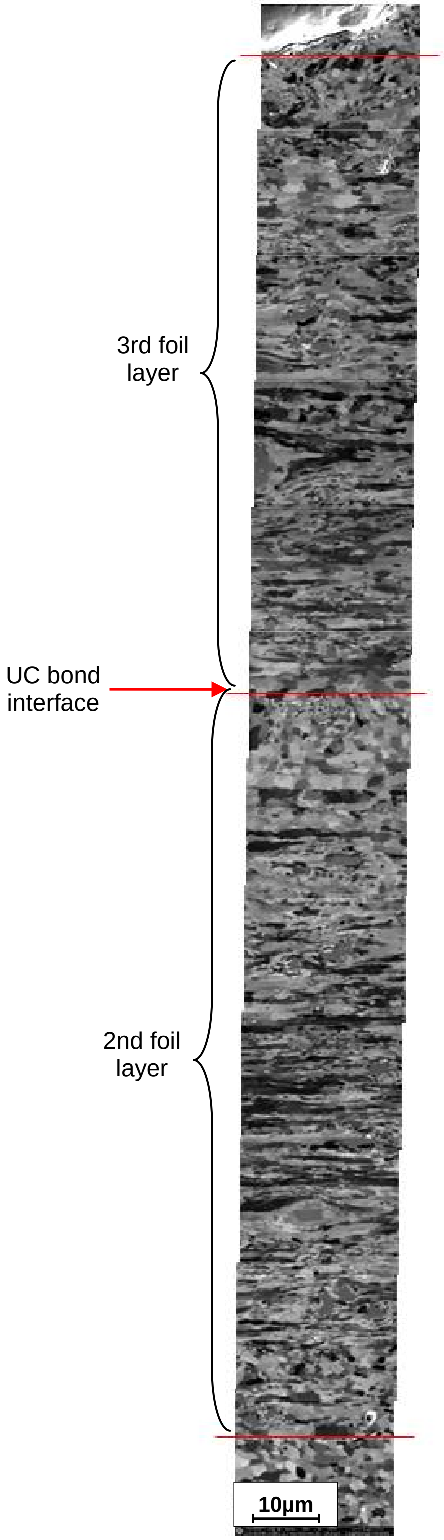

UC Sample B Vertical Characterisation Area

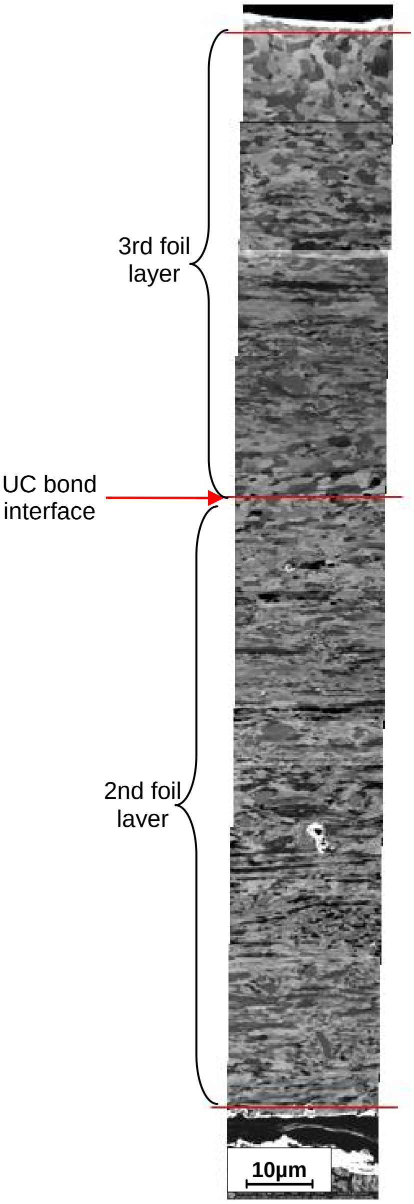

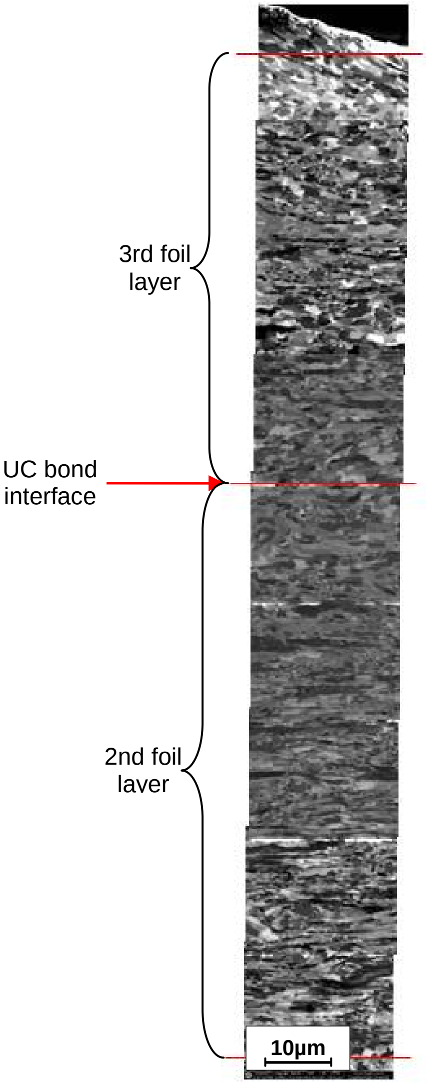

UC Sample C Vertical Characterisation Area

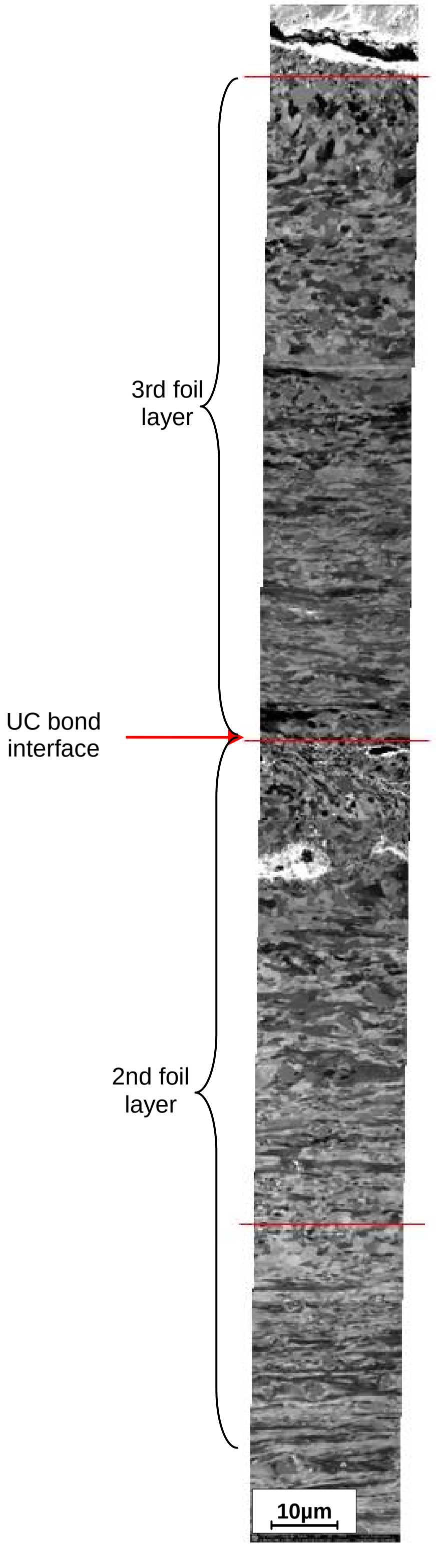

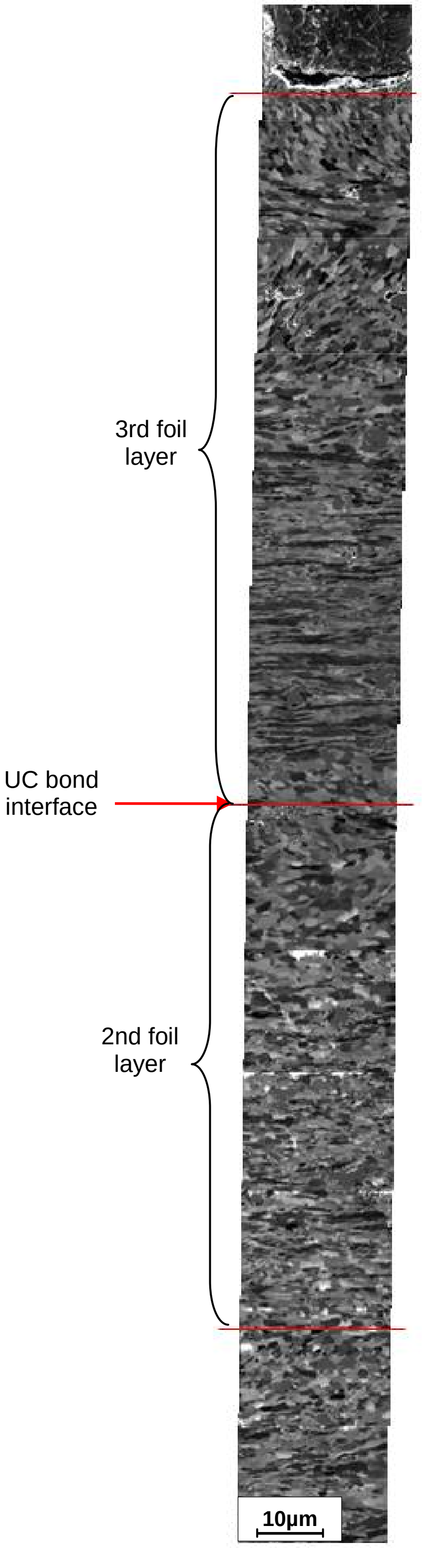

Chapter 5 Appendix - 5.4

Sonotrode A UC Sample Grain Morphology Measurements

Distance From Interface (µm)	Distance From Sample Surface (µm)	Vertical Grain Size, Y (µm)	Horizontal Grain Size, X (µm)	Average Grain Size (µm)	Grain Aspect Ratio (Y/X)
5.0	5.0	0.591	0.655	0.396	0.90
10.0	10.0	0.653	0.840	0.563	0.77
15.0	15.0	0.841	1.464	1.224	0.58
30.0	30.0	0.567	1.314	0.745	0.43
45.0	45.0	0.536	1.382	0.742	0.40
59.0	59.0	0.560	1.416	0.784	0.40
74.0	74.0	0.465	1.478	0.682	0.33
89.0	89.0	0.492	1.507	0.741	0.33
94.0	94.0	0.424	1.143	0.491	0.37
99.0	99.0	0.467	1.094	0.514	0.43
104.0	104.0	0.571	1.268	0.732	0.45
UC Bond Interface					
5.0	109.0	0.646	0.902	0.597	0.74
10.0	114.0	0.770	1.028	0.786	0.80
15.0	119.0	0.719	1.314	0.950	0.54
30.0	134.0	0.568	1.362	0.782	0.42
45.0	149.0	0.459	1.193	0.548	0.39
72.3	176.3	0.487	1.066	0.523	0.46
87.3	191.3	0.443	1.078	0.477	0.41
102.3	206.3	0.457	0.929	0.432	0.49
107.3	211.3	0.646	1.100	0.727	0.60
112.3	216.3	0.717	0.818	0.594	0.87
117.3	221.3	0.615	1.026	0.629	0.60

Sonotrode B UC Sample Grain Morphology Measurements

Distance From Interface (µm)	Distance From Sample Surface (µm)	Vertical Grain Size, Y (µm)	Horizontal Grain Size, X (µm)	Average Grain Size (µm)	Grain Aspect Ratio (Y/X)
5.0	5.0	0.683	1.004	0.686	0.68
10.0	10.0	0.711	1.004	0.709	0.71
15.0	15.0	0.599	0.969	0.597	0.61
30.0	30.0	0.529	0.927	0.502	0.57
46.6	46.6	0.435	0.975	0.429	0.45
61.6	61.6	0.458	0.946	0.437	0.49
66.6	66.6	0.476	1.115	0.533	0.45
71.6	71.6	0.601	0.826	0.496	0.73
76.6	76.6	0.600	1.227	0.736	0.52
UC Bond Interface					
5.0	81.6	0.571	0.905	0.521	0.63
10.0	86.6	0.520	1.222	0.633	0.43
15.0	91.6	0.512	1.480	0.786	0.41
30.0	106.6	0.423	0.997	0.421	0.42
45.0	121.6	0.365	1.024	0.374	0.36
56.7	133.3	0.393	1.142	0.451	0.35
71.7	148.3	0.368	0.985	0.362	0.37
86.7	163.3	0.358	0.908	0.326	0.39
91.7	168.3	0.390	0.901	0.351	0.44
96.7	173.3	0.375	0.857	0.322	0.44
101.7	178.3	0.391	0.921	0.353	0.44

Sonotrode C UC Sample Grain Morphology Measurements

Distance From Interface (µm)	Distance From Sample Surface (µm)	Vertical Grain Size, Y (µm)	Horizontal Grain Size, X (µm)	Average Grain Size (µm)	Grain Aspect Ratio (Y/X)
5.0	5.0	0.741	0.686	0.515	1.07
10.0	10.0	0.732	0.668	0.490	1.10
15.0	15.0	0.848	0.800	0.679	1.06
30.0	30.0	0.622	1.125	0.699	0.55
45.0	45.0	0.596	0.877	0.524	0.69
72.9	72.9	0.516	0.998	0.518	0.52
87.9	87.9	0.373	0.912	0.343	0.41
102.9	102.9	0.419	0.960	0.406	0.44
107.9	107.9	0.492	1.207	0.595	0.41
112.9	112.9	0.458	1.102	0.510	0.42
117.9	117.9	0.646	0.949	0.611	0.68
UC Bond Interface					
5.0	122.9	0.441	0.632	0.279	0.70
10.0	127.9	0.533	0.731	0.390	0.73
15.0	132.9	0.701	1.020	0.699	0.78
30.0	147.9	0.625	0.939	0.587	0.67
41.7	159.6	0.530	0.946	0.506	0.56
56.7	174.6	0.472	1.045	0.494	0.45
71.7	189.6	0.462	0.948	0.438	0.49
76.7	194.6	0.449	0.885	0.402	0.54
81.7	199.6	0.533	1.004	0.534	0.53
86.7	204.6	0.492	0.801	0.394	0.62

Sonotrode induced normal deformation per unit width

The UC process was considered in cross-section (Figure 0-12) in order to calculate the sonotrode induced normal deformation. Two-dimensional peak and surface profiles for each sample (Figure 0-12), based on the measured surface texture parameters (Table 0-1), were used for simplified calculations.

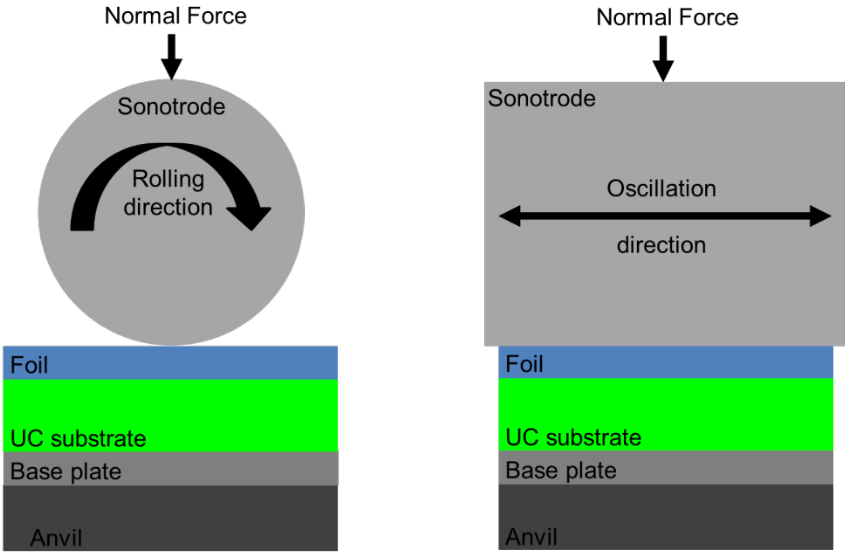

(i) **(ii)**

Figure 0-11: Diagram of the perpendicular (i) and cross-sectional (ii) view of the Alpha 2 UC machine setup.

Table 0-1: Simplified foil surface feature geometry and feature area in cross-section.

Parameter	Sample		
	A	B	C
S_a (µm)	4.48	12.8	14.47
Sal (µm)	28.99	159.42	71.05
Peaks per foil width	862.37	156.82	351.86
Total material displaced (m^2)	0.056	0.160	0.181

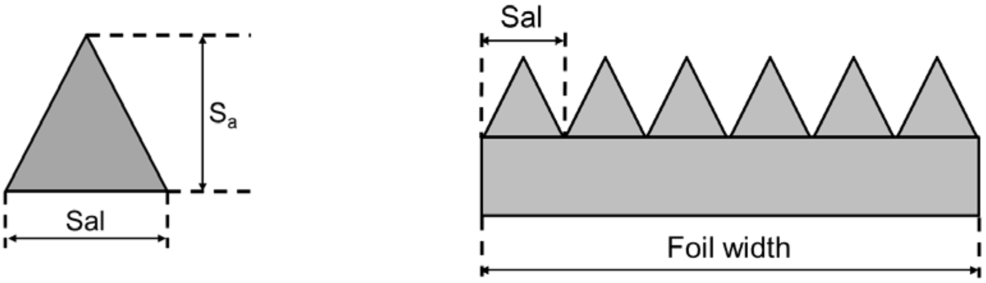

(i) **(ii)**

Figure 0-12: Diagram illustrating simplified peak (i) and surface (ii) cross section for normal deformation calculations.

Example calculations for sample A:

Equation 0-6:

$$Peaks\ per\ foil\ width\ = \frac{Foil\ width}{Sal} = \frac{25000}{28.99} = 862.37$$

Equation 0-7:

$$Cross - sectional\ peak\ area\ = \frac{1}{2}\frac{Sal}{S_a} = \frac{1}{2}\frac{28.99 \times 10^{-3}}{4.48 \times 10^{-3}} = \mathbf{0.056m^2}$$

Chapter 6 Appendix - 6.1

T1 Modified Foil Surface Texture Parameters

Surface Texture Parameters	**Foil Measurements**					
	a	**b**	**c**	**d**	**Av.**	**σ**
S_a (μm)	1.49	1.24	2.33	2.30	1.84	0.56
S_q (μm)	3.17	2.57	4.13	4.75	3.65	0.97
Sku	31.28	19.56	16.31	21.90	22.26	6.43
Ssk	-4.859	-3.508	-3.407	-3.914	-3.922	0.662
Sds (1/mm^2)	44990	57289	54366	47036	50920	5850
Ssc (1/mm)	0.25	0.25	0.41	0.24	0.29	0.08
Sal* (μm)	110.3	143.5	131.3	121.7	126.7	14.1
Str (s = 0.2)	0.568	0.810	0.592	0.698	0.667	0.111
Vmp (μm^3/μm^2)**	0.031	0.125	0.057	0.130	0.086	0.050
Vmc (μm^3/μm^2)**	0.63	0.55	1.32	1.26	0.94	0.41
Vvc (μm^3/μm^2)**	0.83	0.96	1.42	2.27	1.37	0.65
Vvv (μm^3/μm^2)**	0.767	0.602	1.106	1.065	0.885	0.242
Sdr (%)	4.05	4.35	6.20	4.68	4.82	0.95

** s = 0.2*
***p = 10%, q =80%*

T2 Modified Foil Surface Texture Parameters

Surface Texture Parameters	**Foil Measurements**					
	a	**b**	**c**	**d**	**Av.**	**σ**
S_a (μm)	2.40	2.45	1.65	2.56	2.27	0.42
S_q (μm)	3.95	3.68	3.03	4.05	3.68	0.46
Sku	11.95	8.15	19.54	11.01	12.66	4.86
Ssk	-2.818	-2.025	-3.570	-2.722	-2.784	0.632
Sds (1/mm^2)	44533	54663	49920	45905	48755	4554
Ssc (1/mm)	0.36	0.32	0.27	0.29	0.31	0.04
Sal* (μm)	128.1	112.6	78.5	125.0	111.0	22.7
Str (s = 0.2)	0.818	0.772	0.775	0.832	0.799	0.030
Vmp (μm^3/μm^2)**	0.061	0.131	0.070	0.050	0.078	0.036
Vmc (μm^3/μm^2)**	1.18	1.92	0.67	1.55	1.33	0.53
Vvc (μm^3/μm^2)**	1.62	1.92	1.07	1.47	1.52	0.35
Vvv (μm^3/μm^2)**	1.191	0.981	0.846	1.188	1.052	0.169
Sdr (%)	6.61	7.44	6.00	6.23	6.57	0.63

** s = 0.2*
***p = 10%, q =80%*

T3 Modified Foil Surface Texture Parameters

Surface Texture Parameters	Foil Measurements					
	a	b	c	d	Av.	σ
S_a (μm)	3.83	4.18	3.18	3.31	3.62	0.47
S_q (μm)	5.29	5.88	4.77	4.51	5.12	0.61
Sku	6.98	5.85	7.56	4.65	6.26	1.29
Ssk	-1.899	-1.564	-1.858	-1.215	-1.634	0.317
Sds (1/mm^2)	43576	45329	43468	51342	45928	3708
Ssc (1/mm)	0.42	0.41	0.40	0.51	0.43	0.05
Sal* (μm)	116.2	173.2	108.3	149.3	136.8	30.1
Str (s = 0.2)	0.605	0.707	0.741	0.898	0.738	0.122
Vmp (μm^3/μm^2)**	0.108	0.136	0.209	0.165	0.154	0.043
Vmc (μm^3/μm^2)**	4.04	4.12	2.62	3.61	3.60	0.69
Vvc (μm^3/μm^2)**	3.10	4.57	2.67	3.49	3.46	0.81
Vvv (μm^3/μm^2)**	1.189	1.357	1.213	0.933	1.173	0.176
Sdr (%)	9.11	9.29	8.70	10.22	9.33	0.64

** s = 0.2*
***p = 10%, q =80%*

T4 Modified Foil Surface Texture Parameters

Surface Texture Parameters	Foil Measurements					
	a	b	c	d	Av.	σ
S_a (μm)	3.47	1.83	1.93	2.32	2.39	0.75
S_q (μm)	5.65	2.36	3.28	4.05	3.84	1.39
Sku	13.12	17.19	34.39	13.27	19.49	10.11
Ssk	-3.001	-3.563	-5.125	-2.983	-3.668	1.008
Sds (1/mm^2)	47946	46740	42500	44567	45438	2407
Ssc (1/mm)	0.35	0.26	0.32	0.28	0.30	0.04
Sal* (μm)	132.7	116.6	119.7	139.2	127.0	10.7
Str (s = 0.2)	0.592	0.776	0.285	0.672	0.581	0.211
Vmp (μm^3/μm^2)**	0.070	0.031	0.022	0.055	0.044	0.022
Vmc (μm^3/μm^2)**	1.69	0.83	1.07	1.26	1.21	0.36
Vvc (μm^3/μm^2)**	1.95	0.88	1.00	1.87	1.42	0.56
Vvv (μm^3/μm^2)**	1.728	0.930	0.931	1.118	1.177	0.378
Sdr (%)	8.83	5.76	5.31	5.34	6.31	1.69

** s = 0.2*
***p = 10%, q =80%*

T5 Modified Foil Surface Texture Parameters

Surface Texture Parameters	Foil Measurements					
	a	b	c	d	Av.	σ
S_a (μm)	1.14	1.59	1.39	1.24	1.34	0.20
S_q (μm)	3.94	3.34	2.84	2.54	3.16	0.61
Sku	44.63	27.48	26.55	31.24	32.47	8.35
Ssk	-5.452	-4.318	-4.492	-4.813	-4.769	0.499
Sds (1/mm^2)	60118	43630	55135	43254	50534	8440
Ssc (1/mm)	0.25	0.28	0.24	0.26	0.26	0.02
Sal* (μm)	119.1	93.2	138.7	98.2	112.3	20.9
Str (s = 0.2)	0.771	0.675	0.752	0.449	0.662	0.148
Vmp (μm^3/μm^2)**	0.036	0.097	0.023	0.021	0.044	0.036
Vmc (μm^3/μm^2)**	0.68	0.93	0.70	0.73	0.76	0.12
Vvc (μm^3/μm^2)**	0.91	1.63	0.78	0.79	1.03	0.40
Vvv (μm^3/μm^2)**	0.525	0.722	0.690	0.580	0.629	0.092
Sdr (%)	4.40	4.65	4.05	4.02	4.28	0.30

_* s = 0.2_
_**p = 10%, q =80%_

T6 Modified Foil Surface Texture Parameters

Surface Texture Parameters	Foil Measurements					
	a	b	c	d	Av.	σ
S_a (μm)	2.11	3.97	2.93	4.22	3.31	0.97
S_q (μm)	3.82	6.30	4.39	6.31	5.20	1.29
Sku	16.62	15.70	9.30	10.05	12.92	3.78
Ssk	-2.726	-2.970	-2.218	-2.261	-2.544	0.366
Sds (1/mm^2)	46070	44593	44985	54788	47609	4827
Ssc (1/mm)	0.31	0.39	0.41	0.50	0.40	0.08
Sal* (μm)	130.1	133.6	133.4	155.5	138.1	11.7
Str (s = 0.2)	0.803	0.790	0.822	0.711	0.781	0.049
Vmp (μm^3/μm^2)**	0.181	0.126	0.129	0.178	0.154	0.030
Vmc (μm^3/μm^2)**	1.31	3.16	2.45	3.78	2.67	1.06
Vvc (μm^3/μm^2)**	2.11	3.26	2.48	3.70	2.89	0.73
Vvv (μm^3/μm^2)**	0.903	1.602	1.109	1.529	1.286	0.335
Sdr (%)	5.70	8.46	7.25	10.36	7.94	1.97

_* s = 0.2_
_**p = 10%, q =80%_

T7 Modified Foil Surface Texture Parameters

Surface Texture Parameters	Foil Measurements					
	a	b	c	d	Av.	σ
S_a (μm)	3.65	3.64	4.04	3.45	3.69	0.25
S_q (μm)	5.02	5.28	5.55	5.23	5.27	0.22
Sku	6.26	10.81	6.80	10.41	8.57	2.37
Ssk	-1.742	-2.289	-1.734	-2.209	-1.994	0.296
Sds (1/mm^2)	47058	45431	53556	44320	47591	4133
Ssc (1/mm)	0.41	0.37	0.52	0.34	0.41	0.08
Sal* (μm)	134.3	111.6	126.6	119.3	123.0	9.8
Str (s = 0.2)	0.883	0.747	0.869	0.818	0.829	0.062
Vmp (μm^3/μm^2)**	0.124	0.130	0.129	0.137	0.130	0.005
Vmc (μm^3/μm^2)**	3.78	3.53	4.35	2.88	3.64	0.61
Vvc (μm^3/μm^2)**	3.15	3.23	3.93	3.38	3.42	0.35
Vvv (μm^3/μm^2)**	1.120	1.217	1.169	1.283	1.197	0.070
Sdr (%)	10.67	9.05	12.19	7.58	9.87	2.00

** s = 0.2*
***p = 10%, q =80%*

Chapter 6 Appendix - 6.2

T1 Modified Sample Surface Texture Parameters

Texture Parameter	Measurement Number													
	X				Y				Z				Av	σ
	a	b	c	d	a	b	c	d	a	b	c	d		
S_a (µm)	10.84	10.36	11.29	12.28	11.59	12.02	13.53	12.16	10.50	12.21	10.10	12.18	11.59	1.00
S_q (µm)	14.35	13.19	14.70	15.53	14.89	15.32	16.65	16.55	13.86	15.61	13.44	16.37	15.04	1.18
Sku	3.87	3.29	3.56	3.28	3.13	3.22	2.94	4.26	3.40	3.12	4.09	3.90	3.51	0.43
Ssk	-0.249	-0.139	0.239	0.388	-0.039	0.092	0.027	-0.740	0.198	0.093	0.286	-0.206	-0.004	0.304
Sds (1/mm^2)	37348	38860	36507	38861	36299	36724	36329	35267	36127	34766	36972	34609	36556	1362
Ssc (1/mm)	0.77	0.74	0.76	0.77	0.63	0.73	0.73	0.72	0.68	0.74	0.73	0.68	0.72	0.04
Str (s = 0.2)	0.842	0.821	0.797	0.833	0.756	0.693	0.483	0.704	0.889	0.847	0.645	0.447	0.730	0.143
Sal* (µm)	138.7	158.4	141.0	188.5	152.1	142.9	151.3	154.9	131.9	161.7	127.9	127.4	148.1	17.2
Vmp (µm^3/µm^2)**	0.784	0.675	0.888	1.075	0.839	0.924	0.815	0.703	0.863	0.840	1.013	0.903	0.860	0.114
Vmc (µm^3/µm^2)**	12.09	11.61	12.82	13.57	12.65	13.60	15.20	12.96	12.13	13.92	10.79	13.67	12.92	1.18
Vvc (µm^3/µm^2)**	16.31	15.24	18.01	18.46	17.24	17.92	19.93	17.20	17.08	18.88	14.82	18.33	17.45	1.47
Vvv (µm^3/µm^2)**	1.965	1.639	1.611	1.569	1.992	1.735	1.790	2.865	1.554	1.816	1.608	2.264	1.867	0.379
Sdr (%)	36.84	29.77	31.26	31.21	30.15	33.47	32.37	37.33	33.33	32.02	29.54	38.62	32.99	3.07

** s = 0.2*
***p = 10%, q =80%*

T2 Modified Sample Surface Texture Parameters

Texture Parameter	**Measurement Number**													
	X				**Y**				**Z**				**Av**	**σ**
	a	**b**	**c**	**d**	**a**	**b**	**c**	**d**	**a**	**b**	**c**	**d**		
S_a (µm)	10.62	10.96	10.18	10.57	10.74	9.51	11.89	11.22	11.37	11.95	11.22	16.72	11.41	1.81
S_q (µm)	14.61	14.28	13.31	14.02	13.92	13.07	14.80	14.53	14.70	15.21	14.25	21.04	14.81	2.05
Sku	4.61	3.66	3.63	3.85	3.81	4.42	2.93	3.76	3.36	3.32	3.16	3.95	3.71	0.49
Ssk	-0.238	-0.124	-0.037	-0.294	-0.323	-0.533	0.118	-0.123	-0.339	0.389	-0.202	0.734	-0.081	0.350
Sds (1/mm^2)	35972	39469	37189	37496	36175	37829	35643	36133	36005	35966	34799	34187	36405	1413
Ssc (1/mm)	0.69	0.75	0.72	0.73	0.74	0.64	0.67	0.67	0.67	0.69	0.70	0.71	0.70	0.03
Str (s = 0.2)	0.817	0.595	0.894	0.514	0.697	0.478	0.576	0.877	0.724	0.688	0.897	0.637	0.700	0.147
Sal* (µm)	160.1	163.8	152.0	117.9	132.8	152.7	149.0	144.3	149.8	142.2	140.1	157.0	146.8	12.6
Vmp (µm^3/µm^2)**	0.906	0.881	0.700	0.660	0.733	0.746	0.835	0.783	0.659	0.861	0.630	1.426	0.818	0.212
Vmc (µm^3/µm^2)**	11.23	12.07	11.86	12.39	11.90	10.21	13.68	12.55	13.41	13.76	13.19	17.84	12.84	1.89
Vvc (µm^3/µm^2)**	16.30	15.62	15.77	16.19	15.03	12.96	17.62	17.41	16.77	19.84	16.75	27.03	17.27	3.48
Vvv (µm^3/µm^2)**	2.154	1.875	1.621	1.934	1.878	2.161	1.510	1.688	1.963	1.371	1.722	1.663	1.795	0.243
Sdr (%)	33.29	30.43	31.28	38.12	38.46	28.18	26.73	29.43	33.52	36.28	32.24	37.63	32.97	3.98

** s = 0.2*
***p = 10%, q =80%*

T3 Modified Sample Surface Texture Parameters

Texture Parameter	**Measurement Number**													
	X				**Y**				**Z**				**Av**	**σ**
	a	**b**	**c**	**d**	**a**	**b**	**c**	**d**	**a**	**b**	**c**	**d**		
S_a (μm)	6.86	9.01	11.41	11.07	11.25	11.41	10.27	10.99	11.07	12.26	12.64	11.72	10.83	1.55
S_q (μm)	9.36	12.06	14.67	15.18	14.52	14.65	13.05	14.31	13.98	15.65	16.27	15.04	14.06	1.85
Sku	4.71	3.81	3.43	5.88	3.20	3.29	3.35	3.34	2.96	3.10	3.48	3.30	3.65	0.83
Ssk	-0.575	0.128	0.133	-0.500	0.041	-0.104	0.139	-0.208	-0.065	-0.143	-0.067	-0.012	-0.103	0.232
Sds (1/mm^2)	37991	39306	36735	36456	36247	35467	36654	34066	36599	35302	35518	34806	36262	1409
Ssc (1/mm)	0.63	0.66	0.71	0.71	0.68	0.72	0.70	0.68	0.68	0.70	0.70	0.69	0.69	0.03
Str (s = 0.2)	0.559	0.858	0.747	0.819	0.898	0.573	0.875	0.915	0.870	0.868	0.691	0.757	0.786	0.123
Sal* (μm)	145.0	159.3	136.7	172.2	159.6	149.8	154.2	124.0	171.3	160.1	160.0	153.8	153.8	13.7
Vmp (μm^3/μm^2)**	0.486	0.788	0.890	0.907	0.827	0.794	0.747	0.749	0.702	0.844	0.948	0.760	0.787	0.120
Vmc (μm^3/μm^2)**	6.90	9.91	13.38	12.35	12.65	13.33	11.62	12.75	12.66	14.52	14.06	13.15	12.27	2.06
Vvc (μm^3/μm^2)**	9.41	14.40	17.21	16.04	17.62	16.95	15.99	15.94	16.10	17.33	18.42	18.09	16.13	2.39
Vvv (μm^3/μm^2)**	1.580	1.440	1.635	2.106	1.775	1.751	1.372	1.957	1.725	1.902	2.009	1.817	1.756	0.223
Sdr (%)	24.46	27.15	31.76	31.22	28.57	30.70	27.81	33.97	26.63	29.04	28.00	32.19	29.29	2.72

** s = 0.2*
***p = 10%, q =80%*

T4 Modified Sample Surface Texture Parameters

Texture Parameter	**Measurement Number**													
	X				**Y**				**Z**				**Av**	**σ**
	a	**b**	**c**	**d**	**a**	**b**	**c**	**d**	**a**	**b**	**c**	**d**		
S_a (µm)	9.55	10.18	10.02	9.86	12.05	11.69	12.84	14.42	11.63	11.39	13.29	12.02	11.58	1.49
S_q (µm)	12.45	12.84	12.72	12.54	15.15	14.60	16.84	18.76	15.38	15.11	17.27	15.49	14.93	2.04
Sku	4.06	3.12	2.96	3.16	2.95	3.11	4.26	4.51	3.73	3.67	3.47	3.37	3.53	0.52
Ssk	-0.098	-0.109	-0.119	0.021	-0.201	0.008	0.710	-0.603	-0.130	0.008	0.213	0.019	-0.024	0.302
Sds (1/mm^2)	40438	37359	35862	35737	34627	38877	32936	33597	35596	34587	36343	33457	35785	2239
Ssc (1/mm)	0.72	0.77	0.66	0.67	0.69	0.65	0.68	0.72	0.67	0.67	0.71	0.72	0.69	0.03
Str (s = 0.2)	0.852	0.786	0.886	0.925	0.739	0.744	0.761	0.769	0.729	0.736	0.829	0.776	0.794	0.064
Sal* (µm)	169.8	126.6	143.5	151.3	148.7	175.4	127.0	172.4	125.8	145.4	171.8	125.1	148.6	19.9
Vmp (µm^3/µm^2)**	0.668	0.590	0.606	0.663	0.700	0.894	1.302	0.695	0.844	0.880	1.047	0.862	0.813	0.207
Vmc (µm^3/µm^2)**	10.64	11.89	11.94	11.69	14.37	13.85	14.21	16.73	13.00	13.10	14.68	13.33	13.29	1.64
Vvc (µm^3/µm^2)**	14.68	15.33	15.05	14.94	17.68	15.91	21.22	21.69	17.19	16.77	21.15	18.78	17.53	2.61
Vvv (µm^3/µm^2)**	1.520	1.463	1.531	1.422	1.790	1.565	1.463	2.389	2.086	2.024	1.967	1.819	1.753	0.310
Sdr (%)	31.07	36.70	30.33	29.98	33.02	27.47	32.84	34.92	34.27	32.80	33.47	36.79	32.81	2.76

* s = 0.2
**p = 10%, q =80%

T5 Modified Sample Surface Texture Parameters

Texture Parameter	**Measurement Number**													
	X				**Y**				**Z**				**Av**	**σ**
	a	**b**	**c**	**d**	**a**	**b**	**c**	**d**	**a**	**b**	**c**	**d**		
S_a (µm)	11.61	11.64	11.52	10.70	10.72	11.98	11.48	11.96	10.58	13.29	13.26	12.47	11.77	0.90
S_q (µm)	14.79	15.17	15.07	13.62	14.24	15.07	14.81	15.54	13.84	17.53	16.56	16.17	15.20	1.13
Sku	3.11	3.85	3.45	3.15	4.41	3.29	3.56	3.43	4.38	3.33	2.96	3.34	3.52	0.47
Ssk	0.164	-0.538	-0.198	-0.114	0.596	-0.329	-0.214	0.240	0.020	-0.013	0.327	0.188	0.011	0.313
Sds (1/mm^2)	35813	36246	36255	36247	37220	39038	36752	36901	36243	33531	34605	35379	36186	1361
Ssc (1/mm)	0.69	0.66	0.65	0.66	0.69	0.65	0.67	0.70	0.67	0.71	0.74	0.70	0.68	0.03
Str (s = 0.2)	0.522	0.413	0.754	0.697	0.739	0.507	0.599	0.855	0.719	0.381	0.659	0.870	0.643	0.161
Sal* (µm)	160.28	137.93	155.25	158.52	149.79	182.82	164.63	149.07	143.72	137.87	147.77	173.51	155.09	13.74
Vmp (µm^3/µm^2)**	0.821	0.719	0.822	0.718	1.031	0.747	0.856	0.901	0.837	0.938	0.893	0.936	0.852	0.095
Vmc (µm^3/µm^2)**	13.46	12.34	13.16	12.28	11.58	13.75	13.19	13.93	12.42	15.12	14.30	14.59	13.34	1.06
Vvc (µm^3/µm^2)**	18.38	15.45	16.79	15.97	17.43	15.71	15.29	19.45	15.58	20.60	21.70	19.68	17.67	2.24
Vvv (µm^3/µm^2)**	1.581	2.436	2.044	1.667	1.406	1.981	1.977	1.671	1.552	2.345	1.607	1.806	1.839	0.322
Sdr (%)	28.80	28.93	27.25	26.13	27.33	28.07	29.35	32.13	30.84	37.49	33.11	30.41	29.99	3.13

** s = 0.2*
***p = 10%, q =80%*

T6 Modified Sample Surface Texture Parameters

Texture Parameter	**Measurement Number**													
	X				**Y**				**Z**				**Av**	**σ**
	a	**b**	**c**	**d**	**a**	**b**	**c**	**d**	**a**	**b**	**c**	**d**		
S_a (µm)	11.78	12.10	10.54	11.66	11.23	11.54	11.52	10.63	10.65	11.96	10.97	13.77	11.53	0.88
S_q (µm)	15.03	16.10	13.89	15.00	14.80	15.02	14.47	13.14	14.37	16.05	13.91	17.17	14.91	1.11
Sku	3.34	3.96	3.71	3.40	3.93	3.55	3.10	2.92	4.21	4.56	3.51	2.81	3.58	0.52
Ssk	0.147	0.141	-0.343	0.229	0.054	-0.160	0.082	-0.001	0.177	-0.487	0.228	0.177	0.020	0.232
Sds (1/mm^2)	36019	36283	34277	35083	36430	36063	36858	38796	36248	34037	38460	33702	36021	1592
Ssc (1/mm)	0.75	0.74	0.67	0.69	0.70	0.69	0.74	0.67	0.70	0.74	0.69	0.75	0.71	0.03
Str (s = 0.2)	0.850	0.540	0.818	0.769	0.614	0.757	0.793	0.738	0.734	0.570	0.808	0.825	0.735	0.104
Sal* (µm)	136.22	129.57	140.95	147.99	141.61	133.34	187.69	186.00	124.96	155.03	206.37	138.24	152.33	26.39
Vmp (µm^3/µm^2)**	0.907	1.091	0.765	1.052	1.024	0.794	0.740	0.679	0.961	0.795	0.921	0.805	0.878	0.134
Vmc (µm^3/µm^2)**	13.42	13.30	12.37	12.84	12.19	12.33	13.17	12.32	11.46	12.98	12.91	15.95	12.94	1.10
Vvc (µm^3/µm^2)**	17.64	18.91	15.07	17.18	16.54	17.37	17.16	15.43	15.83	17.59	15.84	22.24	17.23	1.92
Vvv (µm^3/µm^2)**	1.663	1.893	1.888	1.669	1.777	2.021	1.636	1.411	1.950	2.368	1.377	1.677	1.778	0.272
Sdr (%)	36.59	36.11	30.68	32.09	28.95	29.40	30.95	26.05	29.91	37.85	28.23	36.75	31.96	3.90

** s = 0.2*
***p = 10%, q =80%*

T7 Modified Sample Surface Texture Parameters

Texture Parameter	**Measurement Number**													
	X				**Y**				**Z**				**Av**	**σ**
	A	**b**	**c**	**d**	**a**	**b**	**c**	**d**	**a**	**b**	**c**	**d**		
S_a (μm)	12.05	9.62	12.16	11.02	9.77	14.71	11.69	11.66	11.47	10.65	10.16	13.12	11.51	1.45
S_q (μm)	15.39	12.61	15.42	14.51	12.89	18.43	15.17	15.04	14.76	13.82	13.20	16.27	14.79	1.60
Sku	3.24	3.89	3.37	3.43	3.99	3.07	3.22	3.32	3.45	3.33	3.47	2.85	3.39	0.31
Ssk	-0.150	-0.182	0.502	0.157	0.485	-0.181	-0.304	0.084	0.288	0.147	-0.213	0.182	0.068	0.274
Sds (1/mm^2)	34291	37076	35338	35790	38730	34908	35595	38063	34850	36018	36515	37473	36221	1375
Ssc (1/mm)	0.73	0.74	0.74	0.73	0.68	0.72	0.71	0.69	0.74	0.72	0.73	0.73	0.72	0.02
Str (s = 0.2)	0.537	0.822	0.757	0.850	0.756	0.884	0.807	0.739	0.667	0.749	0.868	0.805	0.770	0.096
Sal* (μm)	142.2	140.5	141.4	134.7	137.0	168.3	133.6	154.2	128.6	135.9	131.3	154.6	141.8	11.6
Vmp (μm^3/μm^2)**	0.812	0.697	0.939	0.845	0.890	0.794	0.711	0.861	0.911	0.825	0.726	0.811	0.819	0.078
Vmc (μm^3/μm^2)**	14.46	10.99	13.01	12.48	10.73	16.01	14.01	13.13	12.77	11.89	11.72	14.78	13.00	1.59
Vvc (μm^3/μm^2)**	17.29	14.26	20.59	17.69	15.90	21.72	17.07	18.01	18.11	16.85	14.13	20.57	17.68	2.38
Vvv (μm^3/μm^2)**	1.809	1.639	1.421	1.753	1.349	2.345	2.053	1.828	1.575	1.570	1.823	1.610	1.731	0.273
Sdr (%)	34.21	34.10	35.50	36.91	26.53	36.12	36.64	33.18	35.08	30.53	30.33	31.03	33.35	3.15

** s = 0.2*
***p = 10%, q =80%*

Chapter 6 Appendix - 6.3

Modified Sample Bond Strength Measurements

Foil Sample Number	**Weld Speed (mm/s)**	**Weld Force (N)**	**Number of Passes**	**Maximum Peeling Load (N)**				
				X	**Y**	**Z**	**Av.**	**σ**
T1	40	1400	1	-	87.54	83.80	85.67	2.64
T2	40	1400	2	89.06	90.41	88.81	89.43	0.86
T3	40	1400	3	82.90	91.30	103.14	92.44	10.17
T4	40	2000	1	83.49	92.39	90.60	88.83	4.71
T5	10	1400	1	85.79	88.97	91.09	88.62	2.67
T6	10	1400	2	85.09	90.68	111.86	95.88	14.12
T7	10	1400	3	97.36	90.39	-	93.87	4.93

Chapter 6 Appendix - 6.4

Modified Sample Linear Weld Density Measurements

Foil Sample Number	Section Location	LWD (%)							
		1	2	3	4	5	Section Av.	Sample Av.	Sample σ
1	End	32.06	82.11	83.28	47.06	49.76	58.86	**62.08**	**18.46**
	Middle	98.34	52.80	93.74	91.59	73.22	81.94		
	Start	55.43	48.19	35.00	63.64	24.93	45.44		
2	End	72.70	93.05	41.74	33.24	44.28	57.00	**54.60**	**3.91**
	Middle	42.82	59.24	26.00	30.99	91.40	50.09		
	Start	88.76	62.65	41.88	60.70	29.54	56.71		
3	End	62.76	85.04	52.49	49.80	43.79	58.78	**55.92**	**9.13**
	Middle	93.54	54.15	76.05	41.82	50.83	63.28		
	Start	93.50	55.97	0.00	65.98	13.10	45.71		
4	End	46.18	74.88	50.39	76.74	36.85	57.01	**46.57**	**9.28**
	Middle	45.16	11.94	97.85	3.42	37.96	39.27		
	Start	43.74	9.58	88.76	6.65	68.43	43.43		
5	End	96.48	28.63	0.00	17.22	84.75	45.42	**54.40**	**8.82**
	Middle	56.99	80.06	75.37	47.41	13.80	54.72		
	Start	66.08	61.09	86.41	27.66	74.00	63.05		
6	End	92.96	93.64	63.54	51.71	46.77	69.72	**75.31**	**5.89**
	Middle	90.52	80.74	58.75	79.08	98.24	81.47		
	Start	74.58	74.00	94.04	73.80	57.28	74.74		
7	End	56.21	77.13	66.18	19.28	45.65	52.89	**60.27**	**16.72**
	Middle	79.86	89.05	67.45	83.19	77.52	79.41		
	Start	68.46	59.39	54.74	2.83	57.10	48.50		